Metal-Insulator-Metal Plasmonic Colour Filters for CMOS Image Sensor Applications



Nadia Pinton
Somerville College
University of Oxford

A thesis submitted for the degree of
Doctor of Philosophy

Trinity 2020

To my son Ethan

This Thesis is one of my greatest achievement

but being your mamma is my greatest honour

I love you to the moon and back

Acknowledgements

I would like to thank my supervisor, Steve Collins, for the support, the thousands advices and the invaluable guidance throughout the course of this project. More than a supervisor you have been a mentor to me and for that I am very thankful. I would also like to thank my second supervisor, David Cumming, for hosting my research placement at the University of Glasgow and making me feel part of his group. Special thanks go also to James Grant. Thank you for every discussion, every morning chat, every laugh. Thank you for always being available. You are the postdoc that every Ph.D. student should have. Vorrei anche ringraziare le mie amiche più care, Romina e Valeria, per esserci sempre state nel corso di questi anni.

Finally, I would like to thank my wonderful family. Thank you to my fiancé, Martin. I could not have finished this Thesis without your unconditional love, help and support. Even if I do not laugh at all your jokes, I love you with all my heart. I cannot wait to start the new chapter in our life. And thank you to my sweet baby boy Ethan for making the world a better and happier place. Infine, grazie ai miei meravigliosi genitori. Grazie mamma, grazie papà. Grazie di avermi sempre incoraggiato e sostenuto. Non avrei potuto farcela senza di voi.

Abstract

Significant improvement in using plasmonic nanostructures for practical colour filtering and multispectral imaging applications is achieved by exploiting the coupling of surface plasmon polaritons with dielectric optical cavity resonances within a hexagonal array of subwavelength holes in a thin CMOS-compatible metal-insulator-metal (MIM) stack. This architecture overcomes the limitations of all previously reported plasmonic colour filters, namely poor transmission and broad band-pass characteristic, effectively providing a compact approach to selectively filter light. The physical insights established from the electromagnetic near-field patterns and parametric simulation studies are used to accurately tailor the optical properties of the filters.

Measured transmission efficiencies up to 60% and full-width at half-maximum between 45 nm and 55 nm along the entire visible spectrum are achieved - an impressive and unique combination of features that has never been reported before. The non-ideality of the fabrication at the nanoscale is addressed, the issues encountered highlighted and alternative solutions proposed and verified, demonstrating that the working principle of the MIM structure can be successfully extended to other materials and structural parameters.

Statement of Originality

Unless otherwise acknowledged, the content of this Thesis is the result of my own work. None of this material has been submitted for any other degree at the University of Oxford or any other institution.

Chapter 2 and Chapter 3 are reviews. However, the analysis in Section 3.7.4 on the IIM stack is new material. Chapter 4 is a combination of literature, notes taken during Master degree courses, and professional work experience. Chapter 5 is an expanded and more complete review of the parametric dependence of two-dimensional periodic hexagonal nanohole arrays milled through an optically thick Al layer. Sections 5.2.2, 5.3.3 and 5.3.4 are new material. Chapter 6, 7 and 8 are all original work.

Numerical solutions have been evaluated and plotted by my own Matlab scripts. Simulation data presented in this Thesis are the result of my own work. Samples have been fabricated by myself with the support of the JWNC technical staff. The physical and optical characterisations of the samples have been carried out by myself, with the only exception of the TEM characterisation, which has been performed by the staff of the Physics Department at the University of Glasgow.

Nadia Pinton

Contents

1 Introduction **1**

1.1 Motivation 1

1.2 Aims and Objectives 3

1.3 Thesis Outline 4

2 Background on Imaging Systems **7**

2.1 Digital Imaging: Solid-State Image Sensors 8

2.2 Colour Vision and Colour Filtering 11

2.3 Spectral Imaging 16

2.4 Highly Selective Band-Pass Optical Filters 19

2.5 Plasmonic Colour Filters 21

2.6 Summary 26

3 Plasmonics: Fundamentals and Extraordinary Optical Transmission in Nanohole Arrays **28**

3.1 Surface Plasmon Resonances 30

3.1.1 Localised Surface Plasmon Resonances 30

3.1.2 Surface Plasmon Polaritons 34

3.2 Surface Plasmon Polaritons at a Single Flat Interface 35

3.3 Boundary Conditions 37

3.4 Fresnel Coefficients 40

3.5 Conditions for SPP excitations 42

3.6 Dispersion Relation 43

3.6.1 Penetration Depths 48

3.6.2 Damped SPPs and Propagation Length 50

3.6.3 Summary 51

3.7 Coupled SPPs in Plasmonic Waveguides 52

3.7.1 Symmetric IMI Plasmonic Waveguide . . . 57
3.7.2 Asymmetric MIM Plasmonic Waveguide . . . 61
3.7.3 Symmetric MIM Plasmonic Waveguide . . . 64
3.7.4 IIM Plasmonic Waveguide . . . 65
3.8 EOT in Subwavelength Nanohole Arrays . . . 67
3.8.1 Light Transmission through a Single Subwavelength Circular Aperture . . . 68
3.8.2 Fano's Contribution to Plasmonics . . . 74
3.8.3 Dependence on the periodicity of the array . . . 76
3.8.4 Dependence on the materials . . . 79
3.8.5 Dependence on the shape of the aperture . . . 80
3.8.6 Reciprocity of the Structure in Transmission . . . 81
3.8.7 Finite size effects . . . 82
3.9 Summary . . . 82

4 Simulation, Fabrication and Characterisation Methods 84

4.1 Simulation Software: Lumerical FDTD Solutions . . . 85
4.1.1 The Finite-Difference Time-Domain Method . . . 85
4.1.2 Setting-up the simulation environment . . . 87
4.2 Nanofabrication Techniques . . . 90
4.2.1 Metallisation . . . 90
4.2.2 Dielectric Deposition . . . 92
4.2.3 Electron Beam Lithography . . . 96
4.2.4 Dry Etching . . . 105
4.3 Physical and Optical Characterisation Techniques . . . 108
4.3.1 Electron Microscopy . . . 108
4.3.2 Atomic Force Microscopy . . . 113
4.3.3 Microspectrophotometer . . . 118
4.4 Summary . . . 119

5 2D Hexagonal Nanohole Arrays: Analysis of the Starting Structure 120

5.1 Introduction . . . 121
5.2 Characteristic Traits in the Optical Spectra . . . 123
5.2.1 The bottom interface . . . 124
5.2.2 The top interface . . . 128
5.3 Parametric Analysis . . . 130

5.3.1 Diameter . . . 131
5.3.2 Metal Thickness . . . 137
5.3.3 Top cladding layer: thickness and RI . . . 140
5.3.4 RI hole filling material . . . 144
5.4 Summary . . . 147

6 2D Hexagonal Nanohole Arrays: A Change in Dielectric Environment 149
6.1 Introduction . . . 150
6.2 Characteristic Traits in the EOT Spectra . . . 153
6.3 Electromagnetic Near-Field Patterns . . . 155
6.4 Parametric Analysis . . . 157
6.4.1 Cap Layer Thickness and Cavity Length . . . 157
6.4.2 Metal Thickness . . . 160
6.4.3 Diameter . . . 162
6.4.4 Array Periodicity . . . 165
6.5 Summary . . . 168

7 2D Hexagonal Nanohole Arrays: The Metal-Insulator-Metal Stack 170
7.1 Introduction . . . 171
7.2 Characteristic Traits in the Optical Spectra . . . 174
7.2.1 MIM oscillatory modes . . . 177
7.3 Electromagnetic Near-Field Patterns . . . 178
7.4 Parametric Analysis . . . 182
7.4.1 Diameter . . . 182
7.4.2 Thickness of the middle dielectric layer . . . 184
7.4.3 Metal Thickness . . . 186
7.4.4 RI hole filling material and middle layer . . . 189
7.4.5 Cap Layer Thickness and RI . . . 191
7.4.6 Periodicity . . . 193
7.5 Summary . . . 194

8 Nanofabrication and Experimental Results 196
8.1 Patterning of the hexagonal nanohole array . . . 197
8.1.1 Issue 1: Under-Etch of the Middle Layer . . . 199
8.2 Filling of the nanoholes . . . 204
8.2.1 Alternative Filling Material . . . 206

8.3 Summary 210

9 Conclusions and Future Work **211**

9.1 From Broad- to Narrow-Band Plasmonic Colour Filters 212

9.2 Future Works 215

Bibliography **218**

Appendices **231**

A Samples **232**

A.1 Sample S23800: 40/70/40 MIM 233

A.2 Sample S23801: 40/70/40 MIM 234

A.3 Sample S24734: 40/100/40 MIM 235

Chapter 1

Introduction

There is plenty of room at the bottom.

Richard Feynman[1]

1.1 Motivation

The ability to selectively and efficiently filter light in the optical regime is of extreme importance in an increasingly wide range of applications. Visible band-pass optical filters are found in the photo/video cameras that we use daily: from smartphones, tablets, laptops, and gaming consoles to surveillance, automotive and medical systems. Commercial image sensors are usually based on the human eye colour acquisition, i.e. they utilise Red, Green and Blue (RGB) filters to separate the incoming light into its main components so that a colour image can be digitally reconstructed.

In comparison, multispectral sensors have demonstrated a higher colour accuracy[2,3], a result of the separation of the optical spectrum in many colour channels instead of only three, which enable image analysis and machine vision beyond human capability. Moreover, in recent years, there has been a growing interest in multispectral imaging as non-destructive and non-invasive assessment methods to collect and analyse the spectral information from a scene with the purpose of identifying materials[4], locating objects[4] or performing quality and safety diagnosis[5,6]. Many applications require the acquisi-

tion of optical spectral information only over a few well-defined wavelengths of interest [7]. Therefore, multispectral imaging systems, despite the lower spectral resolution than hyperspectral image sensors, are a faster, more suitable and economical alternative.

Recently, fully integrated megapixel snapshot multispectral cameras in the visible regime have been reported [8,9,10]. In these cameras, traditional polymer-based filter technologies were replaced by all-dielectric multilayer stacks of alternating high and low refractive index materials. In addition, the traditional mosaic Bayer pattern was extended to allow the simultaneous acquisition of multiple spectral bands without the need for external dedicated optics. However, despite the narrow passband of the stack filters, their implementation is costly and extremely sensitive to process variations. Moreover, the spatial resolution is constrained by the thickness of the filters - of several microns at the longer wavelengths - and by the photolithography diffraction limit, limiting the minimum size of the pixel area.

The generation of colours through the engineering of metallic nanostructure is a rapidly growing research field and plasmonic colour nanotechnologies - thanks to their ability to control and manipulate light at the nanoscale - display great potential when compared to traditional colour technology [11]. Common applications range from colour printing and digital displays to optical sensing and security devices, and the structures of interest include diffraction gratings, nanoantennas, nanoaperture arrays and multilayer systems [11]. Bright colours have been demonstrated in reflection - for applications such as colour printing [12] - but the structure used is not suitable for image sensor applications. In the last decades, transmissive Plasmonic Colour Filters (PCFs) based on periodic arrays of nanoholes in an optically thick metal layer quickly became one of the most promising alternatives to polymer-based filter technologies for image sensors [13,14,15,16]. However, the relatively broad transmission passbands and relatively low transmission of these filters do not fulfil the requirements for multispectral imaging.

PCFs rely upon the phenomenon of Extraordinary Optical Transmission (EOT) [17]. While transmission through a single isolated nanohole is extremely small, hole arrays can display surprisingly high transmission efficiency, sometimes exceeding unity when normalised to the area of the holes [17,18]. This enhancement results from the active par-

ticipation of the metallic layer in the transmission process. When the incident photons resonantly interact with the coherent electron oscillations present in a conductor Surface Plasmon Resonances (SPRs) arise. They can be distinguished between localised electron oscillations and propagating waves depending on whether they are generated on metallic nanoparticles or along flat metal-dielectric interfaces, respectively[19]. The latter are known as Surface Plasmon Polaritons (SPPs) and their contribution to the phenomenon of EOT is now widely accepted[13,20,21,22].

In this Thesis, alternative approaches to generated highly selective band-pass plasmonic colour filters are proposed and investigated. The design, structural parameter analysis and experimental measurements of Metal-Insulator-Metal (MIM) plasmonic filter arrays are presented and demonstrated. These optical structures display high transmission efficiencies and narrow passbands along the entire visible regime, overcoming the limitations of all previously reported PCFs[23]. Insights into the physical mechanisms of the transmission process are established from the simulated electric and magnetic near-field patterns, which indicate that these technologies exploit the EOT phenomenon concurrently to magnetic and electric resonant cavity modes. The MIM plasmonic filters are an extremely versatile technology that paves the way to monolithically integrate PCFs in commercial CMOS image sensors for high colour accuracy filtering and multispectral applications.

1.2 Aims and Objectives

The main aim of this project was to develop a novel plasmonic nanostructure able to overcome the limitations of previously reported transmissive PCFs, namely broad bandwidth and relatively low transmission efficiency. Project specifications included the suitability to be integrated directly on top of a Complementary Metal Oxide Semiconductor (CMOS) image sensor. This put a constraint on the choice of materials that compose the architecture since the latter must be entirely composed of CMOS-compatible materials that are already available in standard CMOS fabrication process.

The development phases of the project can be described as follows:

- Analysis of current state-of-the-art PCFs based on periodic arrays of nanoholes.
- Identification of loss mechanisms within the structure.
- Simulation of alternative architectures and materials combinations.
- Definition of a fabrication process for the most promising nanostructure.
- Fabrication of the devices.
- Physical and optical characterisation of the devices.

1.3 Thesis Outline

This section provides a description of the chapters that compose this Thesis.

Chapter 2 provides an overview on digital and spectral imaging systems, colour vision and current filter technologies for the visible regime. The beginning of the chapter establishes the need for integrated multispectral applications, outlines the basis of imaging acquisition and briefly describes solid-state image sensor technologies. The notion of colour vision is introduced, standard colour filtering technologies for image sensors are described and their shortcoming highlighted. The chapter continues with a description of spectral imaging and provides an overview of spectral filtering technologies. Finally, the concept of plasmonic colour filters is introduced and the advantages of structured photonic components over conventional filtering technologies are established. The chapter concludes with a literature review on current state-of-the-art plasmonic colour filters.

Chapter 3 is a comprehensive review on plasmonics and lays the theoretical fundamentals of the work presented in this Thesis. The chapter begins with an introduction to surface plasmon resonances and outlines the basis of Localised Surface Plasmon resonances (LSPRs) and Surface Plasmon Polaritons (SPPs). The chapter then focuses on SPPs at a single, flat interface. It provides the conditions of excitation, the dispersion relation and throughly analyse their properties. The chapter continues with the investigation of the coupling of SPPs in a 3-layer system. Insulator-Metal-Insulator (IMI),

Metal-Insulator-Metal (MIM) and Insulator-Insulator-Metal (IIM) plasmonic waveguides are examined and the region(s) of existence of SPP bound modes defined for each configuration. The chapter concludes with the description of the phenomenon of Extraordinary Optical Transmission (EOT) and a review of two-dimensional (2D) Hexagonal Nanohole Arrays (HNAs).

The methods used to simulate, fabricate and characterise the plasmonic nanostructures presented in this Thesis are described in **Chapter 4**. The beginning of the chapter provides an overview of the Finite-Difference Time-Domain (FDTD) method, followed by a description of Lumerical FDTD Solution, the software used to simulate all the optical structures that have been designed during the course of this project, and of the simulation environment. The following part of the chapter is dedicated to the fabrication techniques used to create the devices. Fundamentals and working principles of metallisation, Plasma Enhanced Chemical Vapour Deposition (PECVD), Electron Beam Lithography (EBL) and Reactive Ion Etching (RIE) are presented and addressed in detail. The chapter concludes with a description of the physical and optical characterisation methods used to measure the devices and their performance, namely Electron Microscopy, Atomic Force Microscopy (AFM) and Microspectrophotometry.

Chapter 5 is an expanded review of two-dimensional (2D) Hexagonal Nanohole Arrays (HNAs) milled in an optical thick aluminium (Al) layer. At the beginning of the project, these nanostructures were the most promising Plasmonic Colour Filter (PCF) technology apt to replace colour filter arrays in CMOS image sensor applications and thus they had been chosen as the starting point for the development of more efficient plasmonic architectures. In this chapter, geometrical parameters and materials are throughly analysed and their influence on the optical properties of the arrays examined in detail. By the end of Chapter 5 a novel, successful approach to increase the performance of the filters is established.

Chapter 6 investigates the optical performance of a novel type of 2D HNA PCF based on a thin metallic layer capped with a higher - with respect the substrate - Refractive Index (RI) material. This new design displays relatively narrow features in a specific range of the EOT band and represents the first step towards PCFs for integrated multispectral

applications. However, the transmission spectrum displays a long-wavelength peak that interferes with the selectivity of the narrow peak and generates a considerable amount of optical cross-talk. Therefore further development is required. The chapter provides a comprehensive simulation study that has the purpose of analysing the influence of the structural parameters on the optical response of the array so that further modifications can be applied and its passband performance increased. By the end of Chapter 6 a novel, successful approach to further increase the performance of the filters is established.

Chapter 7 investigates the optical performance of a novel type of 2D HNA PCF based on a three-layer MIM stack. At the beginning of Chapter 7 it is demonstrated how the addition of a thin metal layer on top of the previous structure - exact copy of the bottom one - significantly improves the passband of the filter by substantially reducing the optical efficiency of the long-wavelength peak. The chapter then provides a comprehensive simulation study on the new MIM structure. The final objective is to gain enough understanding of the physical mechanisms involved in the transmission process, as a function of the structural parameters, in order to be able to optimise the MIM design at need and for different uses and applications. By the end of Chapter 7 a final set of parameters for the MIM filter is defined for the subsequent fabrication step.

Chapter 8 presents the experimental results obtained from this project. The fabrication process has been divided into two parts: the patterning of the HNAs in the MIM stack and the filling of the holes. The beginning of the chapter outlines the steps of the first phase of the fabrication process and introduces the results. To ensure reproducibility, insights on the issues encountered during the etching of the MIM stack are presented and solutions are provided. The chapter continues with the description of the second phase of the fabrication process. A further setback in the filling of the holes was encountered, which required to re-optimise the MIM filter for a different hole filling material. At the end of the chapter successful multispectral colour filtering in the visible range is presented.

Chapter 9 summarises the work that has been presented in this Thesis and offers some discussion on future work that could be undertaken as a continuation of this project.

Chapter 2

Background on Imaging Systems

Indeed, we often mark our progress in science by improvements in imaging.

Martin Lee Chalfie[24]

This chapter provides an overview of digital and spectral imaging systems, with a particular focus on the current filter technologies used to separate the electromagnetic spectrum, specifically the optical visible range, into wavebands. The terms digital imaging, image sensor and photodetector are clearly defined in Section 2.1. In the same section, the most common technologies used in the detection of visible optical images are described and compared. Section 2.2 presents the notion of colour vision to explain the choices for standard colour filtering in digital imaging. The concept of spectral imaging is defined in Section 2.3. An overview of the commonly used spectral filtering technologies is provided in Section 2.4. Finally, Section 2.5 introduces the concept of extraordinary optical transmission and plasmonic colour filters. The properties of plasmonic optical filters are examined and the benefits of subwavelength structured photonic components over convention, integrated and not-, optical multispectral filtering technologies presented and analysed. A literature review on the current state-of-the-art plasmonic filters is provided.

2.1 Digital Imaging: Solid-State Image Sensors

Digital photo- and video cameras are established in an extremely broad range of applications. Solid-state image sensors are implemented in high-end applications like medical diagnostic[6,25] and object-detection systems[26], such as imaging radar and sonar. They are also employed as remote sensing[27,28] in satellite and space-related applications. Satellite images, for example, occupy a very important role in many environmental applications. They allow geographical mapping, agricultural assessment, weather forecast and general tracking of human resources[4,29]. However, imaging science is an integral component of modern society and nowadays most of digital cameras are exploited for daily uses.

Mobile, consumer and computing technologies represented 85% of the global image sensor revenue in 2017, with mobile technologies alone representing the 69% of the whole market[30]. Surveillance and automotive are the second and the third largest and most active segments of the image sensor market[30], respectively. This is not surprising. The number of cameras per security system is not limited by human monitoring anymore: rear back-up cameras in automobiles are now mandatory in the US while, for example, collision avoidance or 360° parking assistance in Advanced Driver Assistance Systems (ADAS) require the combined use of several digital cameras. In addition, mobile, security and automotive are all in the middle of a booming expansion, driven mainly by the integration of additional cameras to support new functionalities like biometry and 3D imaging and sensing[30]. According to forecasts, the image sensor market will become even more important in the future, with a substantial 9.4% compound annual growth rate (CAGR) for the next five years[30].

The term *digital imaging* usually refers to the acquisition, processing and storage of a two-dimensional optical image in a numerical format[31], as simply illustrated in Figure 2.1. The fundamental building block in the image acquisition process is the *image sensor*. An image sensor is the electronic device that detects, converts and processes the information contained in an optical image into an electrical format. As displayed in the inset of Figure 2.1, it is composed by three main components, vertically aligned on top of each other: (a) an array of microlenses, (b) an array of optical filters and (c) an array of

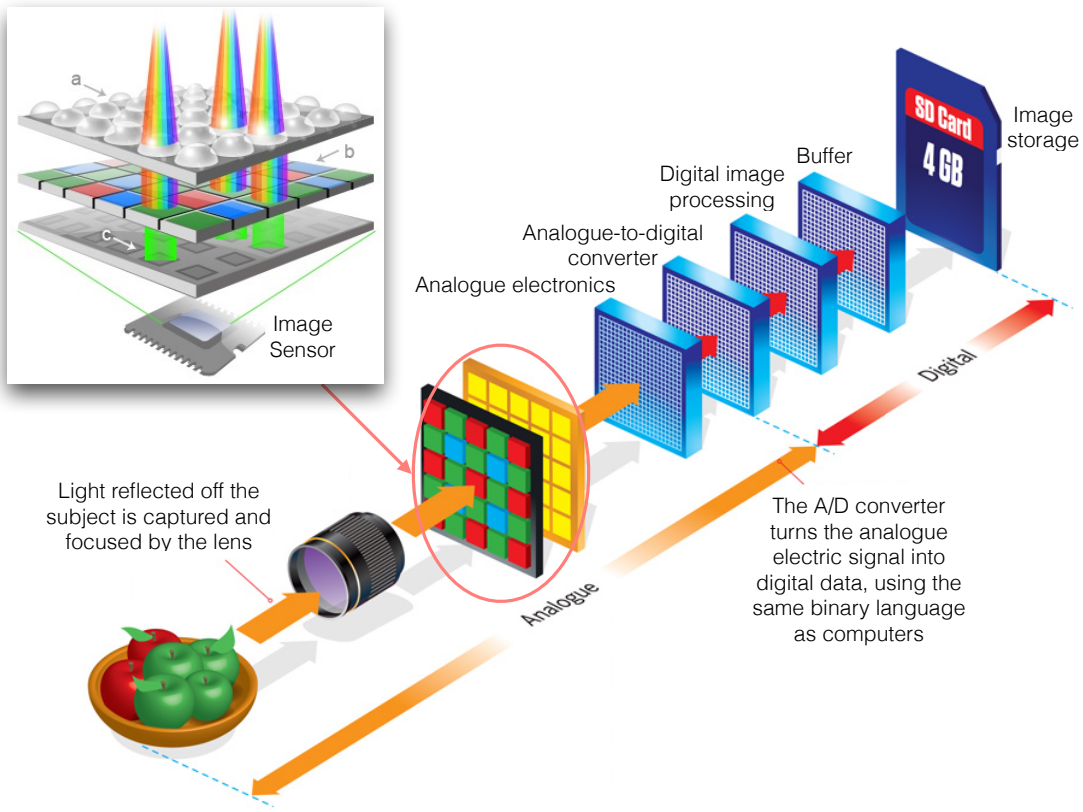


Figure 2.1: Digital imaging acquisition process. Illustration[32] of how a digital camera converts captured light into image pixels. The light reflected from an object or a scene is captured by the external optics of a camera and focused onto the image sensor. The image sensor collects and converts the incoming radiation into an analogue electrical signal. On-chip electronics then amplify the signal, convert it into digital information and process it so that it can be easily stored in a memory hard drive and accessed by the user at need. Inset[33] highlights the three main components of an standard commercial image sensor: (a) array of microlenses, (b) colour filter array and (c) photodetector array.

photodetectors. Each of the microlenses spatially collects the incoming electromagnetic radiation and focuses it underneath, through the respective optical filter, and onto an individual photodetector. Finally, the charges generated at each photodetector are collected, converted into a digital signal by an analog-to-digital converter (ADC) and then processed and stored as a whole, digital reconstruction of a point-in-time snapshot of the optical image.

The photodetector is the light sensitive component and represents the core of the image sensor. It converts the portion of the incident electromagnetic radiation allowed through the optical filters into a displacement of electronic charges, proportionally to the intensity of the radiation and the time of exposure. Each photosensitive element represents a *pixel*, i.e. the basic unit and smallest addressable element of a digital image. In other words, inside a 10 MPixel camera there is an image sensor with an array of approximately 10

millions photodetectors. The smaller the size of a pixel and the higher the number of pixels per a given area, i.e. the density, the greater the amount of detail that can be detected and thus the higher the spatial resolution of a digital image.

The ability to absorb light is directly related to the bandgap energy of the material that constitutes the photodetector, which is usually a semiconductor. Only photons having an energy higher than the bandgap energy may be absorbed. It follows that, accordingly to the wavelength range that is being imaged, the photodetectors of a camera must be constituted of a suitable semiconducting material. For example, silicon (Si) has a bandgap energy of 1.1 eV and hence can detect only wavelengths below 1.1 μm. Instead, indium antimonide (InSb), having a bandgap energy of only 0.18 eV is sensitive to wavelength below 6.9 μm. As a consequence, silicon is commonly used to imaging in the visible regime, whereas indium antimonide is best suited to infrared (IR) imaging [29].

A photodetector may be classified by its detection mechanism (photoelectric, photovoltaic, etc.) and for each type of mechanism there exist several choices of device. However, whatever the physical mechanism that induces a displacement of electronic charges as a consequence of the photon energy absorption, most photodetectors are based on a reverse-biased diode-like structure, i.e. on an interface between a p-type and a n-type semiconducting material, known as *p-n junction*. Currently, two types of image sensor technologies are commonly employed in digital cameras: Charge-Coupled Devices (CCDs) and Complementary Metal Oxide Semiconductor (CMOS) Active Pixel Sensors (APSs).

A CCD sensor consists of an array of closely-spaced photogate detectors, i.e. metal oxide semiconductor (MOS) capacitors with a polysilicon gate as the top terminal. When a bias is applied to the gate of the capacitor, a depletion region is formed at the oxide-semiconductor interface. As the light shines onto the photogates, the photo-generated charges are accumulated and held in the potential well underneath the gate. At the end of the exposure period, the charges are sequentially transferred - through a synchronised sequence of voltage signals - to a neighbouring well, in a sort of analogue shift register, until they reach the end of the row/column where they can be converted into electric signals.

A CMOS Image Sensor (CIS) typically consists of an array of photoreceptors, which is the ensemble of a photodiode plus front-end electronics, such as transistors and amplifiers, and constitutes the basic unit of a CMOS APS. In this case, the charges are transduced into electrical currents or voltages at the pixel level, i.e. photodetector per photodetector. Both CCD and CMOS technologies are made from silicon, based on arrays of light-sensitive pixels and use similar physical processes to detect and convert light into electric signals. However, differences between these two types of sensors lead to a number of advantages and disadvantages [29].

CCD technologies provide excellent digital image quality with remarkably lower noise and dark current when compared to CMOS Image sensors (CISs). However, a CIS has many advantages when compared to charged-coupled devices, including low voltage operation, low power consumption, and - thanks to the compatibility with standard fabrication processes - also low manufacturing costs. Moreover, a major benefit of CMOS technologies is the possibility to integrate all the electronic camera functions onto a single-chip sensor, from signal processing to exposure and timing control to analogue-to-digital conversion. Consequently, nowadays, CMOS APS are the leading mass-market technology in digital imaging applications such as mobile phones, cameras, tablets, etc, i.e. where increased noise is a reasonable compromise for decreased cost and lower power requirements. However, CCD sensors remain the favourite choice in applications where higher quality images are desirable, such as professional digital photography and astronomy [15,26,29,34].

2.2 Colour Vision and Colour Filtering

By definition, *colour vision* is the ability of an organism or machine to distinguish anything that is visible or tangible based on its colour appearance, i.e. on the wavelengths of light that it reflects, emits or transmits. Colours, defined as wavebands in the visible regime of the electromagnetic spectrum, can be measured and quantified in several ways. However, colour vision is species-related and the perception of colour itself is a completely subjective process. In other words, we, as humans, do not have the same colour vision of a snake for example; but, at the same time, each of us might perceive colours in a different way,

depending on how our brain responds to a visual stimulus.

Nowadays, it has been demonstrated that the human eye is sensitive to electromagnetic radiation ranging from 380 nm to 780 nm. Figure 2.2 is a schematic representation of the human eye and the human colour vision. The optical image reflected from an external object passes through the pupil, the iris diaphragm and is projected by the lens at the back of the eye, onto the retina. Inside the retina, a dense network of light-sensitive photoreceptors converts photons into electro-chemical signals. The retina consists of two types of photoreceptors: rod cells and cone cells. The rods are more numerous than cones and allow human vision in dim light conditions. However, rods cannot distinguish colour. Cones are responsible for colour vision and can adapt to widely varying colour and brighter illumination levels. Cones can be distinguished in three different types and are commonly labeled by the colour at which they are most sensitive: blue, green and red. Figure 2.3 displays the retinal response of the human eye. The overlap of the cones and how the brain interprets the neural stimulus received through the optical nerve allow us to see millions of different colours. This constitutes the so-called trichromatic vision.

As general rule, every commercial product on the market is developed to meet the end-user needs. It does not come as a surprise then, that standard commercial image sensors are based on the human eye colour acquisition. In the attempt to emulate the tristimulus light-receptors of the human eye, image sensors commonly utilise a pattern of red (R), green (G) and blue (B) filters, each on top of a photodetector, to separate the incoming light into its main components so that a colour image can be reconstructed digitally pixel-by-pixel. Colour filters are typically composed of transmissive organic or pigmented polymers. Each polymer is chemically optimised to pass only a specific colour. However, engineering a desired spectral responsivity while ensuring the right mechanical properties of the dye - such as ease of application, durability, resistance to humidity and other atmospheric stresses - might become quite a challenging task[37]. Since polymer-based Colour Filter Arrays (CFAs) are partially transparent in the Near-Infrared (NIR) wavelengths and silicon photodetectors are good absorbers in that optical regime, NIR cut-off filters are commonly required in CMOS image sensors[37,38].

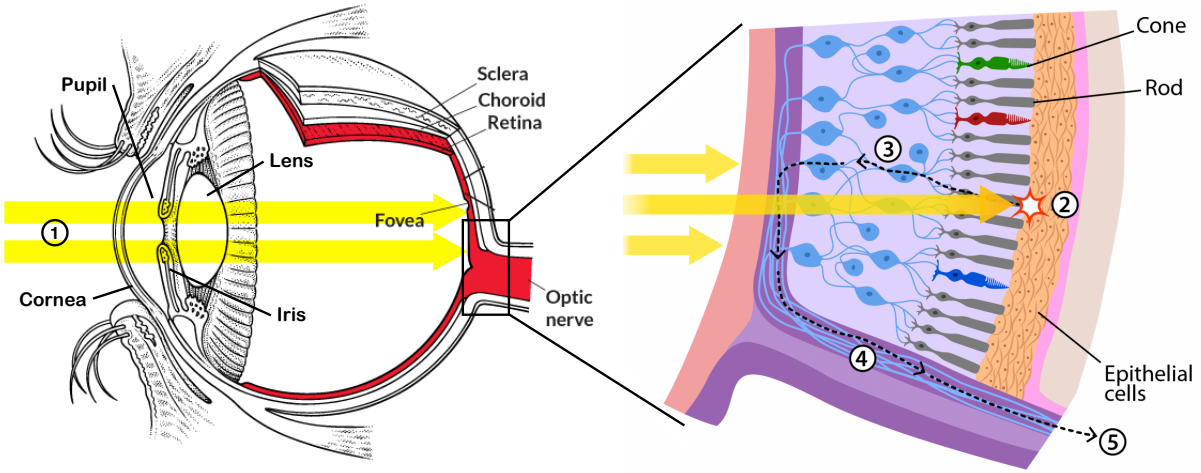


Figure 2.2: Illustration of human colour vision. Illustration of the cross-section of a human eye[35] and the retina light absorption mechanism[36]. 1) Light moves through the lens of the eye and is focused on the back of the eye, onto the retina. The retina contains millions of photoreceptors, which can be divided in two types: rods and cones. 2) When light hits the discs in the outer segment of the rods and cones, photons activate the cells. Rods can be activated in low light, while cones require brighter conditions. The epithelial cells behind them absorbs the light not absorbed by either the rods or the cones. 3) The light absorbed by the photoreceptors is sent as a signal to sets of neural cells. 4) Information travels within the neural cells and reaches the optical nerve. 5) The optical nerve is connected to the brain, which assimilates each signal to generate a complete image.

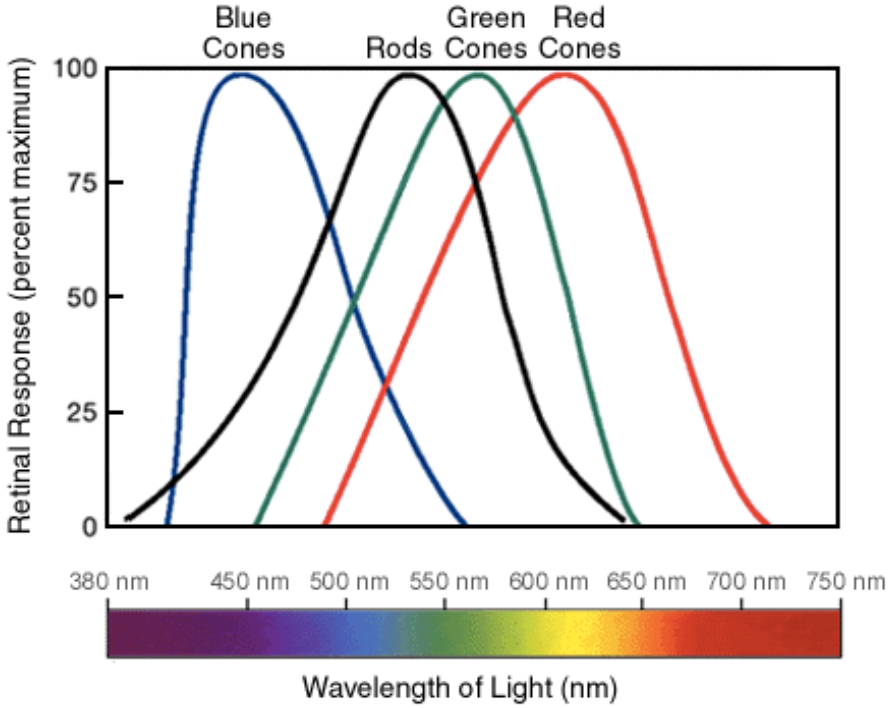


Figure 2.3: Retinal response of the human eye[36]. Normalised absorbance spectra of rods and cones. Rods cannot distinguish colours but allow human vision in dim light conditions. Cones instead are responsible for colour vision. There are three types of cones, each of which is most sensitive to a specific colour (or waveband), namely blue, green and red. Different colours are obtained by the superposition of the stimulus from each cone. For example, the colour yellow results from green and red cones being stimulated while the blue cones have no stimulation.

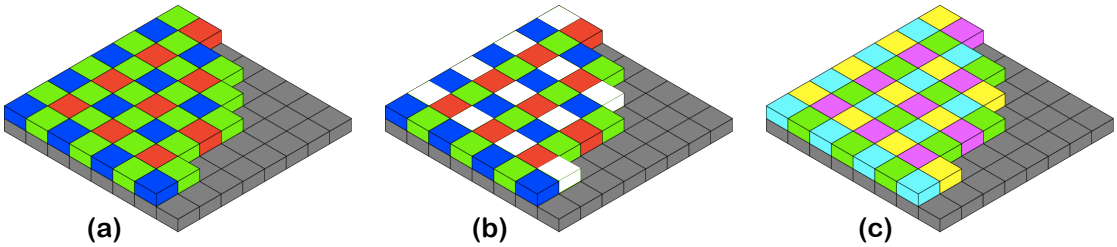


Figure 2.4: Colour filter arrays. Three popular colour filter array patterns used today: a) RGB, b) RGBW, and c) CYGM, where R stands for red, G for green, B for blue, W for white, C for cyan, Y for yellow, and M for magenta.

The most common CFA is the RGB Bayer filter mosaic[39]. Its unit cell consists of a 2 x 2 pixel square, formed by one blue filter, one red filter and two green filters, which is periodically repeated in two orthogonal directions. The filters are arranged in a pattern so that the luminance-sensitive element of the array (green) occur at every other array position, ensuring a dominance of the luminance element in both the orthogonal directions. Twice as many green elements as red or blue are used in order to mimic the physiology of the human eye, which is more sensitive to the green waveband of the electromagnetic spectrum (see Figure 2.3). In 2007, Honda *et al.*[40] proposed an alternative array where one of the green pixel of the Bayer array was replaced with a 'white' pixel, i.e. with an optically transparent layer. The inclusion of the transparent layer ensures an optical transmission efficiency over 95%, resulting in an improved method of measuring the luminance.

An alternative colour filter array is the cyan-yellow-green-magenta (CYGM). CYGM provides higher luminance information - and therefore a wider dynamic range - but at the expense of colour accuracy. This is because the filters have a broader spectral response. In fact, cyan-magenta-yellow (CMY) filters do not produce the true monochromatic colours. Each of them result from the sum of two primary colours which makes it more difficult to determine the colour information accurately. The aforementioned array patterns are illustrated in Figure 2.4a, Figure 2.4b, and Figure 2.4c.

The raw output of Bayer-filter cameras is referred to as a Bayer pattern image. The pixel is the smallest element of an image that can be individually processed in a video display system. We have seen in the previous section that each photodetector has one

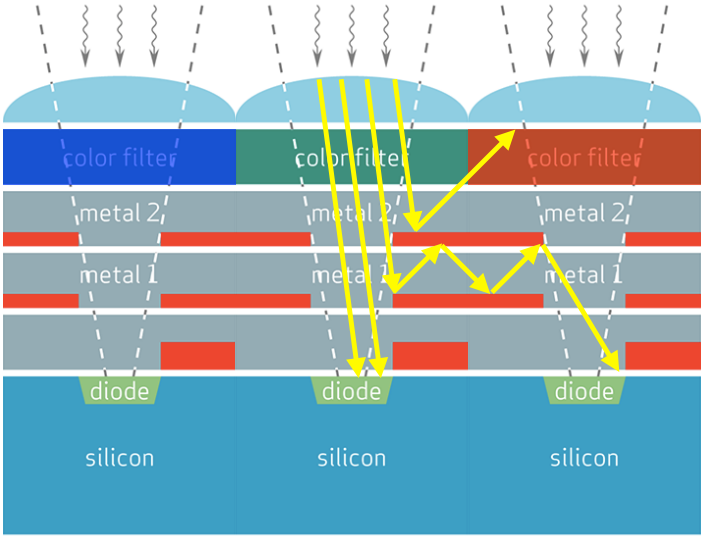


Figure 2.5: Optical Cross-talk Frontside-Illuminated (FSI) image sensor. The optical cross-talk arises from a combination of factors: (i) the thickness of the dyes, (ii) the filter to photodiode distance, and (iii) the high aspect ratio distance to photodiode active area.

single individual colour filter. This means that since each pixel is filtered to record only one of three colours, the data from each pixel cannot fully specify each of the red, green, and blue values on its own. So how can the 'real' colour of an individual pixel be determined? To obtain a full-colour image, the colour of each pixel is assigned through the digital interpolation of the neighbouring contributions, i.e. the colour information detected by the surrounding pixels. This is done through the implementation of various so-called *demosaicing* algorithms[41,42]. These algorithms depend on the array pattern and are extremely important. Highly-performing algorithms can even remove the colour cross-talk introduced by the non-ideality of the filters and thus improve the colour performance of the entire device.

In the past decades, CMOS technology experienced a significant scaling of feature size. Photodetector size has decreased from more that 10 μm to less than 2 μm. The scaling of features size in CMOS technology has resulted in significant improvements in CIS, which enabled digital imaging systems with a better spatial resolution and a potentially higher photosensitive area in the APS. However, for pixel size at the sub 2-μm level, the dye-based filtering elements sustain a considerable amount of optical colour cross-talk, which results in a decreased optical efficiency. Figure 2.5 shows that the optical cross-talk arises from a combination of factors: (i) the thickness of the dyes (of the order of few microns), (ii) the relatively large distance at which they are placed with respect the photodiodes

underneath, and (iii) the high aspect ratio distance to photodiode active area, which increases with the scaling in technology.

The thickness of the organic filters cannot be reduced further due to the low absorption coefficient of the dyes. The dyes cannot be placed closer to the photodetectors because they are not-compatible CMOS process materials and, in particular, cannot sustain the high temperatures of the manufacturing processes. This means that they can only be placed on top of the metal and insulator layers used to connect the pixels, at several microns from the photodetectors beneath. Moreover, the fabrication of each of the colours requires a sequence of several process steps, which lead to expensive manufacturing costs and make very impractical the realisation of multispectral devices. Therefore, it is highly desirable to find new technologies to filter the light at specific wavelengths in the optical regime, which could be more easily incorporated into CIS and were able to overcome the aforementioned issues.

2.3 Spectral Imaging

Spectral imaging combines the advantages of both spectroscopy[1] and conventional imaging technologies:

"If a conventional spectral measurement provides the answer to the question of what and a conventional imaging provides the answer to the question of where, spectral imaging can provide the answer to the question of where is what"[5].

As seen in Section 2.2, humans eyes see the reflected light from the surrounding in three channels: red, green and blue, which belong to the visible spectrum (380 to 700 nm in wavelength). But sight, as the perception of colours, is *species-related*. Snakes for example can see infrared (IR) radiation[43,44] while bumble bees are sensitive to ultraviolet (UV) light[45], both invisible to the human eye. Spectral image sensors allow humans to access different parts of the electromagnetic radiation at the same time. For example, they could make possible to see the world simultaneously in the eyes of a bumble bee (UV

[1]The study of the interaction between matter and electromagnetic radiation

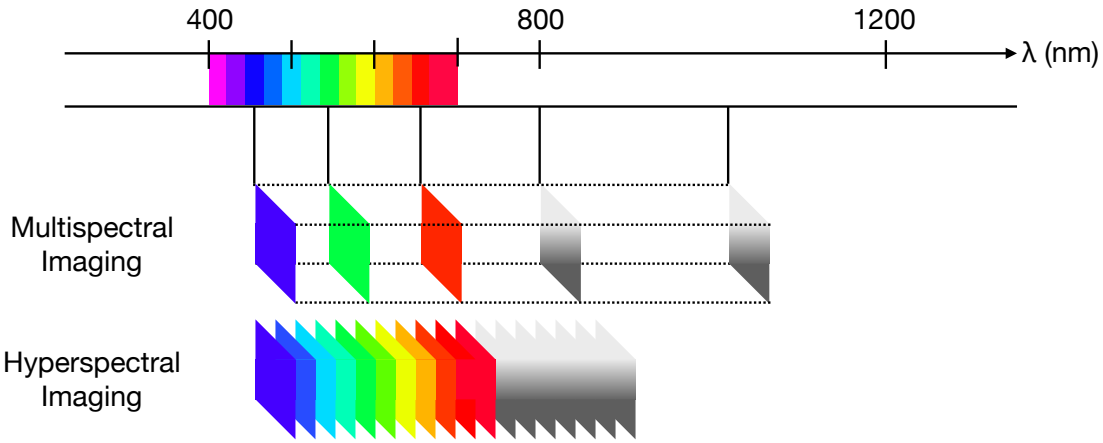


Figure 2.6: Distinction between multispectral and hyperspectral imaging. A system with few discrete bands over a large range of the electromagnetic radiation is considered multispectral. A system with a high number of bands that generates a continuous spectra of the electromagnetic radiation is considered hyperspectral. Usually the full-width at half-maximum of hyperspectral bands is of the order of 10 nm or less while multispectral bands can range between few tens up to even hundreds of nm.

radiation), a human (visible radiation) and a snake (IR radiation).

The information extracted from the spectral data of an image is extremely valuable for a wide range of applications. In recent years, spectral imaging has gained growing interest as non-destructive and non-invasive assessment method to collect and analyse the spectral information from a scene with the purpose of identifying materials [4], locating objects [4] or performing quality and safety diagnosis [5,6]. In the visible range, it could be used for colour measurements, fluorescence imaging [28,46,47], skin tones identification [6,28,48,49], chlorophyll concentration [4,27], mapping of blood oxygen saturation [6,28], and ocean characterisation [4].

As a result of the separation of the visible optical spectrum in many colour channels instead of only three, spectral sensors provide a digital image with more spectral information than traditional colour cameras and thus have demonstrated a higher colour accuracy than standard RGB image sensor. In fact, a spectral sensor in the visible regime does not reconstruct the colour yellow as the sum of the blue and green contributions but it reads it at its own corresponding wavelength of the electromagnetic spectrum. Therefore, a spectral image sensor provides a higher colour depth.

According to the spectral range, spectral resolution, number of bands, their width and in particular the type of acquisition (continuous or discrete), a spectral imaging technique might be distinguished as *multi*-spectral or *hyper*-spectral [28] (see Figure 2.6). A

hyperspectral sensor produces a continuous spectra for all the pixels, while a multispectral sensor gives information at each pixel for discrete ranges of the electromagnetic radiation. The spectral resolution of the bands, i.e. the width - commonly the full-width at half maximum (FWHM) - of each optical filter, define the precision of these sensors. However, also the spatial resolution of the filters should be considered. In fact, if a pixel is too large it could become difficult to identify multiple objects in close proximity because it will provide a lower image resolution. On the other side, if the pixels are too small, then the energy captured by each photosensor is too low, and thus the decreased signal-to-noise ratio reduces the reliability of measured features[6].

Hyperspectral sensors generate a huge amount of digital data, the so-called data cube. They collect information as a set of two-dimensional images, where each image is usually acquired during a scanning procedure and represents a narrow wavelength range of the electromagnetic spectrum. As a consequence, according to the number of spectral bands, the hyperspectral data cube could require extremely long data acquisition times and also incredibly large storage capabilities. Moreover, the processing of the data cube can become computationally challenging and in many cases the complete hyperspectral data cube provides little additional information compared to just a few (typically 3-8) multispectral imaging bands[7,50,51]. Despite some military or scientific studies may need hundreds of spectral channels, there are many more applications that require data over only a few well-defined wavelengths of interest.

In summary, hyperspectral image sensors provide a higher level of spectral detail. On the down side, they generate such a significant amount of digital data that to process and store all the information, even derived from a single acquisition, can become extremely time consuming, computationally challenging and hardware demanding. Moreover, the complete hyperspectral data cube contains a lot of redundant data and many applications require optical information only over few well-defined wavelengths of interest. Therefore, these applications would benefit from higher spatial resolution and significantly lower spectral resolution, making a multispectral imaging system, designed to acquire the spectral information only at several desired wavelengths, a faster, more suitable and economical alternative[5,7].

2.4 Highly Selective Band-Pass Optical Filters

Recent developments in spectral imaging are strongly correlated to the recent technological improvements of optical filters. Alongside with well-established, high resolution dispersive elements such as gratings and prisms used in spatial-scan methods, currently, electronically tuneable filters, such as Liquid Crystal Tuneable Filters (LCTFs) and Acousto-Optical Tuneable Filters (AOTFs), have attracted a lot of interest in the field of spectral imaging. These filters are electro-optical components with no moving parts, and represent compact and robust candidates for wavelength-scan methods.

LCTFs exploit the birefringence property of liquid crystals to select the desired working wavelength of the filter, while AOTFs consist of a special crystal that can be tuned in wavelength by radio frequencies (RF) acoustic waves. They both offer a high spectral resolution, typically of the order of only several nanometers, which makes them well-suited for demanding applications in research, however they present several limitations. They are polarisation dependent and power consuming. In addition, they also present a low spatial resolution and a quite high overall acquisition time, which is limited by the relaxation time of the liquid crystals for the LCTFs (typically of the order of around 50 ms) and by the speed of the acoustic waves in the crystal for the AOTFs (of the order of microseconds). High acquisition times compromise or even exclude the recognition of moving objects or dynamic phenomena, while low spatial resolution limits the size of recognisable features[6,7,9,52]. But most importantly, these devices are bulky and are only suitable as external optical components, i.e. they cannot be integrated on top of a CMOS image sensor.

Integrated multispectral filtering technologies could revolutionise imaging and photography by increasing colour accuracy dramatically compared to present-day RGB focal plane arrays and also by eliminating the need of external optics. In fact, the possibility to monolithically integrate optical filters on top of an image sensor opens the way to compact, high speed and low cost spectral cameras, bridging the gap between research and industry. In 2009, *Ocean Optics* and *Ocean Thin Films*, *Halma plc* subsidiaries, proposed a fully integrated megapixel multispectral imager[7]. In 2014, *IMEC* introduced its novel

snapshot multispectral camera[10]. In both cases, the traditional Bayer colour imaging concept has been extended to the acquisition of multiple spectral bands without the need for external dedicated optics. In the first case dichroic filters are used to separate the light in spectral bands, while in the second integrated Fabry-Pérot filters with distributed Bragg stacks as mirrors are implemented.

In both cases, the filters are all-dielectric multilayer stacks of alternating high-low refractive index materials. Each layer must have a specific thickness so that, thanks to constructive and destructive interferences within the stack, only one narrow band of the electromagnetic spectrum can be transmitted through the stack. The spectral resolution range from several nanometers up to several tens of nanometers and the working wavelength of the filters strongly depends on the thickness of the stack. This means that each filter must have a different total thickness and thus be fabricated in a separate lithographic process. It also means that the performance of the filters, and thus the position of the peak in wavelength, is very sensitive to the tolerances of the fabrication process. Each IMEC filter, for example, is composed of 13 layers (6+6 for the top/bottom Bragg stack and 1 layer to create the cavity), and therefore if the mosaic pattern is composed by a filter-cell of 16 bands the chip has to go through 16 different lithographic processes, and a sequence of 13 depositions for each of the filters. Dichroic filters present a transmission efficiency of about 60% (blue) to 90% (green/red) in the visible regime for normal angle of incidence and high contrast spectral bands. Fabry-Pérot filters show instead a quite poor optical efficiency in the visible regime, below 10% in the blue and green part of the spectrum. In both cases, the spatial resolution of the squared pixels is limited by the photolithography diffraction limit and by the thickness of the filters, which can reach several microns at the longer wavelengths. A pixel pitch as small as 5.5 microns is reported by IMEC's researchers[7,9]. In comparison, common 12-megapixel compact cameras have a pixel size of the order of 1.5 microns or less[53,54].

Polymer-based and all-dielectric multilayer filters suffer of the same issue: they are not easily integrated on top of an image sensor. In both case, the fabrication of each colour requires a sequence of several lithographic steps and becomes even more impractical the higher the number of filters required. In addition, the thickness of the filters - which can

reach several microns - as well as the high ratio distance to photodiode active area both increase the optical cross-talk between adjacent filtering elements. Therefore, an ideal replacement filtering technology should require only one lithographic step. In addition, it should be CMOS-compatible, to be possibly integrated directly on top of an image sensor, and also relatively thin, to not interfere with the other electronics of the component and reduce the optical cross-talk.

The most promising alternative are Plasmonic Colour Filters. They usually employ a single optically-thick metal layer nanostructured with subwavelength periodic features. The advantages of plasmonic colour filters lie in their ease of fabrication, higher reliability to process variations and colour tunability.

2.5 Plasmonic Colour Filters

Promising candidates to replace the standard polymer-based or the all-dielectric multilayer stack multispectral colour filters are the so-called *Plasmonic Colour Filters*. Plasmonic Colour Filters (PCFs) are based upon the phenomenon of Extraordinary Optical Transmission (EOT) discovered by Ebbesen *et al.*[17] in 1998. This phenomenon arises in metal nanostructures from the interaction of the incident light with a particular type of surface resonances, called *Surface Plasmon Resonances* (SPRs). In the past two decades, SPRs have attracted an enormous interest in several fields involving control and manipulation of light at the nanoscale, such as colour filtering, near-field optics, Raman spectroscopy, biosensing and even solar cells[13,55].

Plasmonic colour filters may be divided into two major classes: transmissive and reflective colour filters. As the names suggest, transmissive colour filters reject the entire visible spectrum except for specific transmission bands (or colours); while reflective colour filters reflect those bands and let all the other wavelengths pass. In other words, transmissive colour filters are *band-pass* filters while reflective colour filters are *band-stop* or *notch* filters. Transmissive colour filters are usually utilised as additive colour filters for digital imaging in RGB Bayer arrays. However, transmissive subtractive colour filters for digital imaging in CMY Bayer arrays have also been reported[56,57].

In 2013 Zeng *et al.*[56] reported a novel type of structure based on the counter-intuitive phenomenon of *Extraordinary Low Transmission* (ELT), where specific colours are generated by removing their complementary components from the visible spectrum, for example cyan is obtained by removing the red component. The structure, though, presented low selectivity and a relatively high cross-talk. Moreover, its features are polarisation-dependent. Reflective colour filters have instead major applications in display technologies[58], colour printing[11,59,60,61] and biosensing[58].

The idea of using subwavelength patterned metal layers as integrated colour filters on top of standard 0.18 μm CMOS APSs was first proposed by Catrysse *et al.*[14] in 2003, to alleviate the problems of the CFA architecture. In fact, the implementation of plasmonic colour filters within the image sensor pixel offers several potential advantages[14]: (i) reduced cross-talk by integrating the colour filters close to the photodetectors; (ii) increased efficiency of the microlenses by reducing the pixel surface to pixel photodiode distance since nanostructured metal filters are one or two order of magnitude thinner than colorant layers; (iii) lower fabrication costs by eliminating the need for additional CFA manufacturing steps since the integrated filters may be fabricated in a single metal layer by one lithographic step; and (iv) large spectral design freedom due to the optical tunability of the filters. The latter is probably one of the most important property for integrated colour filters because it allows the control of the transmission spectrum by simply changing the aperture size, shape and separation of the array. *"Owing to this feature, plasmonic colour filters are very cost competitive, especially for multicolour imaging applications"*[62]. Catrysse *et al.*[14] did not actually make any reference to the newly discovered phenomenon of EOT in their article. They attributed the characteristic transmittance of the filters solely to a combination of Rayleight-Wood anomalies (and thus inexplicit to surface EM waves) and Fabry-Perot waveguide modes. Nonetheless, their considerations on the advantages of using nanostructured thin metal films as colour filters remain valid.

In the following years, research groups worldwide started working on the development of CMOS-compatible plasmonic colour filters. This trend sees aluminium (Al) as the favourite choice of metal instead of other metals, e.g. silver (Ag) and gold (Au), which knowingly possess better "plasmonic properties"[17,21]. This is because, despite Al has a

much higher absorption in the visible range than Ag or Au, it also has a higher real part of the permittivity which ensures that the conditions of existence of SPPs are met along the entire range of visible frequencies[2]. Moreover, Al is a CMOS-compatible material.

A particular type of nanostructure also stands out in literature: the two-dimensional (2D) hexagonal array of subwavelength holes. In 2012, a 2D hexagonal array of nanoholes in a 150-nm thick Al layer was integrated on top of a single-pixel CMOS image sensor [15], demonstrating filtering functionality in the visible regime. In the same year, the same structure was re-analysed by Yokogawa *et al.* [62] who put more emphasis to the filter performance aspects required for state-of-the-art image sensor applications, such as the filter transmission dependence on array size, spatial cross-talk, and robustness against defects. In their article, they established that the scattering dynamic of the filters is solely determined by nearest neighbour hole-hole interactions. As a consequence, transmission properties of 2D hexagonal nanohole arrays are extremely robust: the filtering function is maintained either with respect array size and random defects - albeit at a cost in transmission efficiency - and the spatial optical cross-talk from neighbouring filters of different colours is estimated as small as 1 μm. These are attractive features for 2D image sensor applications requiring densely packed filtering elements and make them especially tractable for industrial mass-production. In 2013, Burgos *et al.* [16] demonstrated full-colour plasmonic imaging by directly contacting the plasmonic colour filter array in a Bayer configuration onto a commercial black and white CMOS image sensor.

The field of plasmonic colour filters has significantly evolved since the discovery of the EOT phenomenon. Several different structures have been proposed, periodic, quasi-periodic and even aperiodic arrays, with several different aperture shapes, exploiting different metals or different metal/dielectric combinations [21]. In particular, metal-insulator-metal (MIM) waveguides have attracted considerable interest for subwavelength light confinement [63]. These waveguides - also known as metallic *slot waveguides* or *gap waveguides* - increase the SPP propagating distance [19,64,65], enable subwavelength spatial mode confinement below diffraction limit [64,66] and support both photonic and plasmonic modes [64]. Exploited for molecular sensing applications [67] and photon transport [64], MIM waveguides

[2]Refer to Section 3.5

have been studied also for colour filtering applications. However, among the experimental results published so far and to the best of my knowledge, only a few plasmonic nanostructures displayed high spectral resolution features that could open the way to a "plasmonic multispectral imaging" era.

Plasmonic nanostructures displaying band-pass spectral features potentially narrow enough to be used for spectral imaging have been proposed[68,69,70,71]. In 2008, a triplet of intersected bull's eye structures and a combination of nanoslits with periodic grooves[68] were proposed to selectively filter the light in the visible regime. Despite full-widths at half-maximum (FWHM) of approximately 50 nm, absolute transmissions lower than 10-15% were achieved, probably a result of the high absorption losses of the thick silver layer. In 2010, Metal-Insulator-Metal (MIM) gratings[69] composed by a stack of Al-ZnSe-Al on top of a magnesium fluoride film were presented. However, these MIM grating structures[69] were only a slight improvement on standard single metal film nanohole arrays[15,16], both in terms of transmission efficiency - that reached a maximum of 60% only for the green - and bandwidth - still greater than 100 nm. In fact, as a consequence of the poor colour selectivity, only 5 shades of colour are clearly distinguishable in the so-called *plasmonic spectroscope* proposed. In 2017, Fleischman *et al.*[70] described how by stacking two MIM gratings on top of each other to create a multilayer slot-mode plasmonic filter (MSPF) composed of 5 alternating layers of Ag and SiO_2 it might be possible to achieve colour filters with single transmission band as narrow as 17 nm and approximately 40% peak transmission. Experimental prototypes with a FWHM of 70 nm were demonstrated. Nonetheless, all the above structures[68,69,70] are polarisation dependent, do not use standard CMOS-process materials, and cannot be integrated within a standard microchip because they exploit the air environment to operate. Finally, unprecedented experimental linewidth of ≈ 80 nm and transmission efficiency above 40% have been achieved in the NIR when some of the circular apertures in the unit cell of thin Au hexagonal nanohole arrays were substituted with ellipses[71]. The nanostructure exhibits polarisation insensitivity, however, Au is neither a CMOS compatible material or suitable to filter light in the blue and green parts of the visible spectrum.

At the time the project started, the 2D Al hexagonal nanohole arrays were the most promising candidates to potentially replace conventional RGB dye-filter technology and on-chip dielectric filters, especially for multicolour imaging applications[16,62]. They can be fabricated in one single lithographic step, are CMOS-compatible and do not degrade with ultraviolet radiation. They present high tunability in wavelength and are order of magnitudes thinner than dye technologies or dielectric multi-layer stack filters. They have a high spatial resolution and are also extremely robust to spatial cross-talk. Moreover, extreme ultraviolet lithography or new nano imprinting technologies could allow for high-volume fabrication. However, the relatively broad transmission passbands and low transmission of these filters do not fulfil the requirements for multispectral imaging (yet).

This project concentrates on the improvement of 2D periodic arrays of subwavelength holes and, in particular, on the exploitation of Al due to the well-know compatibility of this metal with CMOS processes and its moderate plasmonic properties in the visible spectrum. The theoretical background for this structural configuration is presented in detail in Section 3.8, while simulations and data analysis for a 2D Al hexagonal nanohole array are provided in Chapter 5.

2.6 Summary

In this chapter an overview on digital and spectral imaging systems has been provided. The standard digital image acquisition process have been described and insights on the working principles of solid-state image sensors have been given. The concepts of photodetection has been introduced and the two main types of image sensor technologies, namely CCD and CMOS APS, presented and compared. Typical spectral imaging approaches and techniques have been analysed and their features compared. The notion of colour vision has also been introduced and common current optical filtering technologies for the visible range examined in detail. Finally, the concepts of extraordinary optical transmission and plasmonic colour filters have been introduced. Subwavelength photonic nanostructures provide a new, promising approach to control and manipulate light at the nanoscale and display great potential when compared to traditional colour technologies. Reduced

cross-talk, lower fabrication costs and large spectral design freedom are only few of their potential advantages. A comprehensive literature review on the current state-of-the-art plasmonic filters has been given.

Chapter 3

Plasmonics: Fundamentals and Extraordinary Optical Transmission in Nanohole Arrays

But what is plasmonics? "You just have Maxwell's equations, some material properties and some boundary conditions, all classical stuff - what's new about that?" Well, would you have predicted that just by imposing appropriate structure on a metal one could make a synthetic material that would turn Snell's law on its head? Or that you could squeeze light into places less than one hundredth of a wavelength in size?

Bill Barnes[19]

The field of plasmonics studies the resonant interactions of light with the free electron densities of highly conductive materials. These resonant interactions are called Surface Plasmon Resonances (SPRs) and their discovery triggered a lot of interest in several research fields in the last 30 years, opening the way to a wide range of applications. This is due to the fact that plasmonic resonant processes display unique properties which lead to a drastic enhancement of the electromagnetic near-fields and enable light confinement below the diffraction limit. As a consequence, by enabling the control and manipulation of light at the nanoscale, surface plasmon-based structures and devices provide new solutions to traditional optical designs. Light guiding[55,66,72,73,74], surface-enhanced

sensing[75], biodetection[76,77,78,79], light harvesting[80,81,82,83] and enhanced optical transmission[13,17,20,21,84,85] are just few of the several potential applications of SPRs. From subwavelength optics to quantum electrodynamics, to physics and bio-photonics, plasmonics became one of the most dynamic and exciting research field of the 21st century.

The objective of this chapter is, first, to provide a detailed summary on the origin and physics of surface plasmon resonances and, then, to address the theory and fundamentals of one the most studied structure in subwavelength optics: the two-dimensional (2D) periodic array of subwavelength apertures whose experiments led to the discovery of the groundbreaking phenomenon of extraordinary optical transmission in 1998. The enhancement of the optical transmission through subwavelength apertures given by the resonant interaction of light with the surface plasmon resonances at a metal-dielectric interface is the main topic of this Thesis and its fundamentals will be presented in detail throughout this chapter.

Section 3.1 introduces the concept of surface plasmon resonances and provides the definitions and the basics of localised surface plasmon resonances and surface plasmon polaritons. Section 3.2 provides an exhaustive study of the surface plasmon propagation constant in the case of a single flat interface. Conditions of existence, trends and key features such as penetration depths and propagation length are analysed in detail. Section 3.7 provides a comprehensive study of plasmonic waveguides and the coupling of SPPs in three-layer systems. Sections 3.2 and Section 3.7 will be extremely important during the analysis of the simulation data to try to understand some of the complex physical mechanisms involved in the transmission process of the devices. Finally, a literature review of the extraordinary optical transmission process and the fundamentals of two-dimensional periodic array of subwavelength apertures are throughly addressed in Section 3.8. This chapter aims to lay the foundations of the simulation results and experimental work presented in this Thesis.

This chapter takes inspiration from previous reviews and some of its sections represent brief accounts of books published on the subject of Plasmonics. Section 3.1, 3.6.2 and 3.4.1 are based on "Plasmonics: Fundaments and Applications" written by *S. Maier* (Reference [19]). Sections 3.4, 3.5, 3.6 (the first part) and 3.7 (up to 3.7.1 included)

reproduce portions of "Waves in Metamaterials" written by *L. Solymar and E. Shamonina* (Reference [89]). The theory of the Asymmetric MIM plasmonic waveguides of Section 3.7.2 derives from "Electromagnetic Waves and Antennas, vol. 2" by *S. J. Orfanidis* (Reference [88]).

3.1 Surface Plasmon Resonances

Surface Plasmon Resonances (SPRs) are collective oscillations of surface charges, a result of the coupling of incident photons with the coherent electron oscillations present in a conductor. They can be distinguished in two main categories of fundamental excitations: propagating waves and localised electron oscillations, depending on whether the resonances are generated along metal-dielectric interfaces or on metallic nanoparticles, respectively. The first fundamental excitation is called Surface Plasmon Polaritons (SPPs) and are evanescent, dispersive electromagnetic waves that propagate along the interface between a dielectric and a highly conductive material. The second fundamental excitation is instead called Localised Surface Plasmon Resonances (LSPRs) and are non-propagating oscillations of the electron plasma in nanosized particles. While SPPs require a coupling mechanism to be excited, LSPRs arise naturally from the diffraction pattern of a conductive nanoparticle in an oscillating electromagnetic field[19].

3.1.1 Localised Surface Plasmon Resonances

Localised Surface Plasmon Resonances (LSPRs) are non-propagating excitations and result from the resonant collective oscillation of the conduction band electrons in metal nanoparticles coupled to an external electromagnetic field[19,86]. Figure 3.1 illustrates the interaction of light with the electron plasma of a metallic nanoparticle. When light interacts with a particle having dimensions much smaller than the wavelength of light, the electric field polarises the particle displacing the electron cloud. This leads to an accumulation of electrons (negative charges) at one side of the particle and to a subsequent surplus of positive charges at the opposite one, both localised at the surface of the particle. The electrostatic attraction between these surface charge densities and the closed geomet-

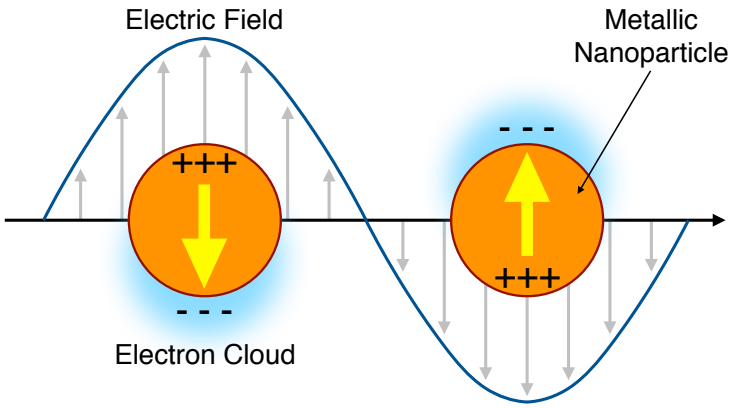


Figure 3.1: Interaction of metal nanoparticles with light. Schematic representation of the effect of an incoming electromagnetic wave on the electron cloud of spherical nanoparticles.

rical boundaries of the particle exert an effective restoring force on the driven electrons, so that a resonance can arise naturally [19]. It follows that plasmon resonant nanoparticles can be excited by direct light illumination and thus do not require a coupling mechanism to compensate for a momentum mismatch (as it will be instead demonstrated for the case of surface plasmon polaritons).

According to the size of the particle, different approaches can be used to analyse its interaction with the external electromagnetic field. Provided that the nanoparticle is much smaller than the wavelength of light in the surrounding medium, a simple quasi-static approximation can be used, which means that the phase of the harmonically oscillating electromagnetic field can be considered practically constant over the particle volume and the nanoparticle can be approximated by an electric dipole [19].

In the quasi-static approximation regime, the optical response of LSPRs are described through the particle *polarisabiity* α, which relates an incoming electric field $\mathbf{E}_0$ with the electric dipole moment $\mathbf{p} = \varepsilon_0 \varepsilon_{\mathrm{r,medium}} \alpha \mathbf{E}_0$ [19,86]. This quantity represents the relative tendency of a charge distribution in a bound system and determines the dynamic response of the system to an external applied field. The polarisability of a metal nanoparticle is a frequency-dependent magnitude that depends on the dielectric functions of the metal, the surrounding medium and on the particle geometry. In the electrostatic approach, the

(complex) dipolar polarisability of a small metal sphere of radius a is given by:[19]

$$\alpha = 4\pi a^3 \frac{\varepsilon_{\mathrm{r,sphere}} - \varepsilon_{\mathrm{r,medium}}}{\varepsilon_{\mathrm{r,sphere}} + 2\varepsilon_{\mathrm{r,medium}}} \tag{3.1}$$

where $\varepsilon_{\mathrm{r,sphere}}$ and $\varepsilon_{\mathrm{r,medium}}$ are the relative permittivities of the particle and the surrounding medium, respectively.

It is apparent from Equation (3.1) that the polarisability experiences a resonant enhancement at its pole. For a lossless metal, the localised surface plasmon resonance appears when:[19]

$$\mathrm{Re}\left[\varepsilon_{\mathrm{r,sphere}}(\omega)\right] = -2\varepsilon_{\mathrm{r,medium}} \tag{3.2}$$

This relationship is called the Fröhlich condition and the associated mode (in an oscillating field) the dipole surface plasmon of the metal nanoparticle. In reality, the incomplete vanishing of the denominator - due to $\mathrm{Im}\left[\varepsilon(\omega)\right] = 0$ - limits the magnitude of α at resonance. The Fröhlich condition reveals a strong dependence of the resonant frequency on the dielectric environment, which red-shifts in frequency as its permittivity is increased. This property is extremely valuable and can be exploited to optically detect changes in refractive index.[19]

A direct consequence of the resonantly enhanced polarisation is a concomitant enhancement of the scattering and absorption efficiencies of the particle, which lead to a field amplification both inside and in the near-field zone outside the particles[19]. For gold and silver nanoparticles, the resonance falls into the visible region of the electromagnetic spectrum. Therefore, they exhibit bright colours in both transmitted and reflected light.

The localised plasmon resonance of a single metallic nanoparticle can be shifted in frequency via alteration of shape and size. The larger the size of the particle (along the oscillating field) the lower the resonant frequency - and thus the larger the resonant wavelength. Intuitively, this can be understood by recognising that the distance between the charges at opposite interfaces of the particle increases with its size, thus leading to a smaller restoring force and therefore a lowering of the resonance frequency. Plasmon resonances can be lowered in frequency (red-shifted in wavelength) also by increasing the aspect ratio of the particle[19].

The quasi-static approach provides a reasonably good approximation for spherical or ellipsoidal particles with dimensions below 100 nm illuminated with visible or near-infrared radiation. For particles of larger dimensions, the quasi-static approximation breaks down due to retardation effects and thus the polarisability expression needs to be modified. A rigorous electrodynamic approach is required, known as *Mie Theory*. However, in simple physical terms, the damping effects lead to an overall shift in the plasmon resonance towards lower energies, which means that the spectral position of the dipole resonance red-shifts with increasing particle size. Moreover, an increase in particle volume also leads to a significant broadening of the plasmon resonance.[19]

Electromagnetic interactions between the localised modes also lead to shifts in the spectral position of the plasmon resonance compared to the case of an isolated particle. Consider small particles of size $a \ll \lambda$ arranged in one-dimensional chain with interparticle spacing $w \ll \lambda$ and $w \gg a$, so that each particle can be treated as a point dipole. According to the polarisation direction of the external field, the interparticle coupling can generate two different modes: a transverse mode when the dipoles oscillate perpendicularly to the direction of the chain, and a longitudinal modes when the dipoles oscillate along the direction of the chain. In the first case, the restoring force acting on the oscillating electrons of each particle is increased by the charge distribution of neighbouring particles and thus the plasmon resonance for the particle ensemble blue-shifts compared to the case of a single isolated particle. In the second case, the restoring force is decreased and thus the plasmon resonance red-shifts. These shifts in resonance energy were experimentally demonstrated using far-field extinction spectroscopy[19].

Electromagnetic dipole resonances akin to that of a metal nanoparticles can arise also in other type of nanostructures, such as *nanovoids*[1]. The polarisability of a nanovoid can be obtained from that for a sphere simply by substituting $\varepsilon_{\mathrm{r,sphere}}(\omega) \rightarrow \varepsilon_{\mathrm{r,medium}}$ and $\varepsilon_{\mathrm{r,medium}} \rightarrow \varepsilon_{\mathrm{r,sphere}}(\omega)$. The polarisability of the nanovoid is thus:[19]

$$\alpha = 4\pi a^3 \frac{\varepsilon_{\mathrm{r,medium}} - \varepsilon_{\mathrm{r,sphere}}}{\varepsilon_{\mathrm{r,medium}} + 2\varepsilon_{\mathrm{r,sphere}}} \tag{3.3}$$

In this case, the dipole moment is oriented antiparallel to the external field and the

[1]Nanovoids are dielectric spherical inclusion in a homogeneous metallic body

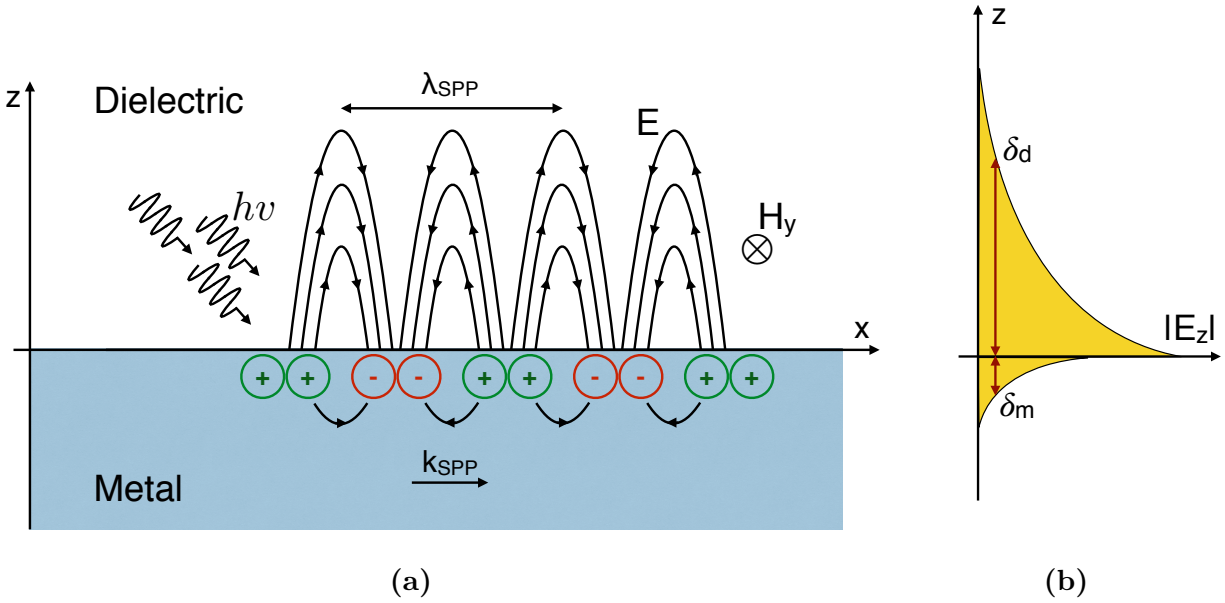


Figure 3.2: Schematic illustration of a SPP propagating at a metal/dielectric interface. (a) Illustration of the electric and magnetic field lines of a surface plasmon polariton propagating along x having propagation constant k_{SPP} and wavelength λ_{SPP}. (b) Plot of the orthogonal field $|E_z|$ with respect z, where δ_d and δ_m represent the decay length into the dielectric and metal, respectively.

Fröhlich condition takes the form:

$$\mathrm{Re}\left[\varepsilon_{\mathrm{r,sphere}}(\omega)\right] = -\frac{1}{2}\varepsilon_{\mathrm{r,medium}} \tag{3.4}$$

While nanovoids are three-dimensional in nature, essentially two-dimensional holes in thin metallic films can also support localised plasmon modes[19].

3.1.2 Surface Plasmon Polaritons

Plasmons are collective oscillations of the free electron density in conductive materials, while the term *polariton* is used to identify a coupled state between an elementary excitation and a photon. Therefore, when plasmons couple with a photon they create another quasiparticle called *plasma polariton*. Surface Plasmon Polaritons (SPPs) are then collective electromagnetic resonant excitations of charges that occur at the interface between a dielectric and a conductor upon interaction with impinging light. These surface waves exhibit very interesting properties. Unlike LSPRs, SPPs are propagating waves that travel along the surface of the conductor. Like LSPRs though, SPPs evanescently decay in the

orthogonal direction and thus display strongly localised fields at the interface.

Figure 3.2 is a schematic illustration of a SPP propagating at a metal/dielectric interface. Figure 3.2a illustrates the electric and magnetic field lines of a surface plasmon polariton propagating along x having propagation constant k_{SPP} and wavelength λ_{SPP}. Note that SPPs have transversal and longitudinal electric fields, while the magnetic field is parallel to the interface and perpendicular to the direction of propagation. The evanescent decay of the orthogonal field $|E_z|$, inside both the dielectric and metal, is plotted in Figure 3.2b. The perpendicular field E_z is enhanced near the surface and exponentially decay with a characteristic length δ_d in the dielectric and δ_m (also called *skin depth*) in the metal.

3.2 SPPs at a Single Flat Interface

This section describes the fundamentals of surface plasmon polaritons at a single, flat interface. To investigate their physical properties, the dispersion relation is examined in detail. Trends and key factors that might affect its behaviour are also identified.

Consider a Transverse Magnetic (TM) polarised[2] electromagnetic wave (A) incident onto a planar interface between two linear[3], homogeneous[4], isotropic[5] and not-absorbing infinite half-space materials[6], medium 1 ($z > 0$) and medium 2 ($z < 0$), as shown in Figure 3.3. In the geometry, propagation is in the x-direction, the transverse confinement is along the z-direction and the layers have infinite extent along the y-direction. This is the most simple geometry sustaining SPPs. At the interface, part of the light (B) is reflected back into medium 1, while the rest (C) is transmitted across the interface and propagates into medium 2. By definition, surface electromagnetic waves, such as surface plasmon polaritons, consist of oscillating surface charges along the direction normal to the interface between two materials with different dielectric functions. This oscillation of

[2]TM polarisation: the magnetic field is perpendicular to the plane of incidence, while the electric filed lies in the plane of incidence. Thus, there is no magnetic field in the direction of propagation of light.
[3]Linear media: constitutive parameters are not functions of the applied field.
[4]Homogeneous media: constitutive parameters are not functions of position.
[5]Isotropic media: constitutive parameters are not functions of direction of the applied field.
[6]Infinite half-space: region that is bounded at one edge and extends to infinity in all the other sides.

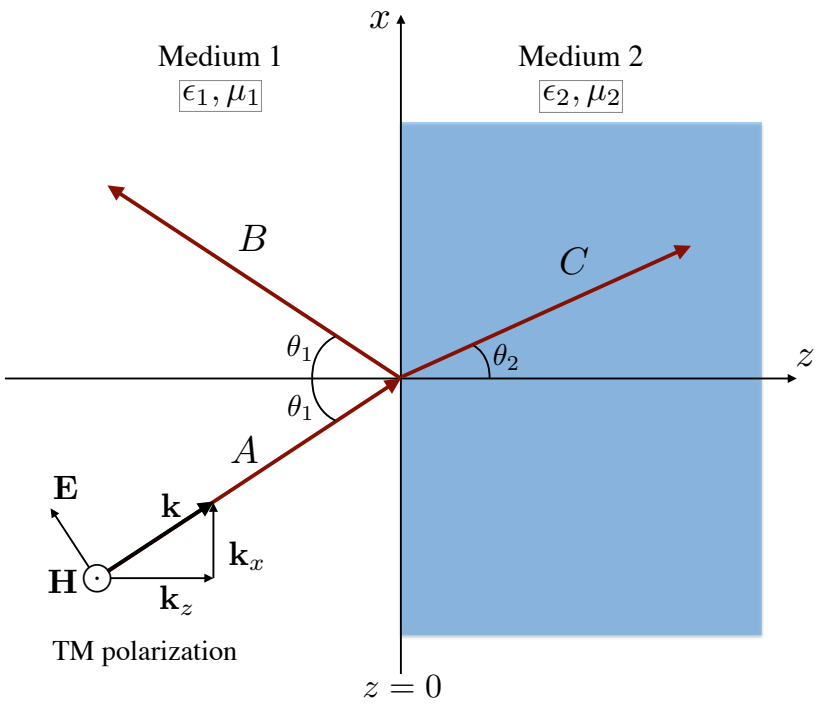


Figure 3.3: TM-polarised light incident onto a single flat interface. Schematic representation of a TM-polarised wave (A) incident onto an interface between two homogeneous, isotropic and not-absorbing infinite half-space media with different dielectric functions, ε_1 and ε_2 respectively. At the interface, part of the light (B) is reflected back into medium 1, while the rest (C) is transmitted across the interface and propagates into medium 2.

charges can only result from the discontinuity of the orthogonal electric field,[87] i.e. E_z in this case. As a consequence, only the case of a TM-polarised wave is considered.

In general, a medium is described by its *constitutive parameters*: the absolute permeability μ and the absolute permittivity ε. The absolute permeability is a measure of how easy a material can be magnetised and thus concentrate magnetic flux. The higher the permeability the easier for the magnetic flux lines to pass through the material. It can be expressed as $\mu = \mu_0\mu_r$, where μ_0 is the magnetic permeability of vacuum[7] and μ_r is a dimensionless quantity called relative permeability. For non-magnetic materials $\mu_r = 1$ and thus $\mu = \mu_0$. Instead, the absolute permittivity is a measure of how an electric field affects a material in terms of generated electric flux per unit charge. The permittivity is directly related to the electric susceptibility χ, which is a measure of how easy a material can be polarised in response to an applied electric field. The absolute permittivity can be expressed as $\varepsilon = \varepsilon_0\varepsilon_r = \varepsilon_0(1+\chi)$, where ε_0 is the electric permittivity of vacuum[8] and ε_r is

[7] $\mu_0 \approx 1.257 \times 10^{-6}$ H/m
[8] $\varepsilon_0 \approx 8.854 \times 10^{-12}$ F/m

a dimensionless quantity known as relative permittivity. In general, $\varepsilon(\omega) = \varepsilon'(\omega) + i\varepsilon''(\omega)$ is a complex valued function of the angular frequency ω. The real and imaginary parts of $\varepsilon(\omega)$ characterise the refractive and absorptive properties of the material. [88]

The single flat interface geometry falls within the realms of the classical electromagnetism framework and therefore the macroscopic formulation of Maxwell's equations can be applied [19]. Boundary-value electromagnetic problems are usually solved by mean of the differential form of Maxwell's equations, which "describe and relate the field vectors, current densities and charge densities at any point in space at any time" [88]. The charge and current densities, ρ and $\mathbf{J}$ respectively, in the Maxwell's equations commonly represent the *sources* of the electromagnetic fields of the system and for wave propagation problems they are localised in space. Thus, assuming a source-free region of space, i.e. considering that the light be generated far away from the interface, the Maxwell's equations simplify as follow:

$$\boxed{\begin{aligned}\mathbf{J} &= 0\\ \rho &= 0\end{aligned}} \quad \Longrightarrow \quad \boxed{\begin{aligned}\nabla \times \mathbf{E} &= -\frac{\partial \mathbf{B}}{\partial t}\\ \nabla \times \mathbf{H} &= \frac{\partial \mathbf{D}}{\partial t}\\ \nabla \cdot \mathbf{D} &= 0\\ \nabla \cdot \mathbf{B} &= 0\end{aligned}} \tag{3.5}$$

where $\mathbf{E}$ is the electric field, $\mathbf{H}$ is the magnetic fields, $\mathbf{B} = \mu\mathbf{H}$ is the magnetic flux density and $\mathbf{D} = \varepsilon\mathbf{E}$ is the electric displacement field. The bold font is used to indicated field vectors.

3.3 Boundary Conditions

Field vectors associated with electromagnetic waves should be continuous functions of position and time, and exhibit continuous derivatives. However, discrete changes in the electrical parameters across an interface between two different media may cause discontinuous distributions of charges. These discontinuities are related to the variations of the field vectors across the interface by what are usually referred to as the *boundary conditions* [88]. In this case, the associated boundary conditions require the continuity at

the interface ($z = 0$) of both the tangential and normal components of the electric and magnetic fields, $E_{t,i}$ and $H_{t,i}$, and $E_{n,i}$ and $H_{n,i}$ respectively:

$$\boxed{\begin{aligned} E_{t,1} &= E_{t,2} \\ H_{t,1} &= H_{t,2} \end{aligned}} \quad \text{and} \quad \boxed{\begin{aligned} D_{n,1} = D_{n,2} \quad &\rightarrow \quad \varepsilon_1 E_{n,1} = \varepsilon_2 E_{n,2} \\ B_{n,1} = B_{n,2} \quad &\rightarrow \quad \mu_1 H_{n,1} = \mu_2 H_{n,2} \end{aligned}} \tag{3.6}$$

Note that if, for example, the tangential components of the electric fields are continuous across a boundary, their derivatives (with respect to the coordinates on the boundary surface) are also continuous. According to Equations (3.5), this ensures continuity of the normal components of the magnetic field [88].

At the interface, *Snell's refraction law* must also be applied. Snell's refraction law describe the relationship between the angles of incidence and refraction when studying the refraction of an electromagnetic wave at the interface between two media with different refractive indices[9]. It states that the ratio of the sines of the angles of incidence θ_1 and refraction θ_2 is equivalent to the reciprocal of the ratio of the indices of refraction n_i of the respective medium i:

$$\frac{\sin\theta_1}{\sin\theta_2} = \frac{n_2}{n_1} \tag{3.7}$$

The incident electromagnetic wave is described by its propagation wavevector $\mathbf{k}$. The magnitude of the wavevector is the wavenumber, which is defined as the number of radians per unit distance:

$$k = \frac{2\pi}{\lambda} \tag{3.8}$$

The wavelength λ is thus the distance by which the phase of a sinusoidal wave changes by 2π radians. It can also be expressed via the frequency of the wave, $f = \omega/2\pi$, as follow:

$$\lambda = \frac{2\pi}{k} = \frac{2\pi c}{\omega} = \frac{c}{f} \tag{3.9}$$

[9]The refractive index (RI) of a material n_i is a dimensionless number that describes how electromagnetic radiation propagates through a medium, and it relates to the constitutive parameters of the material according to $n_i = \sqrt{\varepsilon_{\mathrm{r,i}}\mu_{\mathrm{r,i}}}$.

Since, the speed of light in the material is defined as:

$$c = \frac{1}{\sqrt{\mu\varepsilon}} \tag{3.10}$$

The wavenumber can be rewritten as:

$$k = \frac{\omega}{c} = \omega\sqrt{\mu\varepsilon} \tag{3.11}$$

It is then possible to relate the speed of light, wavelength and wavenumber in the material to the corresponding vacuum values:

$$c = \frac{1}{\sqrt{\mu\varepsilon}} = \frac{1}{\sqrt{\mu_0\varepsilon_0\mu_\mathrm{r}\varepsilon_\mathrm{r}}} = \frac{c_0}{\sqrt{\mu_\mathrm{r}\varepsilon_\mathrm{r}}} = \frac{c_0}{n} \tag{3.12}$$

$$\lambda = \frac{c}{f} = \frac{c_0}{nf} = \frac{\lambda_0}{n} \tag{3.13}$$

$$k = \frac{\omega}{c} = \frac{\omega n}{c_0} = nk_0 \tag{3.14}$$

where $n = \sqrt{\mu_\mathrm{r}\varepsilon_\mathrm{r}}$ is the refractive index (RI) of the material. Note that the speed of light c and the wavelength λ are both reduced by a scale factor n compared to the free-space values, whereas the wavenumber k is increased by a factor of n[89].

From Equations (3.14), the propagation vector of a wave is equal to the product of the free space propagation constant $\mathbf{k}_0$ and the refractive index (RI) n_i of the medium in which the wave is travelling, i.e. $\mathbf{k}_i = n_i\mathbf{k}_0$. Therefore, Snell's refraction law can be rewritten as:

$$\begin{aligned} n_1 \sin\theta_1 &= n_2 \sin\theta_2 \\ \frac{\mathbf{k_1}}{\mathbf{k_0}} \sin\theta_1 &= \frac{\mathbf{k_2}}{\mathbf{k_0}} \sin\theta_2 \\ \mathbf{k_1} \sin\theta_1 &= \mathbf{k_2} \sin\theta_2 \end{aligned} \tag{3.15}$$

Knowing that $k_{x,i} = \mathbf{k}_i \sin\theta_i$, this leads to another boundary condition which imposes that the k_x component of the wavevector along the interface is preserved across the media.

$$\boxed{k_{x,1} = k_{x,2} = k_x} \tag{3.16}$$

Since the propagation wave vector $\mathbf{k}$ of light is proportional to the photon's momentum $\mathbf{p}$

(according to $\mathbf{p} = \hbar\mathbf{k}$, where $\hbar = h/2\pi$ is the reduced Planck's constant[10]), this boundary condition is known as the *conservation of momentum*.

3.4 Fresnel Coefficients

The transmission and reflection of light at the interface between two optically-different media is described by the Fresnel coefficients, which can be obtained by applying the appropriate boundary conditions to the field components derived from the Maxwell's equations. In each medium, the total electric and magnetic fields can each be seen as the sum of a forward and a backward wave. For an incident transverse magnetic polarised wave as represented in Figure 3.3, the electric field has two components, along x and z, while the only magnetic field component is the one along the y-direction. It follows that the equations describing the fields become:[90]

$$\mathbf{E} = \begin{pmatrix} E_x \\ 0 \\ E_z \end{pmatrix} \qquad \mathbf{H} = \begin{pmatrix} 0 \\ H_y \\ 0 \end{pmatrix} \tag{3.17}$$

and that the magnetic field can be easily evaluated as:[90]

$$\begin{aligned} H_{y,1} &= A\mathrm{e}^{-j\mathbf{k}_{\mathrm{inc}}\cdot\mathbf{r}} + B\mathrm{e}^{-j\mathbf{k}_{\mathrm{refl}}\cdot\mathbf{r}} & H_{y,2} &= C\mathrm{e}^{-j\mathbf{k}_{\mathrm{trans}}\cdot\mathbf{r}} \\ H_{y,1} &= \left(A\mathrm{e}^{-jk_{z,1}z} + B\mathrm{e}^{jk_{z,1}z}\right)\mathrm{e}^{-jk_x x} & H_{y,2} &= C\mathrm{e}^{-jk_{z,2}z}\mathrm{e}^{-jk_x x} \end{aligned} \tag{3.18}$$

The electric field components can be derived from the Maxwell-Ampère law:

$$\mathbf{D} = \varepsilon\mathbf{E} \quad \rightarrow \quad \nabla \times \mathbf{H} = \frac{\partial \mathbf{D}}{\partial t} = \varepsilon\frac{\partial \mathbf{E}}{\partial t} \tag{3.19}$$

Assuming that the fields have a harmonic time dependence $\mathbf{E}(\mathbf{r}, t) = \mathbf{E}(\mathbf{r})\mathrm{e}^{-j\omega t}$, the time derivative ∂/∂_t can be replaced with $j\omega$:[90]

$$\nabla \times \mathbf{H} = j\omega\varepsilon\mathbf{E} \quad \rightarrow \quad \mathbf{E} = -\frac{j}{\omega\varepsilon}\nabla \times \mathbf{H} \tag{3.20}$$

[10]The Planck's constant $h \approx 6.626 \times 10^{-34}$ J·s relates the energy carried by a photon to its frequency.

$$\mathbf{E} = \begin{pmatrix} E_x \\ 0 \\ E_z \end{pmatrix} = -\frac{j}{\omega\varepsilon}\nabla \times \mathbf{H} = -\frac{j}{\omega\varepsilon}\begin{vmatrix} \hat{x} & \hat{y} & \hat{z} \\ \frac{\partial}{\partial x} & 0 & \frac{\partial}{\partial z} \\ 0 & H_y & 0 \end{vmatrix} = -\frac{j}{\omega\varepsilon}\begin{pmatrix} -\frac{\partial H_y}{\partial z} \\ 0 \\ \frac{\partial H_y}{\partial x} \end{pmatrix} \tag{3.21}$$

Therefore, it is possible to derive the electric field components along the x-direction:[90]

$$\begin{aligned} E_{x,1} &= \frac{j}{\omega\varepsilon_1}\frac{\partial H_{y,1}}{\partial z} & E_{x,2} &= \frac{j}{\omega\varepsilon_2}\frac{\partial H_{y,2}}{\partial z} \\ E_{x,1} &= \frac{j(-jk_{z,1})}{\omega\varepsilon_1}\left(A\mathrm{e}^{-jk_{z,1}z} - B\mathrm{e}^{jk_{z,1}z}\right)\mathrm{e}^{-jk_x x} & E_{x,2} &= \frac{j(-jk_{z,2})}{\omega\varepsilon_2}C\mathrm{e}^{-jk_{z,2}z}\mathrm{e}^{-jk_x x} \\ E_{x,1} &= \frac{k_{z,1}}{\omega\varepsilon_1}\left(A\mathrm{e}^{-jk_{z,1}z} - B\mathrm{e}^{jk_{z,1}z}\right)\mathrm{e}^{-jk_x x} & E_{x,2} &= \frac{k_{z,2}}{\omega\varepsilon_2}C\mathrm{e}^{-jk_{z,2}z}\mathrm{e}^{-jk_x x} \end{aligned} \tag{3.22}$$

and the electric field components along the z-direction:[90]

$$\begin{aligned} E_{z,1} &= -\frac{j}{\omega\varepsilon_1}\frac{\partial H_{y,1}}{\partial x} & E_{z,2} &= -\frac{j}{\omega\varepsilon_2}\frac{\partial H_{y,2}}{\partial x} \\ E_{z,1} &= \frac{j(-jk_x)}{\omega\varepsilon_1}\left(A\mathrm{e}^{-jk_{z,1}z} + B\mathrm{e}^{jk_{z,1}z}\right)\mathrm{e}^{-jk_x x} & E_{z,2} &= \frac{j(-jk_x)}{\omega\varepsilon_2}C\mathrm{e}^{-jk_{z,2}z}\mathrm{e}^{-jk_x x} \\ E_{z,1} &= -\frac{k_x}{\omega\varepsilon_1}\left(A\mathrm{e}^{-jk_{z,1}z} + B\mathrm{e}^{jk_{z,1}z}\right)\mathrm{e}^{-jk_x x} & E_{z,2} &= -\frac{k_x}{\omega\varepsilon_2}C\mathrm{e}^{-jk_{z,2}z}\mathrm{e}^{-jk_x x} \end{aligned} \tag{3.23}$$

Summarising, the field components for a TM-polarised wave incident onto a flat interface - as represented in Figure 3.3 - are:[90]

$$\boxed{\begin{aligned} H_{y,1} &= \left(A\mathrm{e}^{-jk_{z,1}z} + B\mathrm{e}^{jk_{z,1}z}\right)\mathrm{e}^{-jk_x x} & H_{y,2} &= C\mathrm{e}^{-jk_{z,2}z}\mathrm{e}^{-jk_x x} \\ E_{x,1} &= \frac{k_{z,1}}{\omega\varepsilon_1}\left(A\mathrm{e}^{-jk_{z,1}z} - B\mathrm{e}^{jk_{z,1}z}\right)\mathrm{e}^{-jk_x x} & E_{x,2} &= \frac{k_{z,2}}{\omega\varepsilon_2}C\mathrm{e}^{-jk_{z,2}z}\mathrm{e}^{-jk_x x} \\ E_{z,1} &= -\frac{k_x}{\omega\varepsilon_1}\left(A\mathrm{e}^{-jk_{z,1}z} + B\mathrm{e}^{jk_{z,1}z}\right)\mathrm{e}^{-jk_x x} & E_{z,2} &= -\frac{k_x}{\omega\varepsilon_2}C\mathrm{e}^{-jk_{z,2}z}\mathrm{e}^{-jk_x x} \end{aligned}} \tag{3.24}$$

Finally, by satisfying the boundary conditions at the interface, one simple set of two equations, describing the correlation between incident, reflected and refracted light at a single interface, can be found:[90]

$$\begin{aligned} H_{y,1}\big|_{z=0} &= H_{y,2}\big|_{z=0} \\ E_{x,1}\big|_{z=0} &= E_{x,2}\big|_{z=0} \end{aligned} \tag{3.25}$$

$$\Rightarrow \begin{cases} A + B = C \\ \frac{k_{z,1}}{\omega\varepsilon_1}(A - B) = \frac{k_{z,2}}{\omega\varepsilon_2}C \end{cases}$$

$$A - B = \zeta C \quad \text{with} \quad \zeta = \frac{k_{z,2}\varepsilon_1}{k_{z,1}\varepsilon_2} = \frac{k_{z,2}\varepsilon_{\mathrm{r},1}}{k_{z,1}\varepsilon_{\mathrm{r},2}}$$

$$\left.\begin{aligned} A + B &= C \\ A - B &= \zeta C \end{aligned}\right\} \quad \Rightarrow \quad \left.\begin{aligned} 2A &= C(1+\zeta) \\ 2B &= C(1-\zeta) \end{aligned}\right\} \tag{3.26}$$

$$\Rightarrow \quad \rho_{\mathrm{TM}} = \frac{B}{A} = \frac{1-\zeta}{1+\zeta} \quad , \qquad \tau_{\mathrm{TM}} = \frac{C}{A} = \frac{2}{1+\zeta} \tag{3.27}$$

where ρ_{TM} and $\tau_{\mathrm{TM}} = 1 + \rho_{\mathrm{TM}}$ are the *TM reflection* and *TM transmission coefficients* of the interface, respectively, also know as the *Fresnel coefficients*.

3.5 Conditions for SPP excitations

Mathematically, evanescent waves are characterised by a wavevector with a purely imaginary component perpendicular to the plane of propagation. In this case, surface waves propagate at the interface along the x-direction and thus they must have a purely imaginary component in the perpendicular z-direction. Given a propagation vector:

$$\mathbf{k} = (k_x, k_z) = \hat{\mathbf{x}}k_x + \hat{\mathbf{z}}k_z \quad \rightarrow \quad k^2 = k_x^2 + k_z^2 \quad \rightarrow \quad k_z^2 = k^2 - k_x^2 \tag{3.28}$$

Since k_z has to be imaginary, k_z can be rewritten using the notation of the *propagation constant* γ so that $k_z = -j\gamma$ with $\gamma > 0$. The square of k_z is $-\gamma^2$ [11] and thus $k^2 - k_x^2$ must be negative. This implies that $|k_x| > |k|$ which means that the surface waves have a wave vector k_x larger than the wave vector of the incident light, which results in a momentum mismatch[17,19,87]. A coupling mechanism is thus necessary to excite evanescent surface waves at the interface.

The eigenmodes of the Maxwell's equations at the interface represents surface waves. Eigenmodes are normal mode of vibration of an oscillating system and can be formulated

[11] $j^2 = -1$.

in the absence of an incident field. Therefore, the condition of excitation of surface wave can be determined from Equation 3.26 assuming $A = 0$:[90]

$$\left.\begin{aligned} B &= C \\ -B &= \zeta C \end{aligned}\right\} \quad \Rightarrow \quad \boxed{\zeta = -1} \quad \text{Condition for surface waves excitation} \tag{3.29}$$

The condition $\zeta = -1$ means that the reflection coefficient $\rho_{\mathrm{TM}} = \infty$ (3.27) and thus that there is only a "reflected" wave, while the incident field is zero. Indeed, it follows from $B = \rho_{\mathrm{TM}} A$ (or $A = B/\rho_{\mathrm{TM}}$) that A will tend to zero for finite B and $\rho_{\mathrm{TM}} \to \infty$.

Another requisite on the materials composing the interface is derived from (3.29):[90]

$$\zeta = \frac{k_{z,2}\varepsilon_{\mathrm{r},1}}{k_{z,1}\varepsilon_{\mathrm{r},2}} = \frac{(-j\gamma_2)\varepsilon_{\mathrm{r},1}}{(-j\gamma_1)\varepsilon_{\mathrm{r},2}} = \frac{\gamma_2\varepsilon_{\mathrm{r},1}}{\gamma_1\varepsilon_{\mathrm{r},2}} = -1$$

$$\Rightarrow \quad \text{since} \quad \gamma_i > 0 \quad \boxed{\text{if} \quad \varepsilon_{\mathrm{r},1} > 0 \quad \text{then} \quad \mathrm{Re}\left[\varepsilon_{\mathrm{r},2}\right] < 0} \tag{3.30}$$

It follows that the confinement to the surface demands that surface waves exist only at interfaces between materials with opposite signs of the real part of their dielectric functions, i.e. between an insulator and a conductor.

3.6 Dispersion Relation

Assuming non-magnetic materials (i.e. permeability $\mu_r = 1$), $n_i^2 = \epsilon_{\mathrm{r,i}}$ and thus replacing (3.14) in (3.28) the transverse propagation constant γ can be written as $\gamma_{\mathrm{i}}^2 = \beta^2 - \varepsilon_{\mathrm{r,i}} k_0^2$, where $\beta = k_x > 0$. Starting from the condition (3.29), it is then possible to derive the expressions of the tangential and perpendicular wavevectors at the interface:[89]

$$\gamma_1^2\varepsilon_{\mathrm{r},2}^2 = \gamma_2^2\varepsilon_{\mathrm{r},1}^2$$

$$(\beta^2 - \varepsilon_{\mathrm{r},1}k_0^2)\varepsilon_{\mathrm{r},2}^2 = (\beta^2 - \varepsilon_{\mathrm{r},2}k_0^2)\varepsilon_{\mathrm{r},1}^2$$

$$k_0^2\varepsilon_{\mathrm{r},1}\varepsilon_{\mathrm{r},2}(\varepsilon_{\mathrm{r},1} - \varepsilon_{\mathrm{r},2}) = \beta^2(\varepsilon_{\mathrm{r},1}^2 - \varepsilon_{\mathrm{r},2}^2)$$

$$\beta^2 = k_0^2\frac{\varepsilon_{\mathrm{r},1}\varepsilon_{\mathrm{r},2}(\varepsilon_{\mathrm{r},1} - \varepsilon_{\mathrm{r},2})}{\varepsilon_{\mathrm{r},1}^2 - \varepsilon_{\mathrm{r},2}^2} = k_0^2\frac{\varepsilon_{\mathrm{r},1}\varepsilon_{\mathrm{r},2}}{\varepsilon_{\mathrm{r},1} + \varepsilon_{\mathrm{r},2}} \tag{3.31}$$

$$\Rightarrow \qquad \beta = k_0\sqrt{\frac{\varepsilon_{\mathrm{r},1}\varepsilon_{\mathrm{r},2}}{\varepsilon_{\mathrm{r},1}+\varepsilon_{\mathrm{r},2}}} \quad , \qquad k_{z,1} = \frac{k_0\varepsilon_{\mathrm{r},1}}{\sqrt{\varepsilon_{\mathrm{r},1}+\varepsilon_{\mathrm{r},2}}} \quad , \qquad k_{z,2} = -\frac{k_0\varepsilon_{\mathrm{r},2}}{\sqrt{\varepsilon_{\mathrm{r},1}+\varepsilon_{\mathrm{r},2}}} \tag{3.32}$$

Note that the change in sign in $k_{z,2}$ is given by condition (3.29).

The propagation constant β represents the propagation constant of the surface plasmon polaritons at the interface. Therefore, by substituting β with k_{SPP}, we obtain:[90]

$$\boxed{k_{\mathrm{SPP}} = \beta = k_0\sqrt{\frac{\varepsilon_{\mathrm{r},1}\varepsilon_{\mathrm{r},2}}{\varepsilon_{\mathrm{r},1}+\varepsilon_{\mathrm{r},2}}}} \quad \text{with} \quad \boxed{n_{\mathrm{SPP}} = \sqrt{\frac{\varepsilon_{\mathrm{r},1}\varepsilon_{\mathrm{r},2}}{\varepsilon_{\mathrm{r},1}+\varepsilon_{\mathrm{r},2}}}} \tag{3.33}$$

where n_{SPP} is the SPP refractive index and thus $\varepsilon_{\mathrm{r,SPP}} = (\varepsilon_{\mathrm{r},1}\varepsilon_{\mathrm{r},2})/(\varepsilon_{\mathrm{r},1}+\varepsilon_{\mathrm{r},2})$ is the SPP effective relative permittivity at the interface. The wave vector k_{SPP} is also referred to as the SPP *dispersion relation*. The *dispersion relation* defines the relation between frequency and wave vector. The frequency is hidden in the dielectric functions, which are frequency dependent ($\varepsilon_{\mathrm{r,i}} = \varepsilon_{\mathrm{r,i}}(\omega)$). Equation (3.33) is valid for both real and complex $\varepsilon_{\mathrm{r},2}$, i.e for conductors with and without attenuation.

As seen in (3.30), the essential condition for the existence of surface plasmons is for the interface to be composed by two materials with a positive and a negative real part of their dielectric permittivity respectively, i.e. if $\varepsilon_{\mathrm{r},1} > 0$ then $\mathrm{Re}\,[\varepsilon_{\mathrm{r},2}] < 0$. Therefore, because β and k_0 are both positive and not purely imaginary wave vectors, from Equation (3.31):[90]

$$\frac{\varepsilon_{\mathrm{r},1}\varepsilon_{\mathrm{r},2}}{\varepsilon_{\mathrm{r},1}+\varepsilon_{\mathrm{r},2}} > 0 \quad \Rightarrow \quad \text{since} \quad \varepsilon_{\mathrm{r},1}\varepsilon_{\mathrm{r},2} < 0 \quad \text{than} \quad \boxed{\varepsilon_{\mathrm{r},1}+\varepsilon_{\mathrm{r},2} < 0} \tag{3.34}$$

In other words, to ensure a positive ratio, since the numerator is negative, the denominator must be negative as well. It follows that another condition that has to be satisfied for the existence of SPPs is that $|\varepsilon_{\mathrm{r},2}| > |\varepsilon_{\mathrm{r},1}|$, i.e. the absolute value of the dielectric function of medium 2 has to be greater than the absolute value of the dielectric function of medium 1, given $\mathrm{Re}\,[\varepsilon_{\mathrm{r},2}] < 0$ and $\varepsilon_{\mathrm{r},1} > 0$.

Conditions (3.30) and (3.34) guarantee that β is real and $k_{z,1}$, $k_{z,2}$ are pure imaginary. Setting $\varepsilon_{\mathrm{r},2} = -\tilde{\varepsilon}_{\mathrm{r},2}$ with $\tilde{\varepsilon}_{\mathrm{r},2} \in \mathrm{Re} > 0$ and $\tilde{\varepsilon}_{\mathrm{r},2} > \varepsilon_{\mathrm{r},1}$, we have $\sqrt{\varepsilon_{\mathrm{r},1}+\varepsilon_{\mathrm{r},2}} = \sqrt{\varepsilon_{\mathrm{r},1}-\tilde{\varepsilon}_{\mathrm{r},2}} =$

$j\sqrt{\tilde{\varepsilon}_{\mathrm{r},2}-\varepsilon_1}$, and $\sqrt{\varepsilon_{\mathrm{r},1}\varepsilon_{\mathrm{r},2}}=\sqrt{-\varepsilon_{\mathrm{r},1}\tilde{\varepsilon}_{\mathrm{r},2}}=j\sqrt{\varepsilon_{\mathrm{r},1}\tilde{\varepsilon}_{\mathrm{r},2}}$. Then, Equations (3.32) read:[89]

$$\beta=k_0\sqrt{\frac{\varepsilon_{\mathrm{r},1}\tilde{\varepsilon}_{\mathrm{r},2}}{\tilde{\varepsilon}_{\mathrm{r},2}-\varepsilon_{\mathrm{r},1}}}\quad,\qquad k_{z,1}=-j\frac{k_0\varepsilon_{\mathrm{r},1}}{\sqrt{\tilde{\varepsilon}_{\mathrm{r},2}-\varepsilon_{\mathrm{r},1}}}\quad,\qquad k_{z,2}=-j\frac{k_0\tilde{\varepsilon}_{\mathrm{r},2}}{\sqrt{\tilde{\varepsilon}_{\mathrm{r},2}-\varepsilon_{\mathrm{r},1}}}\tag{3.35}$$

An analytical study of the evolution of the SPPs dispersion relation (3.33) allows to examine more in details their properties. Consider medium 1 to be an ideal dielectric with a real and positive dielectric function $\varepsilon_{\mathrm{r},1}$, while medium 2 is a metal with negligible damping whose dielectric function $\varepsilon_{\mathrm{r},2}=\varepsilon_{\mathrm{r},2}(\omega)$ is described, in its simplest form, by the Drude model according to:

$$\varepsilon_{\mathrm{r},2}=1-\frac{\omega_p^2}{\omega^2}\tag{3.36}$$

where ω_p is the so-called *bulk plasma frequency* of the metal[12]. For most metals, this frequency is of the order of 1000-2000 THz, and falls in the ultraviolet region[19,87,89]. Thus, the conditions (3.30) and (3.34) are easily met for optical frequencies. Substituting (3.36) into (3.33), an explicit form of the SPP dispersion relation in terms of frequency is obtained:[90]

$$k_{\mathrm{SPP}}=k_0\sqrt{\frac{\varepsilon_{\mathrm{r},1}\varepsilon_{\mathrm{r},2}}{\varepsilon_{\mathrm{r},1}+\varepsilon_{\mathrm{r},2}}}=\frac{\omega}{c_0}\sqrt{\frac{\varepsilon_{\mathrm{r},1}(\omega^2-\omega_p^2)}{(\varepsilon_{\mathrm{r},1}+1)\omega^2-\omega_p^2}}\tag{3.37}$$

Notice that, since $k_{\mathrm{SPP}}=\beta>k_0$, the phase velocity $v_p=\omega/\beta$ of the surface waves at the interface is smaller than the velocity of light $c_0=\omega/k_0$. Therefore, on smooth surfaces, SPPs are non-radiative waves and cannot couple with propagating electromagnetic waves[19,89,91,92]. In other words, light alone impinging onto the metal surface cannot excite surface plasmon polaritons. Therefore, at the interface, there is a momentum mismatch that has to be compensated.

Figure 3.4 shows plots of (3.37) for a metal with negligible damping described by the Drude dielectric function (3.36) for (a) an air ($\varepsilon_{\mathrm{r},1}=1$) interface and (b) both an air and silicon dioxide (silica) interface. The frequency is normalised to the plasma frequency ω_p while the propagation constant k_{SPP} is normalised to the plasma wave vector $k_p=\omega_p/c_0$, where c_0 is the speed of light in vacuum. In these plots, both the real (continuous curves) and the imaginary part (dashed-dotted curve) of the wave vector β are shown.

[12]The bulk plasma frequency is defined as $\omega_p=\sqrt{\frac{ne^2}{\varepsilon_0 m}}$, where n is the electron density, e is the electron charge, ε_0 is the vacuum permittivity and m is the electron mass.

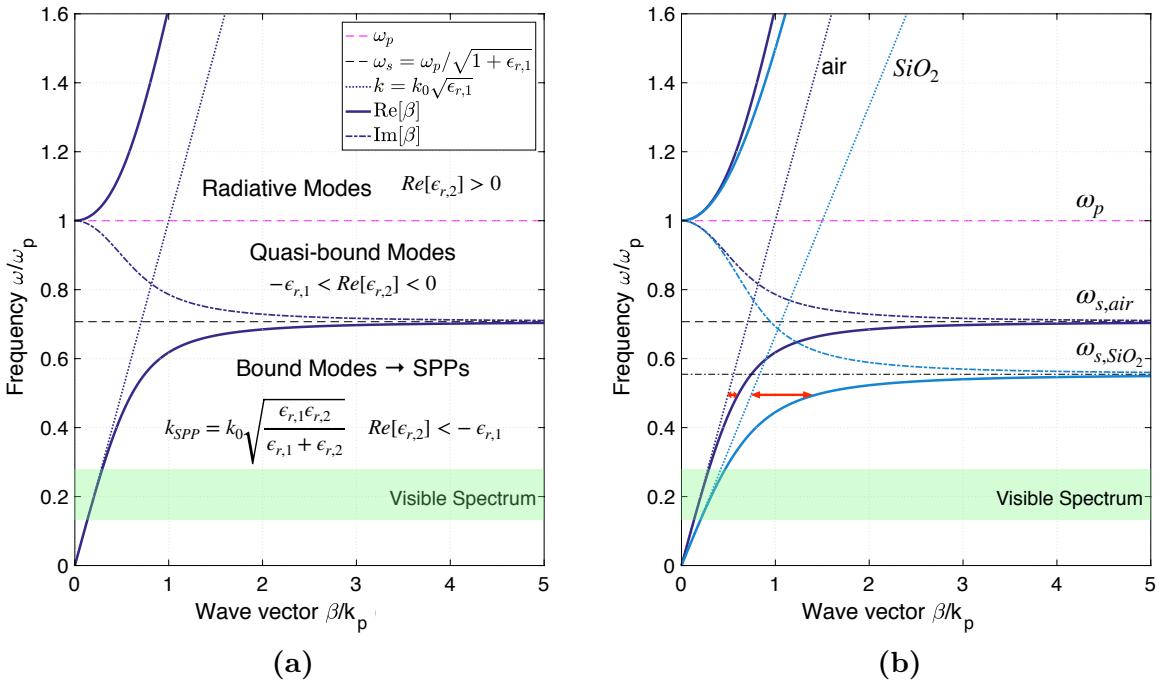


Figure 3.4: Dispersion relation of completely undamped SPPs. (a) Dispersion relation of SPPs for a metal with negligible damping described by the Drude dielectric function (3.36) for (a) an air ($\varepsilon_{r,1} = 1$) interface and (b) both an air and silicon dioxide interface.

Depending upon the frequency (and thus to the sign of the square root in Equation (3.37)), three separate regions can be identified: (i) Bound modes, (ii) Quasi-bound modes, and (iii) Radiative modes. For frequencies higher than the plasma frequency $\omega > \omega_p$, $|k_{\mathrm{SPP}}| < |k|$ and therefore transverse waves are allowed to propagate within the conductor,[19] called *plasma polaritons*. This is referred to as the transparency regime of metals. Instead, the SPP excitations belong to the part of the dispersion curve lying to the right of the dotted blue light line k, i.e. for $|k_{\mathrm{SPP}}| > |k|$. Between the regime of the radiative and bound modes, a frequency gap region with purely imaginary k_{SPP} prohibiting propagation exists[19].

The solid blue line in Figure 3.4a represents the SPP propagation constant and exhibits a nonlinear characteristic. Two asymptotes can be observed:[90]

$$\boxed{\omega \to 0 \qquad \beta \to k_0\sqrt{\varepsilon_{\mathrm{r},1}}}$$
$$\boxed{\beta \to \infty \qquad \omega \to \frac{\omega_p}{\sqrt{\varepsilon_{\mathrm{r},1}+1}} = \omega_s} \tag{3.38}$$

where ω_s is the so-called *surface plasma frequency*. Note that the equality $\omega = \omega_s$ is only fulfilled when $|\varepsilon_{\mathrm{r},1}| = |\varepsilon_{\mathrm{r},2}|$, i.e. when the the denominator of (3.37) $\varepsilon_{\mathrm{r},1} + \varepsilon_{\mathrm{r},2} = 0$.

A condition for the SPPs excitation is that $\varepsilon_{r,1} > 0$, therefore the surface plasma frequency ω_s is always lower than the plasma frequency ω_p. This means that surface waves can only be excited at frequencies lower than the plasma frequency ω_p. However, as mentioned above, there is no intersection point between $k = k_0$ and k_{SPP}, and therefore it is essential to provide an additional wave vector with special phase-matching techniques in order to excite the surface waves at a flat interface. This additional wave vector could be given, for example, through prism coupling or by nano structuring the metal layer.

When the frequency tends to zero, i.e. for small wave vectors, the dispersion relation k_{SPP} at the interface tends to the wave vector of the light line. In other words, the metal behaves 'like a metal'. The charges in the metal follow the displacement field and thus the metal behaves like a perfect mirror, i.e. no light can be transmitted through the interface and thus $B = A$ and $C = 0$. On the other hand, as the SPP wave vector k_{SPP} increases the free electrons in the metal are not able to oscillate as fast as the displacement field anymore. The *split* between the light line and the SPPs propagation constant enlarges, the frequency of the SPPs tends to become constant and approaches the characteristic surface plasma frequency ω_s. In the limit of negligible damping, the SPP wavevector tend to infinity and thus the phase velocity $v_p = \omega/\beta$ of the surface waves tends to zero. *"The mode thus acquire electrostatic character, and it known as the surface plasmon. The surface plasmon is indeed the limiting form of a SPP as β tends to infinity."*[19]

Figure 3.4b highlights how the dielectric function of the dielectric layer affects the dispersion relation of SPPs at the interface, given the same metallic layer. According to (3.38), the higher the relative permittivity of the dielectric $\varepsilon_{r,1}$, the lower the surface plasma frequency ω_s. This means that: (i) SPPs are extremely sensitive to refractive index variations at the interface; (ii) the higher $\varepsilon_{r,1}$, the larger the frequency gap of quasi-bound modes. As a consequence, the choice of dielectric the composes the interface also affects the module of the additional wave vector (red arrows). For a given angular frequency, the higher the relative permittivity of the dielectric the larger the additional wave vector required for the SPPs excitations. On the other hand, $\varepsilon_{r,1}$ variations have only a slight effect on the propagation wavevector of plasma polaritons (radiative modes) which are therefore less apt to sense RI variations.

3.6.1 Penetration Depths

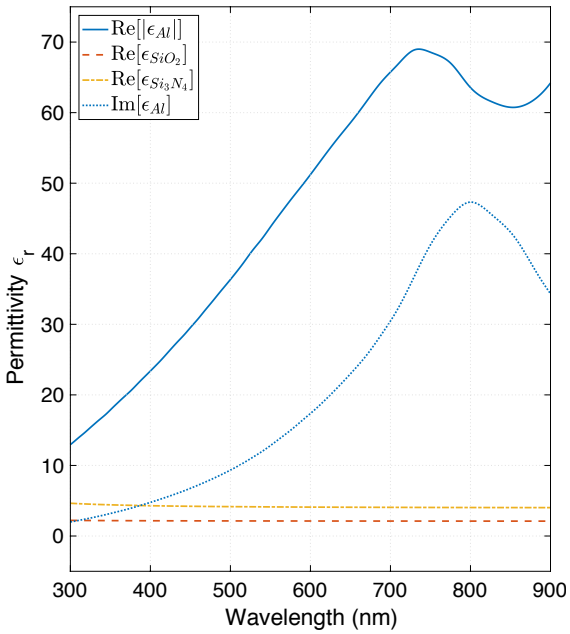
According to the definition, surface plasmon polaritons are orthogonally confined to the interface's plane and display evanescent fields penetrating into both sides of the interface. The quantity that defines the evanescent decay length of the fields perpendicular to the interface is called *penetration depth*. In other words, the penetration depth is the measure of how deep an electromagnetic radiation can penetrate a material. In this case, that is defined as the depth at which the intensity of the electric field $E(z) = E_0 \mathbf{e}^{-|k_z||z|}$ inside the material falls to $1/e$, which corresponds to about 37% of its original value at (or more precisely, just beneath) the surface. Therefore, the SPP penetration depths in the dielectric δ_d and in the metal δ_m are respectively defined by:[87]

$$\delta_d = \delta_1 = \frac{1}{|k_{z,1}|} = \frac{1}{k_0}\left|\frac{\varepsilon_{\mathrm{r},1}+\varepsilon_{\mathrm{r},2}}{\varepsilon_{\mathrm{r},1}^2}\right|^{\frac{1}{2}} \quad \text{and} \quad \delta_m = \delta_2 = \frac{1}{|k_{z,2}|} = \frac{1}{k_0}\left|\frac{\varepsilon_{\mathrm{r},1}+\varepsilon_{\mathrm{r},2}}{\varepsilon_{\mathrm{r},2}^2}\right|^{\frac{1}{2}} \tag{3.39}$$

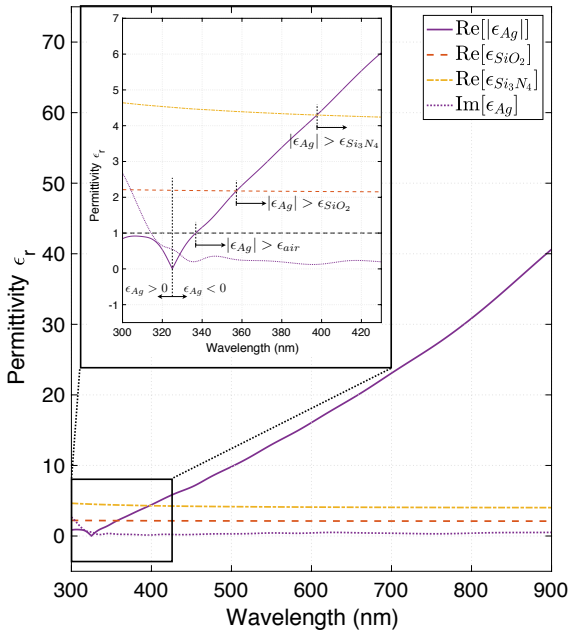
where $k_{z,i}$ represents the negative imaginary part (3.35) of the propagation constant. At low frequencies, the penetration depth can also be referred to as the *skin depth*, the latter term usually applying to metals in reference to the decay of electrical currents.

Figures 3.5a and 3.5b display the relative permittivities of two plasmonic metals, aluminium (Al) and silver (Ag) respectively, with some common dielectric materials. The conditions for SPPs excitation at a metal/dielectric interface, having dielectric functions ε_m and ε_d respectively, are: (i) $\mathrm{Re}\{\varepsilon_\mathrm{m}\} < 0$ and $\varepsilon_\mathrm{d} > 0$, and (ii) $|\varepsilon_\mathrm{m}| > \varepsilon_\mathrm{d}$. In case of Al, those conditions are met along the entire range of visible frequencies. On the other hand, SPPs cannot exist at a silver interface at wavelengths shorter than about 340 nm.

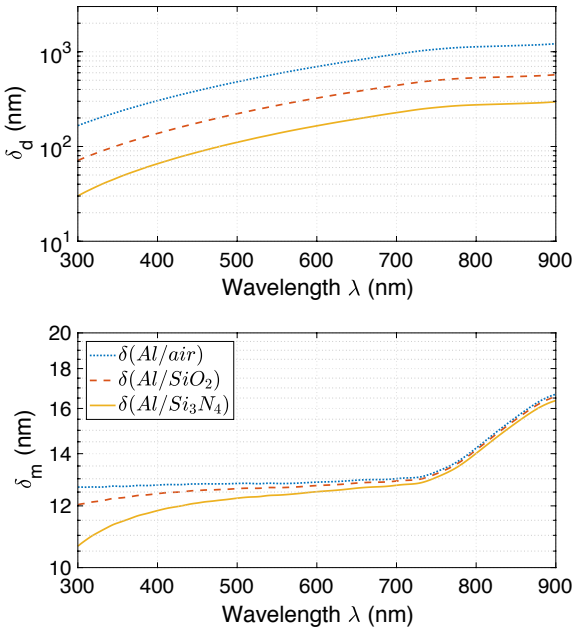
Figures 3.5c and 3.5d are plots of the penetration depths inside the dielectric and the metal for an Al and a Ag interface, respectively. Because of the condition $|\varepsilon_\mathrm{m}| > \varepsilon_\mathrm{d}$, the penetration depth of the surface plasmon polaritons inside of the dielectric is larger than the one inside of the metal, i.e. in the dielectric the field fall off far more slowly. Inside the metals, the electric field decays over depths on the order of about 20 nm over a wide range of frequencies, spanning from the visible to the infrared[19]. Instead, penetration depths in the dielectric are one or two orders of magnitude larger.



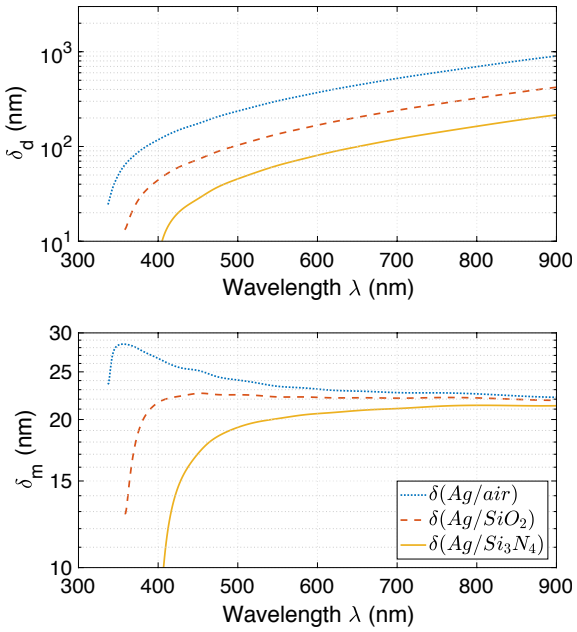
(a) Relative Permittivities of Al, SiO_2, Si_3N_4.



(b) Relative Permittivities of Ag, SiO_2, Si_3N_4.



(c) Penetration Depths at an Al interface.



(d) Penetration Depths at a Ag interface.

Figure 3.5: Relative Permittivities and SPPs Penetration Depths. (a) Real part of the relative dielectric functions ε_r of aluminium (blue solid line), silicon dioxide (red dashed line) and silicon nitride (yellow dot-sashed line), and imaginary part (blue dotted line) of aluminium. (b) Real part of the relative dielectric functions ε_r of silver (purple solid line), silicon dioxide (red dashed line) and silicon nitride (yellow dot-sashed line), and imaginary part (purple dotted line) of aluminium. Note that SPPs condition of existence requires both: (i) $\varepsilon_m < 0$ and $\varepsilon_d > 0$; (ii) $|\varepsilon_m| > \varepsilon_d$. (n,k) data for Figures (a) and (b) were downloaded from the Lumerical default material database[93]. (c) SPP penetration depths inside the dielectric and inside the metal for a Al/air, Al/SiO_2 and Al/Si_3N_4 interfaces. (d) SPP penetration depths inside the dielectric and inside the metal for a Ag/air, Ag/SiO_2 and Ag/Si_3N_4 interfaces.

SPPs are very sensitive to perturbations within their evanescent 'tails'. Therefore, any variation in refractive index (RI) at distances from the interface smaller than about twice the penetration depth will affect the SPP properties. Penetration depths are also a measure of the confinement of the field at the interface. The smaller the penetration depth, the higher the field confinement. The higher the field confinement, the 'more sensitive' are the SPPs to RI perturbations. However, in general, the loss increases when the transverse confinement of a SPP mode increases, as a larger fraction of the modal field is located inside the metal[94].

3.6.2 Damped SPPs and Propagation Length

The above discussion of Figure 3.4 have assumed an ideal conductor with $Im\left[\varepsilon_{\mathrm{r},2}\right] = 0$. However, electrons in real metals suffer both from free-electron and intraband damping[19]. Therefore, $\varepsilon_{\mathrm{r},2}(\omega)$ is a complex value, and with it also the SPP propagation constant k_{SPP}. This implies that, as a SPP propagates along an interface, it loses energy due to the absorption inside the metal. Figure 3.6 shows the dispersion relation of damped SPPs propagating at a silver/air and silver/silica interface. The quasi-bound, leaky part of the dispersion relation between ω_s and ω_p is now allowed, in contrast to the case of an ideal conductor, where $\mathrm{Re}[\beta] = 0$ in this regime. Also, the wave vector of the bounded SPPs now approach a maximum, finite limit $\beta_{\max}$ at the surface plasma frequency ω_s of the system[19].

This limitation puts a lower bound both on the wavelength $\lambda_{\mathrm{SPP,min}} = 2\pi/\,\mathrm{Re}[\beta_{\max}]$ of the surface plasmon, and also on the amount of mode confinement perpendicular to the interface[19]. From (3.39), the SPP penetration depths decrease as the absolute values of the respective wavevectors perpendicular to the interface $|k_{\mathrm{z,i}}|$ increase. Therefore, since $k_{\mathrm{z}} = \sqrt{\beta^2 - \varepsilon_{\mathrm{r},1}k_0^2}$, when the wavevector approaches $\beta_{\max}$ the SPP fields fall off as $\mathrm{e}^{|k_{\mathrm{z,max}}||z|}$ and the penetration depths tend to their lower bounds $\delta_{\mathrm{d,min}}$ and $\delta_{\mathrm{m,min}}$.

Not-negligible damping implies that SPPs travelling at an interface are attenuated. It is then possible to evaluate their propagation length. The tangential electric field E_x at the interface $z = 0$ can be represented as $E_x = E_0\mathrm{e}^{-j\beta x}$. Since $k_{\mathrm{SPP}} = \beta = \beta' + j\beta''$ is a

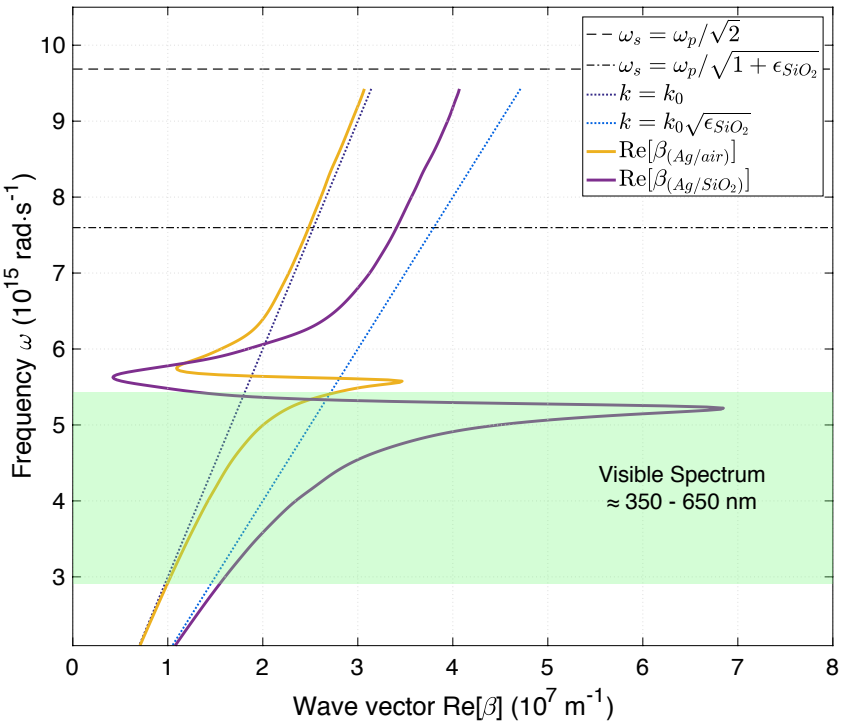


Figure 3.6: Dispersion relation of damped SPPs. Dispersion relation of SPPs at a silver-air (yellow curve) and silver-silica (purple curve) interface. Due to the damping, the SPP propagation wavevector approaches a finite limit at the surface plasma frequency.

complex value, it becomes:

$$E_x = E_0 \cdot \underbrace{\mathrm{e}^{-j\beta' x}}_{\text{propagation term}} \cdot \underbrace{\mathrm{e}^{\beta'' x}}_{\text{exponential decay}} \tag{3.40}$$

The intensity of the surface plasmon decays with the square of the electric field, so at a distance x, the intensity has decreased by a factor of $\mathrm{e}^{-2\beta'' x}$. The propagation length is defined as the distance for the SPP intensity to decay by a factor of 1/e. This condition is satisfied at a length:

$$L_x = \frac{1}{2\beta''} \tag{3.41}$$

A typical propagation length lies between 10 and 100 microns in the visible regime[19]. However, it displays a strong dependence on frequency.

3.6.3 Summary

Summarising we can assert that surface plasma waves on smooth surfaces: (i) exist at an interface between a medium 1 and a medium 2 when for $\varepsilon_1 > 0$ $\varepsilon_2 < 0$, (ii) exist only for

frequency lower than the plasma frequency ω_p, (iii) are slow waves of short wavelength, i.e. for a metal-vacuum interface the phase velocity of SPPs $v_p = \omega/k_{\mathrm{SPP}}$ at the interface is smaller than the velocity of light $c_0 = \omega/k_0$ and $\lambda_{\mathrm{SPP}} < \lambda_0$, (iv) cannot interact with propagating waves since they have a larger propagation constant β, (v) interact with the evanescent near field components of the Fourier spectrum of an object, (vi) can confine the electromagnetic fields over length scales significantly smaller than the wavelength, as long as the fields oscillate at frequencies close to the intrinsic plasma frequency of the conductor.[90]

As displayed in Figure 3.4, at low frequencies the SPP dispersion relation quickly approaches the light line which means that surface plasmon polaritons tend to behave like free propagating light waves and thus they are less apt to be used to generate strongly localised and enhanced fields[95]. However, it is possible to generate slower surface plasma waves by simply placing two or more metal-dielectric interfaces that sustain SPPs in close proximity. This introduces a coupling between the SPPs of the individual interfaces, i.e. the SPPs associated with individual interfaces interact with each other generating SPP-modes. Multiple-interfaces systems can support many different SPP-modes. Some of these modes have a propagation constant much smaller than the SPP wave vector of a single interface making nm-sized field localisation accessible at any wavelength[95,96].

3.7 Coupled SPPs in Plasmonic Waveguides

The previous section thoroughly derived and described the SPPs dispersion relation at a smooth interface between a dielectric and a conductor. This section studies instead the excitation and coupling of SPPs in a three-layer system. Necessary condition for the system to be considered a plasmonic waveguide is that at least one of the layers is metallic, with dielectric constant having negative real-part in the operating frequency range[89]. As opposed to dielectric waveguides, wherein the light is confined in an optically dense core via index contrast with respect the top and bottom cladding layers, plasmonic waveguides confine light to the metal-dielectric interfaces owing to the negative dielectric constant of the metallic region[63].

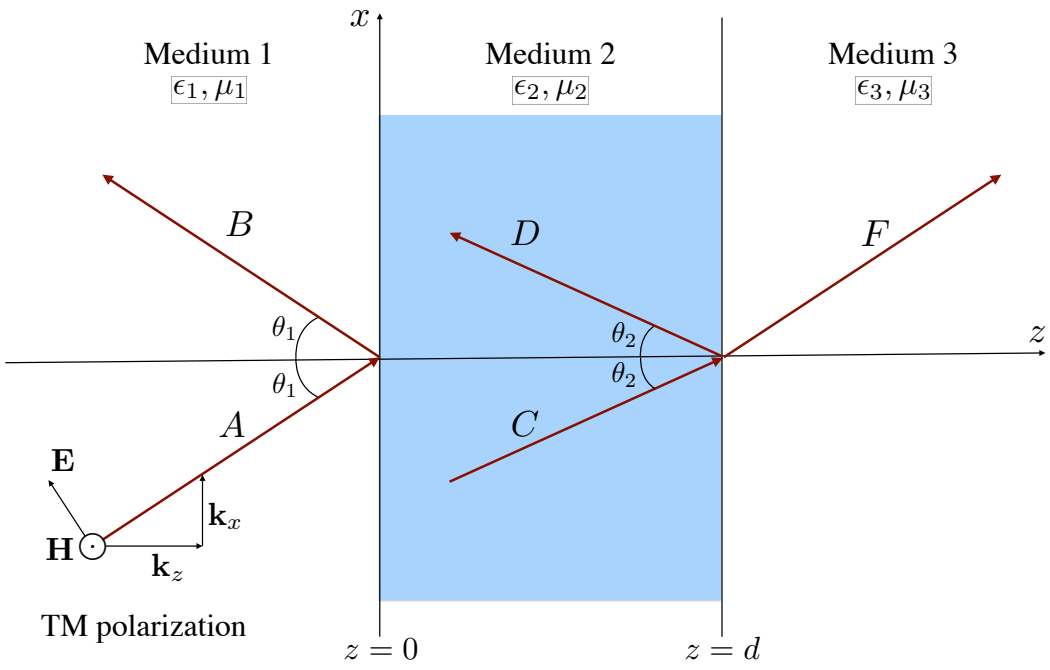


Figure 3.7: TM-polarised light incident onto a generic 3-layer system. Schematic representation of a TM-polarised wave incident onto an single slab with arbitrary dielectric function ε_2 and thickness d, sandwiched between two semi-infinite media having different dielectric functions, ε_1 and ε_3 respectively.

In a plasmonic waveguide, the multiple interfaces are placed in near proximity so that the separation between them is comparable to or smaller than the penetration depth of the surface wave modes. As a consequence, the SPPs at the individual dielectric-conductor interfaces will couple with each other and give rise to bound SPP-modes. Three specific three-layer systems will be considered: (i) an insulator-metal-insulator (IMI), where a thin metallic layer is sandwiched between two infinitely thick dielectric claddings; (ii) a metal-insulator-metal (MIM), where a thin dielectric core layer is sandwiched between two metallic claddings; and (iii) an insulator-insulator-metal (IIM), where a thin dielectric layer is sandwiched between a dielectric and a metal cladding. This study on three-layer plasmonic waveguides will become of use to interpret and to gain a better understanding of the simulation data of the MIM plasmonic filter design developed during the course of the project.

Consider the case of a TM-polarised electromagnetic wave (A) incident onto a slab of arbitrary thickness d sandwiched between two half-space materials, as shown in Figure 3.7. The three layers consist of linear, homogeneous and isotropic materials. The quantities ε_1, ε_2 and ε_3 denote the relative permittivities of the media, that is $\varepsilon_{\mathrm{r,i}} = \varepsilon_{\mathrm{i}}/\varepsilon_0$, with $i =$

$1, 2, 3$, where ϵ_{i} is the permittivity of the i-th medium and ε_0 the permittivity of vacuum. Materials are assumed to be non-magnetic, i.e. $\mu_{\mathrm{r,i}} = 1$ and thus $\mu_1 = \mu_2 = \mu_3 = \mu_0$. Propagation is in the x-direction, the transverse confinement is along the z-direction, and the layers have infinite extent long the y-direction. We are interested in the coupling of surface plasmon modes within the middle layer (layer 2).

The field components in every medium are recovered from the single-interface case (3.24):[90]

$$\begin{cases} H_{y,1} = \left(A\mathrm{e}^{-jk_{z,1}z} + B\mathrm{e}^{jk_{z,1}z}\right)\mathrm{e}^{-jk_x x} \\ E_{x,1} = \dfrac{k_{z,1}}{\omega\varepsilon_1}\left(A\mathrm{e}^{-jk_{z,1}z} - B\mathrm{e}^{jk_{z,1}z}\right)\mathrm{e}^{-jk_x x} \\ E_{z,1} = -\dfrac{k_x}{\omega\varepsilon_1}\left(A\mathrm{e}^{-jk_{z,1}z} + B\mathrm{e}^{jk_{z,1}z}\right)\mathrm{e}^{-jk_x x} \end{cases}$$

$$\begin{cases} H_{y,2} = \left(C\mathrm{e}^{-jk_{z,2}z} + D\mathrm{e}^{jk_{z,2}z}\right)\mathrm{e}^{-jk_x x} \\ E_{x,2} = \dfrac{k_{z,2}}{\omega\varepsilon_2}\left(C\mathrm{e}^{-jk_{z,2}z} - D\mathrm{e}^{jk_{z,2}z}\right)\mathrm{e}^{-jk_x x} \\ E_{z,2} = -\dfrac{k_x}{\omega\varepsilon_2}\left(C\mathrm{e}^{-jk_{z,2}z} + D\mathrm{e}^{jk_{z,2}z}\right)\mathrm{e}^{-jk_x x} \end{cases}$$

$$\begin{cases} H_{y,3} = F\mathrm{e}^{-jk_{z,3}(z-d)}\mathrm{e}^{-jk_x x} \\ E_{x,3} = \dfrac{k_{z,3}}{\omega\varepsilon_3}F\mathrm{e}^{-jk_{z,3}(z-d)}\mathrm{e}^{-jk_x x} \\ E_{z,3} = -\dfrac{k_x}{\omega\varepsilon_3}F\mathrm{e}^{-jk_{z,3}(z-d)}\mathrm{e}^{-jk_x x} \end{cases}$$

By applying the boundary conditions (3.6) and (3.16)[13]:[90]

at z = 0

$$\begin{cases} H_{y,1} = H_{y,2} \\ E_{x,1} = E_{x,2} \end{cases}$$

$$\boxed{\begin{cases} A + B = C + D \\ A - B = \zeta_{(z=0)}(C - D) \end{cases}}$$

at z = d

$$\begin{cases} H_{y,2} = H_{y,3} \\ E_{x,2} = E_{x,3} \end{cases}$$

$$\boxed{\begin{cases} C\mathrm{e}^{-jk_{z,2}d} + D\mathrm{e}^{jk_{z,2}d} = F \\ \zeta_{(z=d)}\left(C\mathrm{e}^{-jk_{z,2}d} - D\mathrm{e}^{jk_{z,2}d}\right) = F \end{cases}}$$

[13]Note that the condition on $E_{z,i}$ leads to the same set of equation as $H_{y,i}$

$$A + B = C + D \qquad (1)$$

$$A - B = \zeta_{(z=0)}(C - D) \qquad (2)$$

$$Ch_- + Dh_+ = F \qquad (3)$$

$$\zeta_{(z=d)}\,(Ch_- - Dh_+) = F \qquad (4)$$

with $\zeta_{(z=0)} = \dfrac{k_{z,2}\varepsilon_1}{k_{z,1}\varepsilon_2}$ $\zeta_{(z=d)} = \dfrac{k_{z,2}\varepsilon_3}{k_{z,3}\varepsilon_2}$

$$\begin{cases} h_- = \mathrm{e}^{-jk_{z,2}d} \\ h_+ = \mathrm{e}^{jk_{z,2}d} \end{cases} \quad \Rightarrow \quad h_- = \frac{1}{h_+}$$

(3)=(4):

$$Ch_- + Dh_+ = \zeta_{(z=d)}(Ch_- - Dh_+)$$

$$-Ch_-(1 - \zeta_{(z=d)}) = Dh_+(1 + \zeta_{(z=d)})$$

$$\rightarrow \quad D = -C\frac{1 - \zeta_{(z=d)}}{1 + \zeta_{(z=d)}}h_-^2 = -C\rho_d h_-^2 \qquad \text{with} \qquad \rho_d = \frac{1 - \zeta_{(z=d)}}{1 + \zeta_{(z=d)}}$$

(1)+(2) :

$$2A = C(1 + \zeta_{(z=0)}) + D(1 - \zeta_{(z=0)})$$

$$\tau_0 A = C + D\rho_0 \qquad \text{with} \qquad \tau_0 = \frac{2}{1 + \zeta_{(z=0)}} \quad \rho_0 = \frac{1 - \zeta_{(z=0)}}{1 + \zeta_{(z=0)}}$$

$$\rightarrow \quad \tau_0 A = C(1 - \rho_0\rho_d h_-^2)$$

$$\boxed{\Rightarrow \qquad \frac{C}{A} = \frac{\tau_0}{1 - \rho_0\rho_d h_-^2}}$$

Transmission after the 1st interface

$$\boxed{\Rightarrow \qquad \frac{D}{A} = \frac{-\tau_0\rho_d h_-^2}{1 - \rho_0\rho_d h_-^2}}$$

Reflection from the 2nd interface

(3.42)

(1)-(2):

$$2B = C(1 - \zeta_{(z=0)}) + D(1 + \zeta_{(z=0)})$$

$$\tau_0\frac{B}{A} = \left[\frac{C}{A}\rho_0 + \frac{D}{A}\right]$$

$$\boxed{\Rightarrow \qquad \frac{B}{A} = \frac{\rho_0 - \rho_d h_-^2}{1 - \rho_0\rho_d h_-^2}}$$

Reflection from the 1st interface

(3) :

$$\frac{F}{A} = \left[\frac{C}{A}h_- + \frac{D}{A}h_+\right]$$

$$\boxed{\Rightarrow \qquad \frac{F}{A} = \frac{\tau_0\,(1 - \rho_d)\,h_-}{1 - \rho_0\rho_d h_-^2}}$$

Slab transmission, transfer function

(3.43)

The surface plasmon resonance condition corresponds to a pole of F/A, that is, the vanishing of the denominator, $1 - \rho_0\rho_d h_-^2 = 0$. Thus, the expression to solve is:[90]

$$(\zeta_{(z=0)} + 1)(\zeta_{(z=d)} + 1) = h_-^2(\zeta_{(z=0)} - 1)(\zeta_{(z=d)} - 1)$$

with $h_- = \mathrm{e}^{-jk_{z,2}d}$, $\rho_0 = \frac{1-\zeta_{(z=0)}}{1+\zeta_{(z=0)}}$, and $\rho_d = \frac{1-\zeta_{(z=d)}}{1+\zeta_{(z=d)}}$, of which $\zeta_{(z=0)} = \frac{k_{z,2}\varepsilon_1}{k_{z,1}\varepsilon_2}$, $\zeta_{(z=d)} = \frac{k_{z,2}\varepsilon_3}{k_{z,3}\varepsilon_2}$, and where $k_{z,i} = -j\gamma_\mathrm{i}$.

Then, it follows:[90]

$$h_-^2 = \frac{(\zeta_{(z=0)}+1)(\zeta_{(z=d)}+1)}{(\zeta_{(z=0)}-1)(\zeta_{(z=d)}-1)}$$

$$\mathrm{e}^{-2\gamma_2 d} = \frac{\left(\frac{\gamma_2\varepsilon_1}{\gamma_1\varepsilon_2}+1\right)\left(\frac{\gamma_2\varepsilon_3}{\gamma_3\varepsilon_2}+1\right)}{\left(\frac{\gamma_2\varepsilon_1}{\gamma_1\varepsilon_2}-1\right)\left(\frac{\gamma_2\varepsilon_3}{\gamma_3\varepsilon_2}-1\right)}$$

$$\mathrm{e}^{-2\gamma_2 d} = \frac{\frac{\varepsilon_1}{\gamma_1}\left(\frac{\gamma_2}{\varepsilon_2}+\frac{\gamma_1}{\varepsilon_1}\right)\frac{\varepsilon_3}{\gamma_3}\left(\frac{\gamma_2}{\varepsilon_2}+\frac{\gamma_3}{\varepsilon_3}\right)}{\frac{\varepsilon_1}{\gamma_1}\left(\frac{\gamma_2}{\varepsilon_2}-\frac{\gamma_1}{\varepsilon_1}\right)\frac{\varepsilon_3}{\gamma_3}\left(\frac{\gamma_2}{\varepsilon_2}-\frac{\gamma_3}{\varepsilon_3}\right)}$$

$$\boxed{\mathrm{e}^{-2\gamma_2 d} = \frac{\left(\frac{\gamma_2}{\varepsilon_2}+\frac{\gamma_1}{\varepsilon_1}\right)\left(\frac{\gamma_2}{\varepsilon_2}+\frac{\gamma_3}{\varepsilon_3}\right)}{\left(\frac{\gamma_2}{\varepsilon_2}-\frac{\gamma_1}{\varepsilon_1}\right)\left(\frac{\gamma_2}{\varepsilon_2}-\frac{\gamma_3}{\varepsilon_3}\right)}} \tag{3.44}$$

Equation (3.44) can be rewritten as:[89]

$$\mathrm{e}^{-2\gamma_2 d} = \frac{\left(\gamma_2+\gamma_1\frac{\varepsilon_2}{\varepsilon_1}\right)\left(\gamma_2+\gamma_3\frac{\varepsilon_2}{\varepsilon_3}\right)}{\left(\gamma_2-\gamma_1\frac{\varepsilon_2}{\varepsilon_1}\right)\left(\gamma_2-\gamma_3\frac{\varepsilon_2}{\varepsilon_3}\right)}$$

$$\mathrm{e}^{-2\gamma_2 d} = \frac{(\gamma_2+\gamma_1\rho_1)(\gamma_2+\gamma_3\rho_3)}{(\gamma_2-\gamma_1\rho_1)(\gamma_2-\gamma_3\rho_3)}$$

$$\boxed{\mathrm{e}^{2\gamma_2 d} = \frac{(\gamma_2-\gamma_1\rho_1)(\gamma_2-\gamma_3\rho_3)}{(\gamma_2+\gamma_1\rho_1)(\gamma_2+\gamma_3\rho_3)}} \tag{3.45}$$

where $\rho_1 = \varepsilon_2/\varepsilon_1$ and $\rho_3 = \varepsilon_2/\varepsilon_3$.

Solutions to Equation (3.44), or Equation (3.45), can be found numerically.

Note that a plasmonic waveguide can support different types of modes. It can support non-radiative, plasmonic bound modes, i.e. modes whose field energy is carried at or near the metal-dielectric interfaces of the system rather than at the centre of the film like e.g. in dielectric waveguides[89]. It can support radiative, plasmonic leaky modes[97]. Finally, it can also support *oscillatory modes*. In contrast to plasmonic solutions that have a value for γ that is predominantly real-valued, oscillatory modes have a propagation constant γ that is dominantly imaginary[89]. Therefore, the nature of the numerical solutions will depend upon the choice of the initial guess(es) within the frequency-wave vector space.

3.7.1 Symmetric IMI Plasmonic Waveguide

A IMI plasmonic waveguide consists of a metal film ε_{m}, sandwiched between two dielectric layers, namely a substrate $\varepsilon_{\mathrm{d,s}}$ and a cladding $\varepsilon_{\mathrm{d,c}}$. Consider that the substrate and the cladding are the same: $\varepsilon_{\mathrm{d,s}} = \varepsilon_{\mathrm{d,c}} = \varepsilon_{\mathrm{d}}$. If the distance between the two interfaces is small enough for the single SPPs to interact with each other, the symmetric IMI plasmonic waveguide can support only two non-radiative, bound SPP-modes: one symmetric and one antisymmetric with respect to their field distributions[90]. The wave fronts are tilted in towards the metal[89].

Two analytical solutions can be derived to describe these bound SPP-modes. The symmetry with respect of the dielectric layers implies that $\zeta_{(z=0)} = \zeta_{(z=d)} = \zeta$ and thus the transfer function of the slab (3.43) can be written as:[90]

$$\frac{F}{A} = \frac{4h_{-}\zeta}{(\zeta+1)^2 - h_{-}^2(\zeta-1)^2} \tag{3.46}$$

with

$$\zeta = \frac{k_{z,m}\varepsilon_d}{k_{z,d}\varepsilon_m} = \frac{\gamma_m\varepsilon_d}{\gamma_d\varepsilon_m} \qquad \text{and} \qquad h_{-} = \mathrm{e}^{-jk_{z,m}d} = \mathrm{e}^{-\gamma_m d} \tag{3.47}$$

where $\gamma_i^2 = -k_{z,i}^2 = k_x^2 - \varepsilon_{\mathrm{i}}k_0^2$ and $k_x = \beta = k_{\mathrm{SPP}}$. Then, $\gamma_i = \sqrt{k_{\mathrm{SPP}}^2 - \varepsilon_{\mathrm{i}}k_0^2}$.

As previously stated, in order to find the surface modes, it is necessary to look for the eigensolutions of the system. An eigensolution exists when there is an output without an input, and so the denominator is set to zero:[90]

$$\boxed{(\zeta+1)^2 - h_{-}^2(\zeta-1)^2 = 0}$$

$$(\zeta+1) = \pm h_{-}(\zeta-1)$$

$$\zeta(1 \mp h_{-}) = -(1 \pm h_{-})$$

By substituting h_{-}, and knowing that $\frac{1\mp\mathrm{e}^{-2x}}{2\mathrm{e}^{-x}} = \frac{\mathrm{e}^{x}\mp\mathrm{e}^{-x}}{2}$ and $\coth(x) = \frac{1}{\tanh(x)} = \frac{\mathrm{e}^{x}+\mathrm{e}^{-x}}{\mathrm{e}^{x}-\mathrm{e}^{-x}}$,

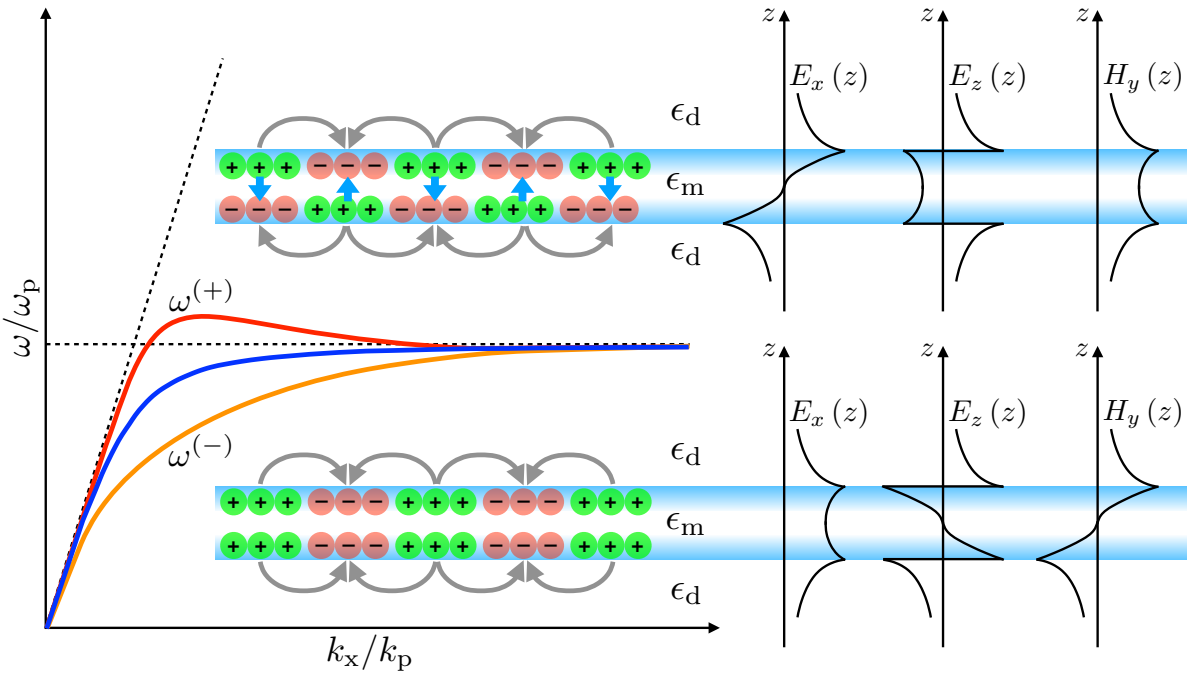


Figure 3.8: Bound SPPs on thin metal films in a IMI structure. Schematic representation of the dispersion relation of the coupled antisymmetric (upper branch - red solid line) and symmetric (lower branch - orange solid line) modes for an insulator/metal/insulator multilayer system with a thin metal core thickness. The blue solid line represents the dispersion relation of SPPs at a single flat metal/insulator interface. Next to each bound-SPP mode, the respective charge and fields' (as a function of z) distributions are delineated. For the upper mode: E_x is odd, E_z and H_y are even. For the lower mode: E_x is even, E_z and H_y are odd.

the equivalence becomes:

$$\zeta\left(1 \mp \mathrm{e}^{-\gamma_m d}\right) = -\left(1 \pm \mathrm{e}^{-\gamma_m d}\right)$$

$$\zeta\left(\mathrm{e}^{\gamma_m \frac{d}{2}} \mp \mathrm{e}^{-\gamma_m \frac{d}{2}}\right) = -\left(\mathrm{e}^{\gamma_m \frac{d}{2}} \pm \mathrm{e}^{-\gamma_m \frac{d}{2}}\right)$$

$$\swarrow \qquad\qquad \searrow$$

$$\zeta\left(\mathrm{e}^{\gamma_m \frac{d}{2}} - \mathrm{e}^{-\gamma_m \frac{d}{2}}\right) = -\left(\mathrm{e}^{\gamma_m \frac{d}{2}} + \mathrm{e}^{-\gamma_m \frac{d}{2}}\right) \qquad \zeta\left(\mathrm{e}^{\gamma_m \frac{d}{2}} + \mathrm{e}^{-\gamma_m \frac{d}{2}}\right) = -\left(\mathrm{e}^{\gamma_m \frac{d}{2}} - \mathrm{e}^{-\gamma_m \frac{d}{2}}\right)$$

$$\boxed{\zeta = \frac{\gamma_m \varepsilon_d}{\gamma_d \varepsilon_m} = -\coth\left(\frac{\gamma_m d}{2}\right)} \qquad \boxed{\zeta = \frac{\gamma_m \varepsilon_d}{\gamma_d \varepsilon_m} = -\tanh\left(\frac{\gamma_m d}{2}\right)} \qquad (3.48)$$

$$\text{or } \zeta = \frac{\gamma_d \varepsilon_m}{\gamma_m \varepsilon_d} = -\tanh\left(\frac{\gamma_m d}{2}\right) \qquad \text{or } \zeta = \frac{\gamma_d \varepsilon_m}{\gamma_m \varepsilon_d} = -\coth\left(\frac{\gamma_m d}{2}\right) \qquad (3.49)$$

Upper mode: LR-SPP (TM_0) Lower mode: SR-SPP (TM_1)

Therefore, in case of a symmetric IMI system where the thickness d of the metal slab is small enough so that the SPPs at the two metal/dielectric interfaces can interact with

each other, bound SPP-modes are generated and the SPP dispersion relation at a single flat interface (3.33) splits into a pair of equations (3.48) [90]. These two solutions can only be solved numerically. Figure 3.8 is a schematic representation of the dispersion relation of the bound SPP-modes in a symmetric IMI structure. The figure also displays the charge distribution and the transverse electric and magnetic fields, E_z and H_y respectively, and the longitudinal electric field E_x as a function of z for each coupled mode. The upper brach of the solution is usually indicated by $\omega^{(+)}$ and the lower brach by $\omega^{(-)}$. The adjectives *upper* and *lower* indicate the solutions above (higher frequency) and below (lower frequency) the unperturbed dispersion relation for the single interface, respectively.

For the upper mode, the transverse electric and magnetic fields E_z and H_y, respectively, are symmetric as a function of z, whereas the longitudinal electric field E_x is antisymmetric as a function of z. Instead, for the lower mode, the transverse electric and magnetic fields $E_z(z)$ and $H_y(z)$, respectively, are antisymmetric and the longitudinal electric field $E_x(z)$ is symmetric. Accordingly to the charge distribution and their oscillation at the interface, which depends on the tangential component of the electric field $E_x(z)$, from now on the upper branch mode will be referred to as the antisymmetric mode while the lower branch as the symmetric mode. The two modes can also be referred to as *Long-Range Surface Plasmon Polaritons* (LR-SPPs) and *Short-Range Surface Plasmon Polaritons* (SR-SPPs), to indicate the upper and the lower branch, respectively. The attributes *long-range* and *short-range* are directly correlated to the propagation length of each mode, as it will be explained more in detail in the next paragraphs. [90]

Since the metal is lossy these bound modes are lossy. But the lower mode is much lossier than the upper one. One simple explanation may be based on the fact that the latter resembles more an electromagnetic wave traveling in vacuum, i.e. it is nearer to the light line. Therefore, because EM waves travel in vacuum with no attenuation, the upper mode travels with a lower attenuation than the lower one. [90]

Another explanation derives from charge oscillations. In the asymmetric mode the field component E_z inside the slab helps the charges to oscillate back and forth between the two surfaces with an amplitude of about the thickness of the slab. In contrast, in the symmetric mode, the charges have the same sign on opposite sides of the slab and

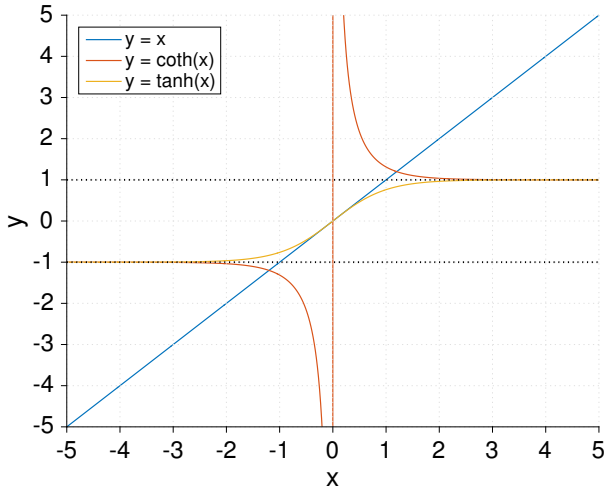


Figure 3.9: $\coth(x)$ and $\tanh(x)$ functions for a generic linearly spaced vector x.

therefore they oscillate parallel to each surface with amplitudes of the order of the SPP wavelength. Since the latter is much greater than the slab thickness, the current densities of the symmetric mode are relatively large, leading to correspondingly large losses. [90]

But, probably, the best explanation is based on the penetration depth in the metal. For a given frequency, the symmetric mode, having a higher k_x, has smaller penetration depths - either inside the dielectric either inside the metal. This implies a higher field confinement which lead to higher losses. On the other hand, the antisymmetric mode has larger penetration depths and lower field confinement, and thus it is less lossy. [90]

In Figure 3.9, the $\coth(x)$ and $\tanh(x)$ functions are plotted for a generic linearly spaced vector x. In the limit of very thick films, $x = \frac{\gamma_m d}{2} \to +\infty$, $\coth(x) = \tanh(x) = 1$ and therefore the equations tend to a single solution which corresponds to the unperturbed dispersion relation for the single interface. Instead, in the limit of very thin films, $x = \frac{\gamma_m d}{2} \to 0$ so that $\coth(x) \to +\infty$ while $\tanh(x) \approx x$, i.e. the split between the modes becomes larger as the slab becomes thinner ($d \to 0$).

Figure 3.10 displays the dependence of the LR-SPP and SR-SPP on the thickness d of the metal slab. Large wavevectors can be achieved at lower energies for thinner films. The thicker the slab the smaller the split between the two modes. Notice that, in the visible regime, when the slab become approximately twice the SPP penetration depth inside the metal ($d \approx 40$ nm) the two modes converge and match the SPP dispersion relation for the single interface.

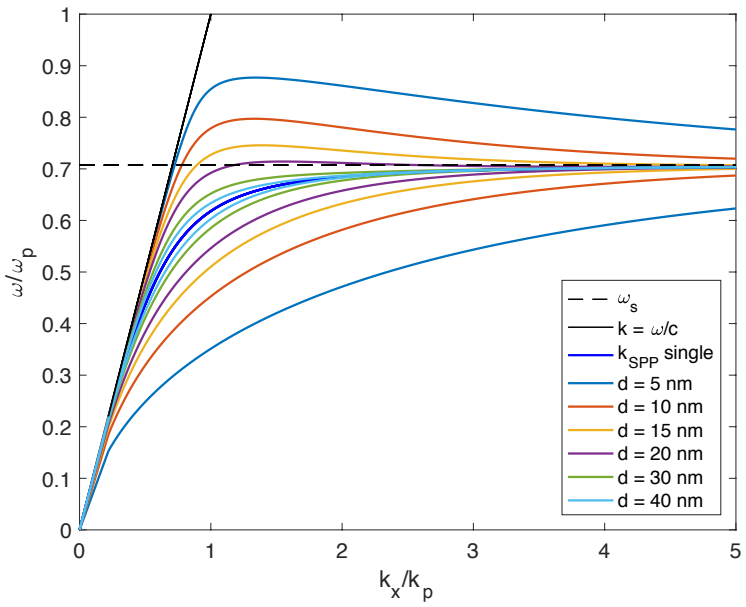


Figure 3.10: Coupled SPPs in a symmetric IMI plasmonic waveguide. (a) Dependence of the coupled SPPs on the thickness d of the slab in a symmetric IMI plasmonic waveguide. The thinner the slab the larger the split between the two plasmonic modes. Large propagation constant can be achieved by using sufficiently small width of the metallic layer.

In IMI plasmonic waveguide, multicentimeter propagation is observed for near-infrared wavelengths where the dispersion relation of the modes follows the light line[64]. However, this long-range propagation is achieved at the expenses of confinement. The confinement of the IMI structure is limited by the decay length into the dielectric cladding and substrate which typically exceeds microns. For confinement below the limit of a conventional dielectric waveguide the penetration depth in the dielectric must be smaller than $\lambda/(2n)$. This condition is met only near the surface plasmon resonance frequency[63].

3.7.2 Asymmetric MIM Plasmonic Waveguide

Consider a thin dielectric layer with thickness d and dielectric constant $\varepsilon_2 = \varepsilon_d$ sandwiched between two thick (semi-infinite) metallic layers having dielectric constant $\varepsilon_1 = \varepsilon_3 = \varepsilon_m$, as shown in Figure 3.11. Let us consider that all three media are lossless, with ε_{d} real positive, and $\varepsilon_{\mathrm{m,c}}$, $\varepsilon_{\mathrm{m,s}}$ real negative, so that we can set $\varepsilon_{\mathrm{m,c}} = -|\varepsilon_{\mathrm{m,c}}|$ and $\varepsilon_{\mathrm{m,s}} = -|\varepsilon_{\mathrm{m,s}}|$.

The SPP dispersion relations $\beta_{\mathrm{c},\infty}$ and $\beta_{\mathrm{s},\infty}$ of the single top and bottom metal-

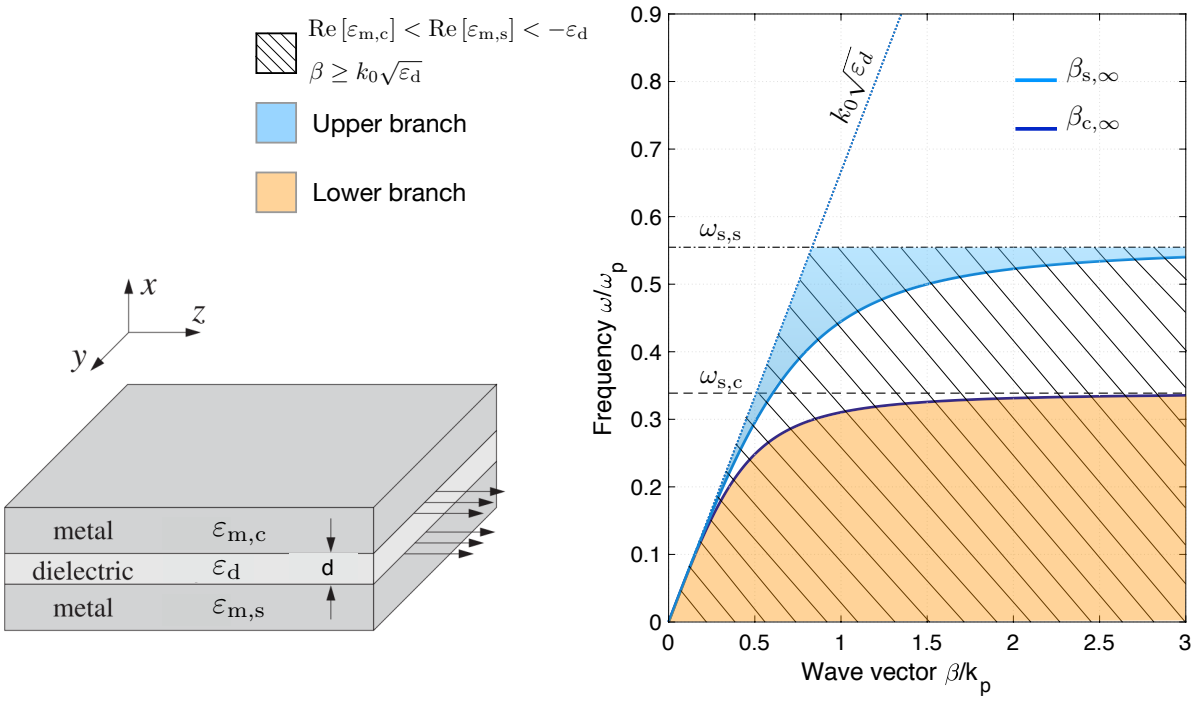


Figure 3.11: MIM plasmonic waveguide. Schematic representation of a MIM plasmonic waveguide and dispersion diagram to highlight the regions of existence of bound SPP-modes.

dielectric interfaces, respectively, are:[89]

$$\beta_{\mathrm{c},\infty}^2 = \frac{k_0^2 \varepsilon_{\mathrm{m,c}} \varepsilon_{\mathrm{d}}}{\varepsilon_{\mathrm{m,c}} + \varepsilon_{\mathrm{d}}} = \frac{k_0^2 \varepsilon_{\mathrm{d}}}{1 - |\rho_{\mathrm{c}}|} \quad , \qquad \beta_{\mathrm{s},\infty}^2 = \frac{k_0^2 \varepsilon_{\mathrm{m,s}} \varepsilon_{\mathrm{d}}}{\varepsilon_{\mathrm{m,s}} + \varepsilon_{\mathrm{d}}} = \frac{k_0^2 \varepsilon_{\mathrm{d}}}{1 - |\rho_{\mathrm{s}}|} \tag{3.50}$$

with $\rho_{\mathrm{c}} = \varepsilon_{\mathrm{d}}/\varepsilon_{\mathrm{m,c}}$ and $\rho_{\mathrm{s}} = \varepsilon_{\mathrm{d}}/\varepsilon_{\mathrm{ms}}$. As we have seen previously, for a single interface to support surface plasmon polaritons, $\beta_{\mathrm{c},\infty}$ and $\beta_{\mathrm{s},\infty}$ must be positive, and hence the conditions $|\rho_{\mathrm{c}}| < 1$ and $|\rho_{\mathrm{s}}| < 1$ must be satisfied. Without loss in generality, we can assume $|\varepsilon_{\mathrm{m,c}}| \geq |\varepsilon_{\mathrm{m,s}}|$. This implies that $0 < |\rho_{\mathrm{c}}| \leq |\rho_{\mathrm{s}}| < 1$ and $\beta_{\mathrm{c},\infty} \leq \beta_{\mathrm{s},\infty}$.

In terms of transverse propagation constants, the system can be describe by:[89]

$$\begin{aligned}
\gamma_{\mathrm{c}} &= \sqrt{\beta^2 - k_0^2 \varepsilon_{\mathrm{m,c}}} = \sqrt{\beta^2 + k_0^2 \left|\varepsilon_{\mathrm{m,c}}\right|} = \sqrt{\gamma_{\mathrm{d}}^2 + k_0^2 \left(\varepsilon_{\mathrm{d}} + \left|\varepsilon_{\mathrm{m,c}}\right|\right)} \\
\gamma_{\mathrm{s}} &= \sqrt{\beta^2 - k_0^2 \varepsilon_{\mathrm{m,s}}} = \sqrt{\beta^2 + k_0^2 \left|\varepsilon_{\mathrm{m,s}}\right|} = \sqrt{\gamma_{\mathrm{d}}^2 + k_0^2 \left(\varepsilon_{\mathrm{d}} + \left|\varepsilon_{\mathrm{m,s}}\right|\right)} \\
\gamma_{\mathrm{d}} &= \sqrt{\beta^2 - k_0^2 \varepsilon_{\mathrm{d}}}
\end{aligned} \tag{3.51}$$

and since $|\varepsilon_{\mathrm{m,c}}| \geq |\varepsilon_{\mathrm{m,s}}| > \varepsilon_{\mathrm{d}}$, $\gamma_{\mathrm{c}} \geq \gamma_{\mathrm{s}} > \gamma_{\mathrm{d}}$. For all plasmonic solutions with positive real β, it is evident that the lateral confinement conditions $\gamma_{\mathrm{d}} \geq 0$ requires that $\beta \geq k_0\sqrt{\varepsilon_{\mathrm{d}}}$. Obviously, also $\beta_{\mathrm{s},\infty} \geq \beta_{\mathrm{c},\infty} \geq k_0\sqrt{\varepsilon_{\mathrm{d}}}$.

For such solutions, because γ_d is real, it follows from (3.45) that in order for the quantity $\mathrm{e}^{2\gamma_\mathrm{d} d}$ to be positive, the quantities $(\gamma_\mathrm{d} - |\rho_\mathrm{c}|\,\gamma_\mathrm{c})$ and $(\gamma_\mathrm{d} - |\rho_\mathrm{s}|\,\gamma_\mathrm{s})$, must either be both positive or both negative. The following relationships are also valid:[89]

$$\begin{aligned} \rho_\mathrm{c}^2\gamma_\mathrm{c}^2 - \gamma_\mathrm{d}^2 &= \left(1-\rho_\mathrm{c}^2\right)\left(\beta_{\mathrm{c},\infty}^2 - \beta^2\right) \\ \rho_\mathrm{s}^2\gamma_\mathrm{s}^2 - \gamma_\mathrm{d}^2 &= \left(1-\rho_\mathrm{s}^2\right)\left(\beta_{\mathrm{s},\infty}^2 - \beta^2\right) \end{aligned} \tag{3.52}$$

Therefore, the possible ranges for the two plasmonic modes are:[89]

$$\left.\begin{aligned} (\gamma_\mathrm{m} - |\rho_\mathrm{c}|\,\gamma_\mathrm{c}) > 0 \\ (\gamma_\mathrm{m} - |\rho_\mathrm{s}|\,\gamma_\mathrm{s}) > 0 \end{aligned}\right\} \quad \Leftrightarrow \quad \beta_{\mathrm{s},\infty} \le \beta < \infty \qquad \text{Lower branch: } \mathrm{TM}_0 \tag{3.53}$$

$$\left.\begin{aligned} (\gamma_\mathrm{m} - |\rho_\mathrm{c}|\,\gamma_\mathrm{c}) < 0 \\ (\gamma_\mathrm{m} - |\rho_\mathrm{s}|\,\gamma_\mathrm{s}) < 0 \end{aligned}\right\} \quad \Leftrightarrow \quad k_0\sqrt{\varepsilon_{\mathrm{d,c}}} \le \beta \le \beta_{\mathrm{c},\infty} \qquad \text{Upper branch: } \mathrm{TM}_1 \tag{3.54}$$

Therefore, in this region, - similarly to the IMI case - there are two type of plasmonic modes: a symmetric-like TM_0 mode that has no cutoffs, and an antisymmetric-like TM_1 mode with a lower cutoff[89]. Figure 3.11 highlights the regions of existence of the bound SPP-modes in case the metals at either sides of the dielectric slab have different properties and both interfaces can support separate SPPs. Note that mode cutoff behaviour occur for the upper branch and that no bound SPP-modes are allowed between the two dispersion relations $\beta_{\mathrm{s},\infty}$ and $\beta_{\mathrm{c},\infty}$.

For the lower, symmetric-like TM_0 mode, the film width d is a decreasing function of β, and varies over $0 \le d \le \infty$, where $d = \infty$ at $\beta = \beta_{\mathrm{s,infty}}$. Instead, for the upper, antisymmetric-like TM_1 mode, the width d is an increasing function of β varying over a range $d_\mathrm{cutoff} \le d \le \infty$, with d_cutoff happening at $\beta = k_0\sqrt{\varepsilon_\mathrm{d}}$ and $a = \infty$ at $\beta = \beta_{\mathrm{c},\infty}$[89].

In addition to the plasmonic modes, there are also TE and TM oscillatory modes characterised by an imaginary $\gamma_\mathrm{d} = jk_{z,d}$, with $k_{z,d} = \sqrt{k_0^2\varepsilon_\mathrm{d} - \beta^2}$[89]. Because $k_{z,d}$ is real, the wavenumber β is restricted to the values $\beta \le k_0\sqrt{\varepsilon_\mathrm{d}}$. Thus the range of wavenumber for all oscillatory modes is:[89]

$$\boxed{0 \le \beta \le k_0\sqrt{\varepsilon_\mathrm{d}}} \qquad \text{(Oscillatory modes)} \tag{3.55}$$

All the modes have a lower cutoff found by setting $\beta = 0$, and for all, except the TM_1 oscillatory mode, there is also no upper cutoff thickness - which means that the upper limit $\beta = k_0\sqrt{\varepsilon_\mathrm{d}}$ is reached at infinite width d[89]. The TM_1 mode is a special case. This mode non only has an upper cutoff thickness, but this thickness corresponds exactly to the lower cutoff thickness of the TM_1 plasmonic mode (3.54). Thus, the TM_1 oscillatory mode exists only for thicknesses $d_\mathrm{min} \leq d \leq d_\mathrm{cutoff}$ and for $0 \leq \beta \leq k_0\sqrt{\varepsilon_\mathrm{d}}$, and then it become plasmonic for $d_\mathrm{cutoff} \leq d < \infty$ and $k_0\sqrt{\varepsilon_\mathrm{d}} \leq \beta < \infty$.[89]

3.7.3 Symmetric MIM Plasmonic Waveguide

Consider a thin dielectric layer with thickness d and dielectric constant $\varepsilon_2 = \varepsilon_d$ sandwiched between two thick (semi-infinite) metallic layers having dielectric constant $\varepsilon_1 = \varepsilon_3 = \varepsilon_m$. Consider now the symmetric case where $\varepsilon_\mathrm{m,c} = \varepsilon_\mathrm{m,s} = \varepsilon_m$. The symmetric TM_0 mode is the only mode that exists for the symmetric MIM guide for all values of the gap thickness d, and is known as *gap surface plasmon polariton* (G-SPP) mode[89,95]. This mode exhibits odd symmetry of the longitudinal electric field component $E_x(z)$ and, consequently even symmetry of the transversal field $E_z(z)$. The G-SPP dispersion can be written as:[95]

$$\frac{\gamma_m\varepsilon_d}{\gamma_d\varepsilon_m} = -\tanh\left(\frac{\gamma_d d}{2}\right) \qquad \text{or} \qquad \frac{\gamma_d\varepsilon_m}{\gamma_m\varepsilon_d} = -\coth\left(\frac{\gamma_d d}{2}\right) \tag{3.56}$$

with $\gamma_{m,d} = \sqrt{k^2_\text{G-SPP} - \varepsilon_{m,d}k_0^2}$, where $k_\text{G-SPP}$ denotes the wave vector G-SPP. The G-SPP dispersion relation can be obtained from (3.48) substituting γ_m with γ_d in the argument of the hyperbolic function of the SR-SPP mode.

As in the case of the symmetric IMI plasmonic waveguide, the thinner the gap between the two metal-dielectric interfaces the larger the propagation wavenumber $k_\text{G-SPP}$. Large propagation constants can be achieved even for excitation well below ω_SP, provided that the width of the metal core is chosen sufficiently small. The larger the wavevector the smaller the penetration depth and thus the higher the field confinement at the interface. MIM waveguides can achieve micron-scale propagation with nanometer-scale confinement[64].

3.7.4 IIM Plasmonic Waveguide

Consider now an IIM plasmonic waveguide, where a dielectric layer $\varepsilon_{\mathrm{d},1}$ of finite thickness d is sandwiched between a metal substrate ε_{m} and a dielectric cladding $\varepsilon_{\mathrm{d},2}$. In this case, the light propagates through the structure via only one surface plasmon wave and thus the light will emerge from the structure as if it had passed through a material with an index equal to the mode index[98]. Opposed to the IMI and MIM geometries, this structure does not restrict the guided wave propagation to two dimensions and thus it provides a lower field confinement at the interface.

It is known that the tail of the SPP mode at the metal interface 'feels' changes in the dielectric environment if they happen within approximately two SPP penetration depth $\delta_{\mathrm{SPP,d}}$[19]. Hence, if the finite thickness d of the dielectric layer 1 is lower than $\delta_{\mathrm{SPP,d}}$, the SPP mode will be affected by the presence of the second dielectric layer. The thinner the layer the larger the effect of the second dielectric layer on the properties of the SPP mode. Since the asymmetry of the system does not allow any simplification, to find the eigenmode(s) of the interface it is necessary to solve Equation (3.44) numerically.

Consider the lossless case, with $\varepsilon_{\mathrm{d},1}$, $\varepsilon_{\mathrm{d},2}$ real positive, and ε_{m} real negative so that $\varepsilon_{\mathrm{m}} = -|\varepsilon_{\mathrm{m}}|$. Without loss in generality, we can assume $\varepsilon_{\mathrm{d},1} \geq \varepsilon_{\mathrm{d},2} > 0$. Reasonably, we can write that:

$$\text{if} \quad d \to \infty \qquad \Rightarrow \qquad \beta = \beta_{1,\infty} = \frac{k_0 \varepsilon_{\mathrm{m}} \varepsilon_{\mathrm{d},1}}{\varepsilon_{\mathrm{m}} + \varepsilon_{\mathrm{d},1}} = \frac{k_0 \varepsilon_{\mathrm{d},1}}{1 - |\rho_1|} \tag{3.57}$$

$$\text{if} \quad d \to 0 \qquad \Rightarrow \qquad \beta \approx \beta_{2,\infty} = \frac{k_0 \varepsilon_{\mathrm{m}} \varepsilon_{\mathrm{d},2}}{\varepsilon_{\mathrm{m}} + \varepsilon_{\mathrm{d},2}} = \frac{k_0 \varepsilon_{\mathrm{d},2}}{1 - |\rho_2|} \tag{3.58}$$

with $\rho_1 = \varepsilon_{\mathrm{d},1}/\varepsilon_{\mathrm{m}}$ and $\rho_2 = \varepsilon_{\mathrm{d},2}/\varepsilon_{\mathrm{m}}$. Therefore, the SPP mode β of a IIM waveguide can be found in the range $\beta_{2,\infty} \leq \beta \leq \beta_{1,\infty}$ and it will shift in between the extremes depending on the thickness d of the dielectric layer 1. Note that, unlike IMI and MIM SPP-bound modes, IIM SPP-modes do not have larger wave vectors than the flat interface propagation constant and thus do not provide higher field confinement.

Figure 3.12 highlights the region of existence of IIM SPP-modes in the dispersion diagram (left) and shows how the propagation constant k varies for some values d of thickness

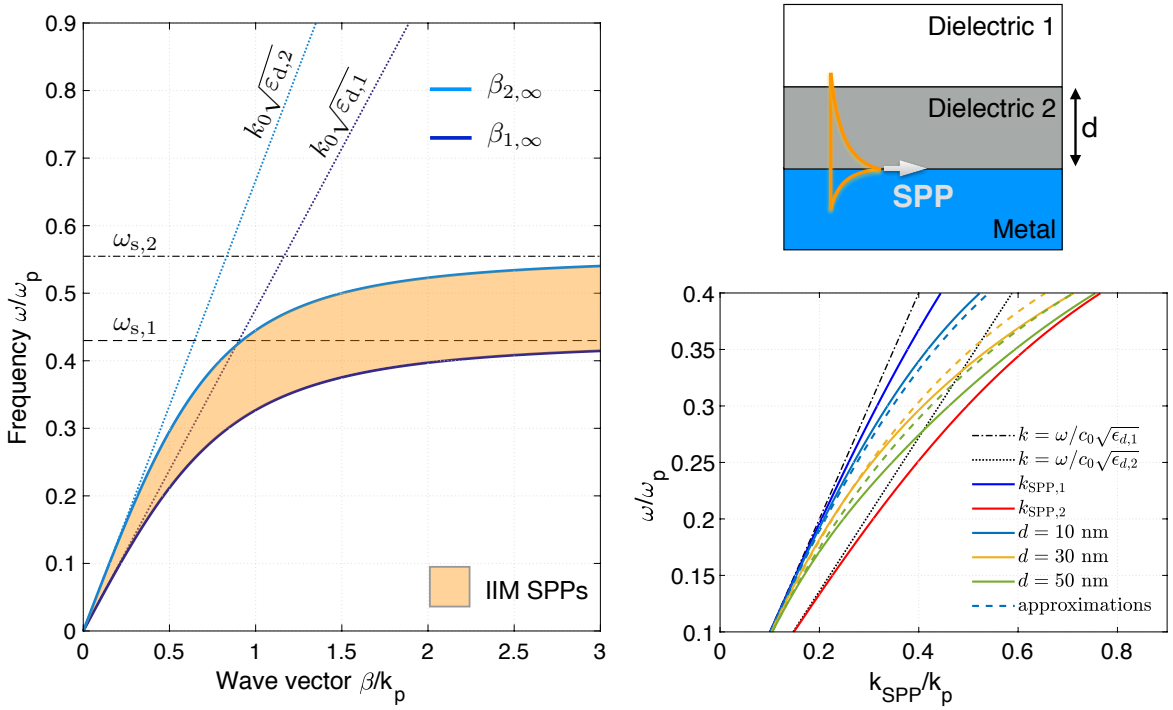


Figure 3.12: IIM plasmonic waveguide. (top right) Schematic representation of a IIM plasmonic waveguide, (left) dispersion diagram to highlight the regions of existence of bound SPP-modes and (bottom right) numerical solutions of Equation (3.44) for some values d of thickness.

(bottom right). Solutions have been evaluated numerically. The approximations, used as initial guesses for the numerical solutions, have been estimated by considering the two dielectric layers as an effective medium and by replacing the effective permittivity value in the formula for the single, flat propagation constant k_{SPP}. Given the parallel polarisation of the incident wave's electric field with respect to the boundary between the materials, the effective dielectric function has been evaluated as:[99]

$$\epsilon_{\mathrm{eff}} = \frac{I_1 \epsilon_{\mathrm{d},2} + (I_2 - I_1)\, \epsilon_{\mathrm{d},1}}{I_2} \tag{3.59}$$

where I_1 and I_2 are the integrals of the electric field exponential decay $\mathrm{e}^{-|k_z||z|}$ inside the dielectric in the ranges $0 - d$ and $d - \infty$, respectively. I_1/I_2 and $1 - I_1/I_2$ are then the volume fractions. In this case, the effective permittivity is effectively given by the arithmetically weighted average of the permittivities of the two materials.

In the visible range, the approximations are a good match to the numerical solutions only for small values of thicknesses, $\approx d \leq 30$ nm. As the thickness d of the middle dielectric layer increases, the numerical solutions approach $k_{\mathrm{SPP},2}$ much faster than the

effective medium approximations at high-frequencies. For completeness of information, it has been verified that the approximations display less agreement with the numerical solutions even in the thin-slab limit when $\varepsilon_{d,2} \geq \varepsilon_{d,1} > 0$, i.e. the middle layer has a lower refractive index than the top dielectric cladding layer, and for dielectrics with a large difference $|\varepsilon_{d,1} - \varepsilon_{d,2}|$. In the latter case, actually, the solver used showed some difficulties in solving Equation (3.44) numerically.

3.8 EOT in Subwavelength Nanohole Arrays

The phenomenon of EOT was first observed in 1998 in the optical transmission properties of 2D periodic arrays of subwavelength circular holes milled in, otherwise opaque, metallic layers[17]. Unexpectedly, these structures displayed sharp peaks in the transmission spectra at wavelengths as large as ten times the diameter of the holes and with a transmission efficiency that sometimes exceeded unity when normalised to the area of the holes, i.e. several order of magnitude greater than predicted by the classical aperture theory as described by Bethe[100] in 1944. In other words, for specific wavelengths, the structure transmitted more light than a large macroscopic hole whose area is equivalent at the sum of all the subwavelength holes of the array, despite the below-unity normalised transmission efficiency of a single subwavelength hole. This can only imply that, in the EOT phenomenon, the metallic layer actively participates in the transmission process. Nowadays, it is widely accepted that this enhancement in transmission results from the active participation of the metallic layer in the transmission process via the resonant interaction of the incident light, the diffraction from every hole, and the Surface Plasmon Resonances (SPRs) generated at the metal-dielectric interfaces of the structure[21,101].

A comprehensive literature on thin metal films perforated with 2D hole arrays can be found even before 1998 in the contest of *metal mesh filters* and *inductive grids*[102]. In fact, 2D periodic hole arrays were already known to act as band-pass filters in several frequency regimes[103] for wavelength larger than the lattice parameter a but shorter than the cutoff wavelength λ_{cutoff} of the aperture, i.e. $a < \lambda < \lambda_{\text{cutoff}}$. Nonetheless, they had never been studied for applications in the optical regime prior Ebbesen's experiments[21].

And, according to Garcia-Vidal *et al.*[21], they had never been studied (like in the EOT case) for wavelengths beyond cutoff, i.e. for wavelengths such that $\lambda_{\text{cutoff}} \leq a < \lambda$.

The discovery of the phenomenon of EOT sparked a large amount of research worldwide aimed to unveil the underlying physical mechanisms involved in the transmission process. Its remarkable features, namely high transmission efficiencies and local fields enhancements, can be exploited in a multitude of different applications[21]. Moreover, EOT-based nanostructures show extremely high engineerability and can be easily tuned in wavelength by varying the apposite structural parameters. During the first report of EOT, Ebbesen *et al.*[17] presented dependencies on hole size, lattice spacing, metal film thickness, and angular dispersion. Later, several other important parameters were analysed, such as the type of metal, the role of symmetry in the dielectric-metal-dielectric layer stack, the finite-size effects of the lattice and the role of the hole shape. In this section a summary of the dependence of the EOT phenomenon on some of the most relevant structural parameters in 2D periodic array is presented. A concise report on the transmission of light through a single subwavelength circular aperture and on Fano's contribution to plasmonic is also provided.

3.8.1 Light Transmission through a Single Subwavelength Circular Aperture

Light transmission through an aperture is accompanied by diffraction. The physics of this process, even in the simplest of geometries, is very complex[19]. In classical optics, calculations on diffraction of light by apertures are usually based on Kirchhoff's scalar mathematical formulation of the Huygens-Fresnel principle[19,104]. This approach can be used quite successfully for large apertures, i.e. when the wavelength of the impinging radiation is small compared to the size of the aperture, and for the purpose of instrumental optics the scalar theory is quite adequate[104]. However, in the subwavelength regime, near-field effects are expected to dominate the response and polarisation effects cannot be ignored[19,104]. Therefore a different approach requiring the full vectorial description via Maxwell's equations have to be used.

In the subwavelength regime, the first accurate theoretical study of the diffraction of electromagnetic radiation by a small hole perforated in a zero-thickness, infinite plane conducting screen was presented by Bethe[100] in 1944. He established that the first-order diffracted field far behind the aperture can be represented as the superposition of an electric and a magnetic dipole located at the centre of the aperture: a magnetic dipole in the plane of the hole and an electric dipole perpendicular to it, both antiparallel to the respective fields in the hole[100,104]. For normal incidence, the aperture is described only by the small magnetic dipole[19].

Assuming that the incident light intensity is constant over the area of the aperture, Bethe also derived a simple expression for the normalised-to-area transmission efficiency of the hole,[14] according to which, the transmission scales as $(r/\lambda)^4$ in the extreme subwavelength limit ($\lambda \gg 2\pi r$). This implies a very weak total transmission for a subwavelength aperture because the optical efficiency quickly drops as λ is increased[19,21]. The scaling $T \propto \lambda^{-4}$ is in agreement with Rayleigh's theory of the scattering by small objects[19].

In the years following its publication, Bethe's theory was open to criticism because it did not correctly predict the field in the vicinity of the aperture[104]. In 1950, Bouwkamp[105] reviewed Bethe's formulation for the electric field in the aperture and discovered that it was an underestimation since it represented only the first term of a power-series. He thus extended Bethe's theory for the case of normal incidence to higher-order approximation, deriving 6 more terms of the power-series solution:[104]

$$T = \frac{64}{27\pi^2}(kr)^4 \left[1 + \frac{22}{25}(kr)^2 + \frac{7312}{18375}(kr)^4 + ...\right] \tag{3.60}$$

Bethe's equations for the distant field, however, did not need modification[104].

The expression of the electromagnetic near-field derived by Bouwkamp[104] reveals high *singularities* at (near) the edges of hole. The tangential components of the electric and magnetic field are finite at the edge of the hole - with the tangential electric component that vanishes at the edge as $\sqrt{d}$, where d is the distance from the edge -, but all the other components of the EM field become infinitely large at the edge as $1/\sqrt{d}$. However, despite

[14] $T = \frac{64}{27\pi^2}(kr)^4$ with $k = \frac{\omega}{c} = \frac{2\pi}{\lambda}$ where ω is the frequency and c is the speed of light.

these singularities, the edge does not radiate energy[104]. Bouwkamp conjectures that the same type of singularities may occur at *"any infinitely large sharp edge, no matter whether the obstacle is plane or curved and independently of the form of the edge"*[104] and since these singularities *"occur in all known solutions, they seem to provide the natural boundary conditions at a sharp edge"*[104]. The presence of the high singularities was experimentally demonstrated in 2008 by Adam *et al.*[106].

The Bethe-Bouwkamp expressions for the normalised-to-area transmission efficiency diverge when $\lambda \leq 2\pi r$ and therefore they show a limited applicability in the EOT case, in which the resonant wavelength is typically two to three times the diameter of the holes[21]. Moreover, the Bethe-Bouwkamp theory has some limitations because it relies on two major approximations: (i) the thickness of the screen is assumed to be infinitely thin, yet at the same time (ii) the screen is considered perfectly opaque due to the infinite conductivity[19].

Recent studies demonstrated that the Bethe-Bouwkamp model largely overestimate the total transmission if a screen of finite thickness $h > 0$ is considered[21]. When assuming a screen of finite thickness h in the subwavelength regime, two regimes have to be considered: (i) the apertures allow only decaying modes; (ii) the apertures allow propagating modes. The transmission characteristics are strongly affected by the presence or absence of propagating modes inside the apertures[107]. In the first case, the transmission decreases exponentially as the thickness h increases, displaying the behaviour characteristic of a tunnelling process. Instead, in the second case, the transmission is much higher due to the waveguide behaviour of the aperture.

Prominent examples of waveguide aperture are circular holes in a perfect electric conductor (PEC) layer with diameter above the cutoff wavelength λ_{cutoff},[108]. For a circular hole $\lambda_{\text{cutoff}} = 3.4r\sqrt{\varepsilon_{\text{hole}}}$,[21] which is determined by the radius r of the hole and the dielectric constant inside the hole $\sqrt{\varepsilon_{\text{hole}}}$. This cutoff condition, for an infinitely long cylindrical waveguide, was established by Lord Rayleigh[109] in 1897 such that $kr = 1.841$, where k denotes the wavevector and r the radius. Obviously if the material inside the holes is not vacuum the cutoff wavelength is increased by a factor of n compared to the free-space value, where n is the refractive index of the material inside the hole. One-dimensional

slits, annular- and C-shaped apertures also display waveguide behaviours[19].

The transmission process of an aperture associated with waveguide modes is completely different from the one obtained from coupled SPP[107]. In the first case, the metal walls of the aperture play an active role in the transmission mechanism. This is because opposite dipoles between the top and bottom surfaces of the metal layer induce current densities flowing parallel to the aperture's walls. This also implies that these waveguide resonances are not very sensitive to the refraction index of the substrate[107]. On the other hand, experiments[110] demonstrated that spectral features associated to the EOT phenomenon in hole arrays depends only on the dielectric properties of the metal within one skin depth of the surface, while the properties of the materials used for the vertical sidewalls of the holes do not affect the transmission enhancement. Moreover, EOT resonances are also extremely sensitive to refractive index variations at the two interfaces. Therefore, statements that cylindrical holes do not support propagating modes when the hole diameter is smaller then $\lambda_0/(2n)$, where λ is the wavelength of incident light and n is the refractive index of the material inside the hole, are very common in literature[111].

However, recent theoretical studies of the transmission problem of metallic cylindrical waveguides have established that these structures can sustain propagating modes below the plasma frequency even for arbitrary small holes[111,112,113], given the appropriate material parameters. The propagating modes of a plasmonic waveguide are confined to the dielectric region of the waveguide and are not purely TM or TE unless the angular momentum $m = 0$[111]. The absence of propagating modes for small holes is true only when modelling the metal as a PEC[112].

In 2005, Shin *et al.*[111] analysed subwavelength cylindrical holes in an optically thick metal film described by the Drude free-electron model and established that the dispersion diagram exhibits three distinctive features: (i) such holes always support propagating modes near the surface plasmon frequency no matter how small the hole are, (ii) the lowest-frequency fundamental plasmonic mode inside the hole has a HE_{11} signature and it is located completely below the surface plasmon frequency, and (iii) when the radius of the hole is small, there exist a stop band for a normally incident plane wave just above the surface plasmon frequency where the light does not transmit. The upper limit of the

stop band is given by the cutoff frequency of the next-higher-order mode with angular momentum $m = 1$, the EH_{11} mode, which can also couple to a normally incident plane wave[111].

In 2006, Webb and Li[113] arrived to the same conclusion that circular waveguides support propagating modes even for arbitrarily small radii. They noticed that the lowest energy mode could have either a HE_{11} signature or a EH_{11} signature, accordingly to the $\varepsilon_m/\varepsilon_d$ ratio, where ε_m and ε_d are the real dielectric constant for the dielectric inside the hole and the metal film, respectively. They also noticed that while the loss increases with the reducing of the hole size, if the hole contains a material with an appreciably positive dielectric constant, the dominant mode can have modest loss over quite a wide wavelength range.

The second approximation of the Bethe-Bouwkamp theory is the infinite conductivity of the layer. Consider then a real metal screen of finite conductivity. If the film is optically thin, the screen cannot be considered perfectly opaque. Therefore, light can tunnel through the screen and the Bethe-Bouwkamp theory - missing one of its assumptions - becomes invalid. On the other hand, if the film is optically thick, i.e. the thickness is on the order of several skin depths, penetration of the incident field inside the screen enables the excitation of localised surface plasmons on the rim of the aperture[114]. The signature of a localised plasmon mode in a single circular hole has been confirmed experimentally in 2005[114].

Localised surface plasmon resonances significantly influence the transmission process[19]. The excitation of localised surface plasmons at a single subwavelength aperture has two important consequences: (i) an increase of the effective diameter, and (ii) an increase in transmission at the wavelengths where the localised modes are excited[21]. In fact, by analogy to the discussion of localised modes in metal nanoparticles and nanovoids, a significant field-enhancement at the aperture rim can be expected, which will increase the transmission at the wavelength where the localised mode is excited. This means that even for an optically thick metal film the finite conductivity of the real metal should be taken into account to correctly analyse the transmission properties of a single aperture in a flat film.

In a real metal with finite conductivity, the evanescent tails of the surface plasmons penetrate into the rim of the aperture by the skin depth[19]. This effectively increases the size of the aperture so that the hole appear larger. Therefore, also the cutoff wavelength of the fundamental waveguide mode substantially increases compared to the physical diameter of the hole[19]. In 2005, Gordon *et al.*[115] analysed the waveguide mode of a subwavelength rectangular hole in a real metal demonstrating the cutoff wavelength of the aperture to be up to 41% larger than Rayleigh's criterion for perfect metals. Therefore, in order to execute a correct normalisation of the transmission coefficient, this significant increase of the cutoff wavelength must be taken into consideration when studying apertures just below cutoff.

The increases in the cutoff condition is due to the penetration of the electric field into the metal and to the SP-coupling between the edges of the holes[115]. The SP-coupling increases as the width of the aperture is reduced, hence, the cutoff wavelength actually increases as the hole-size becomes smaller. To support these findings, in 2006, Webb and Li[113] demonstrated that the cutoff wavelength of a hole waveguide perforated on a metal characterised by a Drude dielectric function does not indeed approach zero when the hole radius tend to zero but to the value λ_p, i.e. the wavelength of the bulk plasmon.

Light exiting a subwavelength circular hole at wavelengths $\lambda > 2d$ - where d is the diameter of the hole - is fully and uniformly diffracted into a half sphere[116]. This diffracted light generates wavevectors also in the direction parallel to the surface of the film and thus allow a portion of the incident light to excite surface plasmon polaritons. The ability of isolated circular hole to generate SPPs has been the main topic of several research studies[117,118,119,120]. The holes can be considered as localised defects within a flat metal surface and act as point-like sources of SPPs. Coupling efficiency up to 20% have been demonstrated[120]. Experiments established that the direction of the surface plasmon propagation is given by the light polarisation and that interference patterns arise if two or more hole lies in close proximity to another along the SPPs direction of propagation[117]. By measuring the light radiated from the rear side of the aperture, those experiments also showed that the transmission process of a singular, subwavelength aperture in a opaque metal layer - which can occur only through the holes - is unambiguously supported by

SPPs[117].

However, radiating energy in all directions with equal strength is often not very practical. Many applications requires a focused beam of energy in only one specific direction, such as antenna, light-emitting diodes (LEDs) or lasers[116]. In 2002, lezec *et al.*[116] demonstrated that it is possible to prevent the isotropic transmission of light of a subwavelength hole by patterning the output side of the hole with a concentric, periodic groove structure. For illumination at normal incidence, a well-defined beam having a full-width at half-maximum (FWHM) divergence of only few degrees has been observed. The light emission is confined to the central area around to hole and since off-axis beams are forbidden by destructive interference, only beams normal to the surface can exist at a specific wavelength dictate by the groove period. These results confirms that even a single subwavelength hole, if surrounded by periodic surface corrugation, can show as large a transmittance enhancement as an array of holes[121].

3.8.2 Fano's Contribution to Plasmonics

In 1902, American physicist Robert W. Wood[122] witnessed the appearance of inexplicable bands in the unevenly distributed reflected light spectra of a sodium diffraction-grating when exposed to an incandescent source. At certain angles of incidence, extremely sharp black and/or very bright lines appeared along the first order reflection spectra of the grating, causing sometimes an anomalous drop from maximum to minimum illumination of approximately 90% and in a range of wavelengths not greater than the distance between the gratings themselves. Interestingly, these *singular anomalies* were polarisation-dependent. In fact, they arose only when there was an electric field component perpendicular to the plane of the grating, i.e. under TM-polarisation. This was the first time that polarisation has been introduced in the theory of diffraction gratings. Wood also observed that the dielectric environment of the gratings could modify the position of the bands in wavelength as a function of the incident angle. At the time, he could not provide an explanation for this phenomenon and concluded his paper stating that the problem was *"one of the most interesting I [he] ever met with"*.

In 1907, Lord Rayleigh[123] produced the first interpretation to the existence of the anomalies observed by Wood. He assigned their position in wavelength to the *"passing-off of a spectrum of higher order"*,[123] i.e. at those wavelengths at which the diffracted light emerges tangentially to the grating surface. However, he could not provide an explanation of the enhanced reflection observed in certain cases.

In 1941, Fano[124] reexamined the theory of Wood's anomalous diffraction gratings in order to assign a physical meaning to the appearance of large at sharp irregularities at well-defined wavelengths in the reflectivity spectra of the gratings. Fano distinguished two types of anomalies: a *sharp* anomaly and a *diffuse* anomaly. The sharp anomaly appears as an abrupt and discontinuous change of intensity - an "edge" - along the spectrum. It was discovered by Rayleigh in 1907 - from whom it takes the name - and occurs when the wave vector of the diffracted light grazes parallel to the plane of the grating[123]. Surprisingly, such anomaly does not depend on the material that constitutes the gratings. The *Rayleigh's anomaly* depends instead on the period of the grating, the angle of incidence of the wavelength, and the refractive index to the surrounding media[124,125].

On the other hand, the diffuse anomaly, also referred to as the *Wood's anomaly'*, extends for a wide interval from the "edge" towards longer wavelengths and consists generally of a minimum and a maximum of intensity (one dark band and one bright band). This anomaly depends upon the optical constants of the grating. In fact, a change of its refractive index (or of the environment) shifts the position of the bands as compared to the edge[124,125,126,127]. Fano assigned the origin of the diffuse anomaly to a forced resonance given by the excitation of superficial waves along the surface of the grating[124,128,129], which are nowadays established to be surface plasmon polaritons.

The Wood-Rayleigh anomalies display strong dependence on the geometry of the grating. In particular, a necessary condition for their existence is the presence of sharp edges in the profile of the grooves. In fact, rubbing off the grating destroys the phenomenon completely, unless the grooves are very narrow. These anomalies are also polarisation dependent. Initially, it was believed that both anomalies could only appear in p-polarisation, i.e. when the electric vector of the incident light is perpendicular to the grating, but subsequent investigations demonstrated that the Rayleigh's anomaly could also occur in

s-polarisation, however under the condition of deep grooves[124,126,127].

The resonance associated with the Wood anomaly exhibits a peculiar, sharp asymmetric profile. For many years, the lineshape of a resonance was generally described by the Lorentzian formula: a linear differential equation that produces a nicely-symmetric, single peaked function. However, the Lorentzian formula does not account for interacting resonances and therefore it is not a good fit to describe the spectral feature of a phenomenon that is not simply the result of the sum of the intensities of completely independent resonances[129].

In 1935, Fano[130] suggested a new formula to describe the asymmetric spectral atomic lines observed in the absorption spectra of a highly excited hydrogen atom. In contrast to a Lorentzian resonance, the Fano resonance exhibits a distinctly asymmetric shape and arises from the interaction of a discrete state with a broad spectral line or continuum[128,129]. Due to their origin, Fano resonances display high sensitivity to changes in geometry and local environment. Therefore, small perturbations can induce dramatic resonance or lineshape shifts. This property renders Fano resonant media particularly attractive for a range of applications[119,129].

Initially, the Fano resonance was regarded as a feature entirely specific to quantum systems. However, "the interaction of leaky modes with incoming radiation leads to similar interference phenomena as in the absorption by Rydberg atoms[15], where a leaky mode can be associated to a discrete state and the incoming radiation to a continuum"[128]. Recently, the Fano resonance has been observed and demonstrated in wide range of structures:[129] plasmonic nanoparticles, plasmonic materials and metamaterials, photonic crystals, and also light transmission through subwavelength apertures[131].

3.8.3 Dependence on the periodicity of the array

As seen in Section 3.2, it is necessary to provide an additional momentum in order to be able to excite surface plasmon polaritons at a flat interface. The additional momentum is given by the reciprocal vectors G_{ij} of the array, where $i \geq 0$ and $j \geq 1$ are integers that

[15] A Rydberg atom is an excited atom with one or more electrons that have a very high principal quantum number.

indicate the diffraction order of the array. For a square arrays of periodicity a_x, G_{ij} are given by:

$$G_{i,j} = \frac{2\pi}{a_x}\sqrt{i^2 + j^2} \qquad i,\, j \text{ integers (with } i \geq 0,\, j \geq 1) \tag{3.61}$$

Instead, for a hexagonal (or triangular) lattice with period a_x, G_{ij} are given by[132]:

$$G_{i,j} = \frac{4\pi}{a_x\sqrt{3}}\sqrt{i^2 + j^2 + ij} \qquad i,\, j \text{ integers (with } i \geq 0,\, j \geq 1) \tag{3.62}$$

According to Equations 3.61 and 3.62, the larger the periodicity the larger the additional wavevector provided by the array.

Consider an electromagnetic wave with wave vector $\mathbf{k}$ (of magnitude $k = 2\pi n_d/\lambda$, where n_d is the refractive index of the medium in which the light is traveling), and impinging onto a metallic array of subwavelength apertures at an angle θ with respect to the normal of the interface.[132] The condition of excitation of SPPs is:

$$\mathrm{Re}\,[k_{\mathrm{SPP}}] = |k_x + G_{ij}| \tag{3.63}$$

where k_x is the component of $\mathbf{k}$ parallel to the interface (i.e. $k_x = ksin(\theta)$, with $k = |\mathbf{k}|$) and G_{ij} is a reciprocal vector of the periodic array. Under the condition of normal incidence $\theta = 0$, then $k_x = 0$ and thus the condition of SPPs excitation is met when $\mathrm{Re}\,[k_{\mathrm{SPP}}] = |G_{ij}|$.

Assume a hexagonal lattice. Combining Equation (3.63) at normal incidence angle with Equation (3.62), and knowing that $k_{\mathrm{SPP}} = 2\pi n_{\mathrm{SPP}}/\lambda$ from Equation (3.33), it is possible to relate the periodicity a_x and the diffraction orders (i, j) of the array with wavelength:

$$\lambda_{(i,j)} = \frac{\sqrt{3}a_x}{2\sqrt{i^2 + j^2 + ij}}\, n_{\mathrm{SPP}}|_{k_{\mathrm{SPP}}=G_{ij}} \tag{3.64}$$

It has been shown experimentally in several studies[13,21,132] that Equation (3.64) is a good approximation for the position of minima in transmission ($\lambda_{(i,j)} = \lambda_{min,(i,j)}$), under the condition of normally incident light. Each of these minima always appears just before (i.e. blue-shifted with respect to) a transmission maximum. $\lambda_{\mathrm{min},(i,j)}$ exhibits a linear dependence on the lattice period and therefore the passband of plasmonic filter can be

linearly shifted in wavelength by varying the periodicity a_x of the array. This is valid even in the case of 1D filters, such as grating-based nanostructures. The larger the periodicity the longer the wavelength at which begins the EOT passband.

The $\lambda_{\min,(i,j)}$ minima are ascribed to the spectral locations of the so-called Wood's anomalies WAs, i.e. $\lambda_{min,(i,j)} = \lambda_{\mathrm{WA}}$. WAs are in fact, by definition, associated with the excitation of surface electromagnetic waves at a metal-dielectric interface and consists of a dark and a bright (EOT) band. The position of $\lambda_{min,(i,j)}$ depends on the optical constants of the system, both the refractive index of the metal that composes the array and the dielectric of the environment. Therefore, a change in these parameters will affect the spectral response of the nanostructure. Moreover, since there are surface plasma waves bound to both the top and bottom metal-dielectric interface of the array, two sets of transmission maxima (minima) will occur if the dielectric on either side of the metal are different.

Given that a 2D periodic array is indeed a periodically corrugated surface like a grating, we can expect Rayleigh's anomalies. As mentioned in the previous section, these anomalies occur in the presence of sharp edges (like the edges of the holes) and at the wavelengths at which a diffracted order appears or disappears at a grazing angle, i.e. parallel to the plane of the array. For an 2D hexagonal array of subwavelength holes, RAs occur when:

$$k = |k_0 \sin\theta + G_{\mathrm{ij}}| \tag{3.65}$$

where k is the wave vector of incident light and k_0 is the wave vector of light in vacuum.

However, it should be pointed out that EOT has been observed also in aperiodic arrays. Experiment with aperiodic arrays showed that although periodicity is absent, well-defined peaks of enhanced transmission clearly emerge in the spectrum, which have been correlated to the spectral locations of the transmission maxima with peaks in the structure factors of the quasi periodic arrangements (i.e. diffraction pattern of the array) [21]. Pacifici *et al.* [132] investigated the influence of the array order in the optical transmission properties of aperiodic and quasi-periodic subwavelength hole arrays and realised that the solely necessary requirement for obtained enhanced optical transmission is to maintain the short-

range order. In other words, the EOT phenomenon arises from the closest-neighbour interactions. In the case of a aperiodic array the additional wave vector can be evaluated as the average distance between the subwavelength apertures[132].

3.8.4 Dependence on the materials

Clearly the choice of metal is very important in the EOT phenomenon, and it has been verified experimentally in several studies[21,110,133]. Two main parameters characterise the influence of the dielectric constant of the metal on EOT peaks: namely, the skin depth (which effectively enlarges the hole size, increasing the transmittance) and the absorption length (since small absorption lengths impair the resonant process). The higher the imaginary part of the dielectric function of the metal the smaller the penetration depth and the higher the absorption. This translates into a lower transmission and a wider bandwidth, respectively. In fact, considering arrays with the same geometrical parameters, good metals with high penetration depths (i.e. small imaging parts) - such as gold (Au), silver (Ag), and copper (Cu) - give rise to significantly high transmission efficiency in the optical range, and the more so at longer wavelengths due to the increasing absolute value of $\mathrm{Re}\{\varepsilon_m\}$ and therefore to the strength of the evanescent fields induced by the SPP at the metal interface. On the contrary, metal presenting large absorption - such as nickel (Ni) and chromium (Cr) - display very low and broad EOT peaks. Some metal, like tungsten (W), cannot even sustain surface plasmons in the optical regime[133].

As seen in Section 2.5, many studies have also been focusing their efforts on the development of Al-based plasmonic colour filters. When compared to the commonly used plasmonic materials, such as Ag or Au, Al has a much higher absorption, that radically increases at longer wavelengths in the visible optical regime. Thus, there are some disadvantages in the use of Al. However, Al also offer a few advantages. First of all, unlike Ag or Au, the conditions of existence of SPPs are met along the entire range of visible frequency (refer to Section 3.6.1). Moreover, Al is a CMOS-compatible material and widely used in standard CMOS fabrication processes. A detail that must not be underestimated when the final objective are commercial applications, since it would reduce the fabrication costs and make the filters compatible to be fabricated directly on

top of an image sensor.

As expected from the SPP dispersion relation (3.33), the spectral response of plasmonic devices is also sensitive to the refractive index of the dielectric material at the metal interface which will affect both the peak position and the transmission intensity [84]. As a consequence, 2D metal hole arrays are able to detect the presence of even a thin dielectric layer [134] and can play a major role in sensing and molecular spectroscopy in the optical range. A recent review of the literature in this field is presented by Garcia-Vidal *et al.* [21]. However, some of the experimental studies on the detection of thin dielectric layer [84] or sensing did not only vary the refractive index of the top layer but also the refractive index of the material inside the nanoholes. Therefore, the results obtained are not only a mirror on the sensitivity of SPPs but should also reflect the effect that the variation in refractive index has on the EM modes inside the hole itself.

3.8.5 Dependence on the shape of the aperture

The EOT phenomenon results from two different types of resonances: (i) localised waveguide resonances, and (ii) surface plasmon resonances, and these contributions cannot be trivially separated in two distinct contributions [135]. Unlike SPPs, localised waveguide modes depend on the holes shape. Therefore, the shape effect can be used to modify the optical response of the array. More specifically, the shape of subwavelength structures can be exploited to generate high local fields, shift the spectrum of localised resonances, or induce novel electromagnetic properties [136,137].

Similarly to the case of LSPRs in a metallic nanoparticles, single apertures are point-like sources of local resonant effects. Therefore, the shape of the aperture will affect the role that local effects have on the transmission properties of a nanostructure. In particular, studies have demonstrated that accordingly to the aspect ratio of the aperture, localised effects could be more or less important, which affect the spectral position and the lineshape of the peaks [21,138]. Elongated shapes, like narrow rectangular holes, exhibit strong shape resonances that are absent in circular holes [137]. Strongly localised modes have also been observed in hole shapes with very acute angles, such as isosceles triangular holes [139].

Localised modes are attractive because they are largely angle independent (provided that the resonant wavelength is much larger than both the size of the hole and the lattice constant)[112]. Localised electromagnetic modes appears spectrally close to the condition of cutoff of the aperture. Therefore, a range of more exotic hole shapes has been explored in order to increase the cut-off wavelength of the individual holes. In particular, annular holes, H-shaped holes and cruciform-shaped holes demonstrated to be quite apt to this purpose[21]. Holes with very acute angle[139] and holes filled with higher index dielectric[108] also display larger cut-offs.

Not only the 'in-plane' shape, but also the shape of the sidewalls of the aperture - i.e. the structure in the holes perpendicular to the film - can modify the optical response of the filters. Tapered holes display enhanced transmission efficiency[18], while hourglass-type apertures exhibit blueshift when the radius of the constriction is reduced[21]. Transmission modes and their corresponding resonances can also be modified by addition of supplemental structures inside the holes. Improved transmission cross sections and narrow transmission resonances can be achieved by filling the holes with a high-index material[108].

3.8.6 Reciprocity of the Structure in Transmission

The extraordinary optical transmission is a complex mechanism that require the entire nanostructure to work as a whole. Physical demonstration of this collective character is given by the fact that EOT devices are symmetric (reciprocal) in terms of transmission[18,101]. They display exactly the same transmission spectrum from either the 'top' and 'bottom' sides, independently from which side the light impinges on. Moreover, surface plasmons from both surfaces of the metal film are discernible in the dispersion diagram, regardless of the illumination. This indicates an anomalously strong coupling between the two sides[101].

However, the reciprocity character does not exclude that reflection from the top and bottom sides might be different, due to the different absorption/diffraction mechanisms within the nanostructure. Søndergaard *et al.*[18] noticed for the two illuminations (top and bottom of the grating) different electric fields at resonance. In both cases, the same reso-

nance was excited but with different efficiencies, causing in one case a stronger absorption (and thus a weaker reflection) with respect the other.

The reciprocity of the structure is not affected by whether the structure itself is also symmetric or not. Nonetheless, varying the dielectric constant on one surface has a strong impact on a SP mode associated with the opposite surface. Studies demonstrated that enhancement of the transmission - by more than an order of magnitude - can be achieved by matching the SP resonance energies on both sides of the metal film[84]. According to them, minimising the energy difference between the SP modes on either side of the metal film maximises the peak transmission intensity.

3.8.7 Finite size effects

In general, theoretical and simulation studies on 2D arrays consider the arrays to have an infinite number of apertures. However, in reality, that is not the case: arrays have finite dimensions and thus also a finite number of apertures. Given that the EOT results from the collective response of the array, it is expected that the transmission will increase as the number of holes forming the arrays increases until it reaches saturation. Indeed, experimental measurements have confirmed this expectation[21]. It has also been found that the number of holes needed for saturations depends very strongly on the size of the holes: the larger the hole diameter, the faster a transmission saturation is reached[140].

3.9 Summary

This chapter was a review, a detailed summary on the theory and fundamentals of SPRs. Definitions and basis of localised surface plasmon resonances and surface plasmon polaritons have been established. The conditions of SPPs excitations have been clearly defined and their properties comprehensively analysed. SPPs consist of oscillating surface charges along the direction normal to the interface between two materials. This oscillation can only result from the discontinuity of the orthogonal electric field and therefore only p-polarised waves can satisfy the condition of SPP excitation. SPPs can only exist

at an interface between materials with opposite signs of the real part of their dielectric functions, i.e. between an insulator and a conductor. Moreover, the absolute value of the dielectric function of the conductor has to be greater than the absolute value of the dielectric function of the insulator. It has also been demonstrate that the SPPs wave vector is larger than the wave vector of light, which implies that special phase-matching techniques should be used to provide the additional wave vector necessary for the SPP excitation. Penetration depths and propagation lengths have been defined. Plasmonic waveguides have been defined and the cases of insulator-metal-insulator, metal-insulator-metal and insulator-insulator-metal analysed. This theory will be useful to examine the properties of the MIM structure that has been developed during the course of this project. Finally, a literature review of the extraordinary optical transmission process and the fundamentals of two-dimensional periodic array of subwavelength apertures have been throughly addressed.

Chapter 4

Simulation, Fabrication and Characterisation Methods

Science is about knowing; engineering is about doing.

Henry Petroski[141]

This chapter describes the simulation, fabrication and characterisation methods exploited to design and engineer the nanostructured photonic architectures that are the topic of this Thesis. The plasmonic nanostructures have been designed and optimised with *Lumerical FDTD Solutions*. This software implements the Finite-Difference Time-Domain (FDTD) method to ascertain the optical properties of the devices. The fundamentals of the FDTD computational technique are presented in Section 4.1, followed by a brief discussion on the software, its capabilities and an overview of the chosen settings for the simulations environment. Section 4.2 focuses on the nanofabrication manufacturing technologies and processes used to manufacture the plasmonic filters. Fundamentals and working principles will be presented and addressed in detail. Finally, Section 4.3 describes the methods used to physically and optically characterise the devices.

4.1 Simulation Software: Lumerical FDTD Solutions

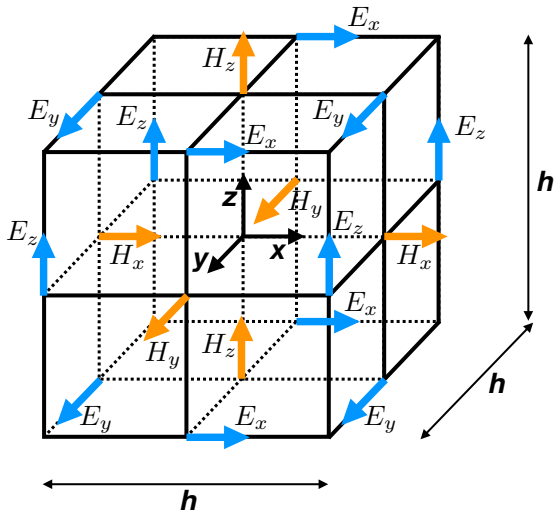
All electromagnetic simulations presented in this Thesis were executed with *Lumerical FDTD Solutions*. This software is a high performance Finite-Difference Time-Domain Maxwell's solver developed by Lumerical Solutions Inc. to specifically deliver powerful and reliable performance over a broad range of optical applications in two and three dimensions. It is equipped with an integrated, user-friendly graphical Computer Aided Design (CAD) environment which offers a compressive library of parameterizable simulation objects and materials. It also provides scripting capability and advanced post-processing and optimisation routines. Structures are designed, simulated under a pre-determined set of conditions, and the results collected and analysed.

4.1.1 The Finite-Difference Time-Domain Method

The Finite-Difference Time-Domain (FDTD) method is a computational full-wave analysis technique for the solution of electromagnetic problems. The FDTD technique was first proposed in 1966 by mathematician Kayne S. Yee[142] and it is based on the applications of the time-domain differential Maxwell's equations and appropriate boundary conditions. In his paper, Yee shows that - given a set of initial boundary conditions involving perfectly conducting surfaces - the numerical solution of the time-dependent differential Maxwell's equations in an isotropic media can be found.

Today, the FDTD method is arguably the simplest and most common numerical method for the solution of Maxwell's equations. Rather intuitive and simple to implement, the FDTD technique can be used to tackle a wide range of complicated problems of arbitrary shape, in particular the ones in which the characteristic dimensions of the domain of interest are somewhere on the order of a wavelength in size. However, being numerical, it is also generally computationally time-expensive and its solutions might require a considerable large amount of memory and storage capability[143].

The FDTD method belongs to the general class of grid-based differential time-domain numerical method. It directly solves the Maxwell's time-dependent differential equations



$$H_x(x + h/2, y, z, t - \Delta t/2)$$
$$H_y(x, y + h/2, z, t - \Delta t/2)$$
$$H_z(x, y, z + h/2, t - \Delta t/2)$$

$$E_x(x, y + h/2, z + h/2, t)$$
$$E_y(x + h/2, y, z + h/2, t)$$
$$E_z(x + h/2, y + h/2, z, t)$$

Figure 4.1: Illustration of the 3D Yee unit cell. FDTD methods store different field components at different grid locations and this discretisation of the electromagnetic field is know as the Yee lattice. The schematic shows the single cubic grid voxel of the Yee lattice. h is the grid spacing. E_x, E_y, E_z are the electric field components. H_x, H_y, H_z are the magnetic field components. The three components of the electric field **E** are store on the edges of the cube (in the corresponding positive directions), while the components of the magnetic field **H** are store on the cube faces. The coordinates of each field component are listed on the right-hand side of the figure.

(3.5) by using finite-difference approximations and proceeding to calculate the fields in incremental steps in space and time through a spatially discretised mesh, or grid. The foundation of the FDTD method is the so-called Yee unit cell, where electric and magnetic field vector components are positioned within a discretised 3D spatial grid - as shown in Figure 4.1. The electric and magnetic field vector components have a precise arrangement within the Yee unit cell. The electric field vector components are placed at the centre of the edges and oriented parallel to the edge itself. The magnetic field vectors, instead, are placed at the centres of the faces and oriented orthogonally to the plane of the face. This fills the space with interlinked Faraday's law and Ampere's law contours[144]. In the FDTD method, both space and time are discretised. In fact, electric and magnetic fields are sampled at discrete alternate half-time steps, following a *leapfrog* scheme. Notice that also the material constitutive parameters are distributed over the discretised mesh of the unit cell and associated with their respective field components[144].

4.1.2 Setting-up the simulation environment

This section provides the know-how to set-up a simulation in *Lumerical FDTD Solutions*[93] to correctly reproduce the simulation data presented in this Thesis. In general, a simulation requires the user to define a set of objects, simulation region, sources and monitors. All the simulation objects are organised within a group, called *model*, in the form of an *object tree* that represents the current simulation. Each object has geometrical and structural parameters that can be conveniently set to define, for example, dimension, position and material composition. *Lumerical FDTD Solutions* has a comprehensive database of materials that are available to use in the simulations. However, it is also possible to define 'new' or complex materials, for example, by importing experimental data or parametrised models. Notice that the objects are listed as they are inserted and, exactly like in computer programming, their order is extremely important. For example, objects override each other and thus to obtain an array of apertures within a layer, the holes must be added after the layer. Similarly, a monitor will not produce any output if it has been inserted before the simulation region.

To simulate the transmission properties of a 2D periodic array of nanoholes it is not necessary (luckily) to built the entire array. We can simply design the unit cell of the array - 5 holes, one in the middle and one at each corner of the rectangular cell - and then add the simulation region with the appropriate dimensions, geometry, and set of boundary conditions. Figure 4.2 displays the unit cell of a 2D hexagonal nanohole array and its simulation region environment in Lumerical. The next paragraphs provides a detailed description on how to set the simulation environment.

The incident light is simulated with a broadband plane wave source that covers a wavelength range of 350 to 800 nm, placed within the silicon dioxide substrate. For normally incident light both the polar and azimuthal angles of propagation, *theta* and *phi*, respectively, are set to zero. The source is polarised with the electric field parallel to the x-direction. To increase the 'resolution' of the simulation, a finer 3D 'override' mesh - which, as the name suggests, overrides the previous mesh parameters of the simulation region - is added to cover the total thickness of the plasmonic filters, i.e. the thickness

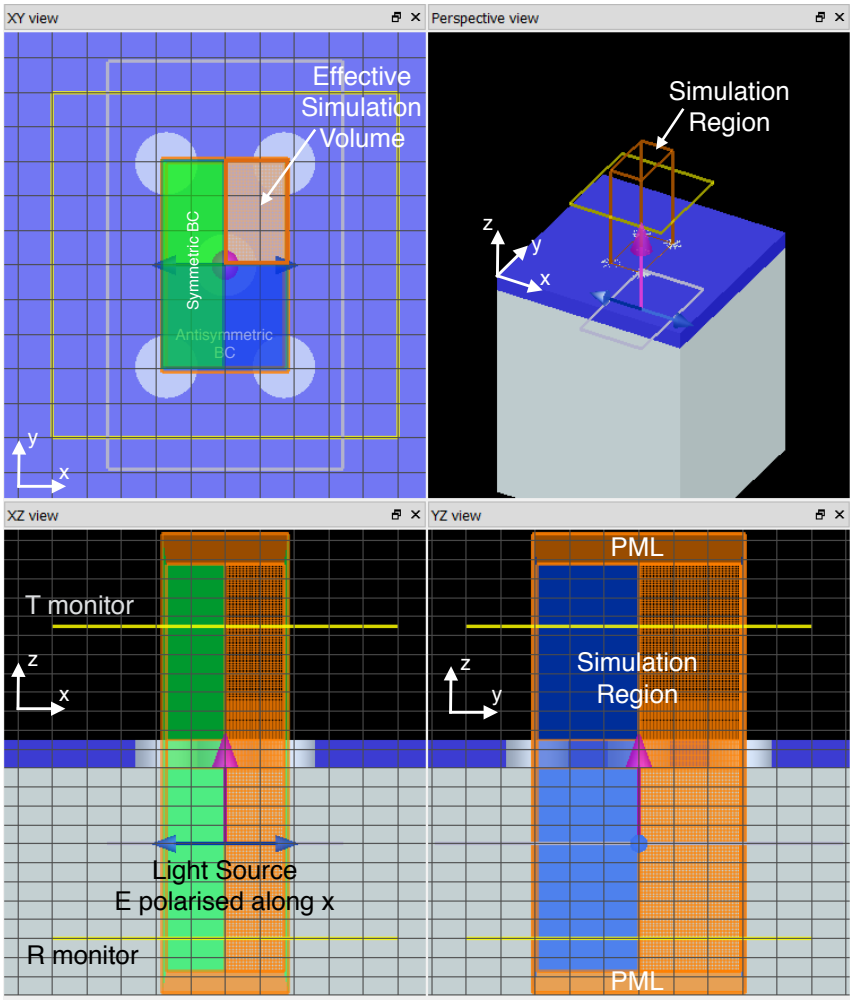


Figure 4.2: Lumerical simulation set-up 2D hexagonal nanohole array. The four images represent the XY view, Perspective view, XZ view and YZ view of the Lumerical simulation model of a 2D hexagonal anole array as described in this Section.

of the metal layer or the stack thickness in case of a single-layer or a multilayer architecture, respectively. The mesh accuracy was set to 0.5 nm. This mesh ensures a higher computational precision in that region. To record the transmission and reflection data of the structure as a function of frequency, *2D frequency-domain field monitors* are added above and below the structure, respectively, and within the borders of the simulation region. Structures do not interfere with monitors, and monitors do not interfere with other monitors. However, sources require a certain amount of space to inject the fields and thus there is a region around them where the fields are not physically meaningful. Monitors should not be place within that region. A 2D index monitor is also added to check the refractive index of each object. Finally, to record electric and magnetic fields data as a function of position and frequency, 2D frequency-domain field monitors were added only

when required, to reduce the simulation computational time and memory requirements.

Using the appropriate set of boundary conditions is crucial to obtain reliable and consistent simulation results. FDTD Solutions supports several types of boundary conditions, but here I am just going to name the few that are relevant to this Thesis. Firstly, to model 'open' boundaries above and below the array, *Perfectly Matched Layer* (PML) conditions are used along z-direction. They absorb electromagnetic waves incident upon and thus eliminate/reduce the possibility of multiple reflection at the top and bottom boundaries of the simulation volume. This basically allow you to have 'reflection-less' boundaries. To control the amount of absorption, it is possible to specify several parameters including the number of layers. Secondly, to reproduce the periodicity of both a structure and the electromagnetic fields, the *Periodic Boundary Condition* is used in the direction(s) of interest (x-y plane). And last but not the least, since the problem exhibits planes of symmetry, the *Symmetric/Anti-Symmetric* boundary conditions can be applied. These boundaries mirror (or anti-mirror) the electric or the magnetic fields and can be used because both the structure and the source are symmetric. In particular, for meaningful results, the sources and the boundary conditions must have the same symmetry. This last boundary condition is extremely useful for computationally expensive simulations. In fact, in our case, it allows to reduce the simulation volume up to 4 times by modelling only a single unit of the array and by applying symmetric/antisymmetric boundary conditions to the fields along the x- and y-direction, respectively, consistently with the source's polarisation. Note that if the plane wave was launched at an angle instead of normal to the surface of the array, the boundary conditions should be changed to *Bloch* because the electromagnetic fields will not be symmetric/anti-symmetric along the same plane of symmetry of the structure anymore.

The basic set-up configuration described in the above paragraphs will be used for all the simulations presented in this Thesis. *Lumerical FDTD Solutions* provides a powerful scripting language to manipulate simulation objects, launch simulations and analyse results. However, the analysis, development and optimisation of a nanostructure requires a huge amount of simulations. Then, to simply and automate the process, scripts were written to sequentially run parametrised simulations and collect the results. The trans-

mission and reflection spectra are plotted and saved as JPEG images, while the data are exported in a **.mat* file. The project itself is also saved, as well as the full list of variables.

4.2 Nanofabrication Techniques

Nanofabrication refers to the design and manufacturing processes of materials and devices with dimensions measured in nanometers. All structures presented in this Thesis were fabricated using the equipments available at the James Watt Nanofabrication Centre (JWNC) at the University of Glasgow. This Section provide an overview of the key techniques used to fabricate the structured nanophotonic devices presented in this Thesis. The detailed fabrication process flow will be outlined in Chapter 8. Fabrication was carried out using typical semiconductor fabrication processes.

4.2.1 Metallisation

According to the application, several factors need to be considered for choosing the most appropriate metallisation technique: the maximum temperature that a substrate can sustain, the requisites on the electrical and mechanical properties of the film, the uniformity of the film, and the morphology of the surface. *Physical Vapour Deposition* (PVD) is a widely used additive method for thin film deposition of metal layers and alloys. The film growth is achieved by accumulation, or condensation, of a vapour of the necessary material onto a cooler substrate. PVD processes are carried out under high vacuum conditions[1] and involve four steps: (i) evaporation, (ii) transportation, (iii) reaction, and (iv) deposition. The most common PVD techniques are *sputtering* and *evaporation*. The latter, in turn, can be divided in two subcategories: thermal and electron beam (e-beam) evaporation. The thin film metallisation used in the fabrication of the plasmonic devices presented in this Thesis was performed by mean of electron beam evaporators.

With respect to other metal coating techniques, the e-beam evaporation method offer several advantages. Unlike thermal evaporation, it can evaporate materials with high

[1] 5×10^{-5} Pa or higher.

melting point temperatures. Long evaporation for thick films are feasible because liners can usually host a great amount of material to be evaporated. In addition, the beam of electrons, guided by the magnetic field, can be scanned across the liner and accelerated to any desired level. This means, respectively, that this technique offers a high materials utilisation efficiency and also that the deposition rate is highly controllable. The deposition rate can be as low as a few angstroms per minute to as high as few microns per minute, resulting in higher density film coatings with increased adhesion to the substrate. Moreover, unlike *Chemical Vapour Deposition* (CVD) techniques, e-beam evaporation does not produce hazardous by-products and it is a high quality no-contaminant process. In fact, no contamination arises from the liner because it is kept at low temperature, and neither from the filament because the magnetic deviation separates contaminants from electrons. Finally, e-beam evaporation operates under vacuum so that multilayers with no air or moisture contamination (Al for example oxidises immediately in contact with air) or alloys are feasible.

A schematic of the e-beam evaporation process is depicted in Figure 4.3. Electrons emission is obtained by heating up a charged metallic thermionic filament - usually tungsten - through an accelerating voltage. Electrons are then accelerated and steered via magnetic fields to strike the target material. Materials are contained in water-cooled crucibles, also called *liners*, situated above the filament. As the temperature within the liner arises above its boiling point[2], the target material evaporates and transitions to a gaseous state, i.e. the atoms will have sufficient energy to leave its surface. The deposition rate is maintained constant by mean of a quartz sensor, which monitors the deposited thickness, and a feedback control system. By using a global shutter placed in front of the substrate(s), the deposition starts only when the desired, constant deposition rate is achieved.

The electron beam evaporators used to fabricate the plasmonic devices are *Plassys MEB 550S* or *Plassys MEB 400S* - depending on the availability. Both the tools have a cryo-pumped load lock and main chamber, a 10kW electron beam source, and use the same type of 99.99999% aluminium in the source. The deposition rate was set at 0.3

[2]Boiling point of aluminium: 2470°C.

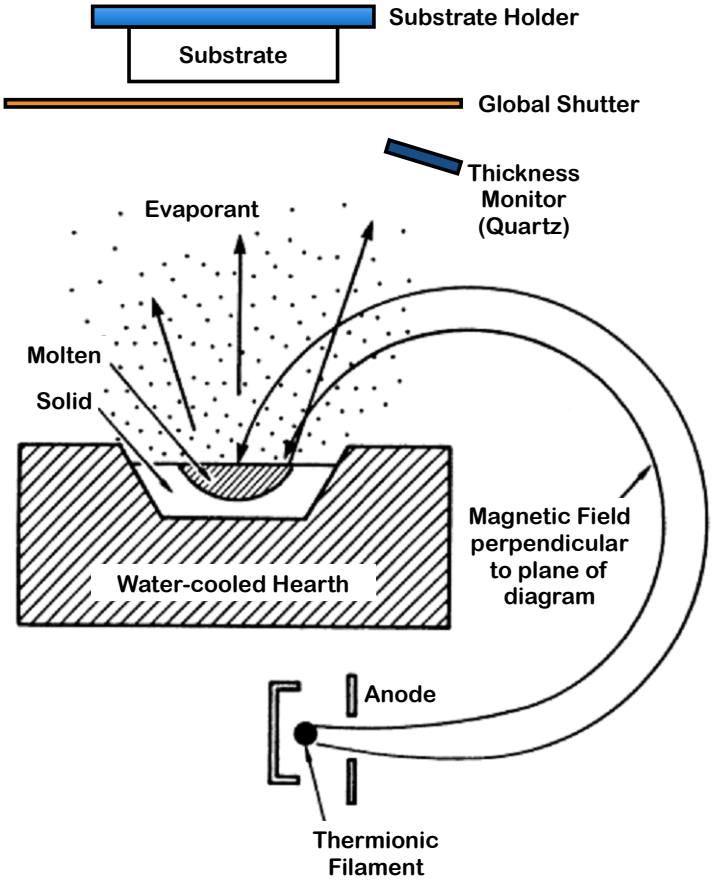


Figure 4.3: Electron Beam Evaporator Physical Vapour Deposition. The target material to be used as a coating is bombarded with an electron beam from a charged thermionic filament which increases the temperature within the liner. Above its boiling point, the target material evaporates and converts into a gaseous state. Atoms in the vapour phase then reach the substrate and form a thin film coating on its surface. Deposition rate is monitored through a quarts sensor.

nm/s. The working pressure during evaporation was around $1 \times 10^{-}6$ torr. Substrates were placed at the centre of the holder to avoid a non-uniform coverage.

4.2.2 Dielectric Deposition

Deposition of dielectric materials is achieved through *Chemical Vapour Deposition* (CVD). CVD is a chemical process technique to grow thin films from vapour phase reactants. CVD produces high-quality and high-performance substances, and is suitable for a wide range of materials, from metals to semiconductors to insulators. There are several types of CVD process, including Atmospheric Pressure CVD, Low-Pressure CVD, Metal-Organic CVD, Atomic-Layer CVD, Plasma-Enhanced CVD, and many more. High temperatures and low pressures are the most common process conditions, but are not necessary. High

temperatures trigger chemical reactions that might not be energetically favourable at room temperature, favour vaporisation processes and increase solid solution ranges[145]. On the other hand, lower temperatures ensure a higher purity of the film and play a critical role in near-end processing in semiconductor manufacturing. Low pressures tend to reduces unwanted gas by-products and improve the film uniformity across the wafer. All CVD methods, however, involve using an energy source to break the reactant gases into reactive species for deposition.

In its simplest form, CVD involves flowing a precursor gas or gases into a vacuum chamber containing one or more heated substrate to be coated. Figure 4.4 highlights the reaction mechanisms that take place inside a CVD reactor chamber. Thin film deposition results from the chemical reactions of the reactant species on and near the hot surfaces. To initiate the reactions, the precursor species must first be adsorbed on the substrates. After the adsorption, the reactive species can remain fixed at the surface sites or migrate along the surface due to a surface diffusion giving rise to nucleation and island growth. Clusters (or nuclei) impinge and grow together to form continuous film. Nucleation is a temperature-dependent process and can affect the step coverage. Finally, volatile surface reaction by-products are desorpted and will be flushed away at the end of the process.

The deposition rate is given by the sum of reaction rate and reactant arrival rate. The surface reaction rate strongly depends on temperature and increases as the temperature increases. At low temperature, reaction rate is slower than reactant arrival rate, i.e. reactants arrive at the surface faster than what they are able to react with surface atoms. As a consequence this regime is called reaction rate limited. Increasing temperature increases the reaction rate. But at very high temperature the reaction rate is much faster than the reactant arrival rate, i.e. reactants cannot arrive fast enough to follow the reaction rate. Therefore the process becomes mass-transport limited and the deposition rate assumes a constant value, completely dependent on the reactant arrival rate. The best working point lies in between these two regimes (see inset of Figure 4.4).

The dielectric layers of the nanostructures presented in this Thesis were deposited using: Plasma-Enhanced CVD (PECVD), for the deposition of silicon dioxide layers, and Inductively Coupled Plasma-Enhanced Chemical Vapour Deposition (ICP-CVD), for the

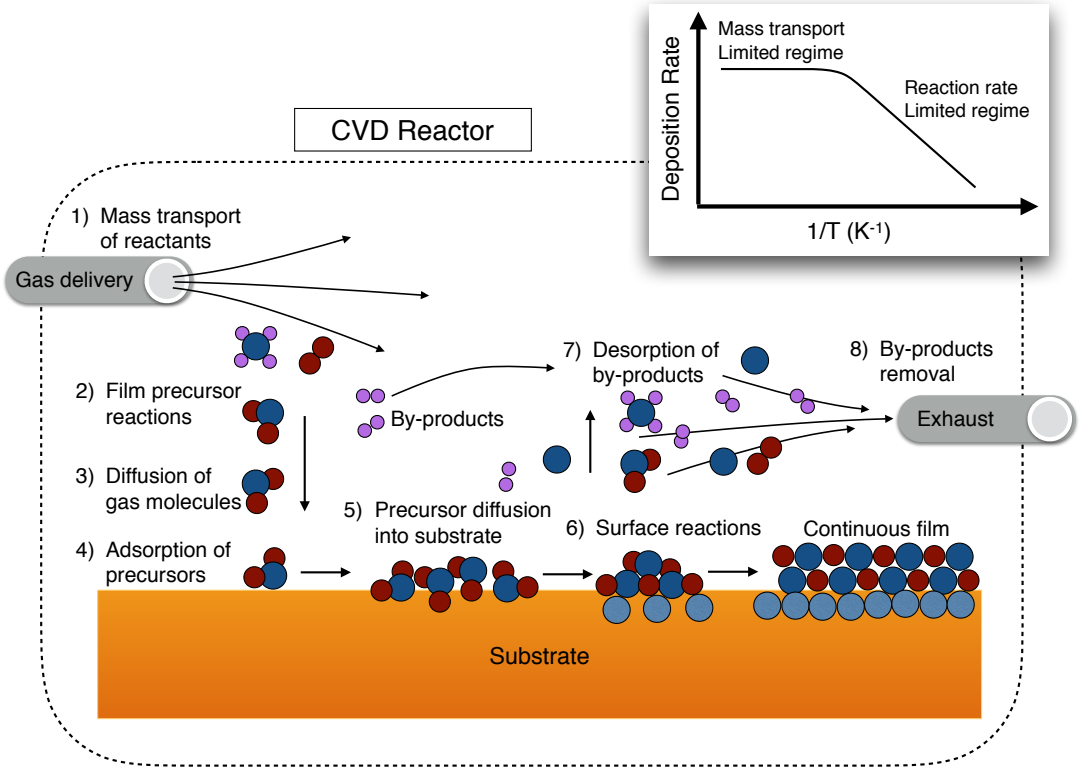


Figure 4.4: Illustration of the surface reaction mechanisms involved during CVD [146]. A vacuum chamber, containing one or more heated substrate to be coated, is filled with precursor gas or gases. Gas particles transported near the substrate are adsorbed and chemically react with the hot surfaces. Reactive species remain at the surface sites or migrate along the surface due to a surface diffusion giving rise to nucleation and island growth. Clusters (or nuclei) impinge and grow together to form continuous film. Volatile surface reaction by-products are then desorpted and will be flushed away at the end of the process. Inset: deposition rate vs. substrate temperature. At low temperatures the deposition rate is limited by the reaction rate of the reactants with the surface atoms, while at high temperatures the deposition rate is limited by the reactant arrival rate.

deposition of silicon nitride layers. Silicon dioxide depositions were carried out using an *Oxford Instruments PECVD 80+*, while the silicon nitride depositions were carried out using an *Oxford Instrument System 100 ICP 180 PECVD*. The latter is a high density plasma tool for room temperature deposition of low stress silicon nitride[3].

PECVD, as the name suggests, is a chemical vapour deposition process which involves the exploitation of a plasma[4]. The plasma produces energetic electrons, ions and free radicals which assist the chemical reactions during the deposition process. The plasma forces reactions that would not be possible at low temperatures. In this way, the substrate temperature does not need to be as high as for CVD, which is advantageous for

[3]breakdown voltage of 4×10^6 V/cm for 5-nm thick films.
[4]Highly ionised gas containing an approximately equal number of positive ions and electrons.

temperature-sensitive substrates. In PECVD processes, the substrate is typically heated to 250 °C to 350 °C, depending on the specific film requirements. In comparison, CVD requires temperatures of 600 °C to 800 °C. Finally, plasma-assisted processes permit higher degrees of freedom to achieve film properties.

In general, the plasma is generated by applying a RF-driven power to a chamber filled with reactant gases. The electromagnetic field accelerate the free electrons, increasing their kinetic energy. When the electrons elastically collide with the neutral particles of the gas, they ionise or dissociate the reactant gases generating chemically reactive radicals[5] and contributing more electrons to the process. These are called cascading collisions and it is said that the reaction is sustained. Radicals that return to their ground state (by re-acquiring an electron) emit visible photons creating the visible glow typical of the plasma. The colour of the glow is characteristic of the gas(es) used. When the steady state (i.e. the plasma) is reached, the ionisation process equals the recombination process. Plasma aside, the PECVD deposition mechanism is the same as in CVD as described previously, but with radicals instead of neutral reactants. Radicals that reach the substrate[6] are adsorbed and chemically react on its surface. Reactive species remain on the surface and form a thin coating layer, while by-products are desorpted and flushed away.

The difference between standard PECVD and ICP-CVD lies mainly in the type of reactor used to generate the plasma. Standard PECVD processes use a parallel-plate reactor: the substrate is placed on the bottom electrode (anode) - which is grounded and heated up to a constant temperature - and a capacitively-coupled plasma (CCP) is produced by applying a Radio-Frequency (RF) power to the top electrode. ICP-CVD systems use instead a RF inductively-coupled plasma source, driven by a magnetic potential generated through a coil wound around the dielectric walls of the vacuum chamber. ICP-CVD has several advantages compared to PECVED (or CCP-CVD). It provides higher plasma densities and a reduced ion bombardment of the growing film surface. Additionally, ICP-CVD deposited thin films have a very good spatial homogeneity due to the uniform plasma distribution in radial and axial direction.

[5] A radical, in chemistry, is an atom, a molecule, or an ion that has at least one unpaired valence electron. These unpaired electrons make radicals highly chemically reactive.
[6] Most radicals are electrically neutral so their transport to the surface is by gas phase diffusion.

Modelling a CVD system can be quite complex because the interrelationships among controllable experimental parameters, process variables and coating properties are considerably intricate[145]. The development of a stable and reliable CVD process requires long and well-planned parametric studies and an extremely high knowledge of the machine. That is why most cleanroom, like the JWNC, already provide a defined range of deposition process and allow users to vary only few process parameters or none at all.

4.2.3 Electron Beam Lithography

In general, in nanofabrication, it is not possible to etch layers, grow or deposit materials only in desired area of interest. Therefore, to reproduce a pattern onto a surface it is necessary to perform a lithographic step. The term *lithography* includes all the techniques used to transfer a desired pattern into a radiation-sensitive polymer layer, called resist. This layer works as a mask material that, in turn, will protect or expose specific areas of the underneath substrate from, for example, a subsequent etching or deposition process. In this way, a specific pattern (or its negative) can be recreated. There exist several lithographic techniques and several different exposure tools. The most common technique used in the semiconductor manufacturing industry is called *photolithography* or optical lithography. It uses light to transfer the pattern from a pre-fabricated *photomask* to the photoresist.

Photoresists are photosensitive organic mixture which contain (i) an inactive polymer resin (a binder that provide mechanical properties), (ii) a photo-active compound (PAC), and (iii) surfactants and solvents to control the mechanical properties of the base resin, maintaining it in a liquid state. Essentially there are two types of resists: *positive* resists and *negative* resists. In positive resists, photons break the polymer chains to make them more soluble to a developing solution, i.e. the photo-induced chemical reaction enhances the resist dissolution. In this way it is possible to replicates the same pattern of the resist onto the wafer. In negative resists, photons induces cross-linking of the polymer chains to make them less soluble to a developing solution so that the inverse pattern of the exposed resist areas is replicated onto the substrate. An important characteristic to consider during the choice of a photoresist is the *contrast*. High-contrast resist allow a

more accurate reproduction of the pattern onto the substrate.

However, in optical lithography, the minimum resolution of a feature is limited by the light diffraction limit, i.e. by the wavelength of the light that is used, and also largely depends on the type of exposure tool used (contact, proximity or projection). Current state-of-the-art photolithographic tools use deep ultraviolet (DUV) or extreme ultraviolet (EUV) light to allow minimum feature sizes down to 50 nm and 13.5 nm, respectively, but they are still under development for high volume use. Recently, new techniques had became more and more available for the mass-production of nanoscale devices such as nano-imprinting and x-ray lithography. The latter being the most promising candidate for next-generation lithography for the semiconductor industry.

Another lithographic technique is *Electron Beam Lithography* (EBL), which uses a focused beam of electrons instead of light to expose radiation-sensitive resists. Electrons possess wave-like properties with smaller wavelengths than photons (at the same energy) that can reach $0.2-0.5$ Å - about 10 times less than x-ray wavelengths. Therefore, e-beam lithography is capable of much greater patterning resolution, sometimes as small as a few nanometers. Unlike optical lithography, e-beam lithography is a mask-less lithography. EBL reproduces a pattern in the resist through direct writing and thus eliminates the requirement for a photomask which results in increased flexibility in the pattern designs. E-beam lithographic tools are highly automated, and enable extremely low resolution and accurate alignment. However, they do have some limitations. Although nm-scale beams can be formed, electron scattering usually limits the resolutions to features larger than 10 nm. Moreover, they are expensive and have a low throughput because they require long exposure times, proportional to the area of exposure. Therefore, they are not suited for mass-production.

A similar type to lithography is *Ion Beam Lithography* (IBL), which uses a focused beam of ions instead of electrons. The higher mass of the ions leads to a reduced scattering and thus to a higher resolution (≈ 8 nm) than x-ray or e-beam lithography. Nonetheless, this method suffers from random space-charged effects, causing broadening of the ion beam, and can create crystal defects within the exposed area due to ion implantation.

The nanostructures presented in this Thesis have been fabricated using electron beam lithography. The JWNC is equipped with a *Vistec VB6* EBL tool. The part of the EBL system that forms the electron beam is normally referred to as the column. An EBL column typically consists of: (i) an electron source (gun) to generate the beam, (ii) two or more stages of electromagnetic lenses to align and collimate the beam - reducing its energy spread - as it moves down the column, (iii) blanking plates to turn on and off the beam at need, (iv) apertures to limit and define the beam size, (v) deflection coils to deviate the beam during the exposure, and finally (vi) an electron detector to assist with focusing and to locate eventual alignment marks on the surface of the sample. Note that the deflection lenses can only *locally deflect* the beam over a distance of few micrometers. Therefore to cover large size wafer, the stage has to move. Accurate displacements in X-, Y-, Z-directions[7] are achieved through the use of piezoelectric tables and laser interferometry control.

A schematic of a typical EBL column is shown in Figure 4.5. The column must always remain under vacuum (10^{10} torr or better) and only the wafer chamber may open for wafer loading/unloading. The EBL system is extremely sensitive to temperature variations, mechanical vibrations and electromagnetic interference. Therefore, it is usually placed on an anti-vibration ground at the lowest level of a building in a functional and isolated room that is thermally and electromagnetically insulated.

To generate the electron beam, electrons are emitted from a solid-phase conducting source and accelerated by a voltage[8]. Free electrons inside the metal leave the tip of the emitter only if they gain enough energy to tunnel through the electrostatic potential barrier. This happens when the supplied energy is higher than the metal work function of the material. Energy may be supplied either through heating (thermionic emission) or/and electric field (field emission, also known as cold cathode emission).

The VB6 uses a thermal field emission source. It combines a sharp tungsten (W) needle of the field emission source and the heating of the thermal source (see right end side of Figure 4.5). The energy is supplied through an electrostatic field but, to avoid atom

[7]Accuracy $\approx$ 50 nm.
[8]Typical acceleration voltage beams are 5, 30, 50 and 100 kV.

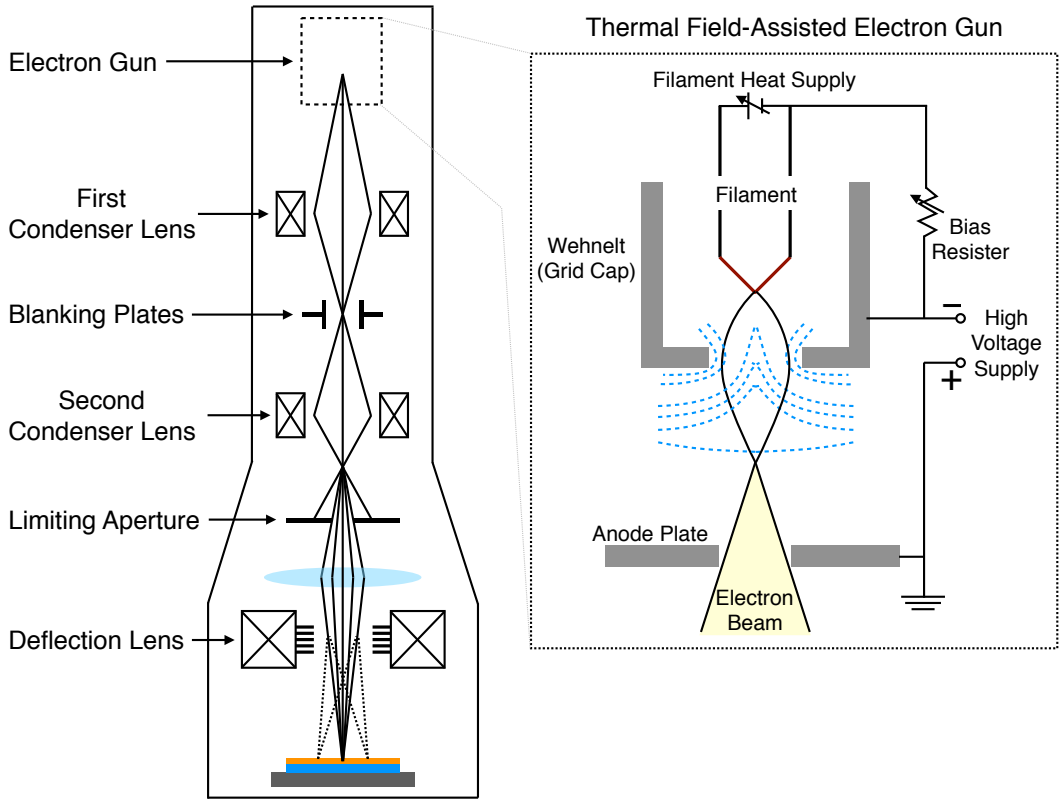


Figure 4.5: Schematic of a typical EBL column. An EBL column typically consists of: (i) an electron source (gun) to generate the beam, (ii) two or more stages of electromagnetic lenses to align and collimate the beam, (iii) blanking plates to turn on and off the beam at need, (iv) apertures to limit and define the beam size, (v) deflection lenses to deviate the beam during the exposure, and finally (vi) an electron detector to assist with focusing and to locate eventual alignment marks on the surface of the sample.

adsorption at the surface of the tip and lower the extraction potential of the material, the filament is also heated up at about 1800 Kelvin.

Electron source properties depend on the choice of material and type of emission, and therefore a type of source can be more or less suitable according to the application. An electron gun has three distinctive attributes: (a) size, (b) brightness, and (c) energy spread (measured in electron volts). The source size determines the amount of demagnification the lenses must provide in oder to have a suitable, small beam spot at the wafer level. The brightness is the analogue of the optical intensity: the brighter the electron source, the higher the current in the electron beam. Instead the energy spread is the analogue of the spectral purity for a monochromatic laser. Although it is desirable to have a low energy spread at the source level, space charge interactions between electrons increase the energy spread of the beam as it moves down the column.

A thermal field emission source - like the one exploited in the VB6 at the Glasgow

facility - offer several advantages. It features a brightness almost as high as cold field emission sources, a very small source size, but a moderate energy spread. However, compared to a cold cathode type, its emission current is very stable. In fact, because of the constant assisted heating, the emitter tip is less prone to adsorb residual gases present in the environment and thus reliable operation can be achieved for months at a time.

The lithographic patterns for the EBL tool are designed in Tanner L-Edit CAD software. The final layout is then exported in the GDSIII file format and transferred to another software called Beamer. Beamer converts pattern shapes to machine-specific formats, chopping polygons into rectangles and trapezoids, and decomposing large patterns into non-overlapping main fields and subfields. This process is called *layout fracturing* and is a fundamental step for EBL. Figure 4.6 illustrates the concept of layout fracturing. The surface of the sample is divided into main fields which are accessed by mechanical movement of the sample stage. Within a main field, the stage does not move. The main fields are divided into numerous, smaller sub-fields. To access the subfields the beam is deflected by the main deflection coils and within each subfield subfield deflection coils control the position of the beam to expose the resist and write the rectangles and trapezoids that compose the pattern[147]. Each rectangle and trapezoid is filled by an array of individual beam shots. Finally, the job file is submitted to the beam writer using the Java based BELLE software.

To control the EBL process, several parameters have to be defined. These include beam spot size, resolution and variable resolution unit (VRU). To write the pattern, the electron beam exposes a point on a grid, then moves on to the next point, until the shape is completed. The beam step size is defined as the center-to-center spacing of the shots and is given by the product of resolution and VRU (see example in Figure 4.6). Note that if the beam spot size is larger than the resolution, for a VRU equals to 1 the beam shots will superimposes. Finally, another important parameter is the e-beam dose, i.e. the number of electron per unit area of exposure.

EBL usually provides two exposure protocols: raster scanning and vector scanning (see Figure 4.7). In raster scanning mode all the points of a wafer are scanned and the beam is turned off when an area does not need to be exposed. There is no need

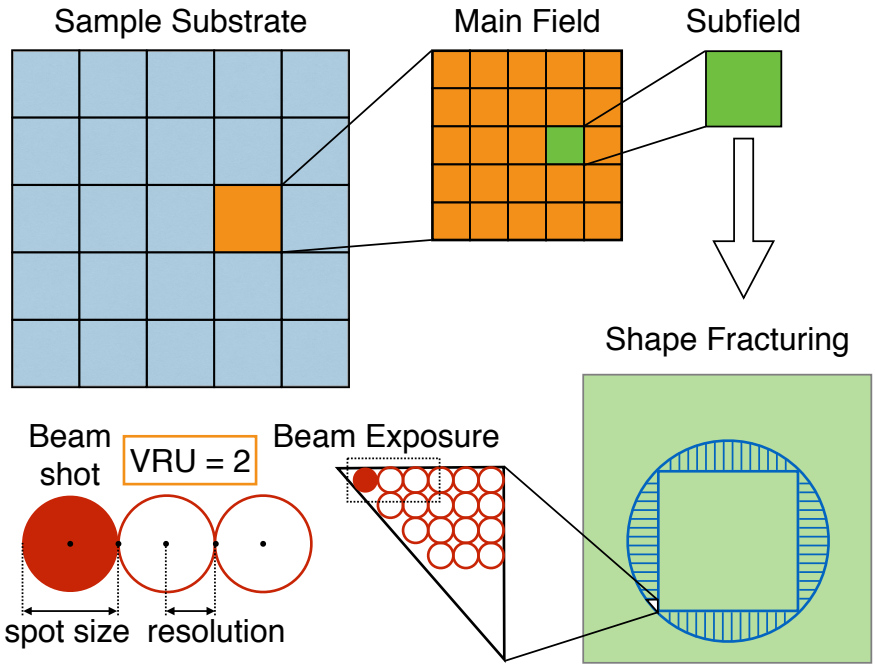


Figure 4.6: Layout fracturing for EBL and e-beam exposure. Layout fracturing is a fundamental step for EBL. The surface of the sample is divided into main fields. The main fields are then divided into numerous, smaller sub-fields. Within each subfield subfield deflection coils control the position of the beam to expose the resist and write the rectangles and trapezoids that compose the pattern. Each shape is filled by an array of individual beam shots. The beam step size, defined as the center-to-center spacing of the shots, is given by the product of resolution and VRU.

to modify the deflection direction of the beam and thus the beam stabilisation time is limited. This method is suitable when the surface to expose cover the highest percentage of the total wafer surface. Instead, in vector scanning mode only desired areas of the wafer are exposed and therefore it can save a significant amount of processing time. This method is suitable for sparse features. However, because of the frequent change of beam direction, the beam stabilisation time is increased. The Vistec VB6 uses the vector scanning method. Nonetheless, in both case, EBL has a very limited throughput - in particular when compared to standard photolithography - and thus is not suitable for high-volume manufacturing.

Extremely accurate direct writing is achieved by mean of a collimated Gaussian electron beam, i.e. a beam whose energy distribution is approximated by a Gaussian. This type of beam can displays a spot down to about few nanometers and allows a very good control of the dose deposited at each pixel during exposure. Typical e-beam doses are in the hundreds of $\mu C/cm^2$ but can go as low as 1 $\mu C/cm^2$. The higher the dose the longer

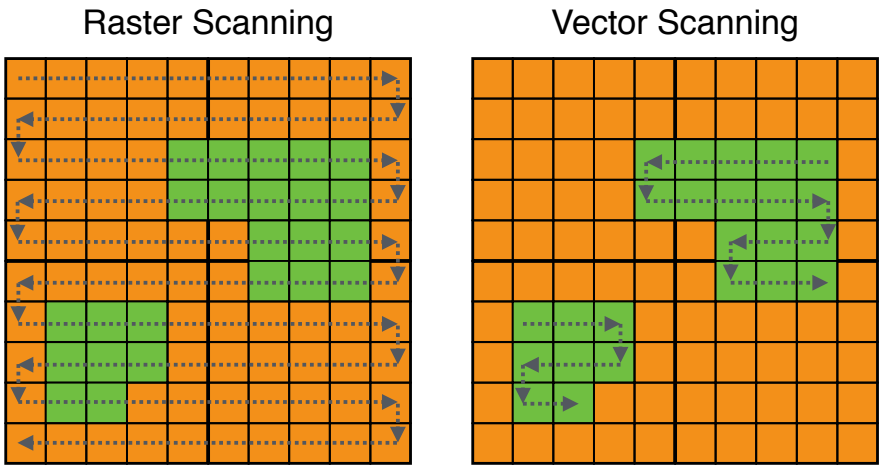


Figure 4.7: EBL exposure protocols. EBL usually provides two exposure protocols: (left) raster scanning and (right) vector scanning. In raster scanning mode all the points of a wafer are scanned and the beam is turned off when an area does not need to be exposed. Instead, in vector scanning mode only desired areas of the wafer are exposed and therefore it can save a significant amount of processing time.

the exposure time because more electrons have to be deposited at each scanning step. Similarly, given a same dose, the smaller the beam size the longer the exposure.

The minimum electron beam write time (T) to expose a given area (A) for a given electron dose (D) is given by their product divided by the beam current (I): $T = D \cdot A/I$. For example, assuming an exposure area of 1 cm^2, a dose of 100 μC/cm^2, and a beam current of 1 nA, the resulting minimum write time would be 10^5 seconds (just below 28 hours). Note that this minimum writing time does not include time for positioning, scanning (blanking, deflecting, etc) nor consider possible corrections and adjustments that may become necessary during the writing.

Despite an accurate control and electron beam widths of only few nanometers, there are several factors that determine the feature resolution limit of an electron beam system. In fact, even if the minimum feature size of EBL is not limited by diffraction, EBL tools are complex and impose practical limitations. One of the main limitation to the minimum feature size is the *Proximity Effect* which causes the dose distribution to be wider than the scanned pattern, and subsequently generates variations in the pattern shapes during exposure. This is due to the fact that when the electron beam hits the target, different types of electron-matter interactions occur, which affect the exposure area of the beam by providing a non-zero dose to the resist outside the scanned pattern. "For example, a

narrow line between two large exposed areas may receive so many scattered electrons that it can actually develop away (in positive resist) while a small isolated feature may lose so much of its dose due to scattering that it develops incompletely." [148]

As the incident electrons penetrate the materials - resist as well as the substrate stack[9] - they experience many scattering events, undergoing either inelastic (forward scattering) or elastic (backscattering) collisions. The forward scattering process is due to electron-electron interactions: an electron collides with an electron from one of the atoms in the resist/substrate. This interaction typically deflects the incident electron by a small angle, statistically broadening the beam, and leaves the atom in an excited (one of its electrons goes in an excited state) or ionised (one electron leaves the atom, creating a *secondary electron* in the material) state.

Secondary electrons are responsible for the bulk of the actual resist exposure process. They do not typically have high energies and thus, given the short range of interactions, they contribute little to the proximity effect. However, they also effectively broaden the beam diameter. On the other hand, the backscattering process originated from electron collisions with a heavy particle, such as an atom nucleus, which leads to wide-angle scattering. The incident electron retains (most of) its energy, but drastically changes its direction. The majority of the electrons do not stop in the resist but penetrate the substrate and contribute to resist exposure by scattering back into the resist and causing subsequent inelastic or exposing processes. Backscattering events are what causes to the proximity effect.

Figure 4.8a displays the electron interaction volume generated during an EBL exposure, as obtained by a Montecarlo simulation. The upper curves indicate the forward- and back-scattered components of the beam. It is clear that the feature resolution limit is not determined solely by the beam size but also by the forward scattering (or effective beam broadening) in the resist, while the pitch resolution limit is determined by the backscattering process. The forward scattering can be minimised by using a thinner resist and/or higher energy electrons. However, higher acceleration voltages might increase

[9]Typical electron acceleration voltages are 10-100 keV therefore the mean free path of an electron is 10 μm or more, which is almost two orders of magnitude greater than the resist thickness. It follows that electrons easily penetrate either the resist and the substrate.

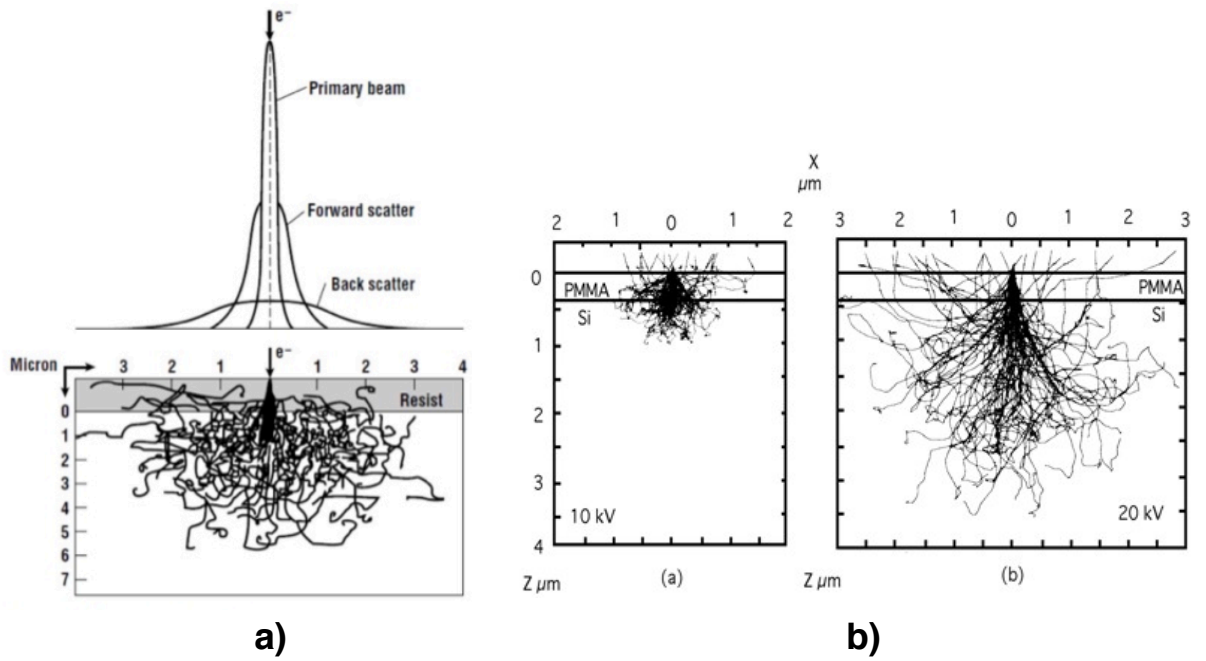


Figure 4.8: Montecarlo simulations of electron interaction volumes generated during an EBL exposure. a) Montecarlo simulation of electron trajectories during an EBL exposure[149]. The upper curves indicates the forward- and back-scattered components of the beam. b) Monte Carlo simulation of electron scattering in resist on a silicon substrate at a) 10 kV and b) 20 kV. Reprinted from *[Kyser, D. F., and N. S. Viswanathan."Monte Carlo simulation of spatially distributed beams in electron beam lithography" Journal of Vacuum Science and Technology 12.6 (1975): 1305-1308.]*[150] with the permission of AIP Publishing.

the backscattering[148] by increasing the backscatter depth into the substrate (see Figure 4.8b). Finally, the interaction volume increases as a function of the mean atomic weight of the materials. Therefore, low atomic weight substrates will reduce the backscattering process.

Given the aforementioned considerations on the proximity effect, and in spite of the several techniques to counteract the proximity effect, it is often necessary to determine experimentally the exact dose needed to achieve a specific result. It should also be considered that, at the resist level, the EBL tool needs to provided a minimum threshold energy, or *dose-to-clear*, just clear a pixel size area in the resist for a given process. Therefore, to figure out the *right* dose, it is common procedure for a new process to reproduce a same pattern several times on the same sample, each time using a different e-beam dose. Then, to determine the dose that produced the better result, the patterns are physically and optically characterised.

4.2.4 Dry Etching

Etching is used in micro- and nanofabrication to chemically remove layers or parts of them from a surface. Surface areas that do not have to be removed must be protected by using a 'masking' material. The term *dry* refers to the type of reactants used during the etching process. Unlike wet etching, which uses liquid-phase etchants, dry etch reactants come from a gas or vapour-phase source and are typically ionised. Wet etching is a cheap, highly selective process that does not damage the substrate. On the other hand, dry etching eliminates the handling and waste management of dangerous acids and solvents, and it only uses a small amounts of chemicals. But, more importantly, it is a controllable process: it provides repeatable, stable performance with a wide process window, and it is a directional etching, i.e. etch profiles can be either isotropic or anisotropic without the need of using crystals orientation. Dry etching requires specialised (and expensive) equipments, but provides neat, high resolution and faithful lithographic transfer.

There are two kinds of dry etches: plasma and non-plasma based etching processes. Plasma etching plays a key role in the fabrication of high-performances devices[151]. Plasma-based etchings exploit the generation of reactive ions or free radicals species typical of a plasma to remove materials chemically. Plasma-based deposition and etching techniques rely exactly on the same working principle, but exploit different chemistry reactions to either deposit or instead remove a specific layer/material, respectively. Figure 4.9 displays a typical plasma-based process chamber. As in the case of plasma-enhanced deposition techniques (see Section 4.2.2), the exploitation of a plasma during the etching process offer several advantages: (i) perform reactions at lower temperatures, (ii) can provide directionality and (iii) higher process controllability. Controlling ion density, electron temperature, and the plasma potential are of the utmost importance for ensuring a uniform etching.[152]

In the work presented in this Thesis, materials were etched by mean of Reactive Ion Etching (RIE) tools, namely *Oxford Instruments System 100 RIE T-gate* and *Oxford Instruments RIE 80+*. Reactive etching is a chemical process that exploits the free radicals of the plasma. It is an isotropic process and displays very high selectivity. On the

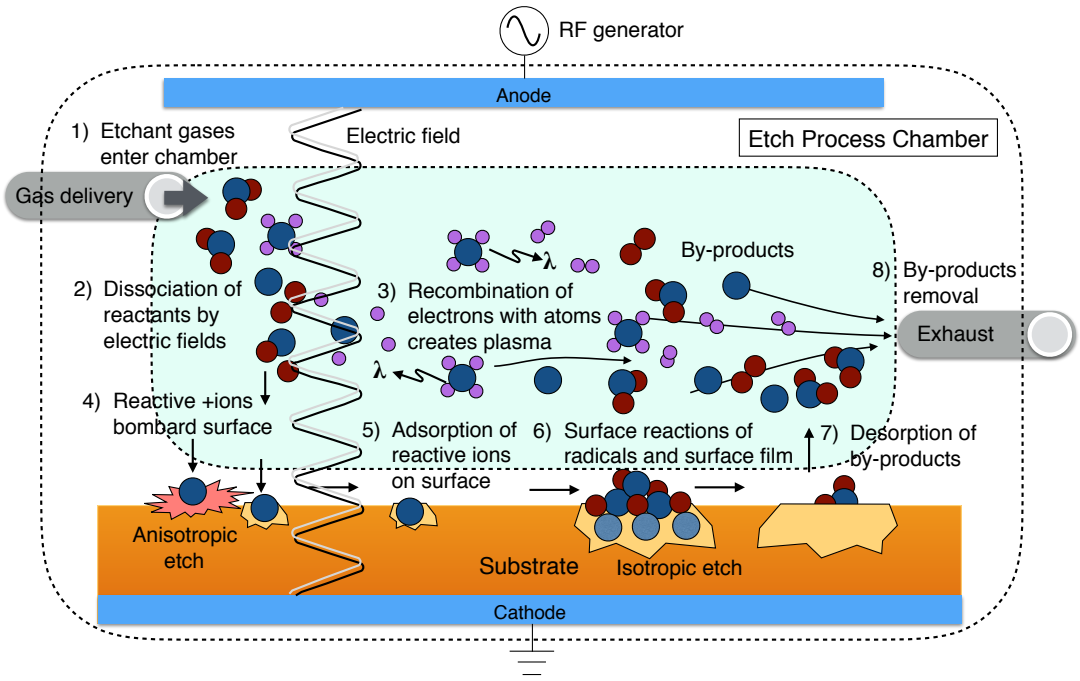


Figure 4.9: Illustration of the etching mechanisms within a plasma-based process chamber[146]. A vacuum chamber is filled with reactant gas or gases. The electric fields dissociate the reactants into high-energy electrons, ions and free radicals. The recombination of electrons with atoms generate and sustain the plasma. The substrate is positioned on a negatively charged electrode, therefore positively charged ions accelerates towards the surface of the sample causing physical etching by high-energy impact. Reactive ions are then adsorpted on the surface where react causing chemical etching. Volatile surface reaction by-products are then desorpted and will be flushed away at the end of the process. Plasma-based etching processes play a key role in the fabrication of high-performances devices.

other hand, ion etching is a mechanical (physical) etching. It is an anisotropic process with low selectivity and etch rate. Reactive Ion Etching is a combination of this two processes that involves chemically active species and energetic ion bombardment. RIE is faster than either pure physical or spontaneous chemical etching. Moreover, because ion bombardment is a direction etching, RIE displays anisotropic characteristics, with reduced lateral etch rate and vertical sidewalls. RIE is essential in case of high aspect ratio features[153].

In RIE, the selectivity is chemically provided by the choice of the gases that compose the plasma. Aluminium (Al) was etched using a silicon tetrachloride ($SiCl_4$) -based plasma. Chlorine containing gases are commonly used to etch Al. However, aluminium (tri)chloride ($AlCl_3$) by-products generated in Al plasma etching through chlorinated vapours are a major concern. The volatility of this by-products is relatively low, and so redeposition and/or adsorption might take place on the sample as well as on the chambers

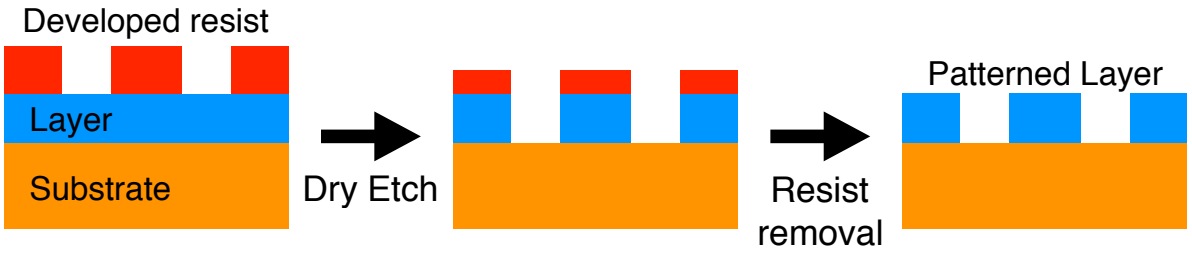


Figure 4.10: Dry etching process flow. After the lithographic step, the resist has been developed and the sample is ready for etching. Dry etching will reproduce the pattern in the resist in the underlaying material. At the end of the etching process, the remain resist can be removed, leaving the patterned layer on the substrate.

walls. Thus, it is important to remove the $AlCl_3$ by-products from the chamber during and after each etch run. Al etching also suffers of an initially inhibition period due to the removal of the thin (but quite hard) native oxide layer always present on Al surfaces - aptly called *aluminium oxide breakthrough time*. This time may vary according to the plasma conditions and the type of gas used.

Silicon nitride was instead etched in CF_4- or SF_6-based plasmas, more specifically using either a mixture of sulphur hexafluoride and nitrogen (SF_6 / N_2) or trifluoromethane (fluoroform) and argon (CHF_3 / Ar). The process is fairly straightforward, however, it is impossible to achieve selectivity against silicon oxide in CF_4- or SF_6-based plasmas. Nitride-to-oxide selectivity is roughly 2:1-10:1 [153].

Figure 8.2 illustrates a typical process flow for dry etching. After the lithographic step, the resist has been developed and the sample is ready for etching. Dry etching will reproduce the pattern in the resist in the underlaying material. At the end of the etching process, the remain resist can be removed, leaving the patterned layer on the substrate. Note that the etching will affect also the resist. Therefore, it is desirable to use a resist with high dry etch resistance. Moreover, consideration must be given to resist thickness with regards to the thickness of material that is to be etched and the material-to-resist selectivity so that the resist will not be etched away before the end of the process, leaving the whole surface of the underlaying layer unprotected.

4.3 Physical and Optical Characterisation Techniques

Physical characterisation techniques are extremely important because allow to assess the quality of a device and of a manufacturing process. The physical features of the photonic nanostructure presented in this Thesis were characterised by mean of electron microscopy - namely Scanning Electron Microscopy (SEM) and Transmission Electron Microscopy (TEM) - and Atomic Force Microscopy (AFM). Specifically, SEM was used to characterised the feature's horizontal dimensions, such as width of apertures and distance between them. TEM was instead used to characterise the cross-sections of few samples. While SEM was a readily available tool within the JWNF, TEM required the assistance of an external laboratory and therefore it has been exploited only a couple of times, in case of extreme necessity. Finally, AFM was used to characterise the vertical dimensions of the nanostructures. On the other hand, the optical filters performance in the visible range were determined through microspectrophotometry. This section provide an overview of the basis and working principles of all the aforementioned characterisation techniques.

4.3.1 Electron Microscopy

Electron Microscopy (EM) is an imaging technique that uses a beam of accelerated electron as source of illumination (instead of light as in standard optical microscopy) to obtain high-resolution images of biological or non-biological specimens. This technique is fundamental for the analysis and characterisation of nanostructures because it provides extremely accurate morphological details. The wavelength of electrons can be up to 100,000 times shorter than that of visible photons and therefore electron microscopes have a higher resolving power and resolution than light-based microscopes,[154] which are also limited by diffraction. Electron microscopes are an indispensable piece of equipment for biology, life sciences, material sciences and all the disciplines associated to micro/nanotechnologies fabrication.

As discussed in Section 4.2.3, when highly energetic electrons penetrate a specimen they experience many scattering events. These interactions can be either *elastic* or *inelas-*

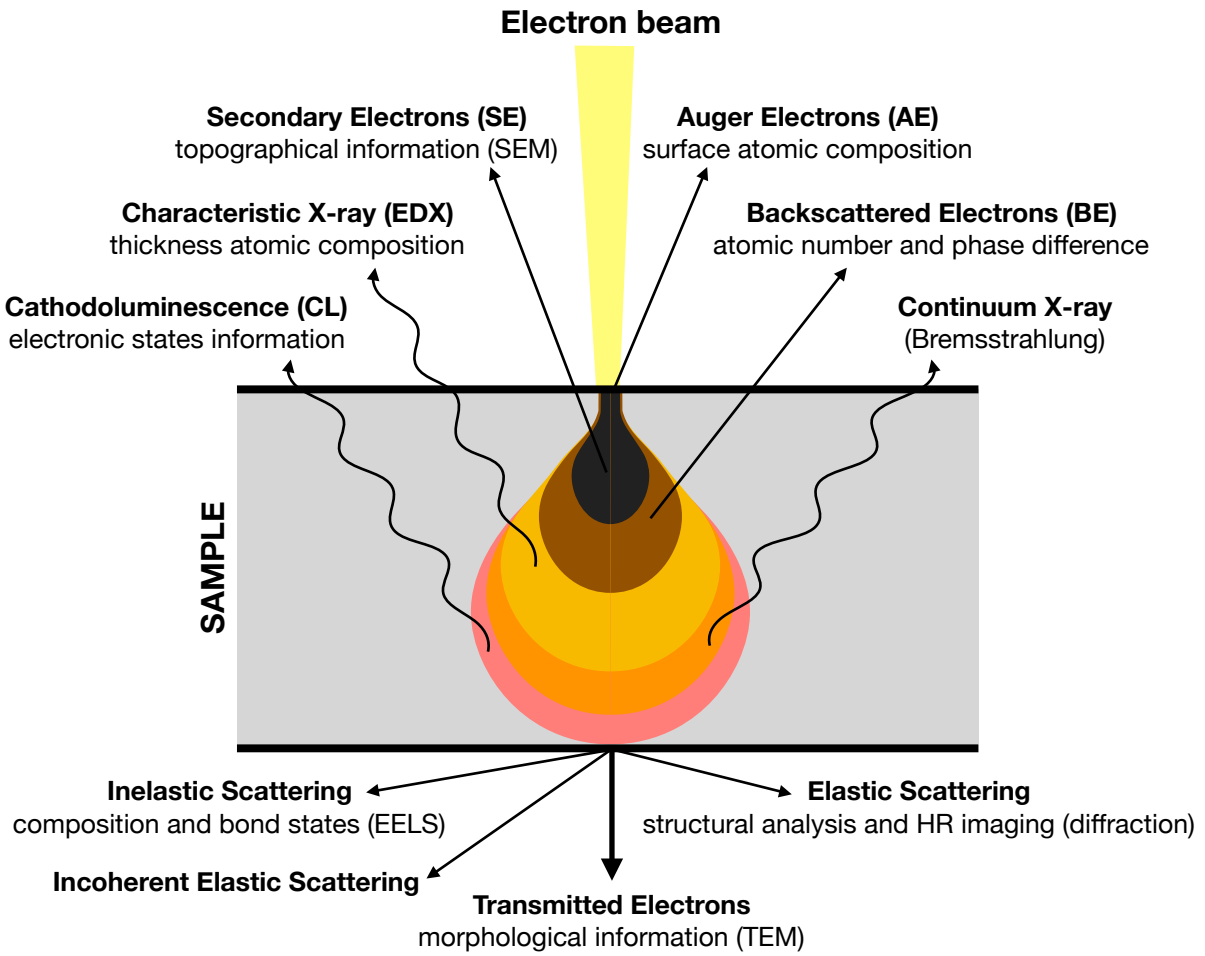


Figure 4.11: Schematic of the electron interaction volume. When highly energetic electrons penetrate a specimen they experience many scattering events and thus electron interactions generate different signals. Each signal results from interactions of the electron beam at various depths within the sample and thus contains different information about its surface topography and composition.[155]

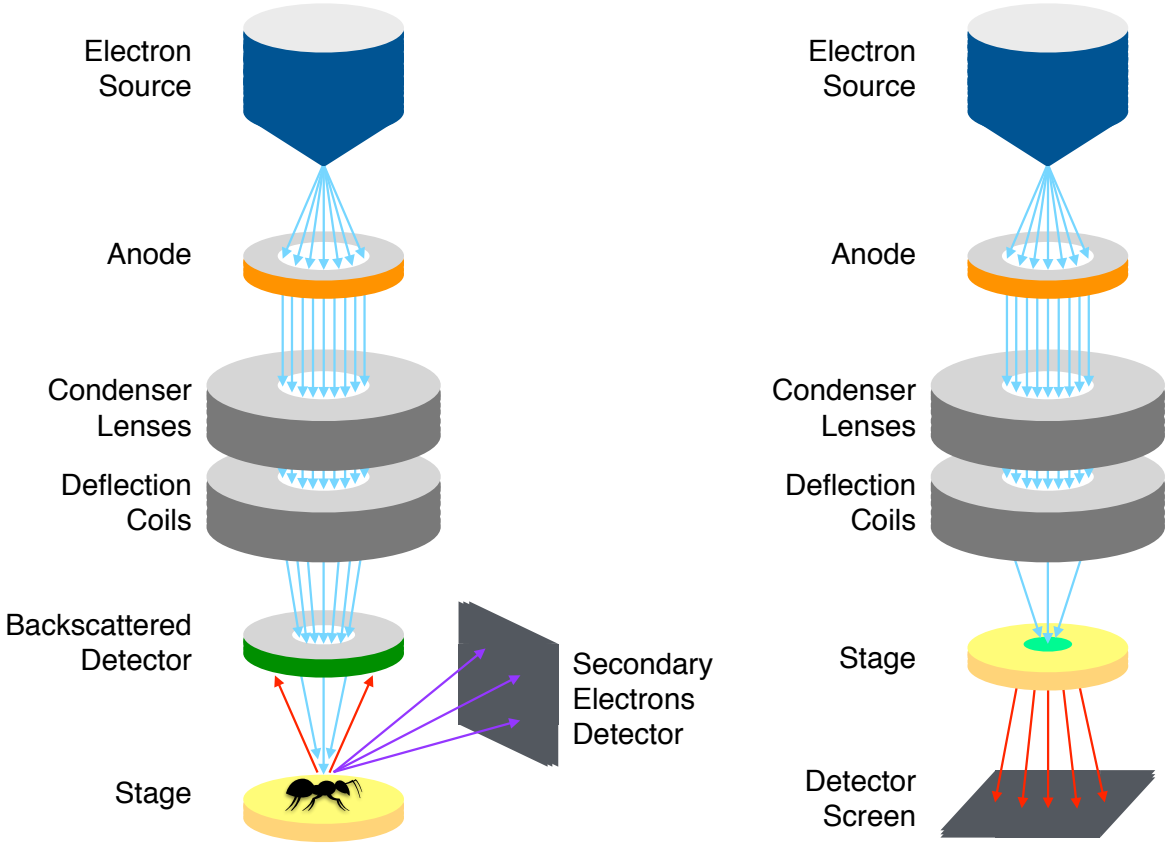
tic, according to whether energy is transferred from the incident electrons to the sample particles or not, respectively. More specifically, electron interactions generate different signals (see Figure 4.11): Auger electrons (AE), secondary electrons (SE), reflected or back-scattered electrons (BSE), X-rays, photons, cathodoluminescence (CL), plasmons, transmitted electrons, etc. Each signal results from interactions of the electron beam at various depths within the sample and thus contains different information about its surface topography and composition. For example, Auger electrons and other secondary electrons with rather small energies are readily absorbed in any material and thus only those generated close to the surface can leave the sample. It follows that they give information only about the surface of a sample. On the other hand, back-scattered electrons

have the same energy as the incoming beam and thus penetrate the sample more easily. As a consequence, they provide information about a much thicker portion of the sample. Therefore, according to the type of electron microscope used and the type of signals that are detected different information can be obtained.

A typical electron microscope is composed by: (i) an electron source (gun) to generate the beam, (ii) two or more stages of electromagnetic lenses to align and collimate the beam, (iii) deflection coils to deviate the beam during the exposure, (iv) apertures to limit and define the beam size, (v) objective lenses to focus the beam on the sample, and finally (vi) electron detectors to provide real-time observation and image recording of the specimen surface. Basically an electron microscope column is almost equivalent to an EBL column. And in fact, by using relatively low cost accessories, it is possible to convert an electron microscope into an electron beam lithography system. This conversion is actually quite common for labs on a limited budget. The two most common types of electron microscopes are: Transmission Electron Microscope (TEM) and Scanning Electron Microscope (SEM). The schematic diagrams of a typical TEM and SEM are displayed in Figures 4.12a and 4.12b, respectively.

A fundamental difference between TEM and SEM lies on the type of particles used to create an image. Elastic interactions are manly exploited in TEM and electron diffraction methods. Instead, inelastic electron-matter interactions are predominantly used in SEM and analytical electron microscopy. TEM detects the electrons *transmitted* through a specimen to form an image, while SEM records the electrons *reflected* (emitted) from the surface of a specimen. As a result, TEM offers invaluable information on the inner structure of the sample, such as crystal structure, morphology and stress state information, while SEM provides information on the sample's surface and its composition. Clearly, in TEM the acceleration voltages are much higher than in SEM due to the necessity of entirely penetrate the specimen. Typical acceleration voltages range between 1 and 30 kV for a SEM and between 60 and 300 kV for a TEM.

Another difference between TEM and SEM consists in the image formation. As the name suggests, in SEM the beam of electrons is focused to a fine point and then scanned line by line over the sample surface in a rectangular raster pattern. Electrons are captured



(a) SEM. **(b) TEM.**

Figure 4.12: Schemes of a typical Scanning Electron Microscope and Transmission Electron Microscope at comparison. A typical electron microscope is composed by: (i) an electron source (gun) to generate the beam, (ii) two or more stages of electromagnetic lenses to align and collimate the beam, (iii) deflection coils to deviate the beam during the exposure, (iv) apertures to limit and define the beam size, (v) objective lenses to focus the beam on the sample, and finally (vi) electron detectors to provide real-time observation and image recording of the specimen surface. The main differences between a SEM and a TEM lies in the type of particles used to create an image and in the image formation itself. Also, TEM provide a significantly higher optical spatial resolution.

and counted by detectors at each point and the image is displayed on a computer screen. SEM allows to analyse large surface areas at a time. On the other hand, TEM uses a broad(er), static beam and so only a small area of the sample can be analysed at a time. TEM operates on the same basic principles as the light microscope. When the electron beam emerges from the specimen, objectives lenses collect and magnify the electron information. The image is then recorded by projecting the magnified electron image onto a imaging device, such as a fluorescent screen, or a sensor, such as a scintillator, connected to a CCD camera. The recorded image is basically a 'shadow image' of the specimen with its different parts displayed in varied darkness according to their density.

The darker areas of the image represent those areas of the sample that fewer electrons are transmitted through while the lighter areas of the image represent those areas of the sample that more electrons were transmitted through.

SEM provide a 3-dimensional image of the surface of the sample, while TEM provides a 2-dimensional picture of the inner structure of the sample. However, one of the most pronounced differences between the two methods is the optimal spatial resolution that they can achieve; SEM resolution is limited to 0.5 nm, while with the recent development in aberration-corrected TEM, images with spatial resolution of even less than 50 pm have been reported [156]. Moreover, TEM has a much higher magnifying power than SEM. TEM can magnify up to 2 million times compared to the 50,000 times of SEM [156,157].

Specimen to be viewed under an electron microscope may require processing to become a suitable sample. Due to the requirement for transmitted electrons, TEM samples must be very thin, generally below 150 nm, and in cases that high-resolution imaging is required, even below 30 nm (so that the thickness is comparable to the mean free path of the electrons that travel through the samples), whereas for SEM imaging there is no such requirement. SEM samples need of little or no effort for sample preparation and can be directly imaged by mounting them on an aluminium stub. For example, a quite common sample preparation - especially important for the study of specimens with the SEM - consists in a conductive coating. To prevent the accumulation of electrostatic charges at the specimen - due to the electron irradiation at which the sample is subjected during imaging - an ultrathin coating of electrically-conducting material (such as gold, gold/palladium, platinum, etc.) is deposited on its surface, either by high vacuum evaporation or by low vacuum sputter coating. [158]

In contrast, TEM sample preparation is a quite complex and technically challenging procedure that requires additional tools to perform. The samples need to be very thin, as flat as possible, and the preparation technique should not induce any artefacts (such as precipitates or amorphization) to the sample. Many methods have been developed, including electropolishing and mechanical polishing. However, more recently, focused ion beam (FIB) methods have been used to prepare thin samples from larger specimens. Because FIB can be used to micro-machine samples very precisely, it is possible to mill

very thin membranes from a specific area of interest in a sample. Often, a thick conductive coating is also deposited on top of the sample to improve contrast during imaging and provide support to the thin membrane. TEM samples are mounted on dedicated grids and holders.[156]

In general, if you need to look at a relatively large area and only need surface details, SEM is ideal. If you need internal details of small samples at near-atomic resolution, TEM will be necessary[156]. TEM allows you to observe details as small as individual atoms, giving unprecedented levels or structural information at the highest possible resolution. TEM give information about internal structures, which SEM cannot provide. However, TEM can only be used on a limited range of specimens, thin enough to let electrons pass through them, and tends to be more demanding than SEM. In particular, the thinning process is technically challenging and requires additional tools to perform. So, while SEM cannot see features to the level of detail as a TEM can, it is much faster, less restrictive, and can sometimes be performed with limited or no sample preparation.

All the devices fabricated during the course of the doctorate degree were imaged using a *FEI Nova NanoSEM 630* Scanning Electron Microscope (SEM). Typical acceleration voltage: 10 kV. Working distance: 5.5 mm. Detector: Through the Lens Detector (TLD). Mode: Secondary Electrons (SE). This type of physical characterisation was necessary to measure the dimensions of the features, establish the quality of the devices and also of the fabrication process. In a couple of occasions, however, when it became necessary to establish the internal structure of the devices, cross-sections of the samples were cut by mean of a *DualBeam Focussed Ion Beam* (FIB) System and imaged with a Transmission Electron Microscope (TEM) at the Kelvin Nanocharacterization Centre facilities (*School of Physics and Astronomy, University of Glasgow*).

4.3.2 Atomic Force Microscopy

Atomic Force Microscopy (AFM) or Scanning Force Microscopy (SFM) is a type of Scanning Probe Microscopy (SPM) for very-high-resolution imaging. Like a SEM, a SPM is an instrument used for the analysis of surface properties at the nanoscale. However,

these microscopes do not use lenses. SPMs use a physical point probe to scan a sample back and forth and collect data. Data gathered during the scanning process originate from the interaction of the atomically-sharp tip of the probe with the surface of the sample. The resulting two-dimensional grid of data points is then used to form an image on a computer screen. The first SPM was the Nobel-prize winning Scanning Tunnelling Microscope (STM) developed at the IBM Research Lab in Zurich by Gerd Binnig and Heinrich Rohrer in 1982. This was the first technology to be recognised as having atomic resolution capability and its invention triggered the development of several further SPM techniques.[159,160,161]

STM is a non-optical electron-based microscope which exploits the quantum mechanical effect of *tunnelling*[10]. It works by raster scanning an atomically-sharp metal tip over a conductive surface. When the tip is brought in proximity (typically in the 4-7 Å range) to the surface of the sample and a bias voltage is applied between the tip and the sample, electrons can tunnel from the tip to the surface or vice versa, even though they are not in electrical contact, which results in a net electron current. The amount of tunnelling current depends upon tip position, applied voltage and local density state of the sample. This provides the basis for the imaging.

The tip is mounted on a piezoelectric actuator to control its vertical position and lateral displacement, and a feedback loop circuit can be used, for example, during constant-current mode. STM is a very important technique in determining the atomic structures and electronic states of a surface. It is also very useful for studying friction, surface roughness, defects and surface reactions in materials like catalysts. However, STM is not the optimal tool to topographically map the surface of a sample. In fact, despite a sub-nanometer spatial and vertical resolution, STM is limited to very clean, stable, smooth and conductive surfaces. It also require excellent isolation from vibrations and it is extremely dependent on tip quality.[161,162,163,164]

[10]Quantum tunnelling occurs when a subatomic particle (such as an electron) passes through a potential barrier even though it does not possess enough potential energy to do it, as predicted by the laws of classical mechanics. In terms of quantum mechanics, electrons have wavelike properties that does not end abruptly at a wall or barrier, but taper off quickly. Therefore, if the barrier is thin enough, their probability function may extend into the next region and through the barrier. Given enough electrons, some will indeed move through and appear on the other side. This effect is called tunnelling.

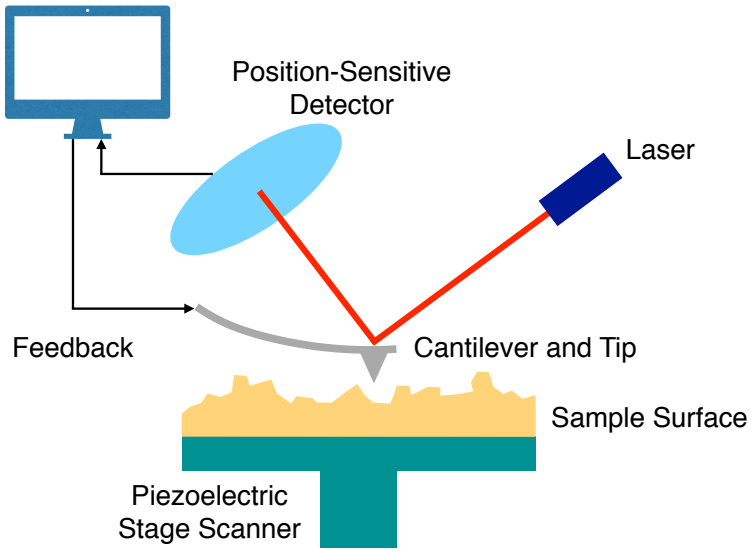


Figure 4.13: Schematic of an Atomic Force Microscope. A sharp tip is mounted at the end of a cantilever and raster-scanned over a sample surface. The deflection of the cantilever (in static mode), or the amplitude and frequency of its vibration (in dynamic modes) are monitored through a laser beam reflected off the flat, mirror-like top surface of the cantilever. This reflected laser beam is tracked by a position sensitive photo-detector (PSPD), consisting of a four-segment photo-detector, that picks up the vertical and lateral motion of the probe. During the imaging process, a feedback loop system helps to modulate and maintain constant certain parameters.

Topographic imaging at the nanoscale is one of the main scopes of AFM. AFM might not have the same atomic resolution capability of STM but it does not suffer of its limitations in terms of sample requirements. AFM has the advantage of imaging almost any type of surface, including polymers, ceramics, composites, glass, and biological samples. Also, it can be performed in a vacuum, ambient, gas or liquid environment. The latter becomes particularly relevant in certain aspects of biology, where hydrated samples need to be tested.[165]

AFM is often used in combination of SEM to fully characterise a sample. Sometimes with images generated by SEM, it can be difficult to determine the slope of a surface or the height of a feature. Conversely, AFM provides height information, making it easy to determine if surface features on a thin film are rising or falling. AFM also provides a greater level of detail than SEM on a highly smooth surface, as SEM is not as efficient in resolving subtle changes. AFM may not be able to provide information on the elemental composition of a sample, however it can determine a number of other compositional properties: including stiffness, friction, electrical forces, capacitance, magnetic forces, conductivity, viscoelasticity, surface potential, and resistance.

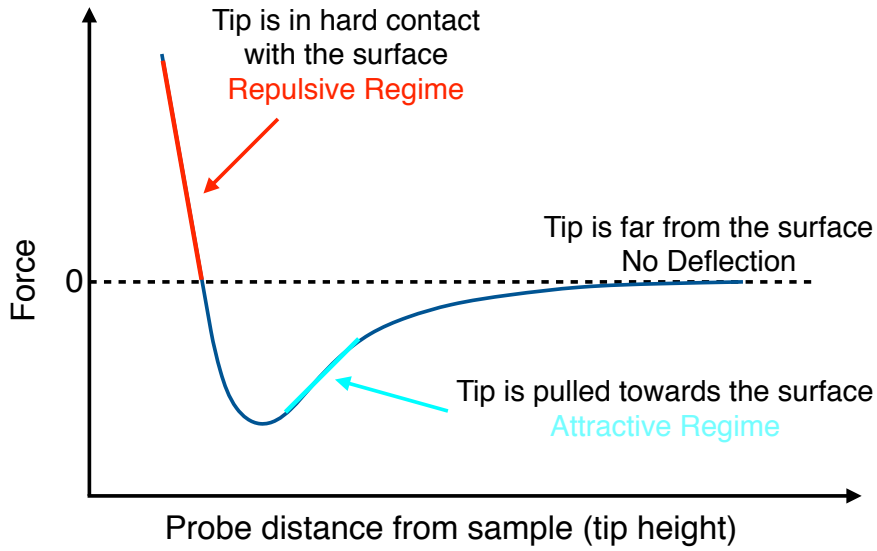


Figure 4.14: Atomic forces vs. Distance. Atomic forces change depending on the vertical distance of the probe from the sample. As the tip approaches the surface, the close-range, attractive force between the surface and the tip cause the cantilever to deflect towards the surface. However, as the cantilever is brought even closer to the surface, such that the tip makes contact with it, increasingly repulsive force takes over and causes the cantilever to deflect away from the surface.

A schematic diagram of the working principle of a AFM is displayed in Figure 4.13. Analogous to how a STM works, a sharp tip mounted at the end of a cantilever is raster-scanned over a sample surface using a feedback loop to adjust certain parameters during imaging. However, unlike STM, AFM uses atomic forces to map the tip-sample interaction and not electron tunnelling. Atomic forces change depending on the vertical distance of the probe from the sample (see Figure 4.14). As the tip approaches the surface, the close-range, attractive forces between the surface and the tip cause the cantilever to deflect towards the surface. However, as the cantilever is brought even closer to the surface, such that the tip makes contact with it, increasingly repulsive forces take over and cause the cantilever to deflect away from the surface. These forces are not measured directly, but are calculated by measuring the deflection of the cantilever[11]. The deflections towards or away from the surface are monitored through a laser beam reflected off the flat, mirror-like top surface of the cantilever. This reflected laser beam is tracked by a position sensitive photo-detector (PSPD), consisting of a four-segment photo-detector, that picks up the vertical and lateral motion of the probe.[166,167]

[11] According to Hooke's law: $F = -kx$, where F is the force, and k and x are the stiffness and the deflection of the cantilever, respectively. Therefore, by knowing the stiffness of the cantilever and its deflection it is possible to calculate the force that caused that deflection.

There are three different AFM modes used for topography imaging: one static mode, also called contact mode, and two dynamic modes, tapping mode and non-contact mode. In contact mode, the tip is dragged across the sample surface. Near to the surface of the sample, attractive forces can be quite strong, causing the tip to 'snap-in' to the surface. Therefore, contact mode usually exploits repulsive forces which means that the tip is in 'hard contact' with the surface. The contours of the surface can be measured by either measuring the deflection of the cantilever or using a feedback system that adjusts the height of the cantilever to maintain a constant deflection. In tapping mode the cantilever vibrates near its resonance frequency with an amplitude of up to 200 nm, touching the surface of the sample at every oscillation. Atomic forces cause the amplitude to decrease as the tip gets close to the surface, and the height of the cantilever adjusts through the feedback loop to keep the amplitude constant. Instead, in non-contact mode, the tip vibrates slightly above its resonance frequency, very close to the surface of the sample but without touching it. The amplitude of oscillation is typically a few nanometers (< 10 nm) down to a few picometers. In this regime, the probe measures the Van der Walls forces which tend to decrease the resonant frequency of the cantilever. The feedback loop system helps to maintain the oscillation frequency constant by adjusting the distance from the tip to the sample. For all the modes, the topographic image of the surface sample is obtained by recording the distance between the tip and sample at each point.[168] Non-contact mode AFM does not suffer from tip or sample degradation effects. Tapping mode results in less damage to the sample than contact mode and is more accurate than non-contact mode when moisture is present on a sample.

The atomic force microscope is a powerful tool that is invaluable if you want to measure incredibly small samples with a great degree of accuracy. Unlike rival technologies it does not require either a vacuum or the sample to undergo treatment that might damage it. One of the major downsides is the single scan image size, which is of the order of 150x150 micrometers, compared with millimetres for a scanning electron microscope. Another disadvantage is the relatively slow scan time, which can lead to thermal drift on the sample.[168]

4.3.3 Microspectrophotometer

A UV-Visible-NIR microspectrophotometer is a scientific instrument used to measure the optical spectra of microscopic samples. It consists of a microscope, capable of operation in transmission or reflection mode, combined with dispersive optics and a CCD detector for spectral measurements. The dispersive element is used to separate the light into its constituent wavelengths which are then detected by the image sensor. Microspectrophotometers are very flexible instruments and can be configured to measure the transmittance, absorbance, reflectance, polarisation, fluorescence and photoluminescence spectra of sample areas ranging from 20 to 120 microns[169].

The optical properties of hexagonal nanohole arrays were measured in transmission mode using a *Foster+Freeman ffTA/MS Microspectrophotomer*. The instrument was calibrated before each recording with an optical transmission filter manufactured from glass doped with a mixture of rare-earth elements (Didymium = Neodymium + Praseodymium). Furthermore, before each transmission measurement baselines must be acquired in either bright and dark conditions. After these initial calibration steps are complete, the filter is placed on the microscope stage and aligned using the camera. Data was collected from a spot size of 100 μm with unpolarised halogen-bulb light, colour temperature 6000 K, wavelength range 400 nm to 1000 nm (no IR blocking filter). Illumination was set to bright-field mode at normal incidence. Collimator was used to ensure collimated light was hitting the surface of the arrays. An objective lens with a optical magnification of 4.0X and numerical aperture (NA) of 0.25 was used to collect the light. The software automatically remove the dark background and normalise the light to the spectrum from the white light source. The normalised transmission spectrum is then displayed on the computer and can be exported for further analysis.

4.4 Summary

This chapter provided an overview of the techniques underlying the design, fabrication and characterisation of the structured photonic materials that are presented in this Thesis. A brief description of the FDTD technique has been outlined with a focus on the simulation software: Lumerical FDTD Solutions. All devices presented in this Thesis have been simulated using Lumerical FDTD Solutions which has been an essential tool in the design and optimisation of the nanostructures. The fabrication techniques employed to make the devices presented in this work have also been outlined in this chapter. Further detail on the specifics of the fabrication processes will be explored in subsequent chapters.

Physical and optical characterisation techniques have been described and their working principle outlined. Electron microscopy was used to obtain high-resolution images of the samples to either characterise the in-plane dimensions of the features, such as hole diameters and periodicity, or to investigate specific cross-sections. Atomic force microscopy was used to take topographic images of the samples and thus characterise the vertical dimensions of the nanostructures, such as hole depths. Microscpectrophotometry was necessary to characterise the optical spectra of the plasmonic devices.

Chapter 5

2D Hexagonal Nanohole Arrays: Analysis of the Starting Structure

In this chapter, plasmonic colour filters based on a single, optically-thick aluminium layer patterned with periodic hexagonal nanohole arrays (HNAs) are examined. According to literature, these nanostructures are the most promising architectures to replace integrated CFAs in CMOS image sensor applications and therefore they have been chosen as the starting point for the development of novel and more efficient plasmonic colour filters.

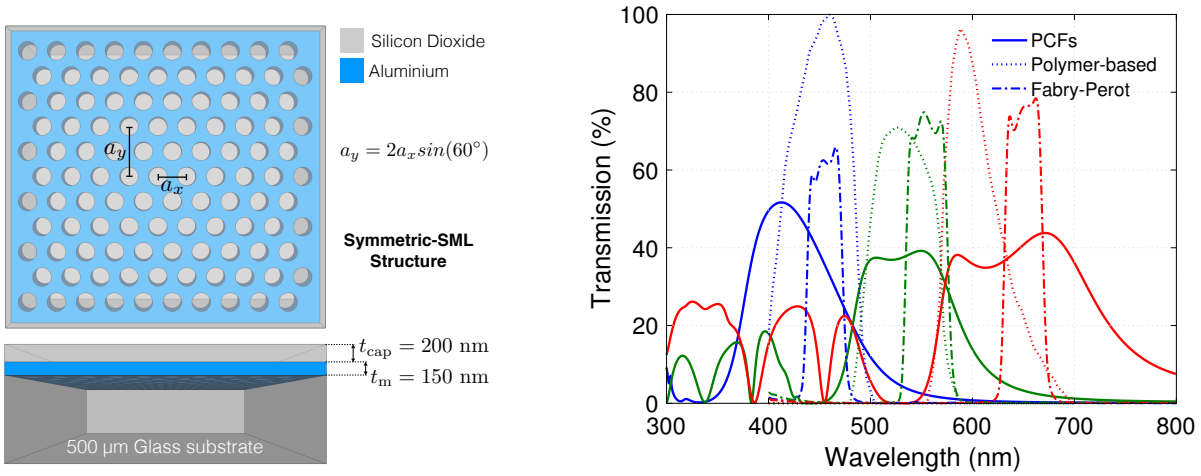
Section 5.1 introduces the state-of-the-art for single metal layer HNAs and compares the spectral responses of the three RGB filters with commercially available alternatives. Section 5.2 highlights the characteristic spectral features of periodic hexagonal nanohole arrays, correlating the appearance of specific minima in transmission with the excitation of SPPs and the emergence of diffractive effects. Section 5.3 is a detailed parametric analysis of single metal HNAs and presents the dependence of the optical response of the filters on their geometrical and constitutive parameters, namely diameter, metal thickness, and also cladding and hole filling materials. Electromagnetic near-field patterns at points of interest are plotted and examined. Finally, the main observations and remarks are recapitulated in Section 5.4.

5.1 Introduction

Single metal layer plasmonic filters based on periodic hexagonal arrays of subwavelength holes have been analysed in previous literature. However, those studies had the tendency to focus mainly on general behavioural trends, often in a restricted range of values and mostly limited to the transmission. This chapter, instead, wants to supply a more complete and broader review on this particular type of plasmonic filters. The final objective of the simulation studies presented in this chapter is to gain enough insights so that targeted modifications to improve the passband characteristics of the filters can be applied. It will be demonstrated in Chapters 6 and 7 that the detailed analyses of each parameter dependence have effectively provided a better understanding of the physical mechanisms involved in the transmission process and led towards higher and narrower transmission features.

In the last decades, PCFs based on periodic arrays of nanoholes in a single, optically thick metal layer quickly became one of the most promising alternatives to polymer-based filter technologies[13,14,15,16]. The most common and exploited architecture corresponds to a 150-nm aluminium hexagonal nanohole array sandwiched between a bottom half-space and a top 200-nm silicon dioxide layers[15,16]. This particular nanostructure was therefore chosen to be the starting point for the development of new and more efficient PCFs. The schematic top and side perspective views of this type of filter is displayed in Figure 5.1a and, because of its symmetry along z-, in terms of top and bottom *cladding* materials, from hereinafter it will be referred to as *Symmetric Single Metal Layer* (*Sym-SML*) PCF.

In Figure 5.1b, the simulated optical transmissions of three Sym-SML arrays (solid lines) - having different periodicities to selectively filter the blue (a_x = 240 nm), green (a_x = 340 nm) and red (a_x = 420 nm) part of the visible spectrum - are plotted and compared to the RGB spectral sensitivities of a commercial photo camera[170] (dotted lines) and to the RGB optical efficiencies of commercially available Fabry-Pérot filters[171] (dash-dot lines). It is evident the PCFs lack transmission efficiency when compared to these other two technologies. Moreover, consider a target range of acquisition in the visible spectrum of approximately 300 nm (roughly from 400 nm to 700 nm as shown



(a) Top and side perspective view **(b)** Comparison RGB tristimulus

Figure 5.1: Single, optically-thick Al layer HNA and optical response. (a) Schematic top and side perspective view of a 150-nm Al hexagonal nanohole array sandwiched between a bottom *half-space* - 500-μm - glass substrate and a top 200-nm SiO_2 cap layer. The parameters a_x and a_y represent the periodicities along the x- and y-direction, respectively, and their relationship is reported on the right-hand side of the top view. The nanostructure is here-on referred to as *Symmetric Single Metal Layer* (Sym-SML) because the top and bottom interfaces are composed of the same pair of materials. (b) Comparison of the RGB transmission curves of three Sym-SML arrays (solid lines) - having different periodicities to filter the light at different wavebands - with the RGB spectral sensitivities of a Sony DXC 9000 camera [170] (dotted lines) and the RGB transmission efficiencies of commercially available Fabry-Pérot filters [171] (dash-dot lines). The blue plasmonic filter is given by an array periodicity a_x of 240 nm and a diameter $d = 140$ nm, while the green and red plasmonic filters have a_x of 340 nm, $d = 180$ nm and a_x of 420 nm, $d = 280$ nm, respectively. PCFs lack in transmission efficiency. Moreover, their passband characteristics are relatively broad and do not satisfy the requirements for multispectral imaging.

in Figure 5.1b) and assume that we want to increase the colour accuracy for example by using twice as many filters. This means that, to avoid a significant overlap between adjacent wavebands, the FWHM of the filters should probably be of approximately 50 nm (or less if we want to use more filters). Therefore, the passband characteristics of PCFs are relatively broad and do not satisfy the requirements for multispectral imaging.

In the following sections, ways to improve the transmission efficiency and the colour discrimination of Sym-SML PCFs are investigated. Their spectral features are analysed, the electromagnetic (EM) near-field patterns at specific points of interest are plotted, and a systematic and detailed study on the dependence of the optical transmission on their structural parameters - namely periodicity, diameter, metal thickness, dielectric environment and hole filling - is presented.

5.2 Characteristic Traits in the Optical Spectra

Single subwavelength holes - whose diameter d is smaller than half wavelength of light - diffract light uniformly into a half sphere around the aperture[116]. A scheme of the diffraction pattern of a nanohole is displayed in Figure 5.2a. The light diffracted by the sharp edges of the nanoholes generates wavevectors also in the direction parallel to the surface of the film. This allows a portion of the incident light to excite SPPs. However, even if a single subwavelength aperture in a metallic layer displays plasmonic properties, the EOT phenomenon needs the 'array' to exist. In fact, it is the collective resonant behaviour of all the holes together that boost the transmission efficiency and thus the EOT phenomenon would not be possible without the array.

The diffraction of light from a periodic structure also causes the appearance of anomalies at well-defined wavelengths. SPPs and diffractive effects such as Rayleigh Anomalies (RAs) are important influences on the EOT spectra of periodic arrays[172]. Both of them are closely correlated to the periodicity of the array and their position in wavelength can be easily evaluated through a pair of simple equations. SPPs have a resonant character and appear when the Bragg coupling condition is satisfied, i.e. when the real part of the SPPs propagation constant k_{SPP} matches the sum of the incident light wavevector with one of the reciprocal wavevectors G_{ij} provided by the periodicity of the array:

$$\mathrm{Re}\left[k_{\mathrm{SPP}}\right] = \left|k \sin\theta + G_{\mathrm{ij}}\right| \tag{5.1}$$

where k is the wave vector of the incident light and i, j are integers with $i \geq 0$, $j \geq 1$.

On the other hand, RAs are non-resonant spectral features that occur at the onset of the (i, j) diffraction order of the periodic array, i.e. when:[173]

$$\frac{\omega}{c_0}\sqrt{\epsilon_d} = \left|k \sin\theta + G_{\mathrm{ij}}\right| \tag{5.2}$$

where ϵ_d is the permittivity of the medium in which the light is traveling before impinging on the array.

For light normally incident onto the array ($\theta = 0$), the wavelengths $\lambda_{\mathrm{min,ij}}$ and $\lambda_{\mathrm{RA,ij}}$ at which the conditions 5.1 and 5.2, respectively, are met can be written as:

$$\lambda_{\mathrm{min,ij}} = \frac{\sqrt{3}a_x}{2\sqrt{i^2+j^2+ij}}\, n_{\mathrm{SPP}}|_{@k_{\mathrm{SPP}}=G_{\mathrm{ij}}} \tag{5.3}$$

$$\lambda_{\mathrm{RA,ij}} = \frac{\sqrt{3}a_x}{2\sqrt{i^2+j^2+ij}}\, n_{\mathrm{d}}|_{@k_{\mathrm{SPP}}=G_{\mathrm{ij}}} \tag{5.4}$$

where n_{SPP} (refer to Equation (3.33)) and n_{d} are the indices of refraction of the SPPs and of the dielectric the light is travelling through before impinging on the array. The RIs are frequency dependent and thus the values used to evaluate the wavelengths are the ones at which the conditions are met.

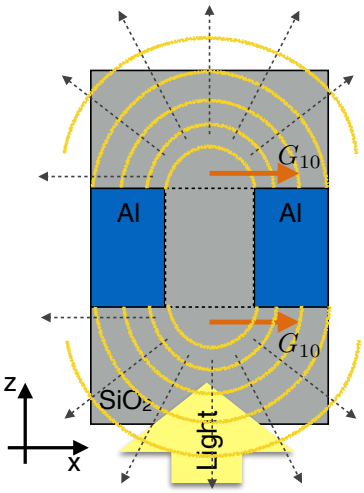
When Equations 5.1 and 5.2 are satisfied, minima in transmission T appear. $\lambda_{\mathrm{RA,ij}}$ and $\lambda_{\mathrm{min,ij}}$ can be tuned over a large spectral range by changing the surrounding dielectric environment or by changing the excitation conditions [173]. Unlike $\lambda_{\mathrm{RA,ij}}$, $\lambda_{\mathrm{min,ij}}$ can be shifted in wavelength also by changing the material that composes the array. The transmission maxima, or EOT peaks, appear then red- shifted in wavelength with respect $\lambda_{\mathrm{min,ij}}$. Fano associated the excitation of SPPs along the surface of a periodic structure with the origin to the Wood's anomaly [124,128,129]. Therefore $\lambda_{\mathrm{min,ij}}$ identifies also with the beginning of a diffuse anomaly. As a consequence, the diffuse anomaly actually corresponds to the EOT band.

5.2.1 The bottom interface

Consider the bottom aluminium/silicon dioxide (Al/SiO_2) interface of the Sym-SML structure (see Figure 5.2b). This can be considered as an interface between two half-space materials because even if the thicknesses of both the layers are finite, the SPP penetration depths δ_{SPP} inside the metal and the dielectric - $\delta_{\mathrm{SPP},m}$ and $\delta_{\mathrm{SPP},d}$ respectively[1] - are both shorter than the Al and SiO_2 thicknesses, t_{Al} and $t_{\mathrm{SiO_2}}$, respectively.

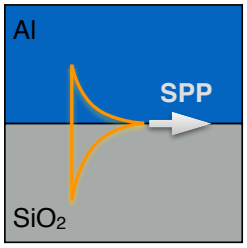
Figure 5.2 highlights the correlation between the excitation of SPPs, the occurrence of RAs, and the appearance of minima in transmission for the three RGB filters. The letters A, B, C indicate the position of the minima $\lambda_{\mathrm{min,10}\downarrow}$, where the $\downarrow$ arrow symbol

[1] Refer to Equations (3.39)

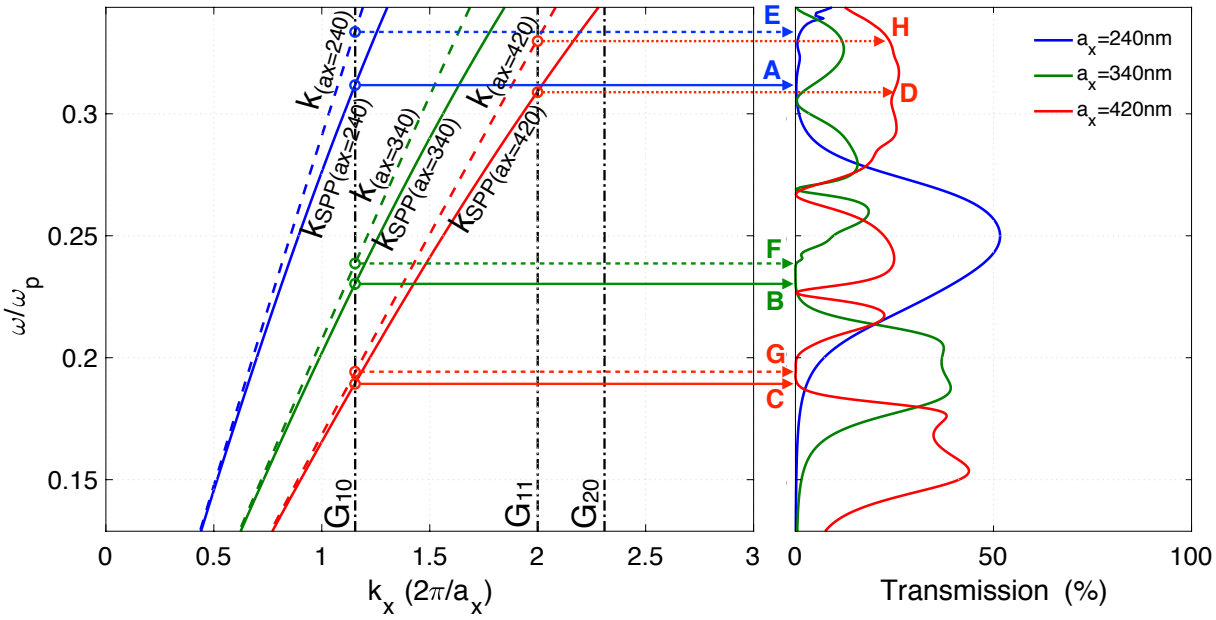


(a) Light diffraction pattern of a nanohole.

$$\delta_{\mathrm{SPP},Al} \ll t_{Al}$$
$$\delta_{\mathrm{SPP},SiO_2} \ll t_{SiO2}$$



(b) SPPs at the bottom Al/SiO_2 interface.



(c) Minima in transmission, RAs and SPPs at the top interface.

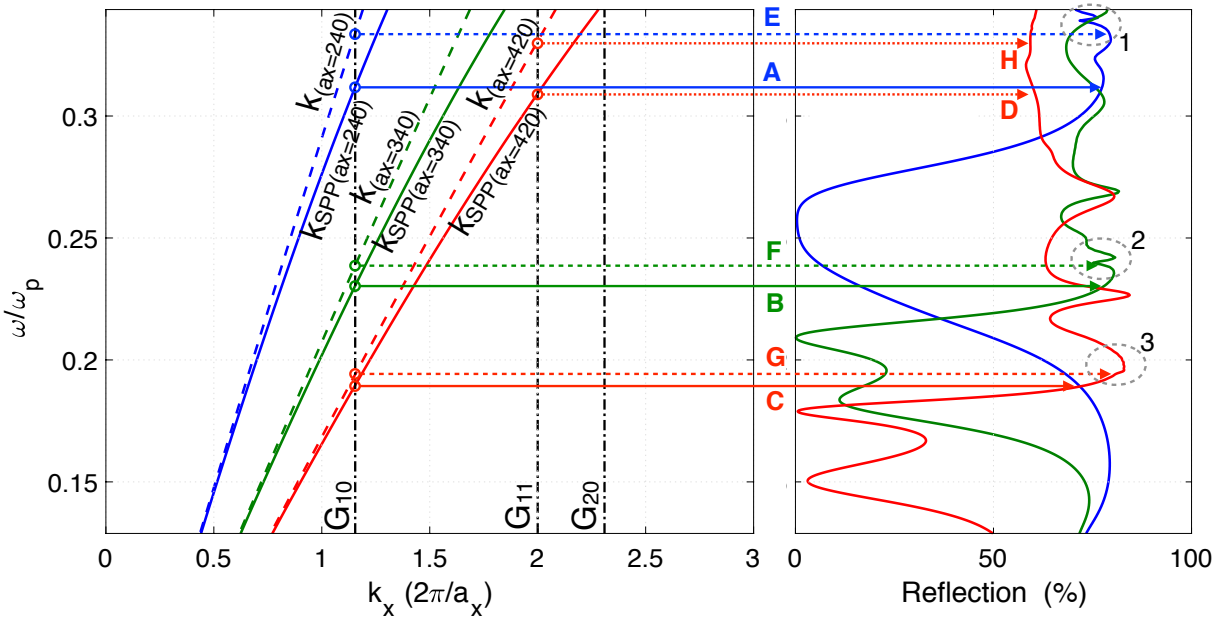
Figure 5.2: Minima in transmission, SPPs and diffractive effects at the bottom interface of the Sym-SML structure. (a) Light diffraction pattern of a single subwavelength hole. The sharp edges of the hole generate wavevectors also in the direction parallel to the surface of the film. (b) Schematic diagram of SPPs at the bottom Al/SiO_2 interface. The interface can be considered a single interface because, despite the finite thicknesses of the layers, the SPP penetration depths δ_{SPP} in the Al and SiO_2 are both smaller than the thicknesses t_{Al} and $t_{\mathrm{SiO_2}}$. (c) Correlation between the excitation of SPPs, the occurrence of RAs, and the appearance of minima in transmission. The letters A, B, C indicate the position of the minima $\lambda_{\mathrm{min},10\downarrow}$, where the $\downarrow$ symbol indicates the correlation to the bottom interface. The letters E, F, G indicate instead the position of $\lambda_{\mathrm{RA},10}$. D = $\lambda_{\mathrm{min},11\downarrow}$, H = $\lambda_{\mathrm{RA},11}$. Left graph: the solid blue, green and red curves represent the SPP dispersion relations at the bottom Al/SiO_2 interface, while the respective blue, green and red dashed lines represent the light line $k = \omega/c$, normalised to three different periodicities - blue$\rightarrow$ $a_x = 240$, green$\rightarrow$ $a_x = 340$, red$\rightarrow$ $a_x = 420$. The vertical, dashed-dotted black lines represent the additional wavevectors G_{ij} provided by the periodicity of the array. The angular frequency ω is normalised to the plasma frequency of Al $\omega_p = 12.04$ eV[174]. Wavevectors are normalised by $2\pi/a_x$. Right graph: the solid blue, green and red curves represent the transmittance of the Sym-SML structure for the three different periodicities.

indicates the correlation to the bottom interface. The predicted positions for $\lambda_{\mathrm{min},10\downarrow}$ are based on the calculations for a planar interface. Despite the presence of the nanoholes, that seems to be a good approximation to estimate their position. The letters E, F, G indicate instead the position of the RAs, $\lambda_{\mathrm{RA},10}$. Finally, the letters D and H indicate the positions of $\lambda_{\mathrm{min},11\downarrow}$ and $\lambda_{\mathrm{RA},11}$, respectively, for the $a_x = 420$ nm case. For these last two points, there is no clear evidence of the correspondence with the appearance of minima in the transmission spectra. This could be due to the fact they they appear at wavelengths lower than the zero-order regime ($\lambda_{\mathrm{RA},10}$) thus their contribution is 'masked' by other physical mechanisms or possibly because the contribution of the (1,1) diffraction order is weaker than the (1,0) one.

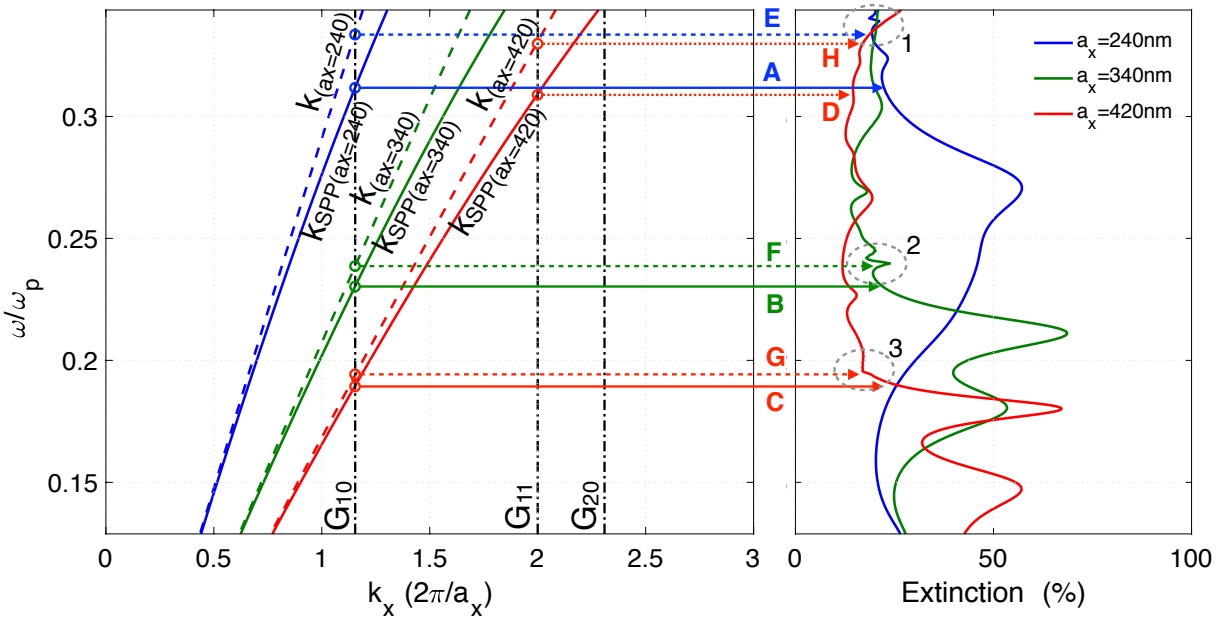
For each periodicity, the EOT passband starts at $\lambda_{\mathrm{min},10\downarrow}$. At higher frequencies, a *zero-T* band can be identified, i.e. a range of wavelengths where the transmission is (or almost) zero. The beginning of these zero-T bands can be associated with the occurrence of the RAs for the (1,0) diffraction order while their end, and thus the beginning of the EOT passbands, with the excitation of SPP modes. The distance between $\lambda_{\mathrm{RA},10}$ and $\lambda_{\mathrm{min},10\downarrow}$ increases with periodicity, and therefore the shorter the periodicity the wider the zero-T band that precedes the EOT passband.

Deeper insights can be gained from the reflectance R and the extinction spectrum E. The reflectance and the extinction efficiencies for the three Sym-SML RGB filters are plotted in Figure 5.3. The extinction spectrum is obtained as E = 100 - R - T and represents the sum of absorption and scattering contributions. It provides a good measure of absorbance only in regions where no propagating diffracted orders are allowed,[85] i.e. only in the zero-order regime, or, in other words, at wavelengths longer than $\lambda_{\mathrm{RA},10}$. According to the reciprocity theorem, the transmittance is the same whether the light is incident on the top or bottom side in the zero-order regime. However, as a direct consequence of the extinction, reflectance data exhibit different behaviour according to which side the light is impinging on[18,85].

Despite the mismatch between sides, studies found correlations between traits in transmittance, reflectance and extinction[85,175,176]. Peaks in transmission in the EOT passband (zero-order regime) are associated with reflectivity minima and absorbance maxima. Sim-



(a) Maxima in reflection, RAs and SPPs at the top interface.



(b) Minima in extinction, RAs and SPPs at the top interface.

Figure 5.3: SPPs excitation and RAs in the reflection and extinction spectra of Sym-SML structures. Distinctive traits associated with the excitation of SPPs and the occurrence of RAs can be found also in the reflection and extinction spectra of the structure. The letters A, B, C indicate the position of the maxima (minima) in reflection (extinction) corresponding to the values of the $\lambda_{\mathrm{min},10\downarrow}$ in transmission as seen in Figure 5.2. The letters E, F, G indicate instead the positions of the $\lambda_{\mathrm{RA},10}$, which appear as maxima in reflection and minima in extinction. D = $\lambda_{\mathrm{min},11\downarrow}$, H = $\lambda_{\mathrm{RA},11}$. The numbers 1-3 indicate sudden changes in the optical spectra. Left graphs: same as described in Figure 5.2. Right graphs: the solid blue, green and red curves represent the reflection (top graph) and extinction (bottom graph) spectra of the Sym-SML structure for the three different periodicities.

ilarly, transmission minima in the zero-order regime are associated with reflectivity maxima and absorbance minima. There are slight differences in the positions of the different extrema but those are expected since they represent different responses of the system [85].

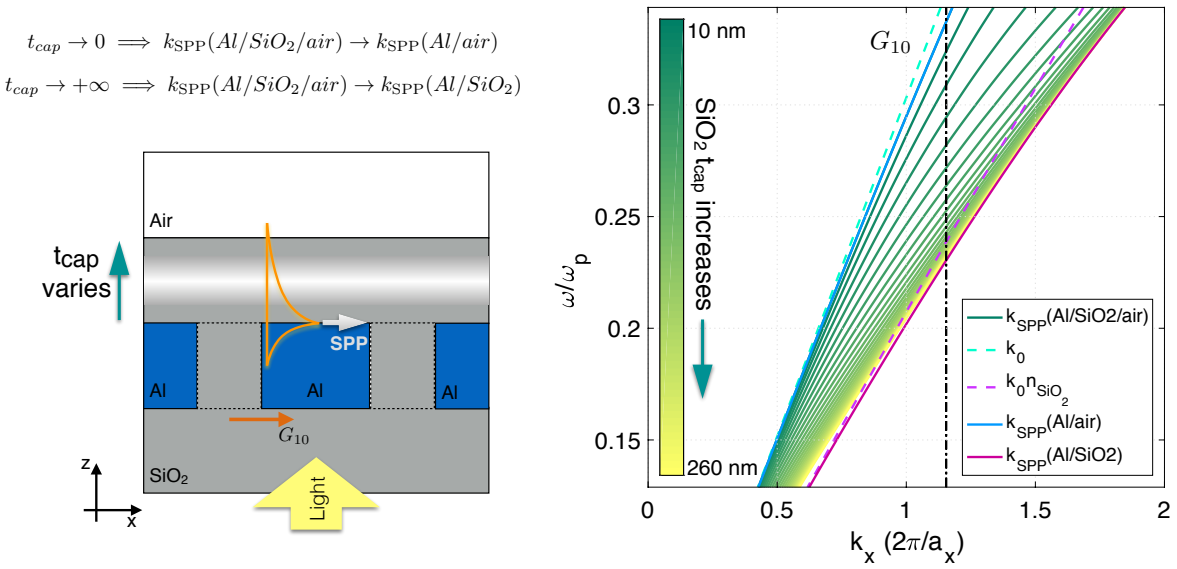
The maxima absorption features in correspondence to peaks in transmission are consistent with the excitation of SPPs. Strong localised fields at the metal surface appear when the incident light couples to a SPP mode. This field enhancement aids the transmission process, however, it is accompanied by losses in the metal. Therefore, enhanced absorption is expected for the same conditions that give enhanced transmission [85].

The occurrence of RAs is characterised by distinctive 'edges', i.e. sudden changes, in either the transmission, reflection and extinction spectra [176] - marked 1-3 in Figure 5.3. The sudden increases in transmission relate to sudden decreases in reflection and to sudden increases in extinction [176]. It can be observed in Figure 5.3 that the distance between the edges and the calculated RAs position decreases with periodicity (or wavelength). In fact, for $a_x = 420$ nm it appears that the $\lambda_{\mathrm{RA},10}$ corresponds exactly to the edge itself. On the other hand, the minima in transmission at the condition of excitation of the SPP modes seem to not have an explicit correspondence in the reflection and extinction spectra, in particular for longer periodicities (wavelengths).

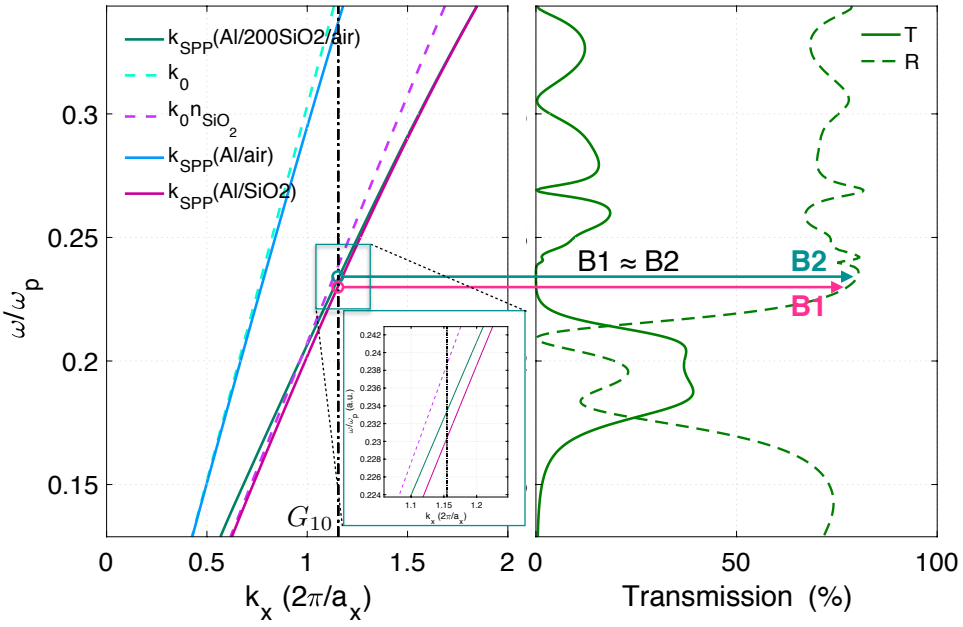
5.2.2 The top interface

Consider now the top Al/SiO_2 interface of the Sym-SML structure. The Al layer can again be considered as a half-space material. However, at wavelengths longer than approximately 480 nm, the SPP penetration depth $\delta_{\mathrm{SPP,d}}$ in the silicon dioxide is greater than the thickness of the SiO_2 cap layer $t_{\mathrm{cap}} = 200$ nm. This means that the tail of the SPPs at the top Al/SiO_2 interface can 'feel' the presence of the surrounding air environment above the SiO_2 cladding layer. It follows that the propagation constant of the SPPs at the top interface differs from the single interface calculation.

When the thickness of the cap layer is shorter than about two-three times the SPPs penetration depth inside the material, the top interface can be modelled as an IIM stack. The IIM SPPs at the top interface have been evaluated numerically. Figure 5.4a shows



(a) Schematic representation of SPPs at the top IIM interface and dispersion relations.



(b) Comparison of the minimum $\lambda_{\text{min},10}$ at the bottom and top interfaces.

Figure 5.4: SPPs at the top IIIM interface and minima in transmission. Array geometrical parameters: $a_x = 340$ nm and $d = 180$ nm. (a) Right: scheme of the SPPs at the top IIM interface. Left: Plot of the numerical solutions of the SPPs at the top IIM interface as a function of the SiO_2 cap thickness t_{cap}. t_{cap} varies from 10 nm to 260 nm. For small thicknesses the solutions tend to the SPPs propagation constant at the Al/air interface. As the thickness increases and becomes comparable to the SPPs penetration depth inside the dielectric, the solutions tend to the SPP propagation constant at the Al/SiO_2. (b) Comparison of the minimum $\lambda_{\text{min},10}$ at the bottom and top interfaces. The SiO_2 cap thickness t_{cap} is comparable to δ_{SPP} inside SiO_2 and thus it is hard to distinguish the two contributions because the IIM dispersion relation almost matches the one for the ideal single flat interface. The angular frequency ω is normalised to the plasma frequency of Al $\omega_p = 12.04$ eV[174]. Wavevectors are normalised by $2\pi/a_x$.

(left) a schematic representation of the SPPs at the top interface and (right) a plot of the respective IIM numerical solutions - normalised by $2\pi/a_x$ with $a_x = 340$ nm - in function of the SiO_2 cap thickness t_{cap} which varies from 10 nm to 260 nm. For small thicknesses the solutions tend to the SPPs propagation constant at the Al/air interface. As the thickness increases and becomes comparable to the SPPs penetration depth inside the SiO_2 , $\delta_{\text{SPP,SiO}_2}$, the solutions tend to the single interface value $k_{\text{SPP(Al/SiO}_2)}$. Note that the solutions do not equal $k_{\text{SPP(Al/SiO}_2)}$ as soon as $t_{\text{cap}} > \delta_{\text{SPP,SiO}_2}$. This is because $\delta_{\text{SPP,SiO}_2}$ is evaluated as the distance at which the electric field equals $1/e$, i.e. about a third of its original value, not when it becomes zero. Note also that the IIM solutions converge faster to the single interface solution $k_{\text{SPP(Al/SiO}_2)}$ at shorter wavelengths (higher frequencies). That is because $\delta_{\text{SPP,d}}$ is smaller in this regime and thus the condition $t_{\text{SiO}_2} \gg \delta_{\text{SPP,SiO}_2}$ becomes true for thinner cap layers.

Figure 5.4b compares the position in wavelength of $\lambda_{\text{min,10}\downarrow}$ and $\lambda_{\text{min,10}\uparrow}$ at the bottom and top interfaces, respectively, for the Sym-SML structure having an array periodicity $a_x = 340$ nm. The SiO_2 cap thickness $t_{\text{cap}} = 200$ nm is comparable to the SPPs penetration depth inside SiO_2 and thus it is hard to distinguish the two contributions because the IIM dispersion relation almost matches the one for the ideal single flat interface and thus $\lambda_{\text{min,10}\uparrow}$ lies within the zero-T band. However, it will be demonstrated later on in this chapter that the excitation condition of IIM SPPs can interfere with the length of the zero-T band - if it happens at shorter wavelengths than $\lambda_{\text{RA,10}}$ - but more importantly also with the optical response in the EOT band when the index of refraction of the top cladding layer is higher than the refractive index of the substrate.

5.3 Parametric Analysis

In this section, a parametric analysis to study the influence that different geometric and physical parameters have on the optical response of 2D hexagonal Sym-SML arrays is presented. This simulation study is used to analyse the device performance within different sets of parameters to identify the best solution for a specific application and to establish educated guesses for possible improvements and developments. For every parameter, the

performances will be evaluated in terms of: (i) efficiency, (ii) optical bandwidth of the filter and (iii) stability to process variations. An analysis of the physical mechanisms involved in the transmission process will also be attempted by identifying characteristic traits and behavioural patterns.

5.3.1 Diameter

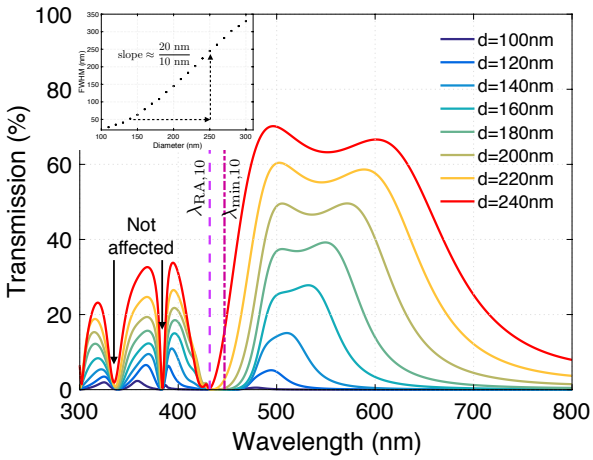
The set of plots and images in Figure 5.5 establishes the influence of the size of the apertures on the optical response of the Sym-SML structure. Figures 5.6a and 5.6b highlight instead the correlation between peaks in transmission, minima in reflection and maxima in extinction in the zero-order regime ($\lambda > \lambda_{\mathrm{RA},10}$), and compare them in terms of efficiency and position in wavelength, respectively. Evidently, increasing the size of the holes has two striking consequences: (i) it significantly increases the amount of light transmitted through the array and (ii) considerably widens the optical passband bandwidth of the filter.

The increase in transmission is a direct consequence of using larger apertures: simply more light can pass through the holes. Consider Figure 5.6a. Note that if the diameter is smaller than 100 nm the transmission efficiency T is less than 1%. For small values of diameter, the efficiency quickly increases by increasing the hole size. However, as the diameter becomes larger than the distance between two adjacent holes ($d > a_x/2$)[2], the ratio efficiency to diameter variation reduces and the transmittance seems to saturate at approximately 90%. Due to the intrinsic absorption properties of the metal, the maximum transmission efficiency of the array will never reach 100%[3].

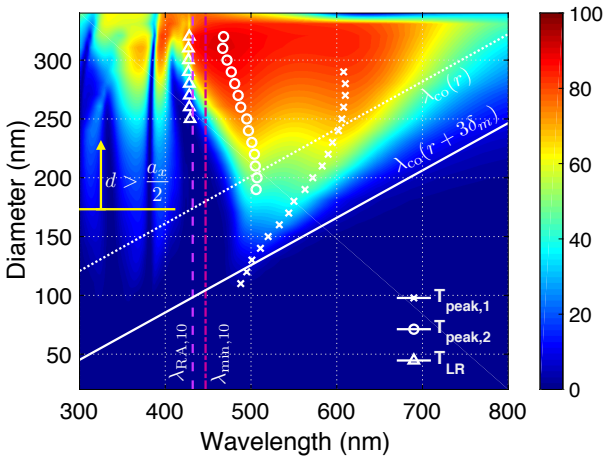
The inset in Figure 5.5a highlights the variation of the FWHM as a function of the diameter. For diameters smaller than approximately 150 nm the slope diameter to FWHM is about 1 : 1. However, above that threshold the FWHM has an increase that is approximately double the increase in diameter, i.e. if the diameter increases of 20 nm, the bandwidth will approximately be 40 nm wider. For example, if the diameter changes from

[2] $d > a_x - d$, $2d > a_x$, $d > a_x/2$

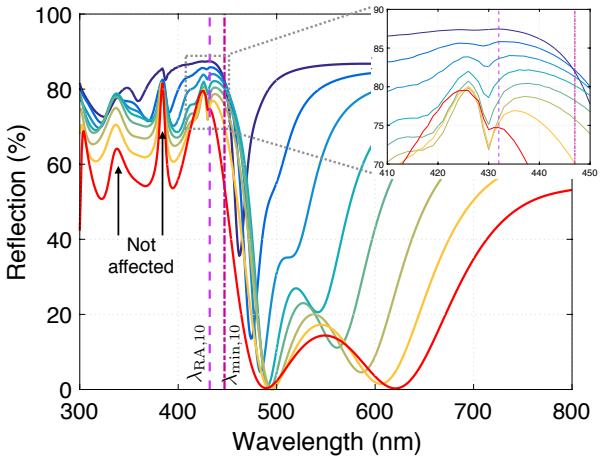
[3] When the diameter equals the periodicity, i.e. the holes physically touch each other, due to the geometry of the array and the shape of the apertures some metal is still present within the structure.



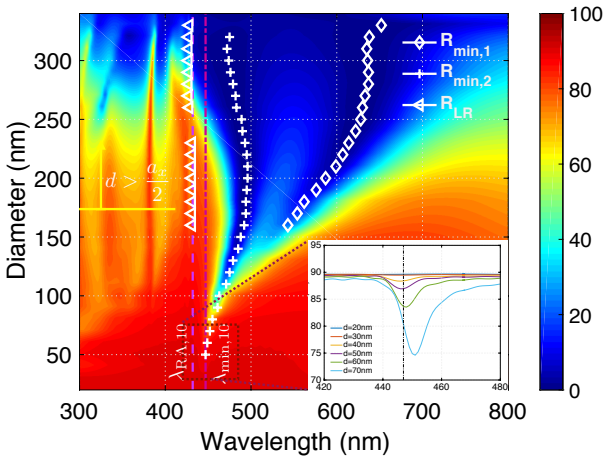
(a) Transmittance



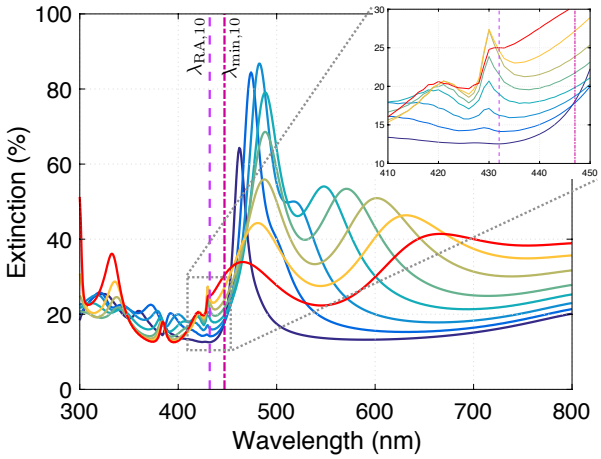
(b) T vs. λ vs. d



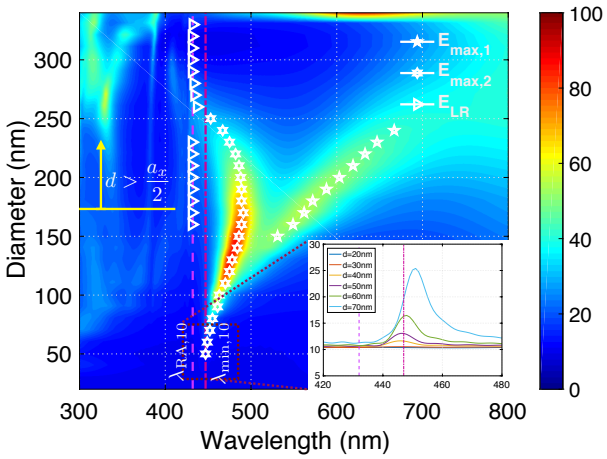
(c) Reflectance



(d) R vs. λ vs. d

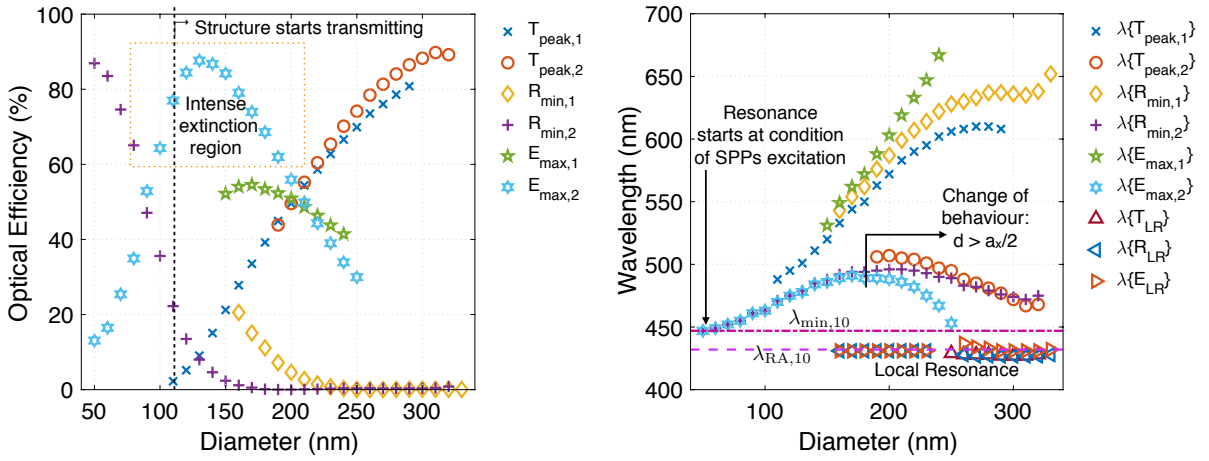


(e) Extinction efficiency



(f) E vs. λ vs. d

Figure 5.5: Influence of the size of the holes on the optical response of the Sym-SML structure. 2D plots and corresponding 2D images of the **(a)**, **(b)** transmission, **(c)**, **(d)** reflection, and **(e)**, **(f)** extinction efficiencies of a Sym-SML array as a function of wavelength and diameter of the holes. The larger the holes the higher the transmission efficiency. However, as the size of the holes increases also the FWHM of the filter increases, reducing its colour selectivity (inset in **(a)**). Insets in **(c)** and **(e)** highlights the presence of a local resonance at approximately $\lambda = \lambda_{\mathrm{RA},10}$ (indicated with the subscript 'LR' in the 2D images). Finally, insets in **(d)** and **(f)** put in evidence the origin of the resonances 1 and 2 when $d \to 0$. Simulation parameters: $a_x = 340$ nm, $t_m = 150$ nm, holes filled with SiO_2, $t_{\mathrm{cap,SiO_2}} = 200$ nm.



(a) Efficiency vs. Diameter **(b)** Wavelength vs. Diameter

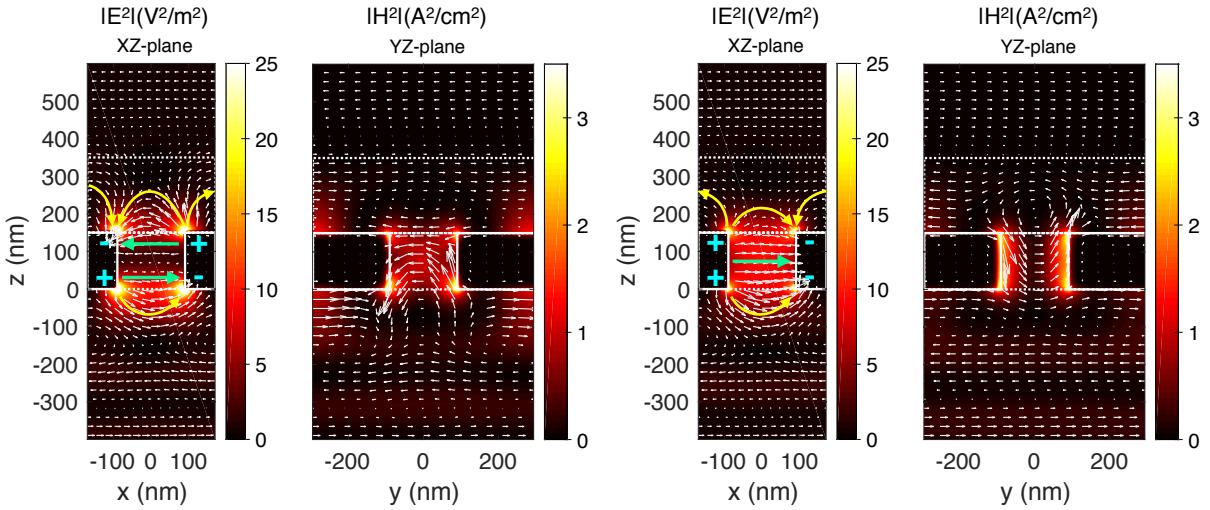
Figure 5.6: Correlation between peaks in transmission, minima in reflection and maxima in extinction in the zero-order regime as a function of the holes' size. Comparison in terms of their **(a)** Efficiency and **(b)** Position in wavelength.

180 nm to 200 nm, the FWHM will extent from approximately 100-110 nm to almost 150 nm. In other words, for a relatively small increase in diameter of about 10%[4] of its value, the bandwidth of the filter will widen as much as to cover approximately half of the total 300-nm visible region instead of only one third. Therefore, the colour selectivity of the array considerably degrades for large values of diameter. This also means that variations in the size of the holes due to the fabrication process might result in a significant increase of the FWHM of the filter.

The broadening of the bandwidth is a direct consequence of the split between the two identifiable maximum peaks in transmission, named for simplicity $T_{\text{peak},1}$ and $T_{\text{peak},2}$ and highlighted by the white cross and circle markers, respectively, in Figure 5.5b. According to Garcia-Vidal *et al.*[21], the existence of these two regimes is given by the evanescent field coupling through the holes of the SPPs at the top and bottom interfaces, which results in coupled symmetric (long-wavelength) and antisymmetric (short-wavelength) electromagnetic modes.

The set of images in Figure 5.7 represents the squared amplitude of the electric and magnetic fields at the transmission maxima $T_{\text{peak},2}$ and $T_{\text{peak},1}$, in the XZ-plane and YZ plane respectively, for a diameter $d = 180$ nm. Note that the charges' configuration reflects Garcia-Vidal *et al.*[21] observations. The short-wavelength peak ($T_{\text{peak},2}$) is the

[4]Standard etching tolerances $\leq 10\%$.



(a) $\lambda\{T_{\text{peak},2}\} = 505$ nm **(b)** $\lambda\{T_{\text{peak},1}\} = 561$ nm

Figure 5.7: Electromagnetic near-field patterns at the transmission maxima. Squared amplitude of the electric and magnetic fields at (a) $T_{\text{peak},2}$ and (b) $T_{\text{peak},1}$.

antisymmetric mode while the long-wavelength peak ($T_{\text{peak},1}$) is the symmetric mode. The antisymmetric mode display a higher concentration of the electric field at the top and bottom edges of the holes with respect the symmetric one. This translates into a higher extinction intensity.

As the diameter increases, the two peaks grow further and further apart, widening the transmission passband of the array. On the other hand, when the diameter decreases the two peaks converge to a unique value in wavelength coincident to the condition of SPP excitation $k_{\text{SPP}} = |G_{10}|$ (see insets in Figures 5.5d and 5.5f, and Figure 5.6b). In other words, the spectral location of the SPPs in the corrugated surface tends to their corresponding value for a single flat metal/dielectric interface, without holes[21]. This is because when the holes size decreases the coupling through the holes between the plasmon resonances of the top and bottom surfaces is reduced and, thus, the structure tends to behave as a flat interface with no holes, i.e. tends to resonate at a single frequency.

The two peaks display, however, a different behaviour in wavelength. As the hole size increases, $T_{\text{peak},1}$ steadily red-shifts in wavelength until it converges to a specific position. On the other hand, $T_{\text{peak},2}$ - reasonably assuming that it behaves like its counterparts in reflection and extinction since it is not easily identifiable for small diameters - red-shifts for $d < a_x/2$ (but slower than $T_{\text{peak},1}$) and then blu-shifts for $d > a_x/2$. This suggests a

change in the optical behaviour of the structure when the distance between the apertures becomes smaller than the size of the apertures.

Figures 5.5d and 5.5f display the variation in reflection and extinction of the structure as a function of wavelength and hole diameter. As highlighted in Figure 5.6, there is a clear correlation between the maximum peaks in transmission, and minima and maxima in reflection and extinction, respectively. Notice that the minima in reflection and the maxima in extinction make their appearance before the structure begins to transmit and are located at the same position in wavelength for small values of diameter. Moreover, it is interesting to observe that these two features arise exactly at $\lambda \equiv \lambda_{\mathrm{min},10\downarrow}$ in the limit $d \to 0$ (see insets of Figures 5.5d and 5.5f).

The purple vertical dashed and dashed-dotted lines represent the positions in wavelength of the RA_{10} and $\lambda_{\mathrm{min},10\downarrow}$, respectively. As expected, the RA_{10} location is consistent in all the simulations results independently of the holes' size. On the contrary, the position of $\lambda_{\mathrm{min},10\downarrow}$ appears to be in disagreement with the transmission data when the diameter becomes significantly large, $d > a_x/2$, because it does not correspond to a minimum anymore (see Figures 5.5a and 5.5b). This is probably due to the fact that the formula for the SPP propagation constant of the single flat interface does not consider the presence of the holes and therefore it becomes less accurate as the holes' size increases.

This should not come as a surprise because the holes effectively introduce 'variations' to the refractive index properties of the metallic layer. The plasmonic filter is a type of artificial composite material and thus its optical properties might be better portrayed for example by an effective medium approximation where the holes are seen as periodical cylindrical 'inclusion' within a uniform metal layer. To the best of my knowledge an analytical approximation for the dispersion relation of SPP on the surface of a 2D array of nanoholes has not been reported yet, and the SPP dispersion relation for a single flat interface is still considered the best approximation to evaluate the position of $\lambda_{\mathrm{min},10}$ outside the metal wire mesh limit of the array.

As the diameter increases, the zero-T band decreases because $\lambda_{\mathrm{min},10\downarrow}$ blue-shifts. Is the blue-shift consistent with an increase of the holes' diameter? Intuitively, in the limit

of a very large diameter, the wave vector k_{SPP} at the interface will tend to the wave vector of light in silicon oxide because the interface tends to disappear leaving a uniform silicon dioxide medium. This is consistent with the observed blue-shift. Therefore increasing the silicon oxide 'inclusions' leads to a reduction of the SPP propagation constant and thus to a smaller SPP effective RI. Note however that in the limit of very large diameter both the minima caused by the RA and the SPP cease to exist because the majority of the light simply pass through the structure.

The black arrows in Figures 5.5a and 5.5c highlights the position of two minima, and corresponding maxima, in the transmission and reflection spectra, respectively. These minima do not correspond to any of the matching conditions for the diffraction orders of the array and their positions are not affected by the variation in diameter. It can be observed in Figure 5.1b that similar minima are also present at the same positions in wavelength in the transmittance of the Sym-SML structure having periodicity $a_x = 420$ nm. This suggests that they are not correlated to the excitation of surface resonances but to a kind of 'resonant destructive behaviour' within the structure. Further considerations will be drawn later on in this section, during the analysis of the influence of a silicon cap layer and its thickness on the optical properties of the structure.

The dotted white line in Figure 5.5b represents the ideal cutoff wavelength of a nanohole milled in a perfect conductor and filled with SiO_2. The ideal cutoff wavelength is defined as $\lambda_{\mathrm{cutoff}} = \lambda_{\mathrm{co}} = 3.4 r n_{\mathrm{hole}}$,[21] where r is the radius of the hole and n_{hole} is the RI of the material inside the hole. However, in reality, studies demonstrated that the cutoff wavelength of a nanohole is larger than the limit set for a perfect conductor and depends on the type of metal layer[19,113,115]. In fact, the evanescent electric field of localised plasmon resonances penetrates the metal, making the hole appear larger than it is from an electromagnetic point of view. The penetration depth inside the metal $\delta_{\mathrm{SPP},m}$, also known as *skin depth*, can reach several tens of nanometers for some metals (and at specific wavelengths). Therefore, at the nanoscale the skin depth's effect on the hole size must be considered.

The solid white line in Figure 5.5b represents a different, effective cutoff wavelength, estimated as $\lambda_{\mathrm{co,eff}} = 3.4(r + 3\bar{\delta}_{\mathrm{SPP,Al}})n_{\mathrm{hole}}$ where $\delta_{\mathrm{SPP,Al}} \equiv \delta_m$ is the skin depth of the

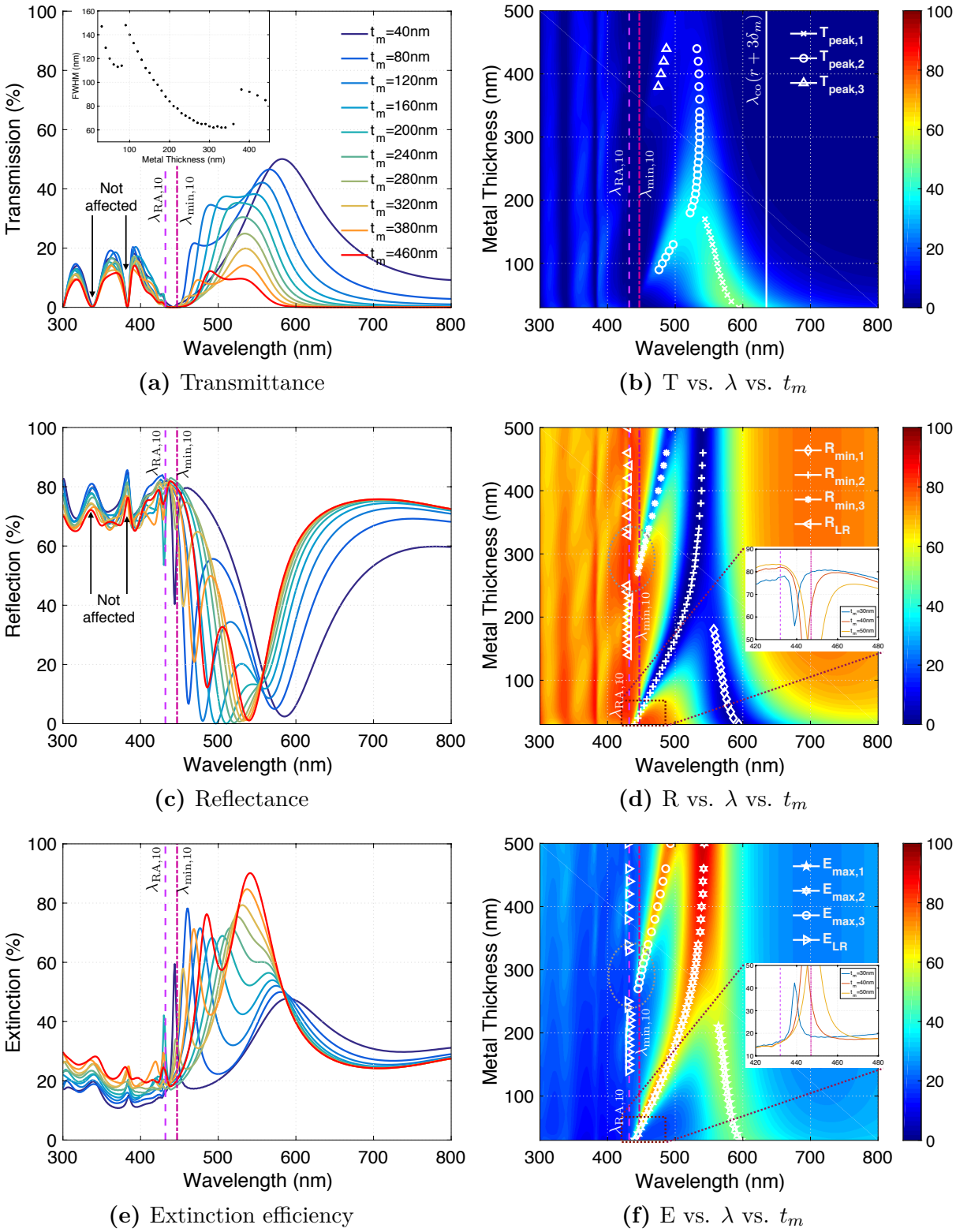
SPPs inside the aluminium. In other words, the geometrical radius has been increased of three times the *average* skin depth to take into consideration the non-ideality of the metal. The skin depth is the depth at which the intensity of the electric field inside the material falls to about 37% of its original value. Therefore, adding three times the average skin depth is basically equivalent to increasing the radius of the full evanescent tail. Given that the array does not begin to transmit until the diameter is larger than 100-120 nm and that $\bar{\delta}_{\mathrm{SPP,Al}} \approx 12$ nm in the visible range, this means that the geometrical diameter had been subjected to an increase between 70% and $\approx 30\%$ with the new formula and so the cutoff wavelength. Above $\lambda_{\mathrm{co,eff}}$ the tails of the transmission curves now remain below approximately 10%. Therefore, this new, effective cutoff seems to be a good approximation to estimate the maximum wavelength limit of the transmission passband of the filter. Clearly, the increase of the geometrical radius here is quite above the experimental values of up to 41% from literature[115]. However, this $\lambda_{\mathrm{co,eff}}$ is just an estimate to roughly evaluate the total bandwidth of the filter in wavelength and so it shall be considered.

Figures 5.5b, 5.5d and 5.5f display the variation in transmission, reflection and extinction of the structure as a function of wavelength and hole diameter. Consider the triangle markers, indicated as T_{LR}, R_{LR} and E_{LR}. These markers highlight the presence of a narrow peak (or dip in case of reflection) in the transmission, reflection and extinction spectra, almost exactly at the occurrence of RA_{10}. This feature become more visible as the diameter increases and can be associated to a Localised Resonance (LR) of the structure. Note that the position in wavelength of this local resonance is not affected by variation in the holes' size.

In summary, it has been observed that the structure displays a low stability to diameter variations and, considering the increase in transmission versus the increase in bandwidth per diameter enlargement, there is no advantage in choosing a larger diameter's size.

5.3.2 Metal Thickness

The set of plots and images in Figure 5.8 establishes the influence of the thickness of the metal layer on the optical response of the Sym-SML structure. Evidently, increasing the



(a) Transmittance **(b)** T vs. λ vs. t_m

(c) Reflectance **(d)** R vs. λ vs. t_m

(e) Extinction efficiency **(f)** E vs. λ vs. t_m

Figure 5.8: Influence of the metal thickness on the optical response of the Sym-SML structure. 2D plots and corresponding 2D images of the **(a)**, **(b)** transmission, **(c)**, **(d)** reflection, and **(e)**, **(f)** extinction efficiencies of a Sym-SML array as a function of wavelength and depth of the holes. The thicker the metal layer the lower the transmission efficiency. As the depth of the holes increases, the resonant modes converge to a unique value in wavelength. Simulation parameters: $a_x = 340$ nm, $d = 180$ nm, holes filled with SiO_2, $t_{\text{cap,SiO}_2} = 200$ nm.

depth of the holes decreases the amount of light transmitted by the filter. For a metal thickness of 500 nm the transmission efficiency lowers below 10%.

The thicker the metal layer the higher the absorption of the structure. In fact, the extinction efficiency increases with the thickness of the metal. The thickness of the metal does not vary the diffraction properties of the top and bottom surfaces. Moreover, we are considering the zero-order regime. Therefore, it is safe to assume that the increase in extinction is given solely by an increase in absorption, which is directly correlated to the higher amount of metal within the structure.

As the depth of the holes increases, the two initial resonant modes converge to a unique value in wavelength. This results in a range of thickness - between approximately 220 and 300 nm - for which only one peak is present in the transmission spectrum and thus a narrower spectral bandwidth down to 60 nm can be achieved. However, the efficiency is quite low and limited to less than 35% due to the high absorption of the structure.

A single peak in transmission can also be observed for thin metal layers. According to Garcia-Vidal *et al.*[21] this is because the EM field of the SPPs is radiated before having the time to split into the two resonant regimes. Since the depth of the holes is of the same order of magnitude of the SPP penetration depth inside the SiO_2, the tails of the SPPs modes inside the holes are very strong. As a consequence, top and bottom interfaces resonate at the same wavelength.

In terms of resonant EM modes within the holes, the second peak $T_{\text{peak},2}$ does not make its appearance in thin metal layers because the thickness of the structure is too thin. From Figure 5.7a, this peak arises from two electric dipoles within the hole, one at the top edge and the other at the bottom edge of the hole oriented in opposite directions. The opposite orientation of the electric dipoles can only exists if there is enough retardation of the electric field between the cavity extremeties. Therefore, if the layer is too thin a second EM mode simply cannot be excited. The fact that, as the metal thickness increases, a third peak (mode) makes its appearance in the optical spectra of the structure (at approximately $t_{\text{m}} = 270$ nm), supports this hypothesis. Note that the second and third mode both arise exactly at the condition of SPPs excitation, $\lambda_{\text{min},10\downarrow}$.

Note that the effective cutoff wavelength $\lambda_{\text{co,eff}}$ is again a very good estimate for the maximum limit of the bandwidth in transmission. Also, the black arrows in Figures 5.8a and 5.8c, that highlight the position of two minima, and corresponding maxima, in the transmission and reflection spectra, respectively, are not affected by variations in the metal thickness. Finally, a localised narrow resonance at approximately RA_{10} makes again its appearance. Quite hidden in transmission, it becomes a distinctive trait in reflection and extinction spectra for few values of metal thickness (approximately around $t_{\text{m}} = 200$ nm) and temporarily disappears when 'new' modes are excited in the holes (refer to Figures 5.8d and 5.8f).

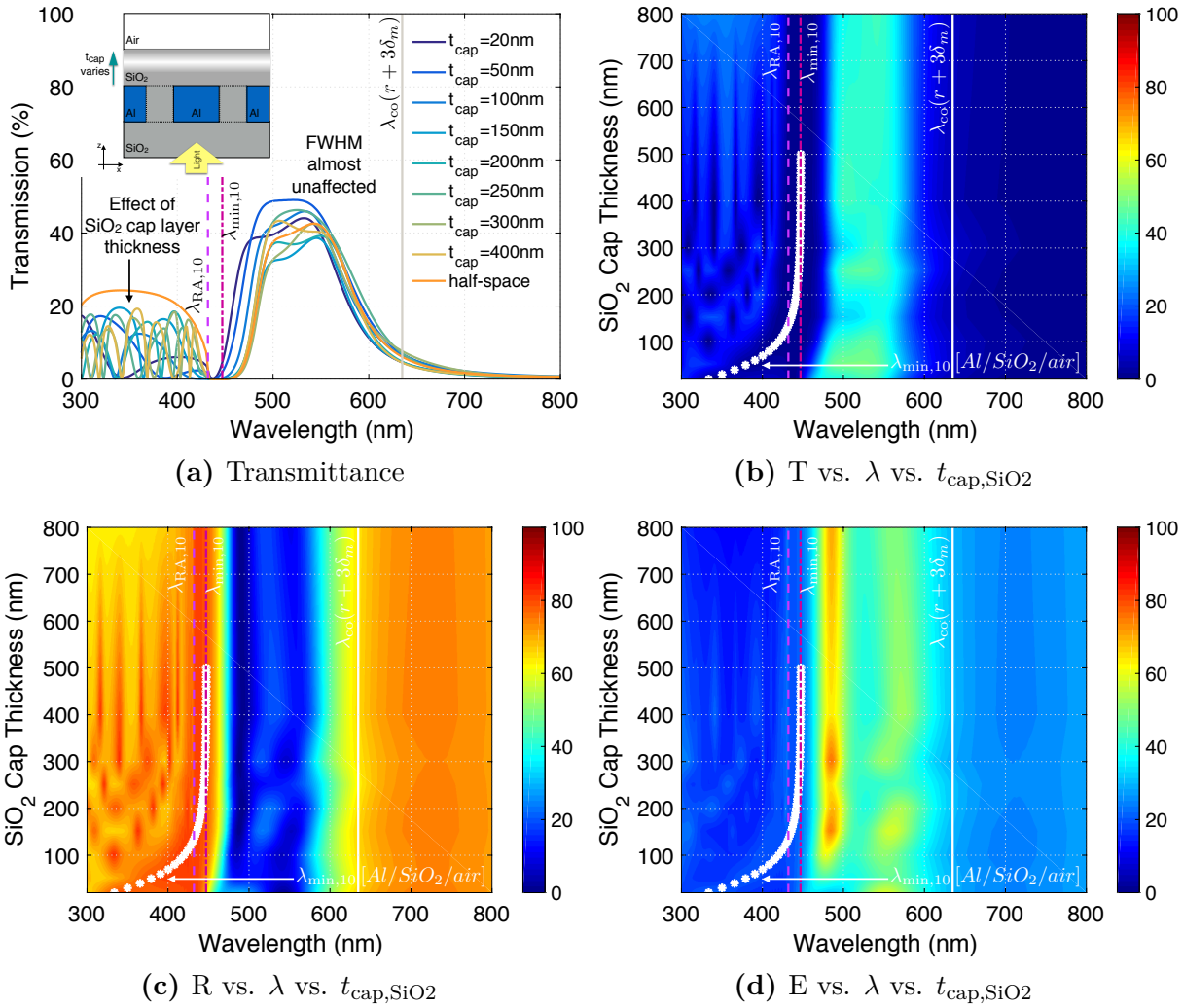
5.3.3 Top cladding layer: thickness and RI

The set of plots and images in Figure 5.9 establishes the influence of the thickness of a silicon dioxide SiO_2 cladding layer on the optical response of the Symmetry-SML structure. Evidently the silicon dioxide cap layer does not significantly affect the filtering properties of the array, neither in terms of transmission efficiency nor in terms of bandwidth.

However, the thickness of the cladding layer does affect the side-bands at shorter wavelengths. This suggest that the minima in that range of wavelengths are given by resonant modes in the cap layer, between the top metal surface and the SiO_2/air interface. In fact, the number of minima increases with the thickness of the cap layer but disappear when the layer become of infinite thickness, i.e. in absence of the interface.

Figure 5.10 shows the electric and magnetic fields at the minimum $\lambda = 383$ nm of the Sym-SML structure having a SiO_2 cap layer of 200 nm (one of the minima highlighted with a black arrow in Figure 5.5a or Figure 5.8a). The images confirm the hypothesis of a resonant mode in the cap layer, propagating along the y-direction.

Consider the white asterisk markers in the 2D images of Figure 5.9. They represents the shift in wavelength of $\lambda_{\text{min},10\uparrow}$, related to the SPPs at the top IIM interface as previously illustrated in Figure 5.4. The variation in wavelength of $\lambda_{\text{min},10\uparrow}$ as a function of the top cladding thickness, is consistent with the simulation results. Note that when $\lambda_{\text{min},10\uparrow}$ is smaller than RA_{10}, the beginning of the zero-T band is given by its position instead.



(a) Transmittance

(b) T vs. λ vs. $t_{\text{cap,SiO2}}$

(c) R vs. λ vs. $t_{\text{cap,SiO2}}$

(d) E vs. λ vs. $t_{\text{cap,SiO2}}$

Figure 5.9: Influence of the thickness of the SiO_2 cap layer on the spectral features of the Sym-SML structure. 2D plot and 2D images of the **(a)**, **(b)** transmission, **(c)** reflection, and **(d)** extinction efficiencies of a Sym-SML array as a function of wavelength and SiO_2 cap layer thickness. The thickness of the SiO_2 cap layer does not significantly affect the transmission efficiency and the optical bandwidth of the filter. Simulation parameters: $a_x = 340$ nm, $d = 180$ nm, $t_m = 150$ nm, holes filled with SiO_2.

Let us now assume to 'remove the symmetry' and use a different material as cap layer. Simulation results establish that - assuming an outer air environment - a cap layer with a RI lower than the RI of the substrate layer does not affect the performance of the filter in the EOT band because the IIM SPP dispersion relation will vary in a range shorter than $\lambda_{\text{min,10}\downarrow}$. So what would happen if the RI of the cap layer was higher than the RI of the substrate?

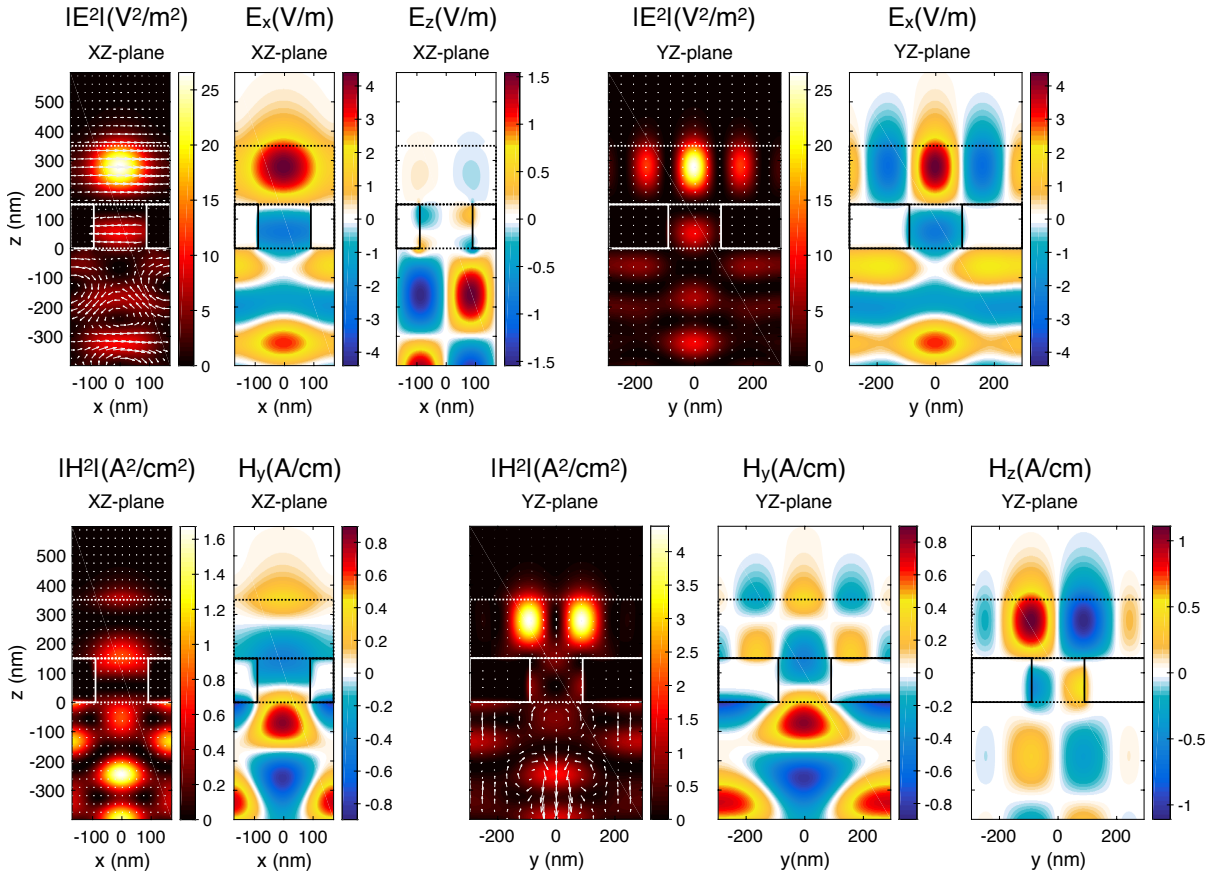
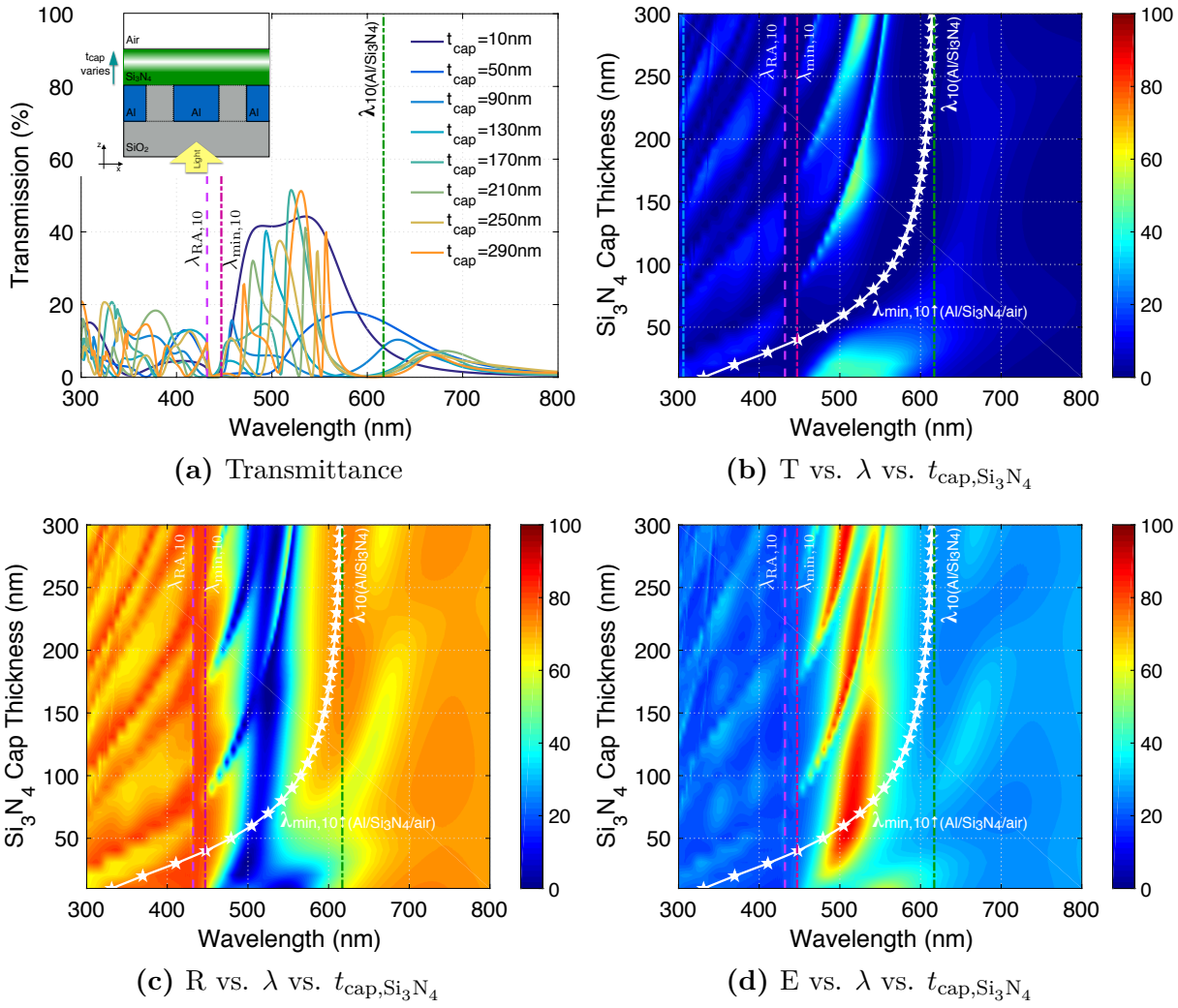


Figure 5.10: Electromagnetic near-field patterns at the minimum $\lambda = 383$ nm. Squared amplitudes of the electric and magnetic fields at the transmission minimum $\lambda = 383$ nm show the presence of a propagating mode along the y-direction within the top SiO_2 cap layer.

The set of plots and images in Figure 5.11 establishes the influence of the thickness of a silicon nitride Si_3N_4 cladding layer on the optical response of a 150-nm Al nanohole array on top of a glass substrate. Evidently the silicon nitride cap layer interferes with the optical response of the array. It has been demonstrated previously that the propagation constant of the SPPs in a IIM stack lies between the two ideal single flat interface solutions corresponding to $t_{\text{cap}} = 0$ and $t_{\text{cap}} = \infty$. In the case of a SiO_2 cap layer, this range does not interfere with the EOT band of the filters because it belongs to wavelengths shorter than $\lambda_{\text{min},10\downarrow}$. However, in the Si_3N_4 case, the region of existence of the IIM SPPs solutions overlaps with the EOT band.

Clearly, the minima resulting from the intersection of the additional wave vector G_{10} with the IIM numerical solutions intersect the EOT band and interfere with the optical response of the system (see Figure 5.11b). It looks almost as if the IIM minimum $\lambda_{\text{min},10\uparrow}$ is cutting its way through the EOT band, abating everything at its passage. $T_{\text{peak},1}$



(a) Transmittance

(b) T vs. λ vs. $t_{\mathrm{cap,Si_3N_4}}$

(c) R vs. λ vs. $t_{\mathrm{cap,Si_3N_4}}$

(d) E vs. λ vs. $t_{\mathrm{cap,Si_3N_4}}$

Figure 5.11: Influence of the thickness of the Si_3N_4 cap layer on the spectral response of a 150-nm Al nanohole array on top of a glass substrate. 2D plot and 2D images of the **(a)**, **(b)** transmission, **(c)** reflection, and **(d)** extinction efficiencies of a 150-nm Al nanohole array as a function of wavelength and Si_3N_4 cap layer thickness. The propagation constant of the IIM SPPs at the top interface interferes with the EOT band of the filter when the thickness of the Si_3N_4 cap layer becomes thicker than 40 nm. Simulation parameters: $a_x = 340$ nm, $d = 180$ nm, $t_m = 150$ nm, holes filled with SiO_2.

remains 'confined' to Si_3N_4 thickness less than approximately 40 nm and completely disappears above that. However, as the cap thickness increases, new narrower peaks make their appearance in the EOT band at approximately $t_{\mathrm{cap,Si_3N_4}} = 90$, 170 and 250 nm. Interestingly, at approximately $t_{\mathrm{cap,Si_3N_4}} = 150-160$ nm there is only a single, narrow peak in the EOT band, which also displays a good efficiency.

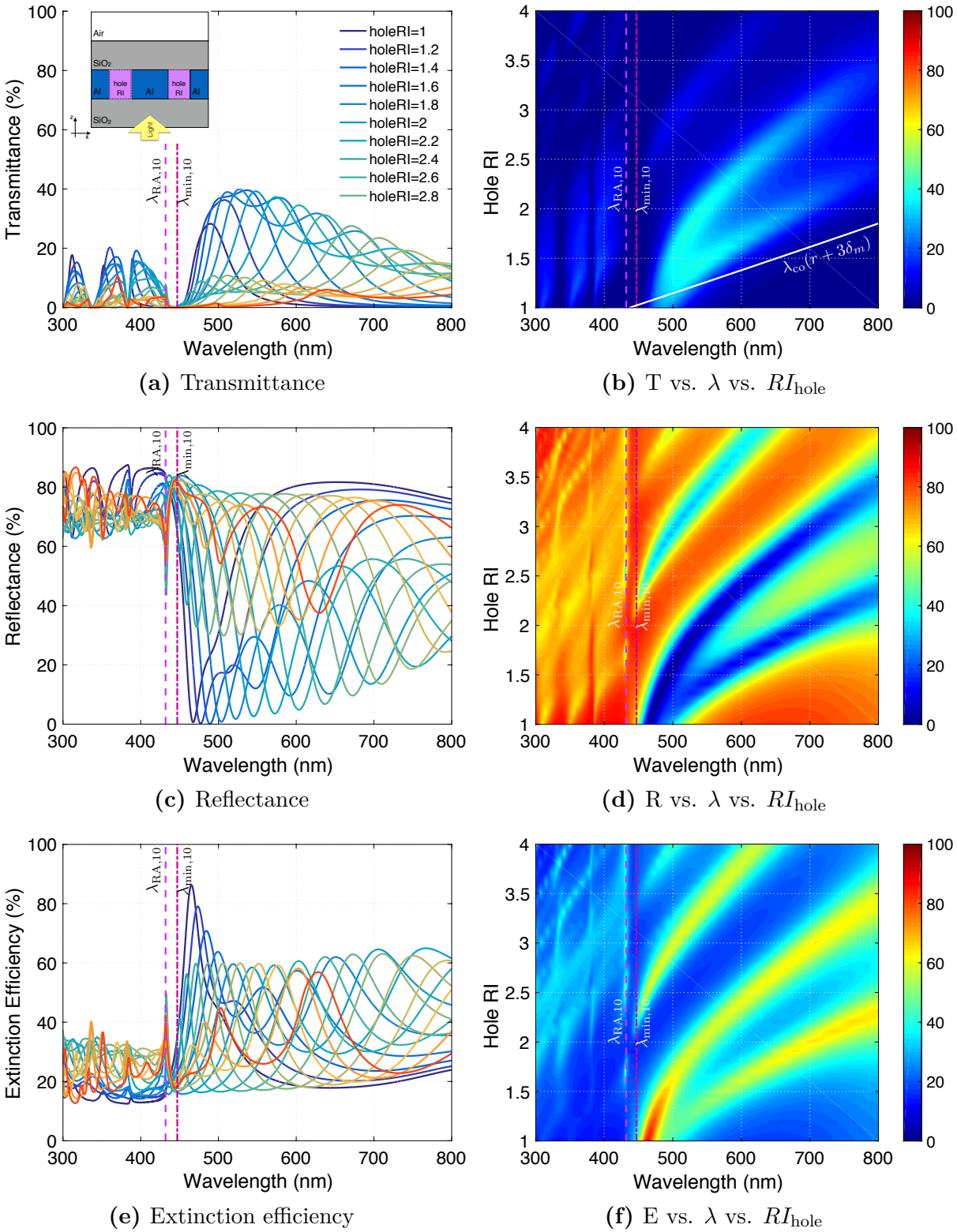
5.3.4 RI hole filling material

The set of plots and images in Figure 5.12 establishes the influence of the refractive index of the filling material inside the holes on the optical response of the Sym-SML structure. Literature suggests that by increasing the RI of the material inside the holes it is possible to increase the transmission efficiency of the EOT peaks[108]. However, from Figure 5.12a that does not seem to be entirely the case for this configuration. The transmittance slightly increases when the RI goes from 1 to about 1.4 but then after a small stall it starts instead to decrease when the RI of the hole filling material rises above 2.

However, simulation results suggest that replacing the SiO_2 hole filling with a higher-RI material could be the first step to improve the transmission efficiency of the device and narrow its bandwidth. In fact, using a higher-RI material inside the hole optically 'splits' the two transmission modes observed in the Sym-SML. The higher the RI the larger the spit between the two peaks. Moreover, the higher the RI the lower the transmission efficiency of $T_{\text{peak},1}$. On the down side, the higher the RI the higher the number of modes in the optical response of the array. These modes first appear in wavelength at approximately $\lambda_{\text{min},10\downarrow}$. Their efficiency in transmission is very low for this structural configuration, but their presence is clearly highlighted in the reflection and extinction spectra.

Studies demonstrated that introducing a cladding layer equal to the substrate material improves the SPP coupling between the two interfaces[84]. From the simulation study on the SiO_2 cap thickness (Figure 5.9) it can be observed that - even if the SiO_2 cladding does not significantly affect the bandwidth or the efficiency - the two peaks slightly approach each other when the thickness of the cap layer becomes considerably thick. So, in this case, would the removal of the SiO_2 cap layer affect the splitting of the two peaks by decreasing the coupling between the two interfaces? As it turns out: yes, it does.

Figure 5.13 establishes the influence of the refractive index of the filling material inside the holes on the optical response of the Sym-SML structure but this time without the 200-nm SiO_2 cap layer. The removal of the cladding layer considerably improves the splitting between the two peaks. Moreover, there is a slight boost in the transmission efficiency of the $T_{\text{peak},2}$ mode for a range of RI between 1.8 and 2.2.



(a) Transmittance

(b) T vs. λ vs. RI_{hole}

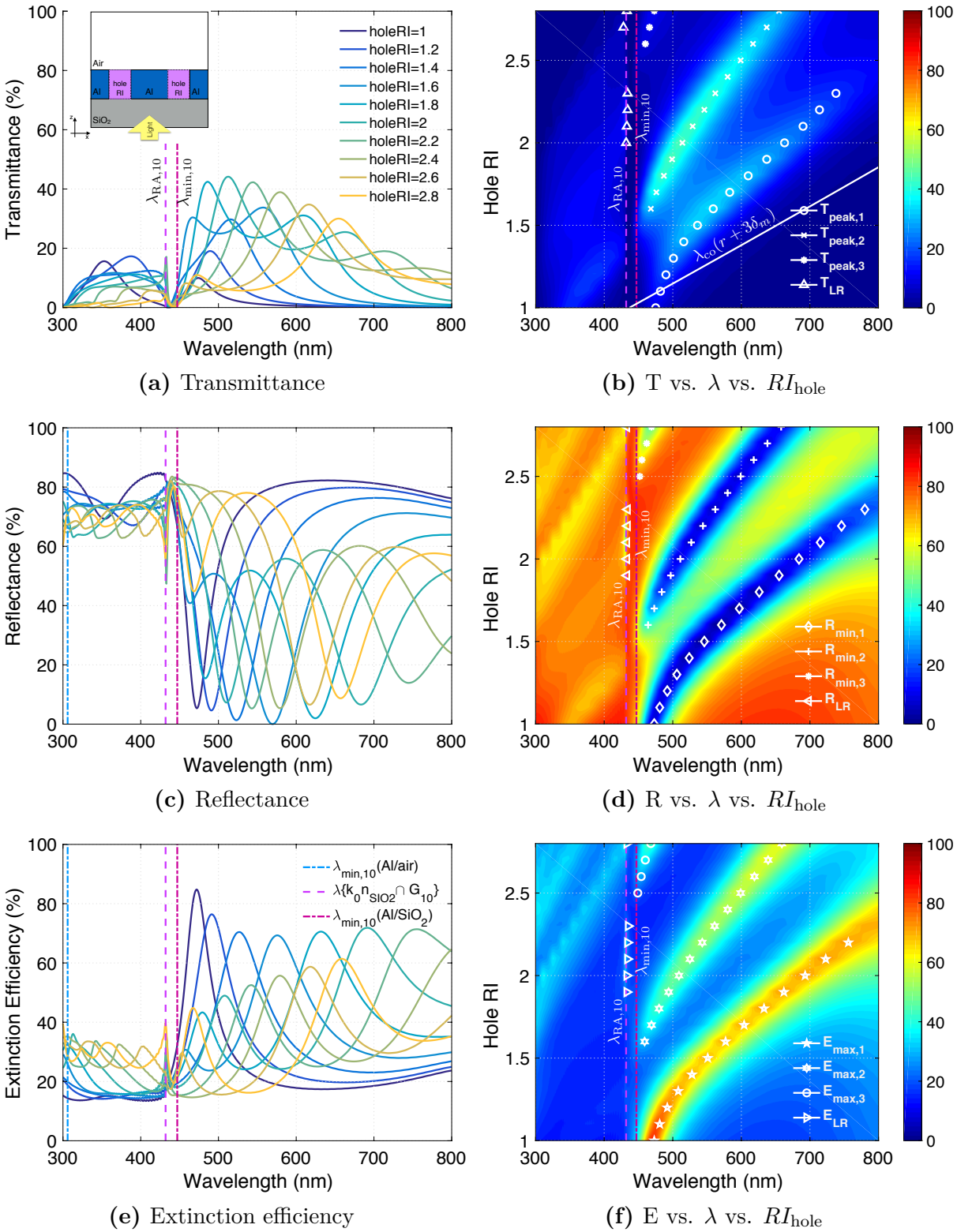
(c) Reflectance

(d) R vs. λ vs. RI_{hole}

(e) Extinction efficiency

(f) E vs. λ vs. RI_{hole}

Figure 5.12: Influence of the RI of the hole filling material on the spectral response of the Sym-SML structure. 2D plots and corresponding 2D images of the **(a)**, **(b)** transmission, **(c)**, **(d)** reflection, and **(e)**, **(f)** extinction efficiencies of a Sym-SML array as a function of the RI of the hole filling material. Increasing the RI of the hole filling material red-shifts the position of the maxima in transmission. Moreover, the higher the RI the larger the split between the two peaks. Simulation parameters: $a_x = 340$ nm, $d = 180$ nm, $t_m = 150$ nm, $t_{\text{cap,SiO}_2} = 200$ nm.



(a) Transmittance **(b)** T vs. λ vs. RI_{hole}

(c) Reflectance **(d)** R vs. λ vs. RI_{hole}

(e) Extinction efficiency **(f)** E vs. λ vs. RI_{hole}

Figure 5.13: Influence of the RI of the hole filling material on the spectral response of a 150-nm Al nanohole array on top of a glass substrate, i.e. a Sym-SML type of structure without the SiO_2 cap layer. 2D plots and corresponding 2D images of the **(a)**, **(b)** transmission, **(c)**, **(d)** reflection, and **(e)**, **(f)** extinction efficiencies of a 150-nm Al nanohole array as a function of the RI of the hole filling material. The removal of the SiO_2 cap layer increases the splitting of the two resonances by decreasing the coupling between the two interfaces. Simulation parameters: $a_x = 340$ nm, $d = 180$ nm, $t_m = 150$ nm, no cap.

5.4 Summary

Sym-SML PCFs are one of the most promising alternative to polymer-based filter technologies, however, they have some limitations. Their transmission efficiency is still relatively low and their bandwidth relatively broad when compared to commercially available filter technologies, making them unfit for multispectral applications. In this chapter, a comprehensive simulation analysis on the influence of geometrical and physical parameters on the optical response of Sym-SML arrays have been presented.

Table 5.1 summarise the dependence of the Sym-SML structure on its structural parameters. Increasing the size of the holes could considerably increase the transmission efficiency of the filter but it also significantly degrades its colour selectivity, therefore it is not advantageous at this stage to choose a larger value of diameter. The metal thickness strongly affects the extinction/absorption properties of the array. The thicker the metal, the higher the absorption and thus the lower the transmittance. Therefore, even if it could be possible to achieve narrower bandwidths by using a thicker metal layer this would not be a convenient trade-off. In fact, no matter what other optimisation would be implemented, it will not be possible to reduce the absorption further down - and thus increase the transmittance of the filter. This is because the absorption is directly related to the amount of metal present in the structure. On the other hand, using a thin metal layer can significantly improve the efficiency of the filter in transmission.

Using a cap layer having a RI equal or smaller than the RI of the substrate material does not significantly affect the lineshape nor the efficiency of the filter. On the contrary, implementing a thick cap layer having RI higher than the substrate can strongly interfere with the spectral features of the EOT band. Interestingly, for a small range of Si_3N_4 cap thickness (approximately around 150-160 nm) a single, narrow peak can be distinguished in the EOT band. Therefore, it is important to consider the dielectric environment of the filters in case the application requires integration within another device.

Finally, it has been observed that by removing the top cladding layer - to reduce the coupling between interfaces - and utilising a higher refractive index material inside the

	Structural Parameters				
	Diameter $d \nearrow$	Metal Thickness $t_m \nearrow$	SiO_2 cap layer $t_{cap,SiO_2} \nearrow$	Si_3N_4 cap layer $t_{cap,Si_3N_4} \nearrow$	Hole RI $RI_{hole} \nearrow$
Efficiency	$\nearrow$	$\searrow$	$\rightarrow$	$\rightarrow$	$\rightarrow$
FWHM	$\nearrow$	$\searrow$	$\rightarrow$	$\searrow$	$\nearrow\searrow$

Table 5.1: Influence of the structural parameters on the transmittance of the Sym-SML structure. When the diameter d increases, the transmission efficiency increases but also the bandwidth. On the other hand, when the metal thickness t_m increases, both efficiency and FWHM decrease. A SiO_2 cap layer does not affect the performance of the filter. On the contrary, a Si_3N_4 cap layer can significantly vary the optical response of the filter: the FWHM can be reduced but the thicker the layer the higher the number of resonant modes in the EOT band. Increasing the RI of the hole filling material can improve the lineshape of the filter.

nanoholes might be extremely advantageous to split the two resonant modes in transmission. The separation in wavelength of the two peaks might lead to a single-peak passband filter and thus to a higher colour selectivity.

The above considerations are extremely important for the improvement of the filters and represent the basis for the development of novel plasmonic colour filters, as it will be demonstrated in the next chapter.

Chapter 6

2D Hexagonal Nanohole Arrays: A Change in Dielectric Environment

In the last chapter, 2D hexagonal arrays of subwavelength nanoholes milled in a 150-nm thick Al layer have been examined through a comprehensive parametric analysis. The objective of the simulation study was to provide an overview of the spectral characteristics of the filters and their parametrical dependences but, also, to identify a novel way to improve their optical performance. More specifically, increasing their transmission efficiency and narrowing their optical bandwidth, in order to make them more suitable for integrated multispectral applications.

In this chapter, a novel and more selective nanostructure for filtering light in the visible range is presented. The structure is also based on a 2D hexagonal array of subwavelength nanoholes, but the metallic layer has been thinned down to few tens of nanometers, a higher-RI material is used as hole filling material and asymmetry has been introduced between the two metal/dielectric interfaces by using a higher-RI cap layer. As a consequence, different physical mechanisms aid the transmission process.

Section 6.1 recapitulates the observations derived from the parametric analysis of the previous Chapter, describes step-by-step the modifications imposed to the Sym-SML structure and compares the results. Section 6.2 correlates the SPPs modes at the bottom and top interfaces with the appearance of minima in transmission. The electromagnetic near-field patterns at specific points of interest are examined in Section 6.3. Section

6.4 is a detailed parametric analysis of the novel asymmetric, thin-metal layer structure and presents the dependence of the optical response on its geometric and constitutive parameters, namely diameter, metal thickness, and also cladding and hole filling materials. Finally, the main observations and remarks are summarised in Section 6.5.

6.1 Introduction

The parametric analysis in Chapter 5 established that the transmission efficiency of the Sym-SML structure could be increased by either increasing the size of the holes or reducing the thickness of the metal layer. On the other hand, the FWHM could be reduced by increasing the metal thickness or by using either a high-RI cap layer either a high-RI material inside the holes. Increasing the diameter of the holes significantly increases the transmission efficiency of the filter, however it also significantly broadens its passband. Similarly, increasing the thickness of the metal layer can narrow the FWHM of the filter but also considerably reduce its efficiency in transmission because of the higher absorption caused by the higher amount of metal present in the structure. Therefore, both of these options have been discarded.

Simulation results suggested that the efficiency of the filter in transmission would benefit if a thinner layer of metal was used. Therefore, to improve the efficiency of the filter, it has been decided to reduce the amount of metal within the structure, and thus the metal has been thinned down to 40 nm. The 40-nm thickness has been chosen because it is thin enough to reduce the absorption losses but thick enough to be approximately 3-4 times the SPP penetration depth inside the Al. In this way, the metal layer can still be considered as an half-space material and it does not allow SPP coupling between the top and bottom interfaces[1].

In addition, to narrow the bandwidth, the SiO_2 hole filling has been replaced with a higher RI material. Simulation data suggested that the best choice for a high-RI material - in terms of either transmission efficiency and bandwidth - would be for it to have a RI of approximately 2. Si_3N_4 has a RI between 2-2.1, accordingly to the deposition

[1]Refer to Figure 3.10.

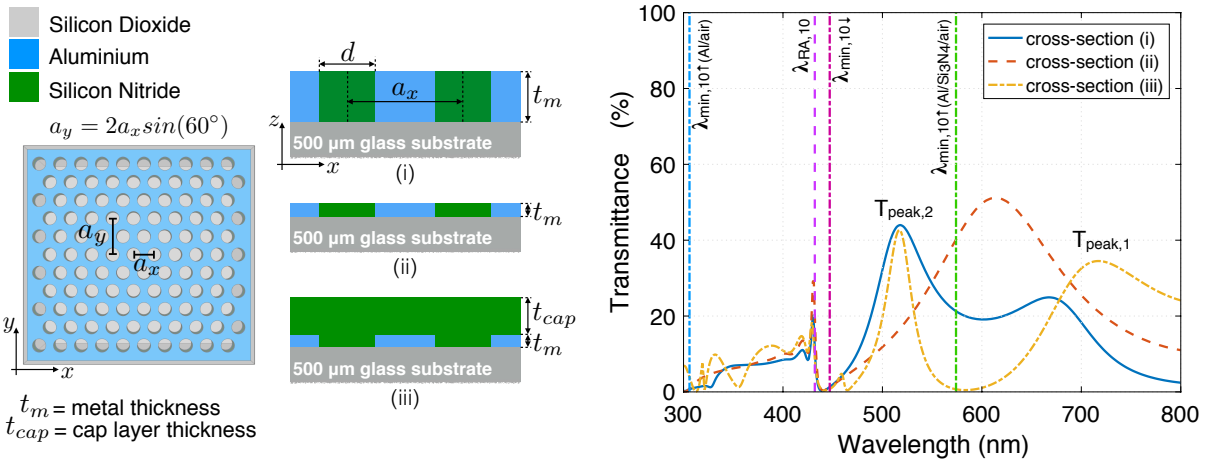
process utilised[177]. Moreover, it is already a well-known and standard material in CMOS fabrication, commonly used in CMOS image sensors, for example, as a dielectric spacer between the metal layer or as a passivation layer[178]. This means that Si_3N_4 matches all the necessary requirements and thus it has been chosen as the higher-RI material.

However, simulation results also established that the number of resonant modes within the structure depends on its thickness. Previous studies compared the subwavelength holes of plasmonic filters to resonant cavities in which the top and bottom surfaces - thanks to the presence of surface plasmon waves - behave like mirror-like interfaces[84]. As a consequence, the depth of the holes represents the length of the cavity. This implies that it might be necessary to 'maintain' the cavity length in order to either see the appearance of a certain mode or either avoid a possible interference introduced by the presence of a supplementary resonant mode.

Therefore, to increase the total thickness of the cavity, it has been decided to introduce a cladding layer made of the same high-RI material of the hole filling material on top of the 40-nm metal layer. Similarly to a slab waveguide, the difference in permittivities between the high-RI material and the substrate (at the bottom) and the outer air environment (at the top) provides (enhances) electromagnetic confinement. In this way, it is as if the cavity - represented by the hole - would virtually extend to the top surface of the cladding layer so that the total thickness of the structure $t_{\text{tot}} = t_{\text{cap}} + t_m$ will act as the effective cavity length of the resonator.

Figure 6.1 compares the transmission characteristics of two SML structures - having silicon nitride inside the holes and a metal thickness of (i) 150 nm[2] and (ii) 40 nm - with respect to the new configuration (iii). The new configuration presents a single, narrow peak within the waveband of interest and thus has a relatively higher optical selectivity with respect the other two configurations. Note the effect that the Si_3N_4 cap layer has on the optical response of configuration (iii) with respect configuration (ii). Without the cap layer there is no narrow peak, because the total thickness of the cavity is not large enough to excite this mode. On the other hand, note that $T_{\text{peak},2}$ arises at approximately

[2]Note that the SiO_2 cap has been removed from the Sym-SML structure in order to reduce the coupling between top and bottom interfaces.



(a) Top and side perspective view

(b) Comparison RGB tristimulus

Figure 6.1: From broad- to narrow-band plasmonic colour filters. (a) Top view (right) of a hexagonal nanohole array and cross-sections for three different configurations of plasmonic filters on half-space SiO_2 substrates having silicon nitride inside the holes and a metal thickness of (i) 150 nm and (ii), (iii) 40 nm. The latter configuration is also capped with a 110-nm Si_3N_4 layer. (b) Comparison of the transmission efficiencies of the three configurations of HNAs. The introduction of a high-RI material results in narrower passband features when the total thickness of the structure is large enough to allow the excitation of the second resonance $T_{\text{peak},2}$. For all the structures: periodicity $a_x = 340$ nm and diameter $d = 180$ nm. The vertical lines represent the positions in wavelength of the minima corresponding to RA_{10} and the conditions of excitation of SPPs at the bottom and top interfaces.

the same resonant wavelength for configurations (i) and (iii), which have the same total stack thickness and the same hole filling material. Therefore, this resonance is highly dependent on the total stack thickness and the hole filling material, in the same way that the resonance of a cavity resonator depends on its effective length and its material.

Configuration (iii) utilises a thin metallic layer of 40 nm to reduce the absorption losses of the filter but has a total stack thickness of 150 nm. The 150-nm value has been chosen accordingly to the simulation data on the effect of a Si_3N_4 cap thickness on the optical response of the Sym-SML structure[3] where for a Si_3N_4 thickness of 150 nm the transmission spectrum displayed a single narrow peak within the EOT band. From now onward configuration (iii) will be referred to as the Asym-(thin)SML structure because of the asymmetry between the top and bottom interfaces in terms of pair of materials and the thin metal layer used.

As expected, the positions of $\lambda_{\text{RA},10}$ and $\lambda_{\text{min},10\downarrow}$ are unchanged with respect the Sym-SML structure presented in the previous Chapter. This is because the type of metal,

[3]Refer to Section 5.3.3

substrate and periodicity are the same. In contrast, the top interface introduces a new minimum in the optical spectra. Configurations (i) and (ii) have a top Al/air interface. Since the dispersion relation k_{SPP}[Al/air] is smaller than k_{SPP}[Al/SiO_2], the corresponding minimum $\lambda_{min,10(air)\uparrow}$ appears at a shorter wavelength than $\lambda_{min,10\downarrow}$.

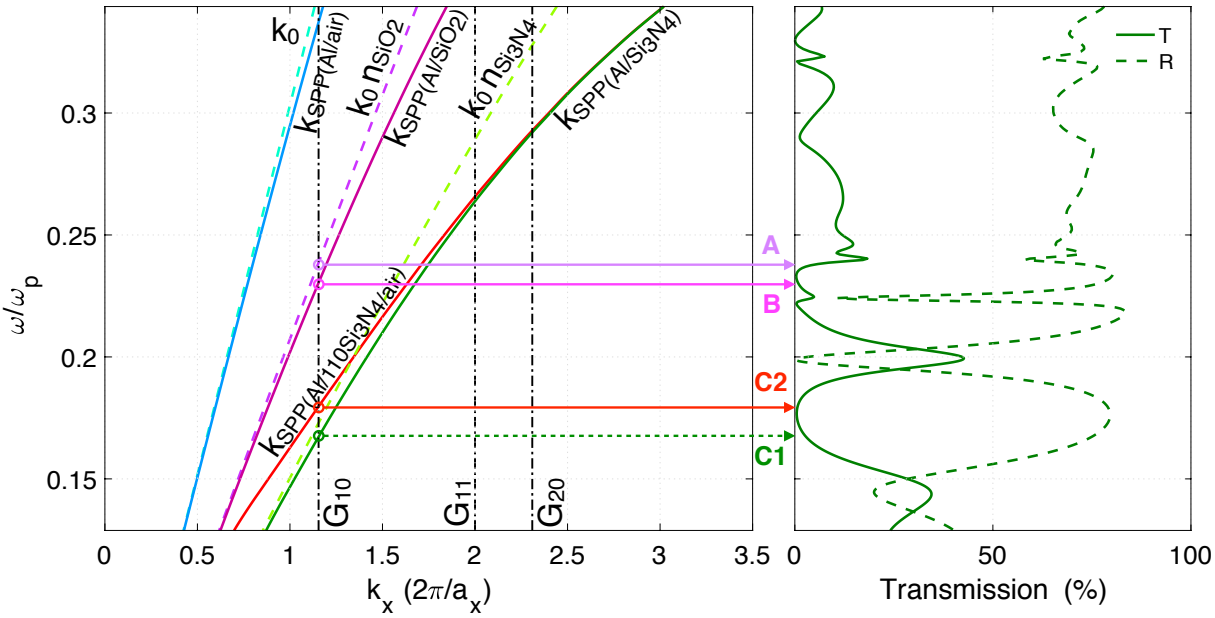
On the other hand, the insulating material at the top metal/dielectric interface of the Asym-(thin)SML structure has a higher-RI than SiO_2. Therefore, the new minimum related to the top interface appears at a wavelength longer than $\lambda_{min,10\downarrow}$, within the EOT band. However, the top interface of the Asym-(thin)SML structure can not be modelled as single interface between two half-space materials, because the thickness of the Si_3N_4 cap layer is of the same order of magnitude of the SPPs penetration depth. Therefore, to evaluate $\lambda_{min,10\uparrow}$ of (iii) the top interface has to be modelled as an IIM stack.

6.2 Characteristic Traits in the EOT Spectra

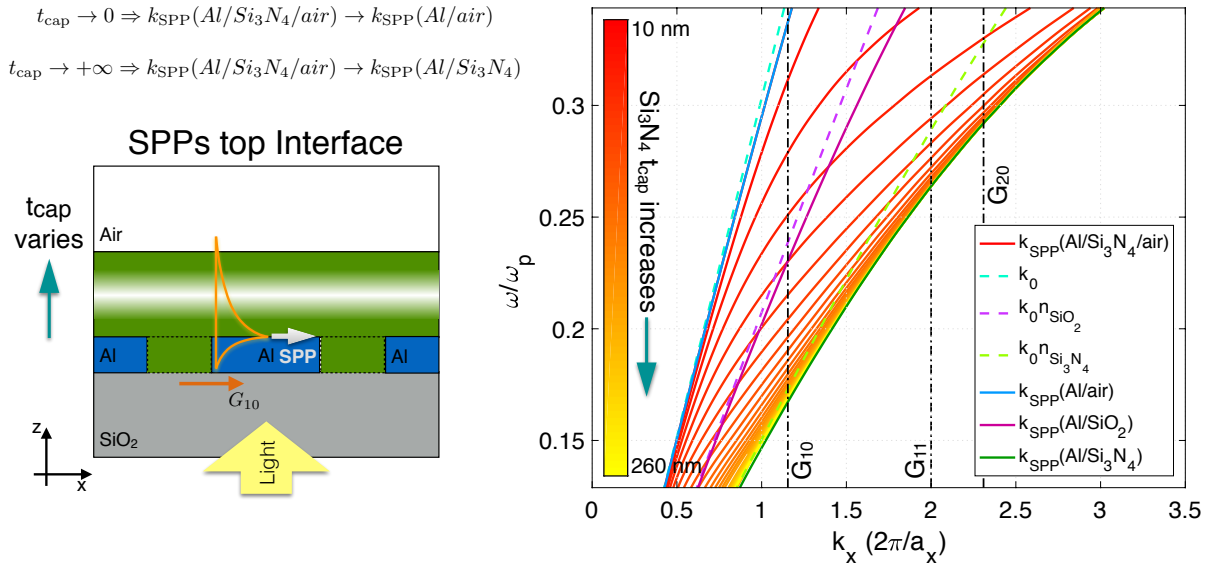
Figure 6.2 highlights the correlation between the excitation of SPPs, the occurrence of RAs, and the appearance of minima in the optical response of the Asym-(thin)SML structure in transmission. The letter A represents the position of $\lambda_{RA,10}$ while the letter B represents the position of $\lambda_{min,10\downarrow}$, where the symbol $\downarrow$ indicate that it refers to the bottom interface of the structure. $\lambda_{RA,10}$ and $\lambda_{min,10\downarrow}$ are the same as in the case of the Sym-SML structure because the type of metal, substrate and periodicity are the same.

As expected, the introduction of a higher-RI (than the substrate) cap layer caused the appearance of a second minimum in transmission at longer wavelengths with respect $\lambda_{min,10\downarrow}$. However, since the Si_3N_4 cap thickness is of the same order of magnitude of the SPPs penetration depth inside the silicon nitride[4], the tail of the surface wave can 'feel' the outer air environment. As a consequence, the top interface cannot be considered a single interface between two half-space materials but has to be modelled as a IIM stack, as described in Section 3.7.4. The letter C1 indicates where would be the position of the minimum in case of a top single interface between Al and Si_3N_4, while the letter C2 indicates the position $\lambda_{min,10\uparrow}$ - where the symbol $\uparrow$ indicate that it refers to the top

[4]Refer to Figure 3.5.



(a) Minima in transmission for the Asym-(thin)SML structure.



(b) Schematic representation of SPPs at the top IIM interface and dispersion relations.

Figure 6.2: Minima in transmission and IIM SPPs in the Asym-(thin)SML structure. (a) Correlation between the excitation of SPPs, the occurrence of RAs, and the appearance of minima in transmission. The letter A represents the position of $\lambda_{RA,10}$ while the letter B represents the position of $\lambda_{min,10\downarrow}$. The letter C1 indicates where would be the position of the minimum in case of a top single interface between Al and Si_3N_4. On the other hand, the letter C2 indicates the position $\lambda_{min,10\uparrow}$ of the 'real' minimum given by the excitation of the SPPs at the top IIM interface. SPPs dispersion relations and light lines are labelled in the Figure, as well as the vertical, dashed-dotted black lines that represent the additional wavevectors G_{ij} provided by the periodicity of the array. (b) Right image: schematic diagram of SPPs at the top air/Si_3N_4/Al IIM interface. Left plot: numerical solutions of the SPPs at the top IIM interface as a function of the Si_3N_4 cap thickness. The solutions tend to $k_{SPP(Al/air)}$ for thin cap layer and converge to $k_{SPP(Al/Si_3N_4)}$ as the thickness of the cap layer increases and become larger than the δ_{SPP} inside the Si_3N_4 layer. For both the plots, the angular frequency ω is normalised to the plasma frequency of Al $\omega_p = 12.04$ eV[174]. Wavevectors are normalised by $2\pi/a_x$.

interface of the structure - of the actual minimum given by the excitation of the SPPs at the top IIM interface.

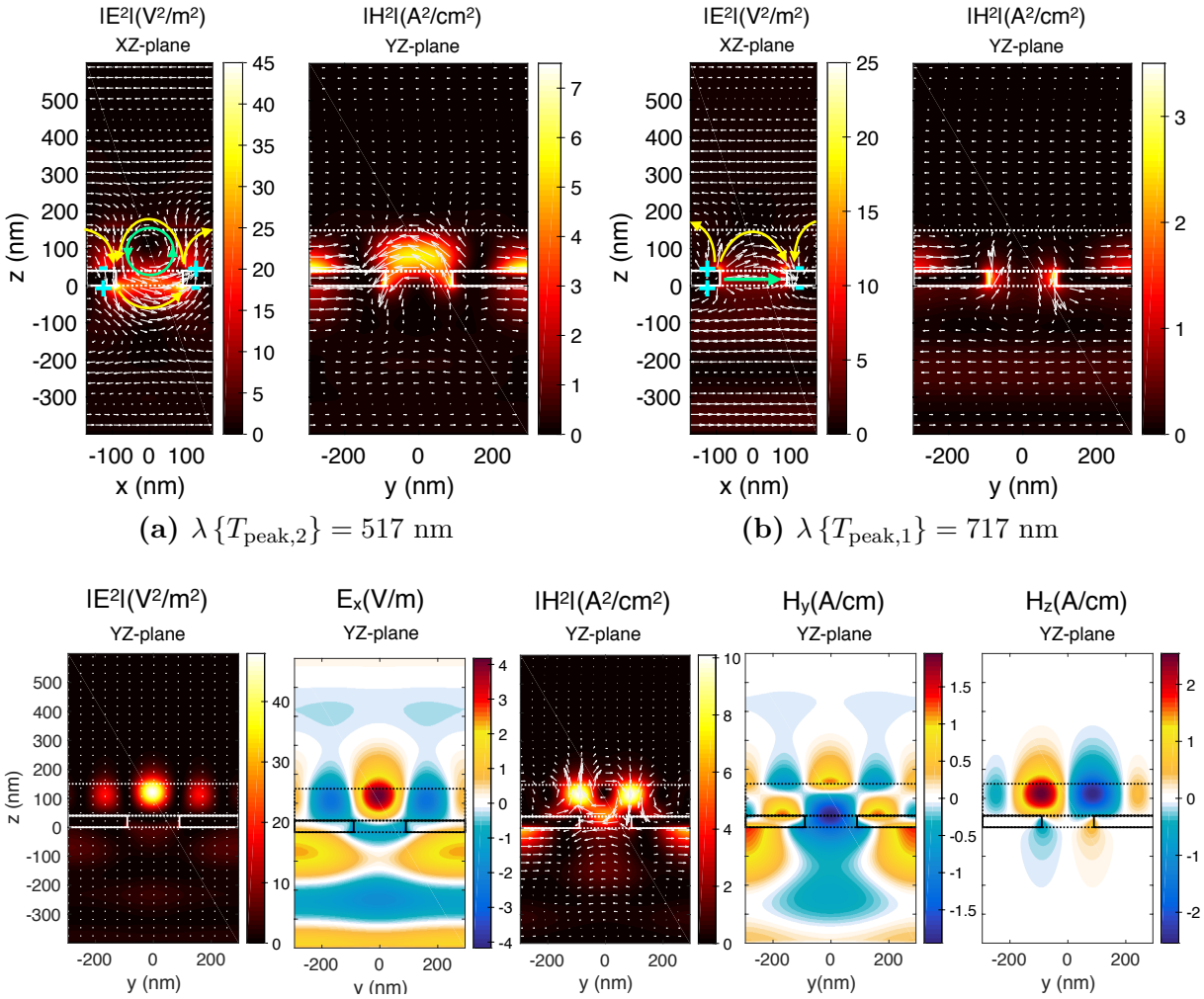
The numerical solutions of the IIM air/Si_3N_4/Al interface are plotted in Figure 6.2b as a function of the Si_3N_4 cap thickness. Note that the dispersion relations of the IIM SPPs as a function of the Si_3N_4 cap thickness lie in between $k_{\mathrm{SPP(Al/air)}}$ and $k_{\mathrm{SPP(Al/Si_3N_4)}}$. If the Si_3N_4 cap thickness tends to zero the solutions tend to the propagation constant $k_{\mathrm{SPP(Al/air)}}$. On the other hand, if the Si_3N_4 cap thickness becomes larger than the SPPs penetration depth δ_{SPP} inside the Si_3N_4, the numerical solutions converge to $k_{\mathrm{SPP(Al/Si_3N_4)}}$. It has been established in Section 3.6 that the SPP dispersion relation of a single interface proportionally increases or decreases as a function of the RI of the dielectric layer if the metal remains the same. This means that in the IIM case, if the cap is thin enough so that the tail of the SPP can 'feel' the air environment, the effective refractive index of the top interfaces lowers as a function of the cap thickness. As a consequence, the thinner the cap layer, the higher the blu-shift in wavelength of $\lambda_{\mathrm{min},10\uparrow}$ with respect the the single interface value.

Note that the resonance $T_{\mathrm{peak},2}$ appears between the two minima $\lambda_{\mathrm{SPP},10}[\mathrm{Al/SiO_2}]$ and $\lambda_{\mathrm{SPP},10}[\mathrm{Al/110nmSi_3N_4/air}]$. This is an extremely interesting feature because it allows to locate the peak independently of all the geometrical parameters of the structure[179].

6.3 Electromagnetic Near-Field Patterns

Physical insights can be obtained from the electric and magnetic near-field pattern of the structure. Figures 6.3a and 6.3b show the squared amplitudes of the electric and magnetic fields at the transmission maxima $T_{\mathrm{peak},2}$ and $T_{\mathrm{peak},1}$ of the Asym-(thin)SML structure, in the XZ-plane and YZ-plane respectively.

The charge configurations and the electric field lines at the top and bottom interfaces are similar to that in the Sym-SML case (refer to Figure 5.7). The short-wavelength peak is still the asymmetric mode, while the long-wavelength peak is the symmetric mode. For $T_{\mathrm{peak},1}$, the magnetic field is still concentrated at the sidewalls of the hole in the YZ-plane while an electric dipole arise inside the hole in the XZ-plane. On the other hand, at



(a) $\lambda\{T_{\text{peak},2}\} = 517$ nm **(b)** $\lambda\{T_{\text{peak},1}\} = 717$ nm

(c) $\lambda\{T_{\text{peak},3}\} = 459$ nm

Figure 6.3: Electromagnetic near-field patterns at the transmission maxima. Squared amplitude of the electric and magnetic fields at (a) $T_{\text{peak},2}$ and (b) $T_{\text{peak},1}$. (c) Squared amplitude of the electric and magnetic fields, and respective components, at the transmission maximum $T_{\text{peak},3}$ nm show the presence of a propagating mode along the y-direction within the top 110-nm Si_3N_4 cap layer. The white arrows in the background represent the electric and magnetic vectors potential, respectively. The green circle represents an electric current loop, while the green arrow an electric dipole. Direction of electric field lines at the metal/dielectric interfaces are highlighted with yellow arrows.

$T_{\text{peak},2}$, an electric displacement current loop appears inside the hole, centred between the bottom and the top interface, which induces an orthogonally-oriented magnetic dipole moment.

In the transmittance of the Asym-(thin)SML structure plotted in Figure 6.2a, a third peak is visible just before $T_{\text{peak},2}$. Figure 6.3c shows the electric and magnetic fields at the this maxima $T_{\text{peak},3}$. Note that in this case a propagating mode inside the Si_3N_4 cap, along the y-direction, is discernible from the EM patterns, similarly to the one observed

in the SiO_2cap layer for the Sym-SML case. However, in that case the peak appeared outside of the EOT band.

6.4 Parametric Analysis

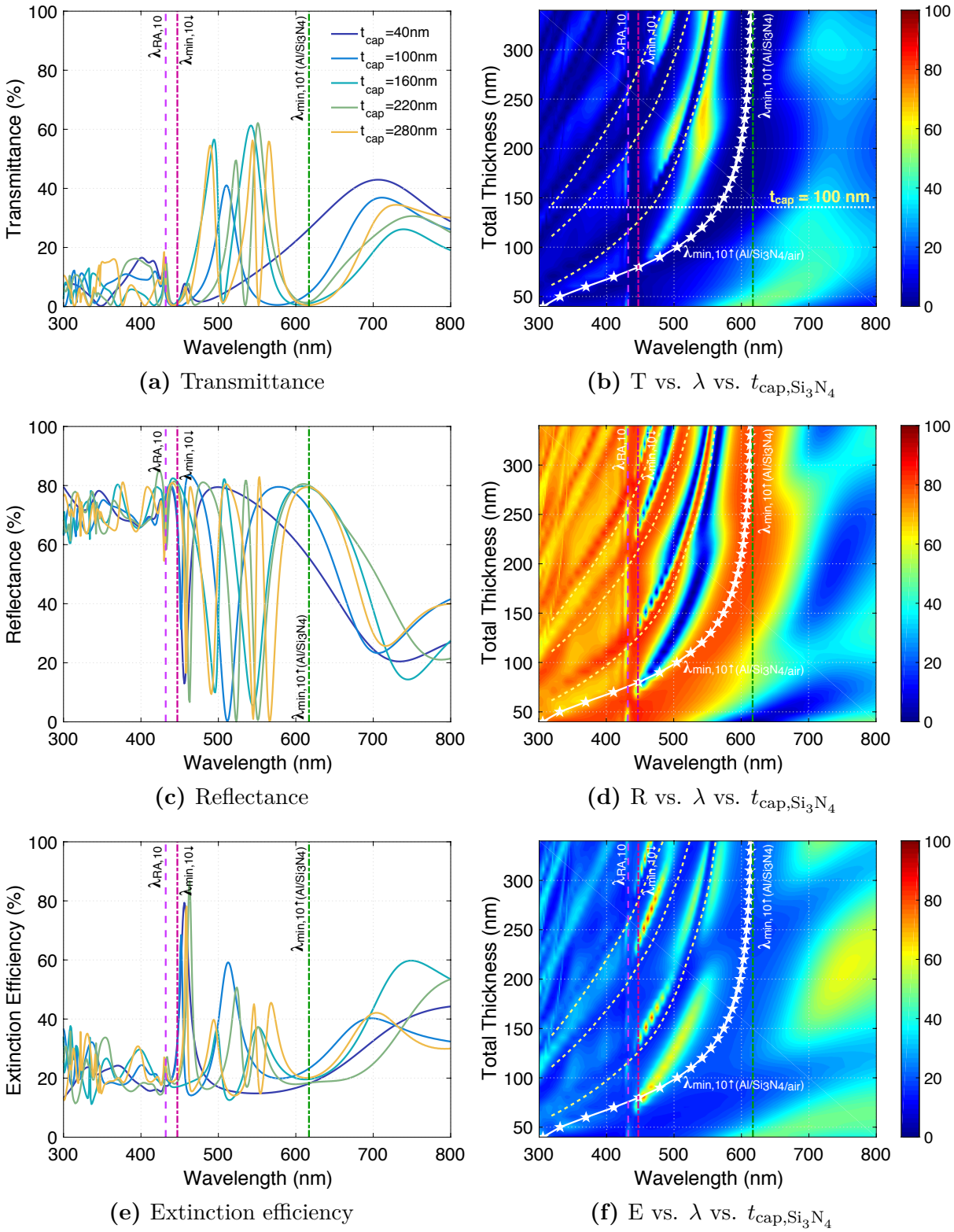
In this Section, a parametric analysis to study the influence that different geometric and physical parameters have on the optical response of 2D hexagonal Asym-(thin)SML arrays is presented. As for the case of the Sym-SML architecture, this study is used to analyse the device performance within different sets of parameters to identify the best solution for a specific application and to establish educated guesses for possible improvements and developments. For every parameter, the performance will be evaluated in terms of: (i) efficiency, (ii) optical bandwidth of the filter and (iii) stability to process variations. An analysis of the physical mechanisms involved in the transmission process will also be attempted by identifying characteristic traits and behavioural patterns.

6.4.1 Cap Layer Thickness and Cavity Length

In Chapter 5 it has been observed that a Si_3N_4 cap layer strongly affects the optical response of the Sym-SML filter in the EOT band. New resonances appear and the number of resonances depends on the thickness of the cap layer. The thicker the cap layer the larger the number of resonances within the structure. Therefore, it is fair to assume that the cap layer thickness is the parameter that will mostly affect the optical response of the Asym-(thin)SML structure.

The set of plots and images in Figure 6.4 establishes the influence of the thickness of the top cap layer on the optical response of the Asym-(thin)SML structure. The white stars indicate the position of $\lambda_{\mathrm{min},10\uparrow}$ as a function of the Si_3N_4 cap layer. Note how the variation of $\lambda_{\mathrm{min},10\uparrow}$ is a perfect fit for a minimum in transmission.

For a total stack thickness $t_{\mathrm{tot}} = t_m + t_{\mathrm{cap}}$ less than approximately 90 nm ($t_{\mathrm{cap}} = 50$ nm) there is only one peak in transmission, $T_{\mathrm{peak},1}$, at wavelengths longer than $\lambda_{\mathrm{Al/Si_3N_4}}$. In absence of the cap, $T_{\mathrm{peak},1}$ appears approximately at the condition $k_{\mathrm{SPP(Al/Si_3N_4)}} = G_{10}$.



(a) Transmittance **(b)** T vs. λ vs. $t_{\mathrm{cap,Si_3N_4}}$

(c) Reflectance **(d)** R vs. λ vs. $t_{\mathrm{cap,Si_3N_4}}$

(e) Extinction efficiency **(f)** E vs. λ vs. $t_{\mathrm{cap,Si_3N_4}}$

Figure 6.4: Influence of the thickness of the Si_3N_4 cap layer. 2D plots and corresponding 2D images of the **(a)**, **(b)** transmission, **(c)**, **(d)** reflection, and **(e)**, **(f)** extinction efficiencies of a Asym-(thin)SML array as a function of the Si_3N_4 cap layer thickness. Simulation parameters: $a_x = 340$ nm, $d = 180$ nm, $t_{\mathrm{m}} = 40$ nm, holes filled with Si_3N_4.

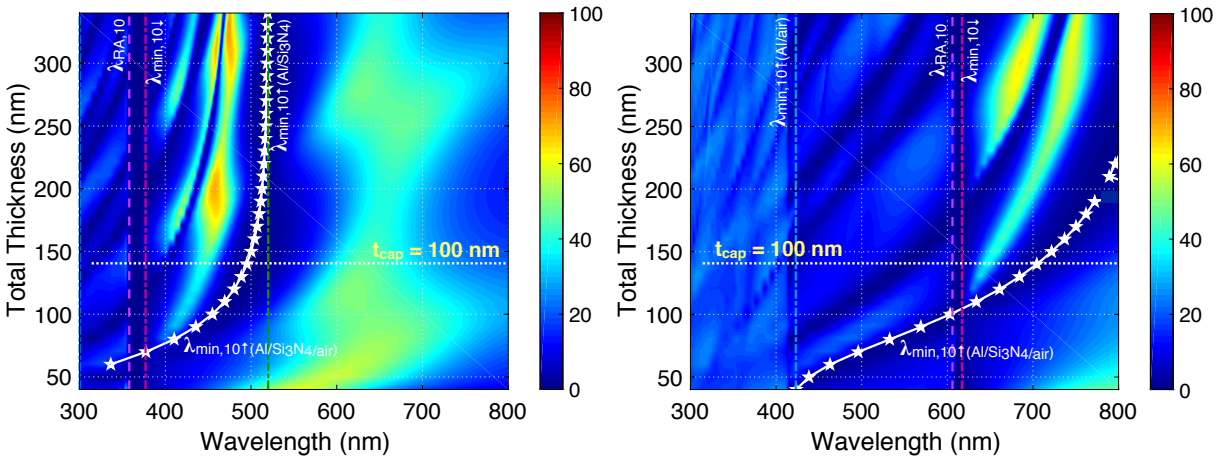
According to the EM of Figure 6.3b, $T_{\text{peak},1}$ arises from the oscillation of an electric dipole along the x-direction in between the sidewalls of the holes. This mode does not have a cut-off. On the other hand, $T_{\text{peak},2}$ requires a stack thick enough to allow to generation of the electric displacement current loop between the bottom interface and the top surface of the cap layer. In fact, this resonant mode makes its appearance only for $t_{\text{tot}} > 90$ nm.

As the Si_3N_4 cap thickness increases, new resonant modes arises. Note that each of these modes, including $T_{\text{peak},2}$, appears at $\lambda_{\text{min},10\downarrow}$ and then redshifts in wavelength as the stack becomes thicker. However, these modes remain confined between $\lambda_{\text{min},10\downarrow}$ and $\lambda_{\text{min},10\uparrow}$.

For a range of thickness between $90 < t_{\text{tot}} \leq 140$ nm there is only one peak in the EOT band between $\lambda_{\text{min},10\downarrow}$ and $\lambda_{\text{min},10\uparrow}$. This is the 'optimal' range to avoid the appearance of other resonant modes but only for the periodicity under analysis, i.e. $a_x = 340$ nm. In fact, it is well-known that cavity-based resonances occur when the length of the cavity is an integral number of half-wavelength of the wave. The effective optical length of a cavity mode can be approximated as $h_{\text{eff}} \approx \alpha\lambda_{\text{res}}/(2n)$, where α is a positive integer larger than zero, λ_{res} is the resonant wavelength of the peak and n is the RI of the material inside the cavity. Therefore, for a constant RI n, the shorter the resonant wavelength, the smaller the cavity length needed to sustain a mode and vice versa.

Hence, the question at which we need to find an answer is: is there a value of thickness for which the Asym-(thin)SML structure display a single-peak characteristic in the EOT band that is suitable for the entire visible range? In order to provide an adequate answer we should analyse the behaviour of the structure at different working wavelengths: one at the lower limit of the visible spectrum, in the blue regime, and another at the upper limit, in the red regime.

The two plots in Figure 6.5 establish the influence of the thickness of the top cap layer on the optical response of the Asym-(thin)SML structure in the blue and red regimes of the visible spectrum, respectively. As expected, in the blue range $T_{\text{peak},2}$ makes its first appearance for lower values of total thickness, with respect the previous case, while in the red part of the spectrum for higher values. We establish that a Si_3N_4 cap thickness of



(a) T vs. λ vs. $t_{\mathrm{cap,Si_3N_4}}$ **(b)** T vs. λ vs. $t_{\mathrm{cap,Si_3N_4}}$

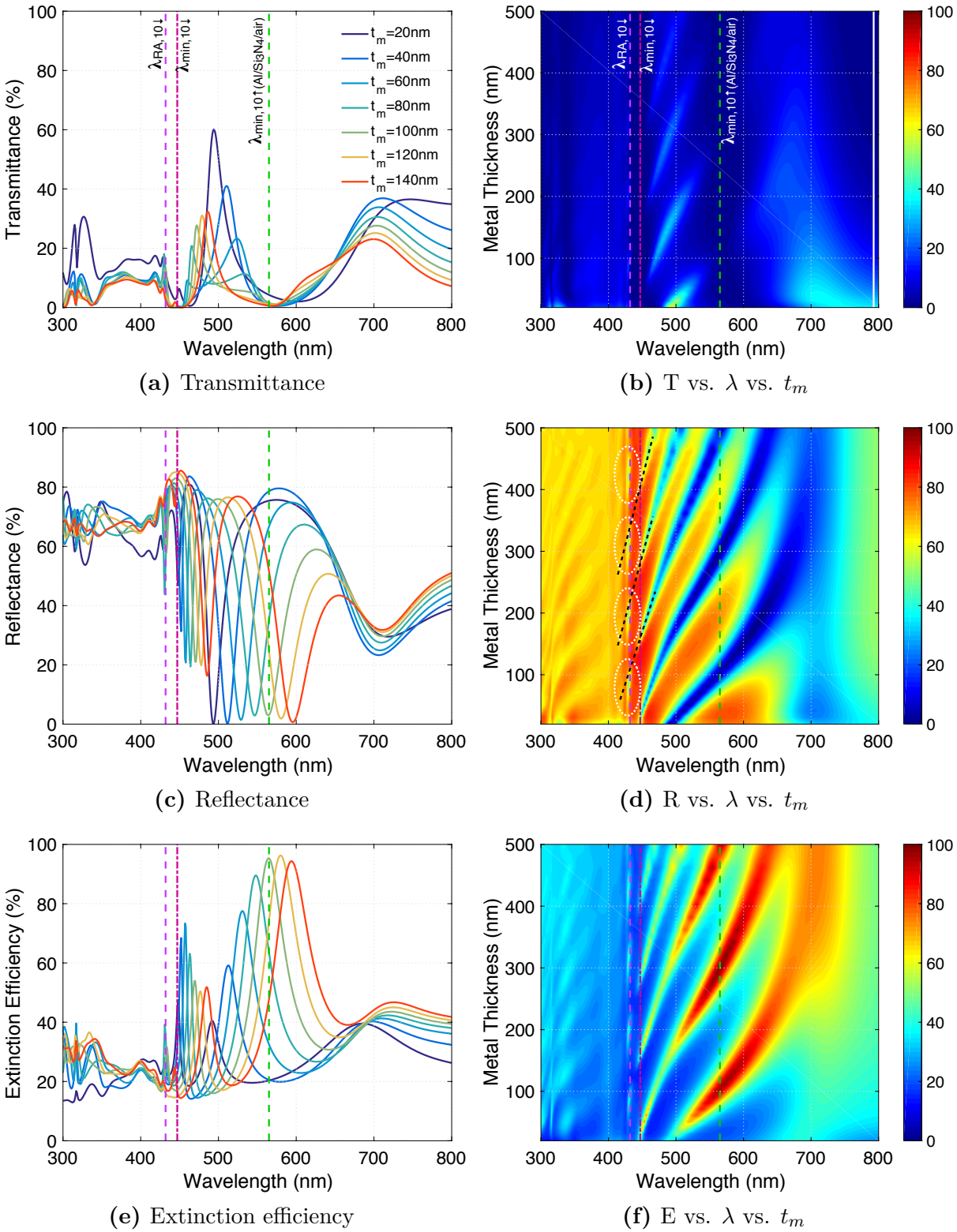
Figure 6.5: Influence of the thickness of the Si_3N_4 cap layer. 2D images of the transmission efficiency of a Asym-(thin)SML array as a function of the Si_3N_4 cap layer thickness for periodicities a_x of **(a)** 280 nm and **(b)** 480 nm. Simulation parameters: diameter $d = \mathrm{round}(a_x/1.8)$ nm, Al thickness $t_m = 40$ nm, holes filled with Si_3N_4.

100 nm is the best choice to optimise the performance of the Asym-(thin)SML filter for the whole visible regime.

6.4.2 Metal Thickness

We have seen in the previous Section that the total stack thickness of the structure has a significant effect on the optical properties of Asym-(thin)SML PCFs. However, the total thickness of the stack cannot only be varied as a function of the Si_3N_4 cap thickness but also as a function of the metal thickness t_{m}. The set of plots and images in Figure 6.6 establishes the influence of the thickness of the metal layer on the optical response of the Asym-(thin)SML structure.

Comparing this simulation study with the one in the previous Section, it is evident that increasing the total stack thickness through the increase of the metal thickness does not affect the performance of the filter in the same way. First of all, as the metal thickness increases the transmission efficiency decreases. Also, unlike the previous case, it appears that only one resonance at the time occupies the EOT band between $\lambda_{\mathrm{min},10\downarrow}$ and $\lambda_{\mathrm{min},10\uparrow}$. The resonance appears at $\lambda_{\mathrm{min},10\downarrow}$. As the total stack (metal) thickness increases, the resonance redshifts. It increases in intensity. It reaches the maximum efficiency in the middle of the EOT band and then the efficiency begins to decrease, until the resonance disappears



(a) Transmittance **(b)** T vs. λ vs. t_m

(c) Reflectance **(d)** R vs. λ vs. t_m

(e) Extinction efficiency **(f)** E vs. λ vs. t_m

Figure 6.6: Influence of the thickness of the metallic layer on the optical response of the Asym-(thin)SML structure. 2D plots and corresponding 2D images of the **(a)**, **(b)** transmission, **(c)**, **(d)** reflection, and **(e)**, **(f)** extinction efficiencies of a Asym-(thin)SML array as a function of the thickness of the metal layer. Simulation parameters: $a_x = 340$ nm, $d = 180$ nm, $t_{\text{cap}} = 100$ nm, holes filled with Si_3N_4.

next to the upper limit of the waveband. As the resonance decreases, a new resonance arises at the lower limit of the waveband which goes through the same behavioural path, and so on.

Another major difference lies in the fact that - in both the reflection and extinction spectra - the new resonances of the system, that before were entirely confined between $\lambda_{\text{min},10\downarrow}$ and $\lambda_{\text{min},10\uparrow}$, are now crossing the upper limit and converge to the same position in wavelength as $T_{\text{peak},1}$.

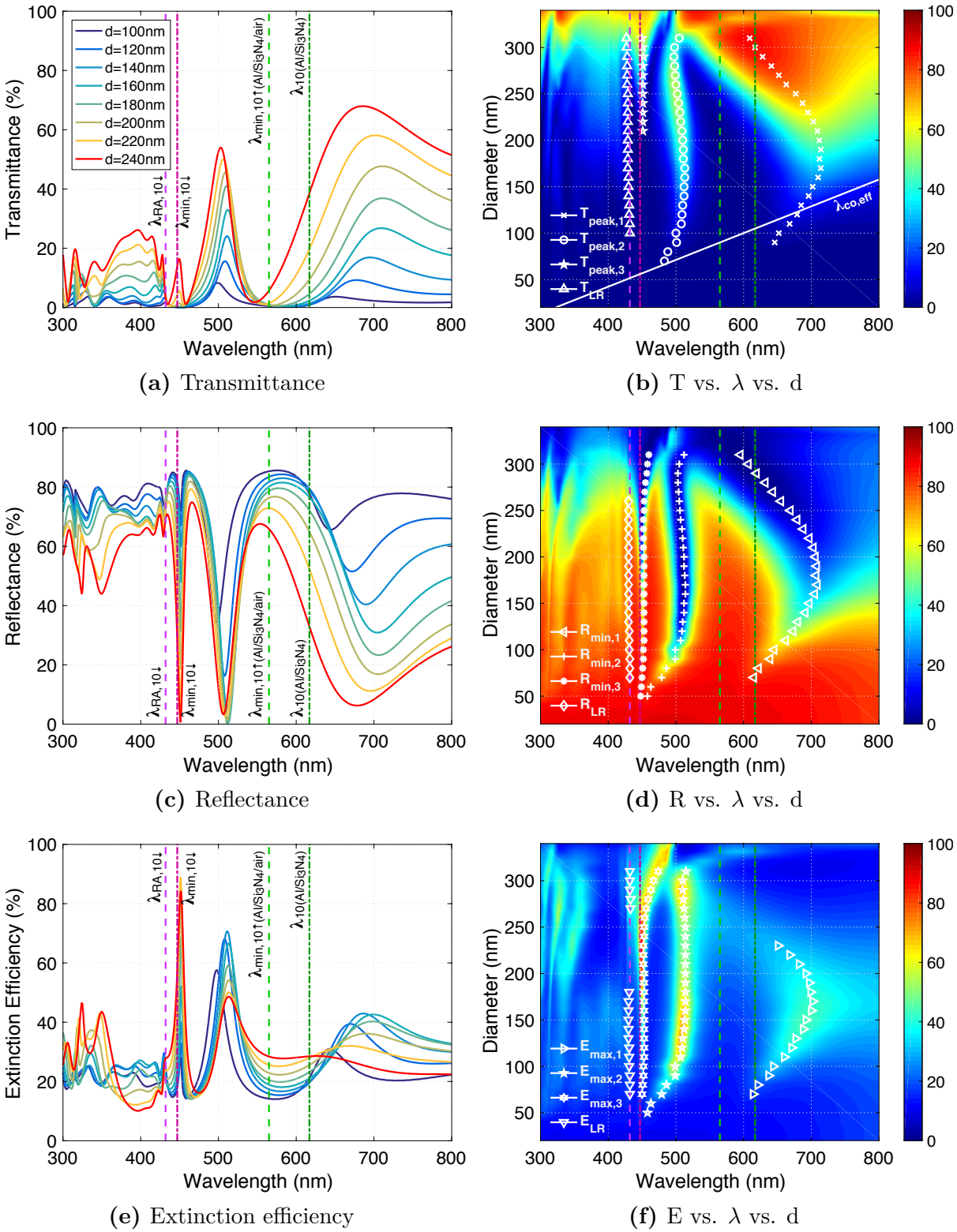
In this case the Si_3N_4 cap thickness is constant and has a value of 100 nm for which the only resonance in the EOT band between $\lambda_{\text{min},10\downarrow}$ and $\lambda_{\text{min},10\uparrow}$ - for the Asym-(thin)SML structure having $a_x = 340$ nm and $t_m = 40$ nm - is $T_{\text{peak},2}$. In addition, EM fields in Figure 6.3c already confirmed the resonance connected to the appearance of a third peak - unlike $T_{\text{peak},2}$ that is resonant cavity mode - is given by a propagating mode in the Si_3N_4 cap layer. Therefore, it should not come as a surprise that the $T_{\text{peak},3}$ resonance does not appear in this case.

6.4.3 Diameter

The set of plots and images in Figure 6.7 establishes the influence of the size of the holes on the optical response of the Asym-(thin)SML structure. As expected, as the diameter increases, the transmission efficiency of the filter increases. However, the transmission efficiency of $T_{\text{peak},1}$ grows significantly faster than $T_{\text{peak},2}$. As a consequence, $T_{\text{peak},1}$ prevails over the other peak as the diameter becomes larger than the distance between two adjacent holes ($d > a_x/2$).

Note that in comparison with the Sym-SML array, the Asym-SML structure starts transmitting at smaller diameter values. In fact, in this case, for a diameter $d = 100$ nm the transmittance of the second peak has almost reached an efficiency of 10% while in the previous case for the same size of the holes the structure just started to transmit, with a transmittance of less than 1%. This is probably due to the higher-RI material inside the holes which makes the holes 'appear larger' by increasing their cutoff wavelength.

Figure 6.8a compares the FWHM of $T_{\text{peak},1}$ and $T_{\text{peak},2}$ as a function of the holes' size.

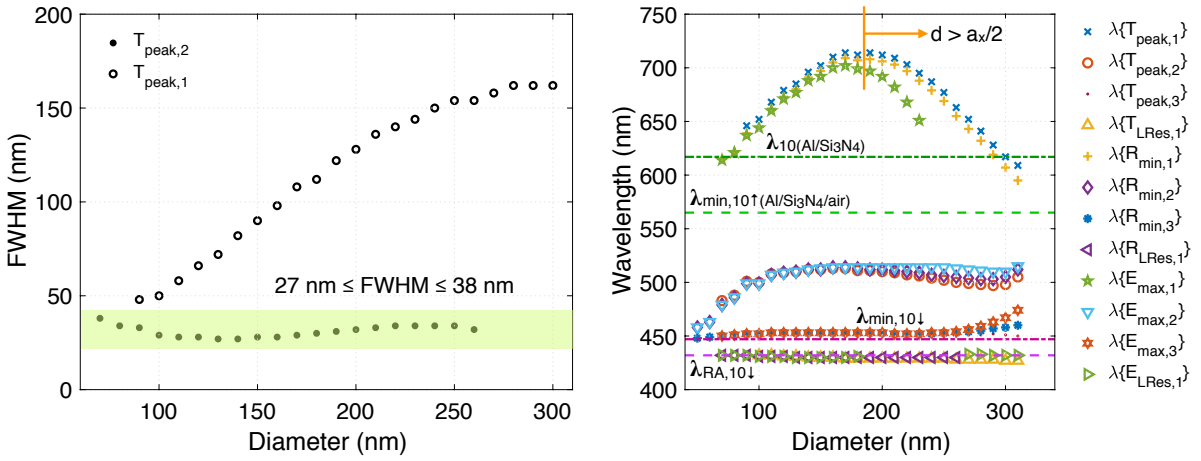


(a) Transmittance **(b)** T vs. λ vs. d

(c) Reflectance **(d)** R vs. λ vs. d

(e) Extinction efficiency **(f)** E vs. λ vs. d

Figure 6.7: Influence of the size of the holes on the optical response of the Asym-(thin)SML structure. 2D plots and corresponding 2D images of the (a), (b) transmission; (c), (d) reflection and (e), (f) extinction efficiencies of a Asym-(thin)SML array as a function of wavelength and diameter of the holes. The larger the holes the higher the transmission efficiency. However, for $d > a_x/2$ the first peak introduces a considerable amount of colour cross-talk that reduces the optical selectivity of the filter. Simulation parameters: periodicity $a_x = 340$ nm, diameter $d = 180$ nm, Al thickness $t_m = 40$ nm, holes filled with Si_3N_4, $t_{cap,Si_3N_4} = 100$ nm.



(a) FWHM **(b)** Peaks (Dips) position in λ vs. d

Figure 6.8: FWHM and peaks' position as a function of the diameter. (a) FWHM and (b) Correlation between the position of peaks in transmission, minima in reflection and maxima in extinction in the zero-order regime as a function of the holes' size.

The FWHM of the first peak greatly increases as the diameter increases. On the other hand, the FWHM of $T_{\text{peak},2}$ remains fairly constant, displaying a maximum deviation from the mean value of merely ± 5-6 nm. In addition, the resonant wavelength $\lambda\{T_{\text{peak},2}\}$ undergoes a very small variation in wavelength, with a maximum deviation of only ± 8 nm. These features are extremely interesting because they ensure the stability of the peak towards possible process variations during the fabrication.

Figure 6.8b shows the correlation between the position of peaks in transmission, minima in reflection and maxima in extinction in the zero-order regime ($\lambda > \lambda_{\text{RA},10}$). Evidently, $T_{\text{peak},1}$ and $T_{\text{peak},2}$ display a different behaviour in wavelength as a function of the diameter. As the hole size increases, $T_{\text{peak},2}$ remains basically constant while $T_{\text{peak},1}$ red-shifts for $d < a_x/2$ and blue-shifts for $d > a_x/2$, quickly approaching the second peak. To maximise the distance between the two peak it would be better to chose a diameter equal to the distance between two adjacent holes, i.e. $d = a_x/2$.

Finally, notice the presence of two localised resonances at approximately $\lambda_{\text{RA},10}$ and $\lambda_{\text{min},10\downarrow}$. The presence of a local resonance at the condition $\lambda = \lambda_{\text{RA},10}$ was already observed during the analysis of the diameter dependence for the Sym-SML structure. However, the resonance at $\lambda = \lambda_{\text{min},10\downarrow}$ did not appear in the optical response of the Sym-SML structure. This resonance is extremely narrow and significantly strong in either reflection and extinction. The positions of both the resonances are unaffected by the size

of the holes. However, the intensity increases as the size of the holes increases.

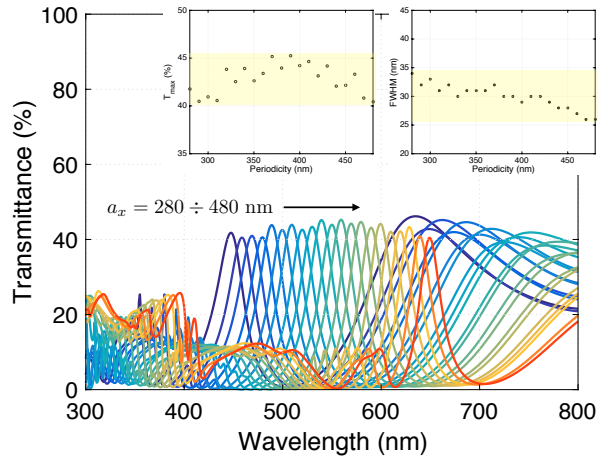
6.4.4 Array Periodicity

The set of plots and images in Figure 6.9 establishes the influence of the periodicity on the optical response of the Asym-(thin)SML structure. As explained previously, varying the periodicity shifts the optical response of the filter along the electromagnetic spectrum[5]. The smaller the periodicity the shorter the working wavelength of the device. In this case, the total stack of the structure is maintained constant to 140 nm (t_m = 40 nm and t_{cap} = 100 nm) as well as a periodicity to diameter ratio equals 1.8 . Note that, in the visible range, the filters efficiency remains quite constant in the 40-45% range. The FWHM is wider at shorter wavelengths and lessen as the periodicity increases. However, it is still confined in quite a small range, between 25 and 35 nm (refer to Figure 6.10a).

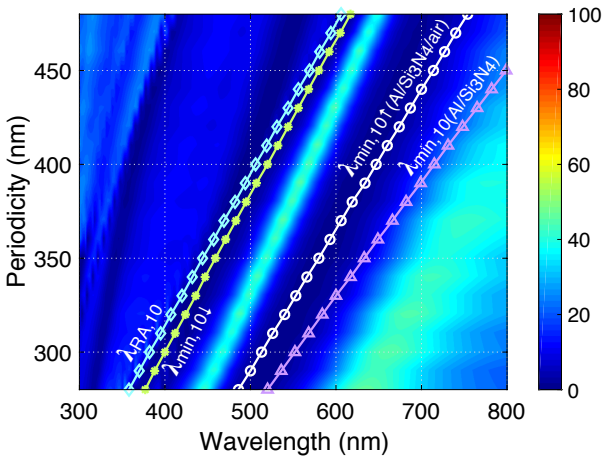
As expected $T_{\text{peak,2}}$ remains confined between $\lambda_{\text{min,10}\downarrow}$ and $\lambda_{\text{min,10}\uparrow}$. However, the peak is closer to the upper limit in the short wave regime and tends to approach the lower limit as the periodicity increases. Figure 6.9e compared the lineshape of $T_{\text{peak,2}}$ as a function of wavelength. The peaks have been overexposed by normalising the wavelength to $\lambda - \lambda_{\text{min,10}\downarrow}$ and confirm the previous observation on the position of the peak. $T_{\text{peak,2}}$ leans towards $\lambda_{\text{min,10}\downarrow}$ at shorter wavelength and towards $\lambda_{\text{min,10}\uparrow}$ at longer wavelengths and presents a hint of a new resonance pushing the peak from the left side. Note that for a_x = 340 nm, i.e. for the periodicity at which we have optimised the device, $T_{\text{peak,2}}$ is approximately at half way between the $\lambda_{\text{min,10}\downarrow}$ and $\lambda_{\text{min,10}\uparrow}$. Would it be possible to maintain $T_{\text{peak,2}}$ at half way between the two minima for each value of periodicity?

The set of plots and images in Figure 6.10 establishes the influence of the periodicity on the optical response of the Asym-(thin)SML structure but this time the total stack of the structure varies with the periodicity. Note that now $T_{\text{peak,2}}$ remains at approximately half way between $\lambda_{\text{min,10}\downarrow}$ and $\lambda_{\text{min,10}\uparrow}$ for every value of periodicity. Figure 6.10e compared the lineshape of $T_{\text{peak,2}}$ as a function of wavelength. Note that now the lineshape is constant with the periodicity. This has been obtained by varying the thickness of the Si_3N_4 cap

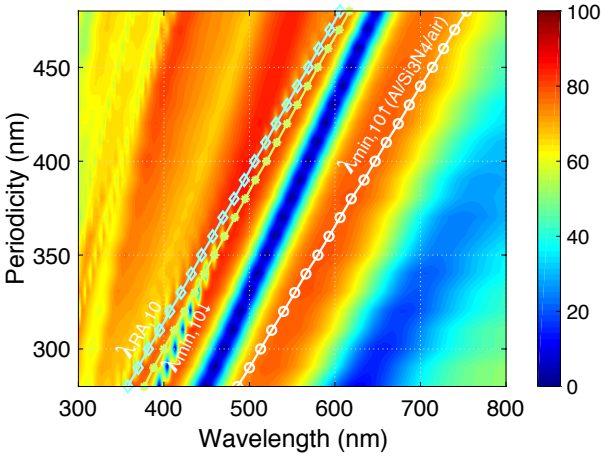
[5]Refer to Section 3.8.3



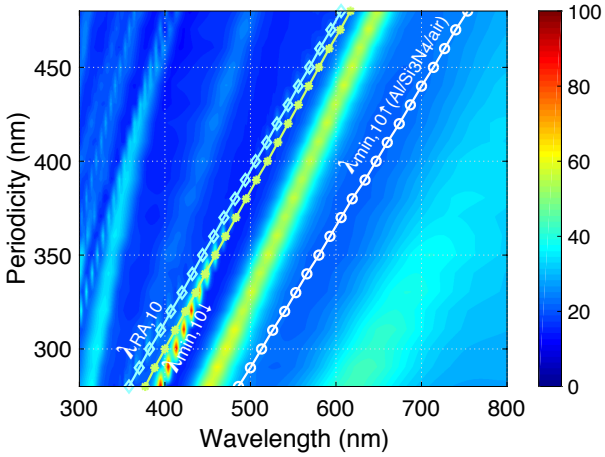
(a) Transmittance



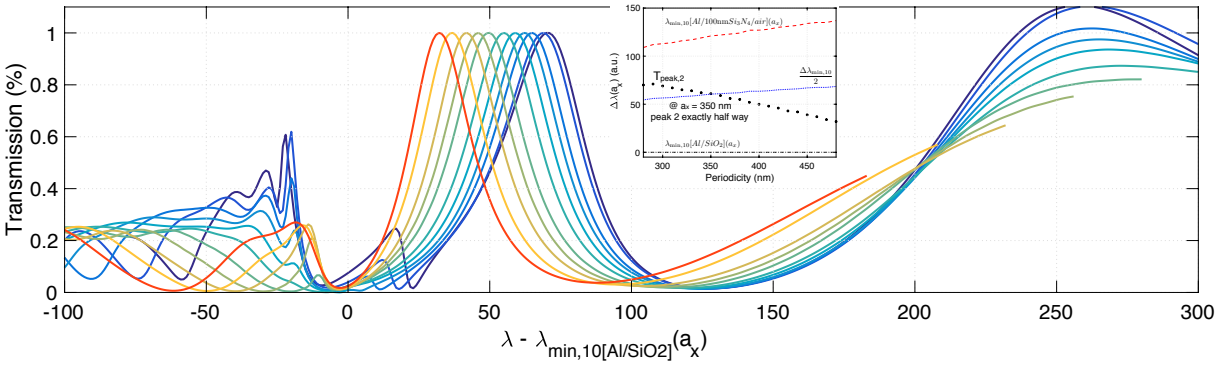
(b) T vs. λ vs. a_x



(c) R vs. λ vs. a_x

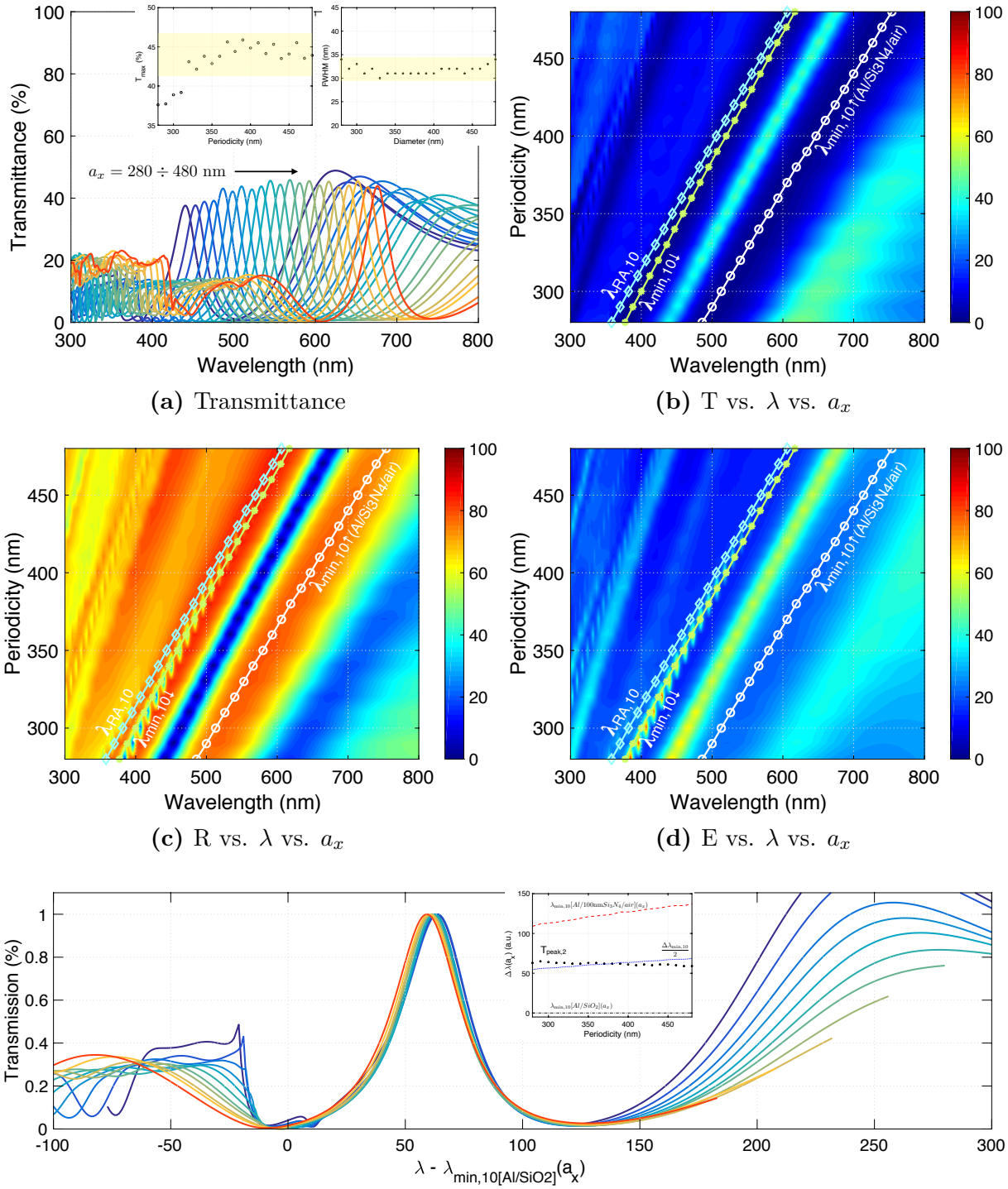


(d) E vs. λ vs. a_x



(e) Normalised transmittance comparison

Figure 6.9: Tuning the optical response of the Asym-(thin)SML structure in wavelength. 2D plots and corresponding 2D images of the (a), (b) Transmission; (c) Reflection and (d) Extinction efficiencies of a Asym-(thin)SML array as a function of wavelength and array periodicity. The smaller the periodicity, the shorter the resonant wavelength(s) of the filter. (e) Lineshape comparison of $T_{\text{peak},2}$ as a function of wavelength. The peaks have been overexposed by normalising the wavelength to $\lambda - \lambda_{\text{min},10\downarrow}$. $T_{\text{peak},2}$ leans towards $\lambda_{\text{min},10\downarrow}$ at shorter wavelength and towards $\lambda_{\text{min},10\uparrow}$ at longer wavelengths. Simulation parameters: $d = round(a_x/1.8)$, Al thickness $t_m = 40$ nm, holes filled with Si_3N_4, $t_{\text{cap},Si_3N_4} = 100$ nm.



(a) Transmittance

(b) T vs. λ vs. a_x

(c) R vs. λ vs. a_x

(d) E vs. λ vs. a_x

(e) Normalised transmittance comparison

Figure 6.10: Tuning the optical response of the Asym-(thin)SML structure in wavelength. 2D plots and corresponding 2D images of the (a), (b) Transmission; (c) Reflection and (d) Extinction efficiencies of a Asym-(thin)SML array as a function of wavelength and array periodicity. The smaller the periodicity, the shorter the resonant wavelength(s) of the filter. (e) Lineshape comparison of $T_{\text{peak},2}$ as a function of wavelength. The peaks have been overexposed by normalising the wavelength to $\lambda - \lambda_{\text{min},10\downarrow}$. The lineshape is now constant with the periodicity. Simulation parameters: $d = \text{round}(a_x/1.8)$ nm, Al thickness $t_m = 40$ nm, holes filled with Si_3N_4, $t_{\text{cap},Si_3N_4} = \text{round}(a_x * 0.23 + 23)$ nm.

layer. The shorter the working wavelength the thinner the cap layer, and vice versa at longer working wavelengths. Now the FWHM is confined in an even smaller range, between 30 and 35 nm, while the transmission efficiency lies mainly around 45%. The ratio periodicity to cap thickness (total stack thickness) have been calculated by optimising the structure in the blue and red regime and then evaluating the linear relationships between them.

Notice that the intensity of $T_{\text{peak},1}$ varies also with the periodicity. The smaller the periodicity the higher the transmission efficiency of $T_{\text{peak},1}$. This appears somehow contradictory to what it has been observed in the diameter study of Section 6.4.3 where the smaller the diameter the lower the transmission intensity of the peak; because if that was the case the maximum intensity of $T_{\text{peak},1}$ should be lower when the periodicity (and thus the diameter) is smaller. Instead, it appears that the actual relationship between the diameter and the transmission efficiency of $T_{\text{peak},1}$ is: the smaller the distance between the holes the higher the transmission efficiency. In fact, when the diameter increases, the distance between the holes decreases and the intensity increases. Similarly, the smaller the periodicity, the smaller the size of the holes but also the shorter the distance between the holes and thus the higher the intensity. This suggests that the total transmittance at $T_{\text{peak},1}$ does not come solely from the electric dipole in between the sidewalls of the holes, but also from another 'source', placed on the top surface of the metal layer. Note in Figure 6.3b the magnetic dipoles that arise in between the holes, on the top surface of the metal layer. Simulation results then suggest that these magnetic dipoles are the main responsible to the transmittance of $T_{\text{peak},1}$.

6.5 Summary

The simulation study on the Asym-(thin)SML structure provided an overview on the spectral characteristic of the filters and their parametrical dependencies. It has been observed that the asymmetry between the bottom and top metal/dielectric interfaces splits the two peaks in transmission - observed in the Sym-SML structure - and confines the narrower peak in wavelength, between the SPPs (1,0) minima of the two interfaces.

The whole bandwidth of this peak is thus given by the distance between those two minima. This notion is extremely helpful to locate the position of the narrow peak in transmission because - independently of the geometrical parameters - it will always appear in that range of wavelengths.

It has also been observed that the total stack thickness of the filter - given by the sum of the metal thickness and the Si_3N_4 cap thickness - strongly affects the position of the narrow peak within the aforementioned range. The peak makes its appearance right next to the condition of existence of the SPP at the bottom interface for $t_{\text{tot}} \geq 80$ nm and red-shifts in wavelength as the total stack thickness increases. Moreover, the thicker the stack the higher the number of resonant modes within the holes.

The Asym-(thin)SML represents a considerable improvement in selectivity with respect the Sym-SML design. Simulation data suggest that a set of filters that covers the entire visible range with a FWHM of 30 nm and transmission efficiency above 40% can be obtained. The transmission efficiency did not improve significantly when compared to the previous case, but the FWHM had been narrowed down to less than a third. However, the main drawback of this configuration is the considerable optical interference of the long-wavelength peak, whose transmittance is given by two contributions: an electric dipole inside the hole in the XZ-plane and magnetic dipoles on the top Al surface in the YZ-plane.

Simulation results presented in this chapter helped to understand some of the physical mechanisms involved in the transmission process of the Asym-(thin)SML structure. In the next chapter it will be demonstrated that by adding a second, thin metal layer on top of the Si_3N_4 cap layer the performance of the filter can be improved further.

Chapter 7

2D Hexagonal Nanohole Arrays: The Metal-Insulator-Metal Stack

In the last chapter, the Asym-(thin)SML structure - composed of a 2D hexagonal array of subwavelength nanoholes milled in a 40-nm Al layer and capped by a 100-nm Si_3N_4 layer that fills also the holes - has been examined through a comprehensive parametric analysis. The design was derived by applying targeted modifications to the Sym-SML plasmonic filter described in Chapter 5. The Asym-(thin)SML design displays a relatively narrow peak in the waveband of interest and represents a significant improvement in selectivity with respect standard PCFs. However, the presence of a second peak at longer wavelengths considerably reduces the optical performance of the filter because - having a transmission efficiency of the same order of magnitude of the narrow peak and a considerably wide bandwidth - it generates a significantly high amount of optical cross-talk.

This chapter establishes how the addition of a second metallic layer on top of the Si_3N_4 cap layer of the Asym-(thin)SML structure changes the optical properties of the filter and considerably reduces the optical contribution from the long-wavelength peak while maintaining the characteristic features of the narrow, short-wavelength peak intact. The new, final structure is composed by a 3-layer metal-insulator-metal (MIM) stack [23]. Insights on the physical mechanisms involved in the transmission process are provided and the spectral characteristics of the MIM filters examined in detail through a comprehensive parametric simulation analysis. By the end of the chapter an 'optimal' set of structural

parameters will be defined for the fabrication of the devices.

Section 7.1 recapitulates the observations derived from the parametric analysis of the previous chapter, describes step-by-step the modifications imposed to the Asym-(thin)SML structure and compares the results. Section 7.2 studies the SPPs modes at the bottom, top and middle interfaces and looks for correlations in the characteristic traits of the EOT spectra of the MIM filters. Electromagnetic near-field patterns at the transmission maxima are examined in Section 7.3 and compared with the electromagnetic near-field patterns at the transmission maxima of the two previous configurations, Sym-SML and Asym-(thin)SML respectively. Section 7.4 is a detailed parametric analysis of the MIM structure and presents the dependence of the optical response on its geometric and constitutive parameters, namely diameter, stack thickness, metal thickness and also cladding, middle layer and hole filling materials. Finally, the main observations and remarks are summarised in Section 7.5.

7.1 Introduction

In the transmission spectrum of a Asym-(thin)SML structure two resonances can be identified: a narrower, antisymmetric resonant mode at shorter wavelengths, $T_{\text{peak,2}}$, and a broader, symmetric resonant mode at longer wavelengths, $T_{\text{peak,1}}$. Unlike the case of the Sym-SML structure, the two resonant modes have well-defined positions in the EOT band of the Asym-(thin)SML structure. The parametric analysis in Chapter 6 demonstrated that $T_{\text{peak,2}}$ is always confined in a specific range of wavelengths, between $\lambda_{\text{min,10}\downarrow}$ and $\lambda_{\text{min,10}\uparrow}$, independently from the geometric and constitutive parameters of the filter; while $T_{\text{peak,1}}$ remains above $\lambda_{\text{min,10}\uparrow}$.

$T_{\text{peak,2}}$ displays a relatively high transmission, above 40%, and a considerably narrow FWHM, of approximately 30 nm, along the entire visible range. Therefore, it would be a quite competitive passband filter for integrated multispectral applications, which as mentioned before should have FWHM of approximately 50 nm or less. However, despite a separation in wavelength of approximately 200 nm between $T_{\text{peak,2}}$ and $T_{\text{peak,1}}$, the latter still generates a considerable amount of cross-talk (in particular for shorter periodicities)

because it has a transmittance that is of the same order of magnitude of the transmittance of $T_{\text{peak},2}$.

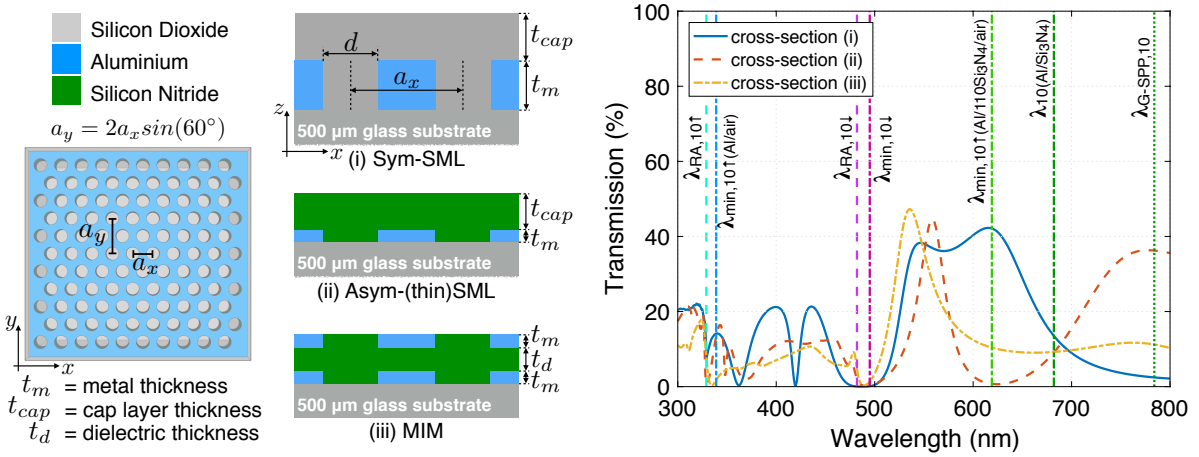
The dependence of $T_{\text{peak},1}$ on the geometrical parameters of the structure has been established from the simulation results. The transmission efficiency of $T_{\text{peak},1}$ could be decreased by reducing the size of the holes or by increasing the metal thickness. However, both of these approaches decrease also the intensity of $T_{\text{peak},2}$ and thus they have been discarded. On the other hand, simulation results also established that the main contribution to the transmittance of $T_{\text{peak},1}$ originates from magnetic dipoles on the top Al surface, in between adjacent holes. It is then fair to assume that if we could somehow 'block' or 'screen' the radiation pattern from these magnetic dipoles, the transmittance of $T_{\text{peak},1}$ should be considerably lowered in intensity.

A second Al layer - exact copy of the bottom one - has been then added on top of the Si_3N_4 cap layer of the Asym-(thin)SML structure to 'screen' the contribution from the magnetic dipoles. The structure is now composed of a 3-layer $Al/Si_3N_4/Al$ stack. However, given the previous considerations on the effect that the total thickness of the filter has on the optical properties of $T_{\text{peak},2}$, the thickness of the Si_3N_4 layer has been reduced to 70 nm so that the total thickness of the structure is 150 nm, given that the metal layers have both a thickness $t_m = 40$ nm.

The optimum value for the total thickness of the Asym-(the)SML filter, evaluated in the previous Chapter, was 140 nm ($t_m = 40$ nm and $t_{\text{cap},Si_3N_4} = 100$ nm). So why the thickness has been increased to 150 nm? The periodicity of the structure chosen as starting development point has been increased from 340 nm to 380 nm, so that the narrow peak $T_{\text{peak},2}$ would be centred in the green region of the visible spectrum, and thus according to simulation results the optimum cap thickness should be increased of 10 nm[1].

Figure 7.1a presents the schematic top view and cross-section of the proposed (iii) MIM architecture, in comparison with the cross-sections (i) and (ii) of the two previously reported configurations - Sym-SML and Asym-(thin)SML, respectively. Their transmission characteristics are presented and compared in Figure 7.1b. The three filters have

[1]Refer to Figure 6.10e. The cap thickness and the periodicity have a linear relationship according to $t_{\text{cap},Si_3N_4} = \text{round}(a_x * 0.23 + 23)$ nm. Hence, for a periodicity $a_x = 380$ nm, $t_{\text{cap},Si_3N_4} = 110$ nm



(a) Top view and cross sections. **(b)** Transmittance comparison.

Figure 7.1: From broad- to narrow-band plasmonic colour filters. (a) Top view of a hexagonal nanohole array and cross sections of three different configurations of plasmonic filters on half-space SiO_2 substrates: (i) Sym-SML: a thick Al layer capped with a SiO_2 layer, holes filled with SiO_2; (ii) Asym-(thin)SML: a thin Al layer capped with a Si_3N_4 layer, holes filled with Si_3N_4; (iii) MIM: a metal-insulator-metal stack of Al-Si_3N_4-Al, holes filled with Si_3N_4. (b) Comparison of the transmission efficiencies of the MIM structure with the Asym-(thin)SML and Sym-SML designs. MIM: t_m = 40 nm, t_d = 70 nm, no cap. Asym-(thin)SML: t_m = 40 nm, t_{cap} = 110 nm. Sym-SML: t_m = 150 nm, t_{cap} = 200 nm. For all the structures: periodicity a_x = 380 nm and diameter d = 210 nm. The introduction of a high-RI material results in a narrow passband feature in the waveband of interest, while the addition of a second metallic layer, an exact copy of the bottom one, greatly reduces the transmission of the broad peak at longer wavelengths and thus the optical colour crosstalk. The vertical lines represent the minima in transmission corresponding to the conditions of SPP excitation at the different interfaces and the appearance of diffractive effects such as RAs, as indicated.

the same total thickness t_{stack} = 150 nm. Note how the addition of the second top thin metallic layer in the MIM structure (from configuration (ii) to (iii)) greatly reduces the transmission efficiency of the second broad peak at longer wavelengths, $T_{\text{peak},1}$, down to a third with respect the Asym-(thin)SML structure. On the other hand, the transmission efficiency and the lineshape of $T_{\text{peak},2}$ remain basically unaffected.

Note however that $T_{\text{peak},2}$ in the MIM configuration is slightly blue-shifted, with respect the Asym-(thin)SML case, and its lineshape is asymmetrical, skewed towards $\lambda_{\text{min},10\downarrow}$. According to previous simulation data on the total stack thickness of the Asym-(thin)SML filter, this suggests that the addition of the second metallic layer has slightly reduced the effective length of the cavity. Therefore, to restore the symmetry in the lineshape of the peak the total stack thickness of the filter should probably be increased.

The vertical lines in Figure 7.1b represent the wavelengths evaluated from the conditions (5.1) and (5.2), for the SPPs excitation and occurrence of RAs as a function of SPP

dispersion relations and additional wavevectors G_{ij}. Note that $\lambda_{\mathrm{RA},10\downarrow}$ and $\lambda_{\mathrm{min},10\downarrow}$ are the same for all the three structures because the type of metal, substrate and periodicity are the same. On a different note, the second minimum in transmission $\lambda_{\mathrm{min},10\uparrow(Al/Si3N4/air)}$ present for the Asym-(thin)SML structure does not seem to find a counterpart in the MIM structure, even if $T_{\mathrm{peak},2}$ remain confined in the same waveband.

$\lambda_{\mathrm{min},10\uparrow(\mathrm{Al/air})}$ and $\lambda_{\mathrm{RA},10\uparrow}$ refer to the SPPs and RAs at the top Al/air interface of MIM structure. $\lambda_{\mathrm{G\text{-}SPP},10}$ is given by the condition $k_{\mathrm{G\text{-}SPP}} = G_{10}$, where $k_{\mathrm{G\text{-}SPP}}$ is the dispersion relation of the gap surface plasmon polariton G-SPP generated from the SPPs coupling between the middle interfaces[2]. $\lambda_{10(\mathrm{Al/Si_3N_4})}$ indicates where would be the position of the minimum in case of a single interface between Al and Si_3N_4.

7.2 Characteristic Traits in the Optical Spectra

Figure 7.2 analyses the correlation between the excitation of SPPs, the occurrence of RAs, and the appearance of characteristic traits in the transmittance and reflectance of the MIM structure. The letters A, B, C and D indicate the positions of $\lambda_{\mathrm{RA},10\uparrow}$, $\lambda_{\mathrm{min},10\uparrow}$ and $\lambda_{\mathrm{RA},10\downarrow}$, $\lambda_{\mathrm{min},10\downarrow}$, where the symbol $\uparrow$ and $\downarrow$ indicate that they refer to the top interface and bottom interface, respectively. These wavelengths correspond to minima in the transmission spectrum. Note the characteristic 'edges' in transmittance and reflectance just before the Rayleigh anomalies.

The letter E indicates where it would be the position of a minimum in case of a single interface between Al and Si_3N_4. This point does not correspond to a specific trait in the optical spectra of the MIM structure, however it seems to be a good approximation to indicate the separation of the two peaks in transmission: $T_{\mathrm{peak},2}$ belongs to the range of wavelengths between D and E, while $T_{\mathrm{peak},1}$ is confined at wavelengths longer than E. Assigning the peaks to specific wavebands is useful because it allow us to know in advance what to expect in the optical spectra of a specific structural configuration, in this case the MIM design, even before running a simulation.

[2]Refer to Section 3.7.3 on symmetric MIM plasmonic waveguides.

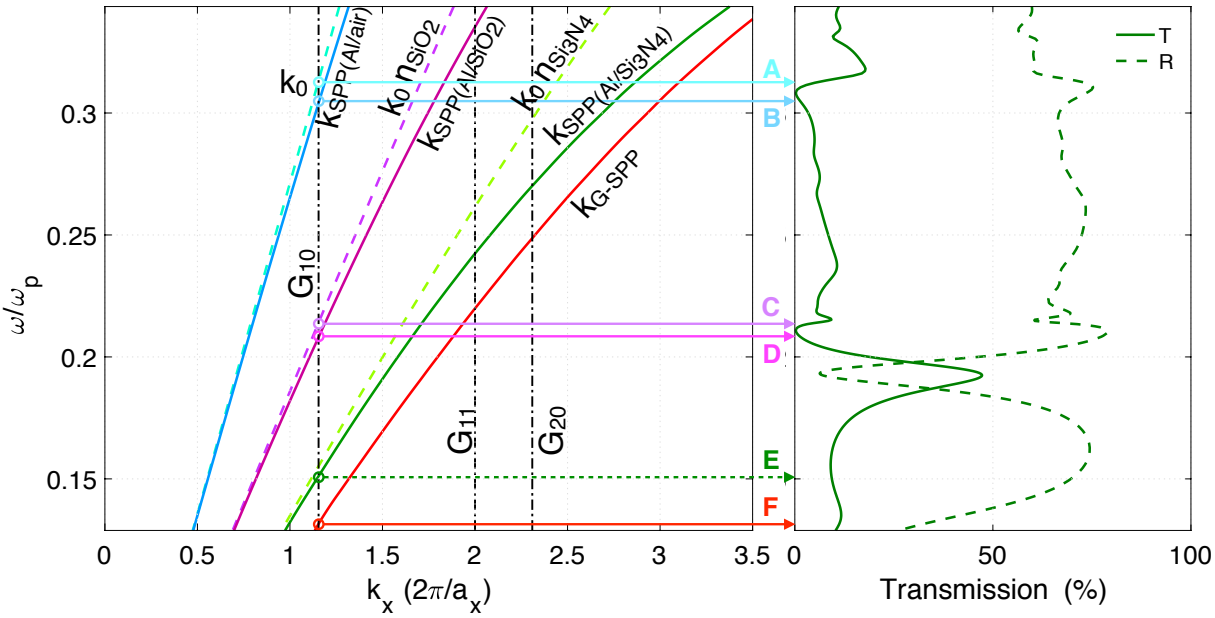
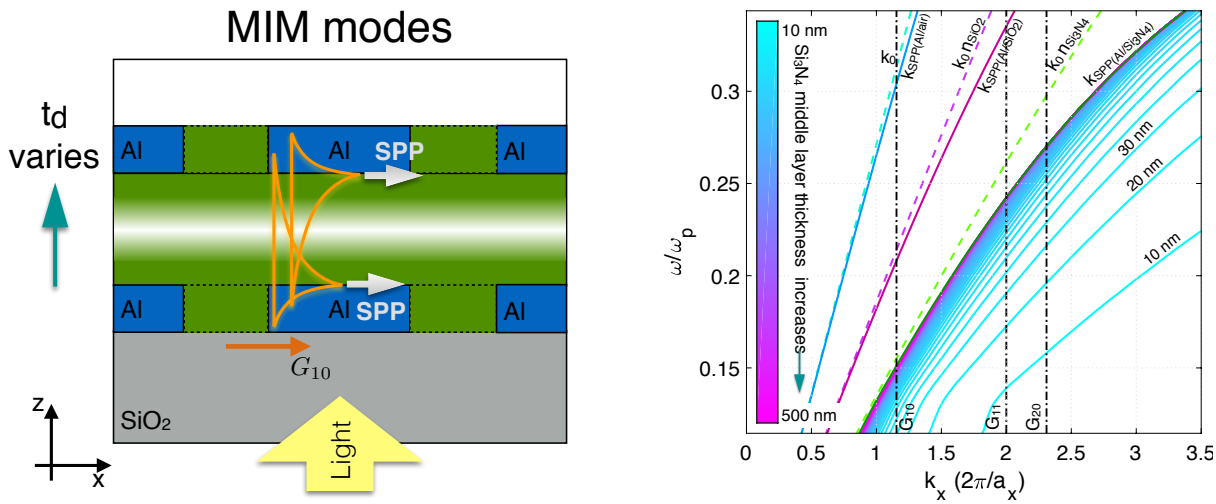


Figure 7.2: SPPs and diffractive effects at the interfaces of the MIM structure. Correlation between the excitation of SPPs at the bottom, top and middle interfaces of the MIM structure and characteristic traits in the optical spectra of the MIM structure. The bottom Al/SiO_2 and the top Al/air interfaces can be considered as single interfaces because, despite the finite thickness of the metal layers, the SPP penetration depth δ_{SPP} inside the Al is 2-3 times smaller than the metal thickness of the layers $t_m = 40$ nm. Instead, the SPPs at the middle Al/Si_3N_4 interfaces couple with each other and the result is the so called Gap-SPP. The letters A, B, C and D indicate the positions of $\lambda_{RA,10\uparrow}$, $\lambda_{min,10\uparrow}$ and $\lambda_{RA,10\downarrow}$, $\lambda_{min,10\downarrow}$. The letter E coincides with the matching of the condition $k_{SPP(Al/Si_3N_4)} = G_{10}$ for a single Al/Si_3N_4 interface. Finally, the letter F indicates the position of $\lambda_{G\text{-}SPP,10}$. Left graph: the cyan, purple, green and red solid lines represent the SPP dispersion relations while the the respective dashed lines represent the light lines, as indicated in the image. The vertical dashed-dotted black lines represent the additional wavevectors G_{ij} provided by the periodicity of the array. The angular frequency ω is normalised to the plasma frequency of Al $\omega_p = 12.04$ eV[174]. Wavevectors are normalised by $2\pi/a_x$. Right graph: the solid green line represents the transmittance of the MIM structure, while the dashed green line represents the reflectance. Periodicity $a_x = 380$ nm, diameter $d = 210$ nm, metal thickness $t_m = 40$ nm and middle Si_3N_4 layer thickness $t_d = 70$ nm.

It is interesting to notice, however, that the wavelength $\lambda_{min,10\uparrow(Al/110Si_3N_4/air)}$ - derived from the SPP at top IIM interface of the Asym-(the)SML structure - seems to be an even better approximation for the upper limit of the narrow peak waveband[3]. It is almost as if the tail of the SPP at the lower middle interface could 'feel' the air environment through the holes and this could somehow constrain the position of the peak in a smaller range, similarly to the Asym-(the)SML structure.

In the MIM structure the top and bottom interfaces are different (asymmetric) but the dielectric at the top interface has a lower RI than the substrate material and thus $\lambda_{min,10\uparrow}$

[3]Refer to Figure 7.1b



(a) Scheme of SPPs in a MIM stack.

(b) Numerical solutions of GAP-SPPs.

Figure 7.3: Gap SPP between the middle interfaces of the MIM structure. (a) Scheme of the coupling of SPPs between the middle interfaces of the MIM structure. (b) Plot of the numerical solutions of G-SPP in a Al/Si_3N_3/Al MIM structure for different gap distances (Si_3N_4 thicknesses) between 10 and 500 nm. The cyan, purple, green and red solid lines represent SPP dispersion relations while the the respective dashed lines represent the light lines, as indicated in the image. The vertical dashed-dotted black lines represent the additional wavevectors G_{ij} provided by the periodicity of the array. The angular frequency ω is normalised to the plasma frequency of Al $\omega_p = 2.24e^{16}$ rad/s[174]. Wavenumbers are normalised by $2\pi/a_x$, with $a_x = 380$ nm.

appears at shorter wavelengths than $\lambda_{\text{min},10\downarrow}$. However, note that the EOT peak does not appear in between those two minima. This implies that the previous observations on the position of $T_{\text{peak},2}$ - while accurate for the Asym-(thin)SML structure - they do not apply to this case. It seems that a better generalisation would be that the peak $T_{\text{peak},2}$ appears between $\lambda_{\text{min},10\downarrow}$ and $\lambda_{10(\text{hole material/Al})}$ (for $n_{\text{hole}} \neq n_{\text{sub}}$).

Finally, the letter F indicates the position of $\lambda_{\text{G-SPP},10}$, i.e. represents the intersection between the dispersion relation of the bound SPP at the middle interfaces - also known as G-SPP - and the additional wavevector G_{10}. Figure 7.3a is a schematic representation of the coupling of SPPs between the middle interface of the MIM structure, while Figure 7.3b is a plot of the numerical solutions of the G-SPP in a Al/Si_3N_4/Al MIM structure for different gap thicknesses. The G-SPP is the only mode that exist in a symmetric MIM waveguide for all values of the gap thickness[89,95]. As the gap thickness increases, the solutions tend to the single interface solution $k_{\text{SPP(Al/Si}_3\text{N}_4)}$. The dispersion relation of the G-SPP mode is greater than or equal to the dispersion relation of the flat (middle layer)/Al interface, and therefore, for any gap thickness, $F \geq E$. However, the point F

does not correspond to a specific trait in the optical spectra of the MIM structure.

The G-SPP mode is the only mode that exists for all values of the gap thickness t_d [89,95], however that is not the only mode that can arise in a MIM plasmonic waveguide. In fact, in addition to the plasmonic modes, there are also oscillatory modes [19,89].

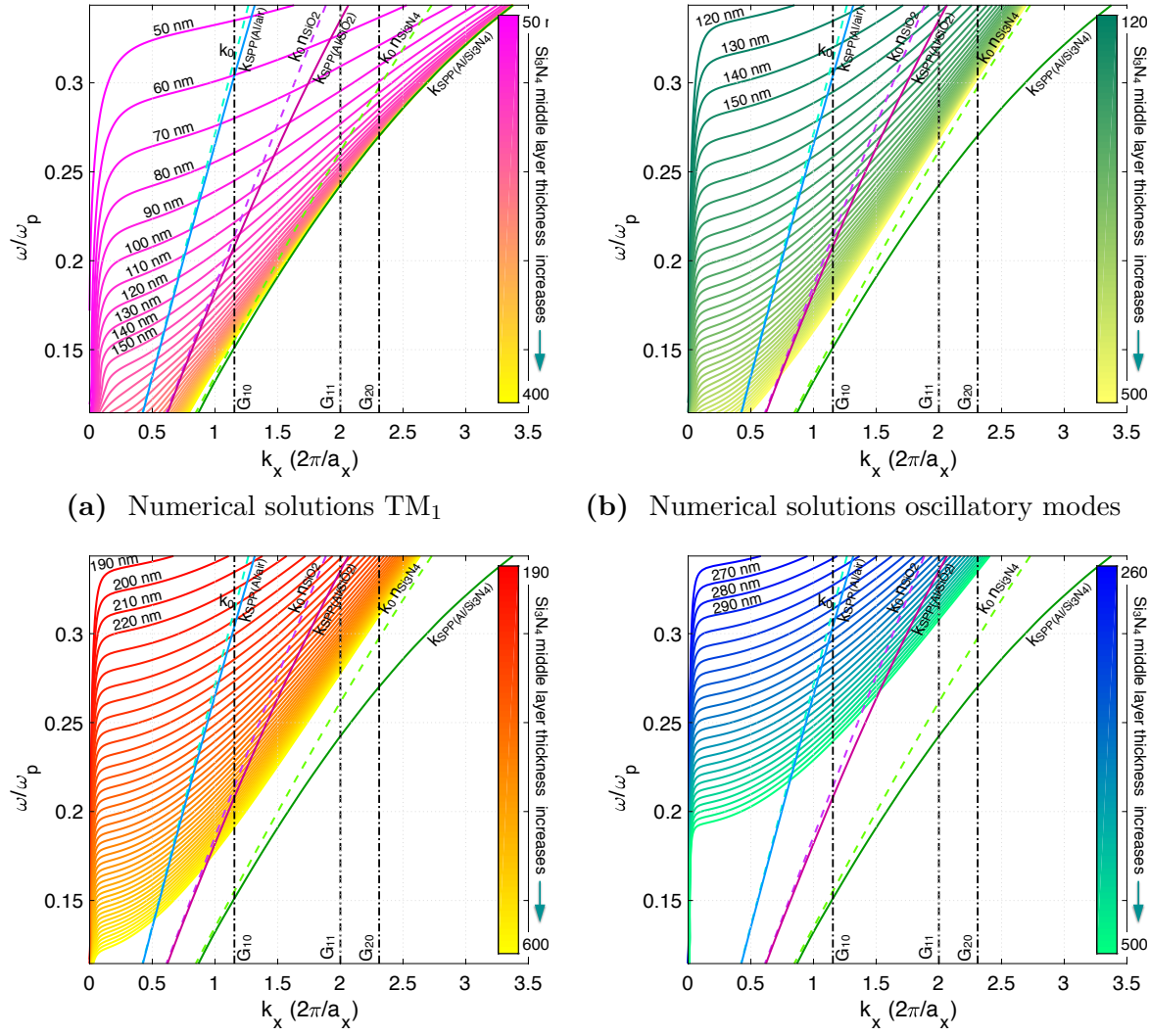
7.2.1 MIM oscillatory modes

According to the pre-defined initial guess, numerical Matlab solvers might provide different solutions to a higher order equation. During the evaluation of the G-SPP we have 'stumbled upon' other solutions for the MIM stack, as a function of the gap thickness. These solutions are plotted in Figures 7.4(a-d). It is apparent that, unlike SPPs modes, they do not belong to the region of bound modes[4]. The wavevectors of the numerical solutions in Figures 7.4b, 7.4c and 7.4d are limited to the range of values $0 \leq \beta \leq k_0\sqrt{\epsilon_{Si_3N_4}}$. Therefore, according to the theory of Orfanidis [89] reported in Section 3.7.2, they are oscillatory modes. As expected, the larger the gap thickness, i.e. the distance between the two metal surfaces, the higher the number of modes inside the waveguide.

Note, however, that the mode in Figure 7.4a differs from the others. In fact, unlike the others that converge to the upper limit $\beta = k_0\sqrt{\epsilon_{Si_3N_4}}$ at infinite gap width, this mode have an upper cut-off thickness at $\beta = k_0\sqrt{\epsilon_{Si_3N_4}}$. However, this mode does not stop at the upper cut-off thickness, it continues through the light line and thus its wavenumber becomes larger than $k_0\sqrt{\epsilon_{Si_3N_4}}$. This means that this mode is an oscillatory mode between $0 \leq \beta \leq k_0\sqrt{\epsilon_{Si_3N_4}}$ and then becomes a plasmonic mode for $k_0\sqrt{\epsilon_{Si_3N_4}} \leq \beta \leq \infty$. Therefore, the upper cutoff thickness of the oscillatory mode corresponds exactly to the lower cutoff thickness of the plasmonic mode. According to the theory this mode is the TM_1 oscillatory/plasmonic mode [89].

Note that for a gap thickness $t_d = 70$ nm there is only one oscillatory mode, the TM_1 oscillatory/plasmonic mode, and it does not cross the EOT band ($\lambda_{TM_1} < \lambda_{min,10\downarrow}$). Oscillatory modes start crossing the EOT band when $t_d \geq 130$ nm.

[4] Refer to Figure 3.4a



(a) Numerical solutions TM_1 **(b)** Numerical solutions oscillatory modes

(c) Numerical solutions oscillatory modes **(d)** Numerical solutions oscillatory modes

Figure 7.4: Oscillatory modes between the middle interfaces of the MIM structure. Oscillatory modes arise in a MIM waveguide when the thickness of the insulating layer is large enough. The cyan, purple, green and red solid lines represent the SPP dispersion relations while the respective dashed lines represent the light lines for different dielectric. The vertical dashed-dotted black lines represent the additional wavevectors G_{ij} provided by the periodicity of the array. The angular frequency ω is normalised to the plasma frequency of Al $\omega_p = 2.24e^{16}$ rad/s[174]. Wavenumbers are normalised by $2\pi/a_x$, with $a_x = 380$ nm.

7.3 Electromagnetic Near-Field Patterns

Figures 7.5 and 7.6 display the squared amplitude of the electric and magnetic fields at the transmission maxima, in the XZ-plane and YZ-plane respectively, for the three configurations represented in Figure 7.1. For the MIM and Aym-(thin)SML designs, a clear confinement of either the magnetic or the electric field suggests that the nanoholes behave like dielectric optical cavity resonators. The two identifiable maximum peaks in transmis-

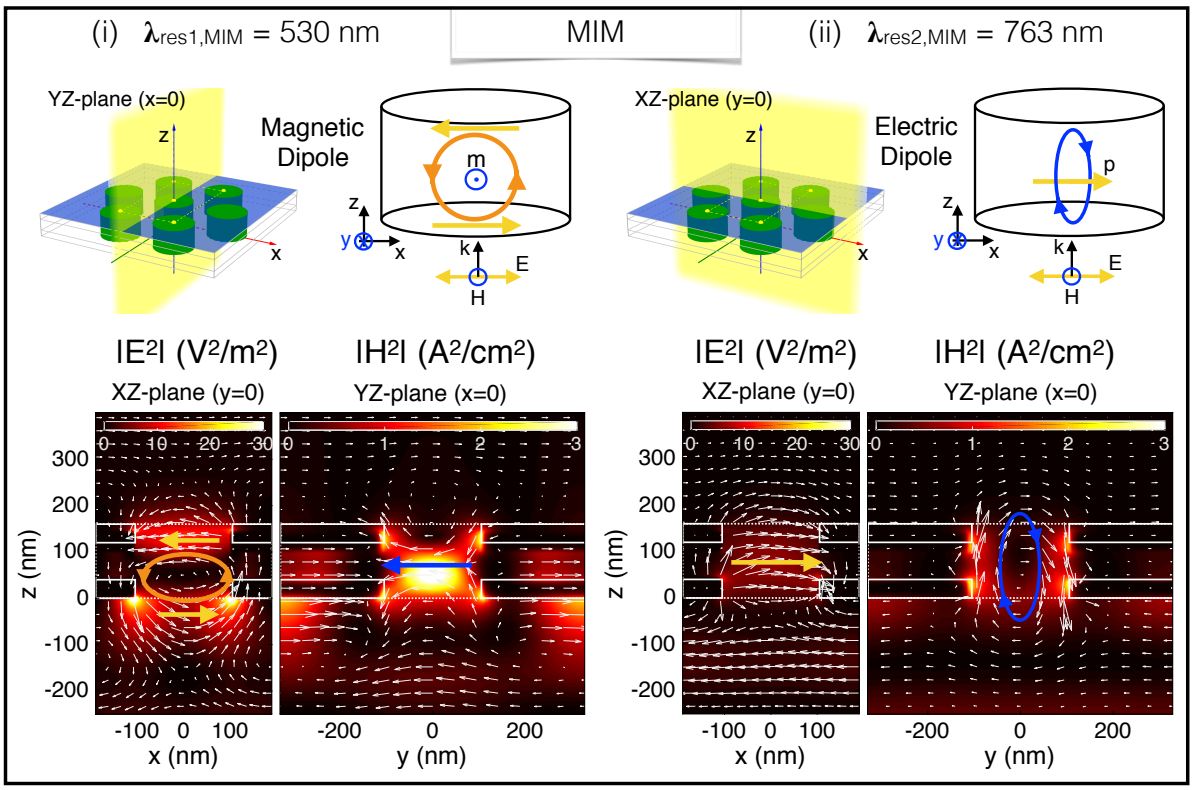


Figure 7.5: Magnetic and electric dipoles at optical wavelengths in the MIM structure. Squared amplitudes of the electric and magnetic fields at resonances, in the XY-plane and YZ-plane respectively, for the MIM structure. The white arrows in the background represent the electric and magnetic vectors potential, respectively. The orange and blue circles represent electric and magnetic current loops, respectively. The yellow and blue thick lines represent electric and magnetic dipoles, respectively. The MIM structure shows a clear confinement of either the magnetic, $\lambda_{res,1}$, or electric, $\lambda_{res,2}$ field, which corresponds to a magnetic or electric dipole respectively.

sion are caused by a magnetic dipole (MD) in the YZ-plane, λ_{res1}, and an electric dipole (ED) in the XZ-plane, λ_{res2}. The appearance of magnetic and electric resonant modes in subwavelength dielectric resonators (DRs) at visible frequencies has been successfully demonstrated in several studies, from dielectric nanoparticles[180,181,182,183] to dielectric resonators nanoantennas[184].

Usually, electromagnetic (EM) confinement in DRs arises from a large difference in permittivity, of the order of tens of units[88,184], between the material that composes the resonator and the dielectric environment. Moreover, the resonance of isolated DRs is solely given by their structural parameters. However, in this case, the confinement of the fields is sustained by the presence of metal at the sidewalls of the holes and the resonant wavelength depends strongly on the coupling of SPRs. Consequently, the resonant modes are given by a collective response of the nanoholes and shift in wavelength with the

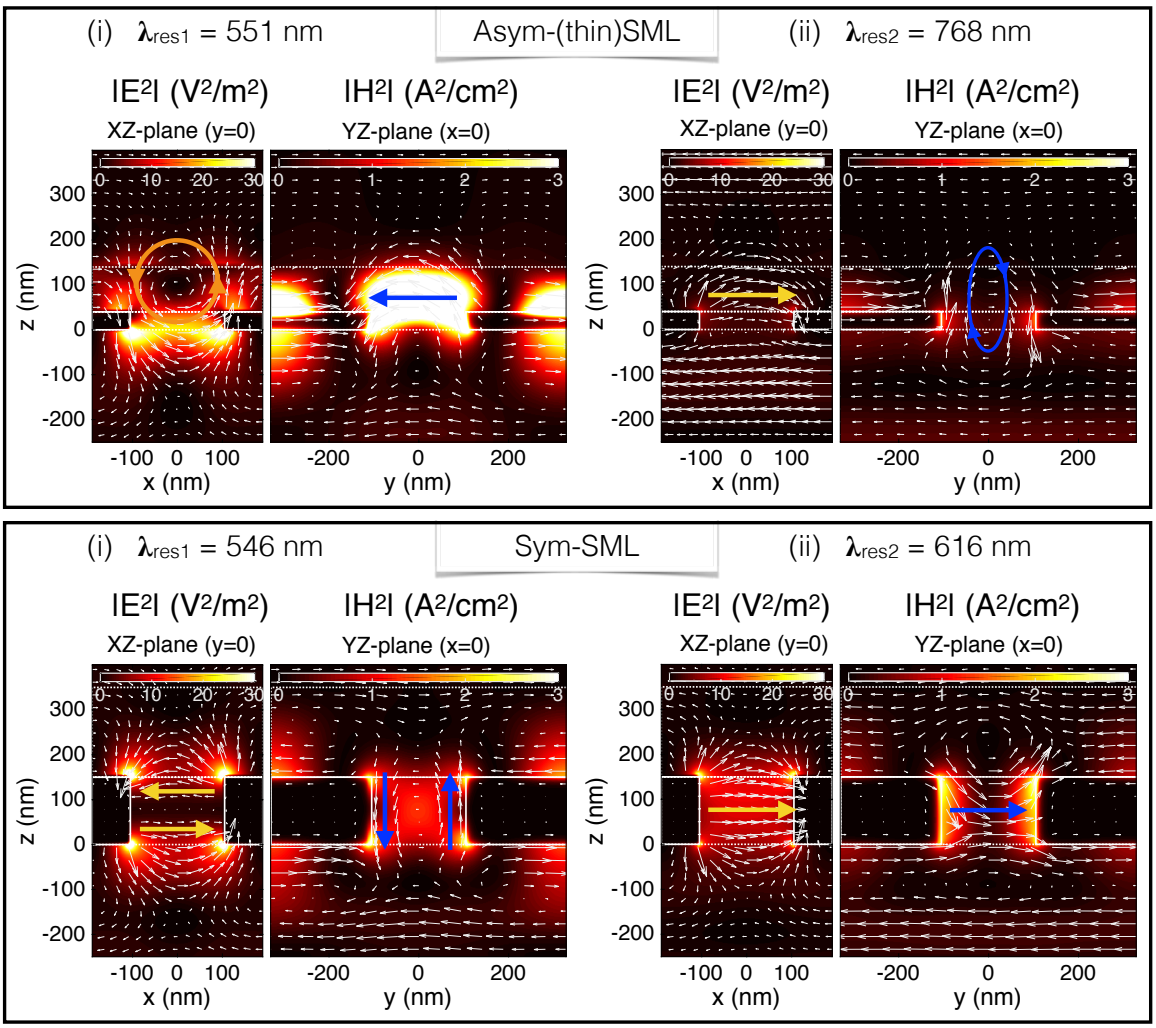


Figure 7.6: Magnetic and electric dipoles at optical wavelengths in the Asym-(thin)SML and Sym-SML structures. Squared amplitudes of the electric and magnetic fields at resonances, in the XY-plane and YZ-plane respectively, for the **(top)** Asym-(thin)SML and **(bottom)** Sym-SML structures. The white arrows in the background represent the electric and magnetic vectors potential, respectively. The orange and blue circles represent electric and magnetic current loops, respectively. The yellow and blue thick lines represent electric and magnetic dipoles, respectively. Similarly to the MIM design, the Asym-(thin)SML structure shows a clear confinement of either the magnetic, $\lambda_{res,1}$, or electric, $\lambda_{res,2}$, field which corresponds to a magnetic or electric dipole respectively. MIM and Asym-(thin)SML structures display a higher degree of confinement of the modes along z due to the higher difference in RI between the hole filling material and the substrate/cap layers. In fact, in the Sym-SML case, the fields can extend inside the substrate and cap layers, which are composed by the same material of the hole filling, and thus the effective length of the cavity modes is larger.

periodicity a_x of the array, which in turn provides the matching condition for the SPP excitations, and establishes the polarisation of the charges and, as a result, also the near-electric field pattern within the nanostructure.

The MD mode is characterized by an electric displacement current loop, which induces an orthogonally-oriented magnetic dipole moment[181,183]. The current loop requires op-

posite orientation of the electric field along z, and thus can only exist when there is enough retardation of the $E_x(z)$ field between the cavity extremities[181]. In contrast, the ED mode originates from the collective polarisation of the nanoholes in response to an external driving field, parallel to the polarisation of the electric field. A magnetic current loop is then induced by the oscillating ED. This current loop can also extend outside the dielectric cavity, enabling the ED mode to exist even when the cavity is too short to support the MD mode. Clearly, the resonant wavelength of the modes depends on the optical length of the cavity.

Knowing that a resonance within a cavity occurs when its length is an integral number of half-wavelength of the wave[88,181,184,185], we can approximate the effective optical length of a cavity mode as $h_{\text{eff}} \approx \alpha\lambda_{\text{res}}/(2n)$, where α is an integer larger than zero, λ_{res} is the resonant wavelength and n is the RI of the cavity. As in the case of DRs or a slab waveguide[88], the higher the RI of the core material with respect the cladding, the higher the degree of confinement and thus the shorter the effective optical length of the mode. This effect can be observed from the fact that the MIM and Asym-SML architectures clearly display a higher degree of confinement of the fields at resonances. In the Sym-SML case, the magnetic field extends into both the silicon dioxide substrate and cap layer, which results in an optically thicker cavity. This means that the resonances of all three structures appear in the same wavelength range despite the difference in RI of the cavity material.

The identification of magnetic and electric dipoles at resonances is extremely interesting for the development of the plasmonic filters. Above the first-order transmission minimum $\lambda_{\text{min}}|_{@k_{\text{SPP}}(\omega)=G_{10}}$, the transmission of the array is given by the superposition of the magnetic and electric dipoles contributions. This insight makes it possible to control these two physical phenomena and thus to optimise the transmission properties of a nanohole array for a specific application by tailoring the choice of geometrical and material parameters.

7.4 Parametric Analysis

In this Section, a parametric analysis to study the influence that different geometric and physical parameters have on the optical response of 2D hexagonal MIM arrays is presented. This study is used to analyse the device performance and to identify the best set of parameters for the fabrication of the devices. For every parameter, the performance will be evaluated in terms of: (i) efficiency, (ii) optical bandwidth of the filter and (iii) stability to process variations.

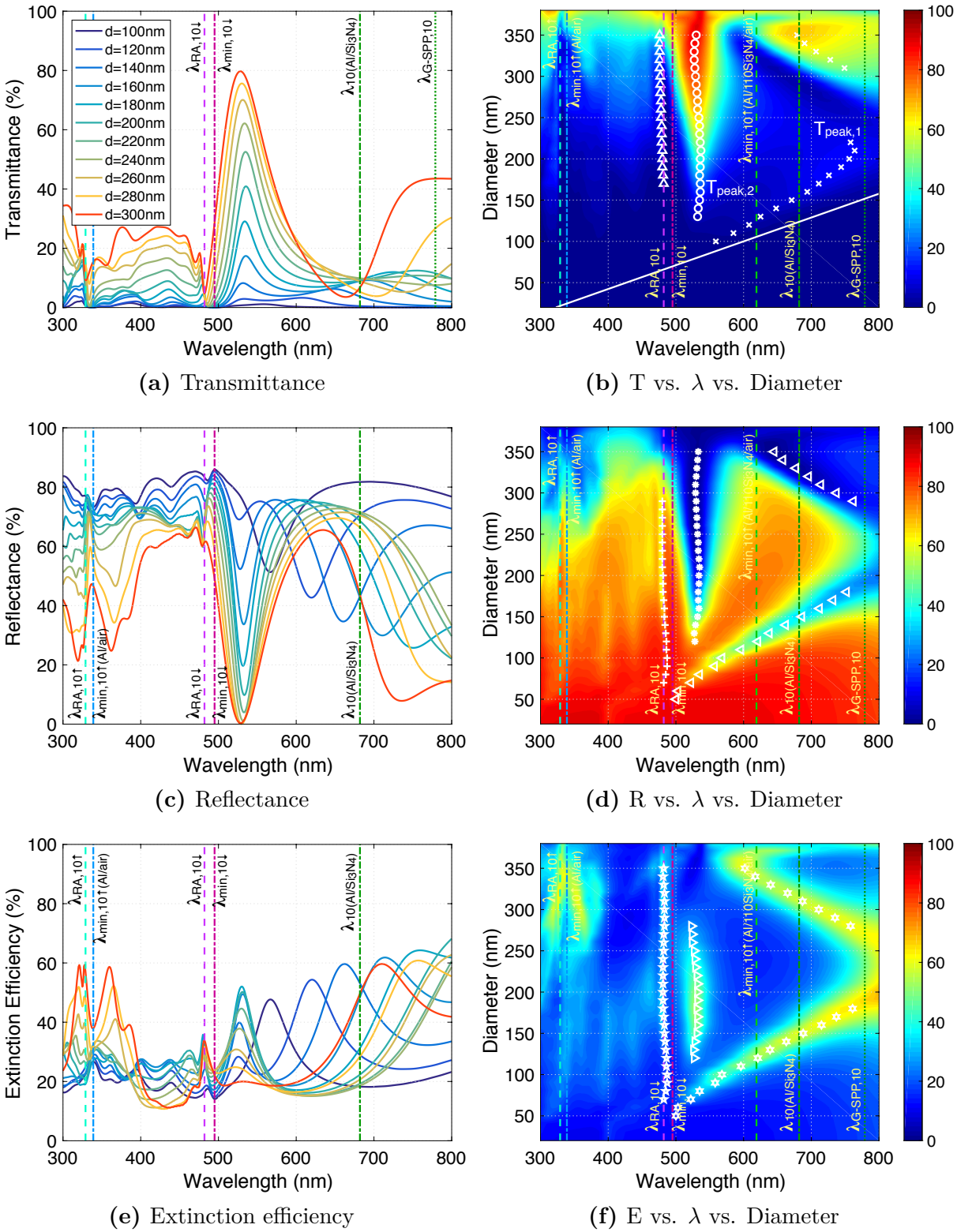
The final objective of this study is to optimise the MIM structure so that it could be used as an integrated multispectral filter for imaging applications in the visible range. The main objectives are: (i) to increase further the transmission efficiency, ideally above 60% so that it becomes comparable with the transmittance of some of the commercially available filters[5]; (ii) maintain a reasonably narrow bandwidth in the range 30-50 nm. Finally, the MIM structure should be optimised to offer the best performance in every range of the visible spectrum but the filters should all have the same total stack thickness in order to be fabricated all in one single lithographic step.

7.4.1 Diameter

The set of plots and images in Figure 7.7 establishes the influence of the size of the holes on the optical response of the MIM structure. By increasing the diameter of the holes it is possible to increase the transmission efficiency of the filter. At the same time, the larger the diameter, the broader the linewidth. Nonetheless, even at the largest value of diameter plotted in Figure 7.7a, the FWHM is approximately 75 nm, which is still 25% narrower than the FWHM of the Sym-SML filters[6], while the maximum transmission reaches 80%.

As expected, because the effective length of the cavity - given by the retardation of the $E_x(z)$ - remain constant, the MD resonant peak ($T_{\text{peak},2}$) displays good stability to variations of the size of the holes. This was already observed for the Asym-(thin)SML

[5]Refer to Figure 5.1b.
[6]Refer to Figure 7.1b.



(a) Transmittance **(b)** T vs. λ vs. Diameter

(c) Reflectance **(d)** R vs. λ vs. Diameter

(e) Extinction efficiency **(f)** E vs. λ vs. Diameter

Figure 7.7: Influence of the size of the holes on the optical response of the MIM structure. 2D plots and corresponding 2D images of the **(a)**, **(b)** transmission, **(c)**, **(d)** reflection, and **(e)**, **(f)** extinction efficiencies of a MIM array as a function of wavelength and diameter. The larger the size of the holes the higher the transmission efficiency of $T_{\text{peak},2}$. Its FWHM also increases but not as significantly as in the Sym-SML case. When $d = 2/3a_x$, the distance between $T_{\text{peak},1}$ and $T_{\text{peak},2}$ is maximised. Simulation parameters: $a_x = 380$ nm, $t_m = 40$ nm, $t_d = 70$ nm, middle layer is Si_3N_4, holes are filled with Si_3N_4, no cap layer.

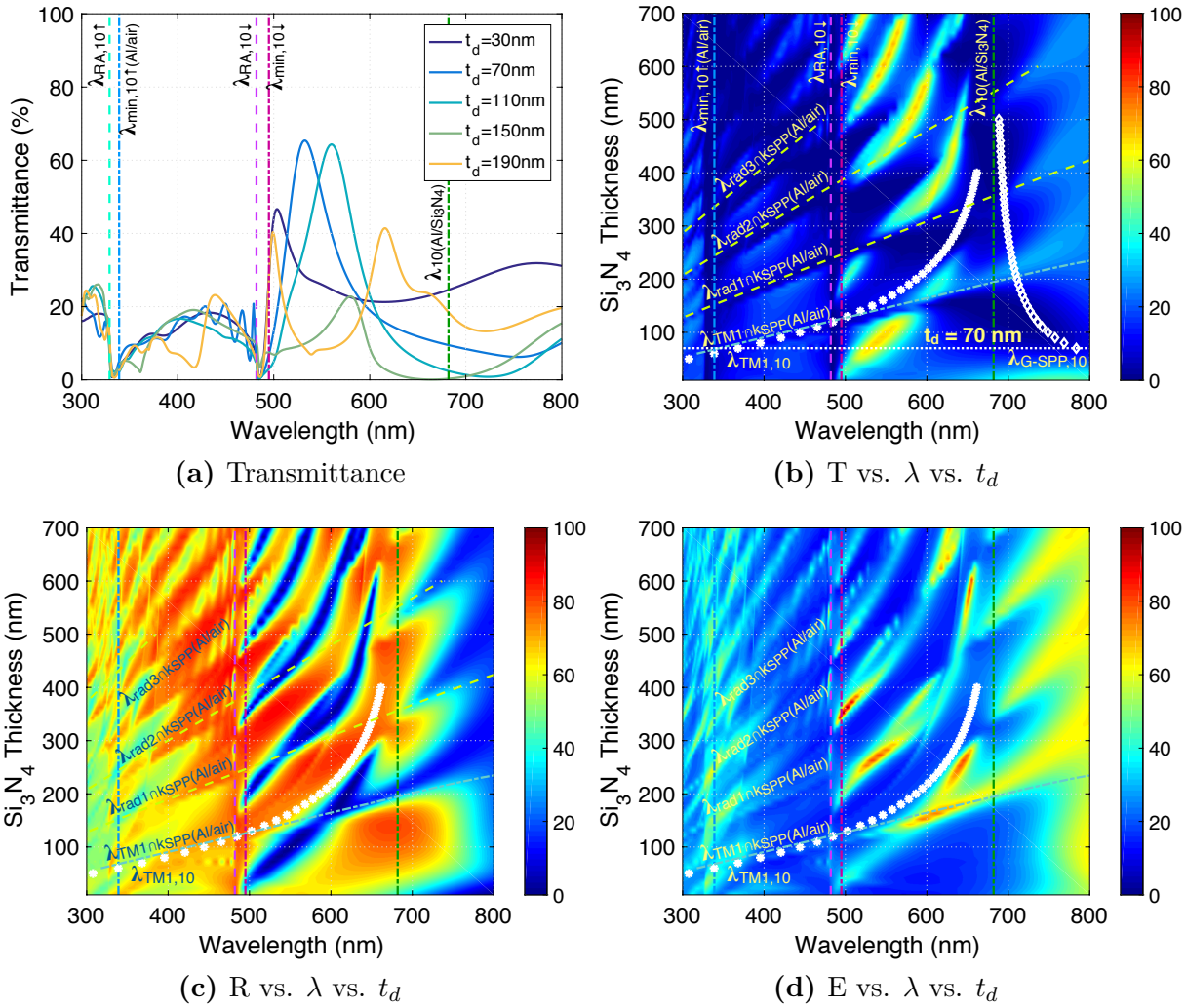
structure. However in the Asym-(thin)SML case the transmission efficiency did not reach - for the same ratio periodicity to diameter - such high efficiency values. This means that, with the MIM design, the efficiency of the cavity has been effectively increased with respect the Asym-(thn)SML case.

Note that $T_{\text{peak},1}$ shifts in wavelength following a pattern similar to that observed for the Asym-(thin)SML structure. For small diameters, the peak red-shifts as the size of the hole increases but it starts to blue-shift when the diameter of the holes becomes larger than approximately 2/3 of the periodicity a_x and not for $d > a_x/2$, as for the Asym-(thin)SML structure. Moreover, in the MIM case the peak originates from the condition $\lambda = \lambda_{\text{min},10\downarrow}$, related to the bottom interface, and not from the condition of excitation of the SPPs at the top Al/Si_3N_4 interface.

Given the aforementioned considerations, it has been decided to increase the diameter from 210 to 250 nm. In this way, we increases the transmission efficiency of $T_{\text{peak},2}$ from 40% to above 60% and 'push' the secondary peak $T_{\text{peak},1}$ as far as possible in wavelength. As the diameter increases, the transmission efficiency of $T_{\text{peak},1}$ increases as well but of less than 5% with respect the previous value. The FWHM of $T_{\text{peak},2}$ almost doubles, reaching approximately 60 nm which is slightly higher that what we hoped for but this is probably the best trade-off between efficiency, FWHM and distance between the peaks.

7.4.2 Thickness of the middle dielectric layer

The set of plots and images in Figure 7.8 establishes the influence of the gap thickness, i.e. of the thickness of the Si_3N_4 middle layer, - and thus also of the total stack thickness - on the optical response of the MIM structure. As for the Asym-(thin)SML case, the thicker the stack the higher the number of resonant modes within the cavity. However, in the MIM case, it appears that these modes are somehow 'interrupted', 'cut-through' by the higher-order oscillating modes of the MIM waveguide that when they match the SPPs dispersion relation $k_{\text{SPP(Al/air)}}$ at the top interface generate a minimum in transmission, probably result of a destructive interference behaviour (see Figure 7.8b). Note that when the mode TM_1 matches the reciprocal wavevector G_{10} another minimum appears. However, as the



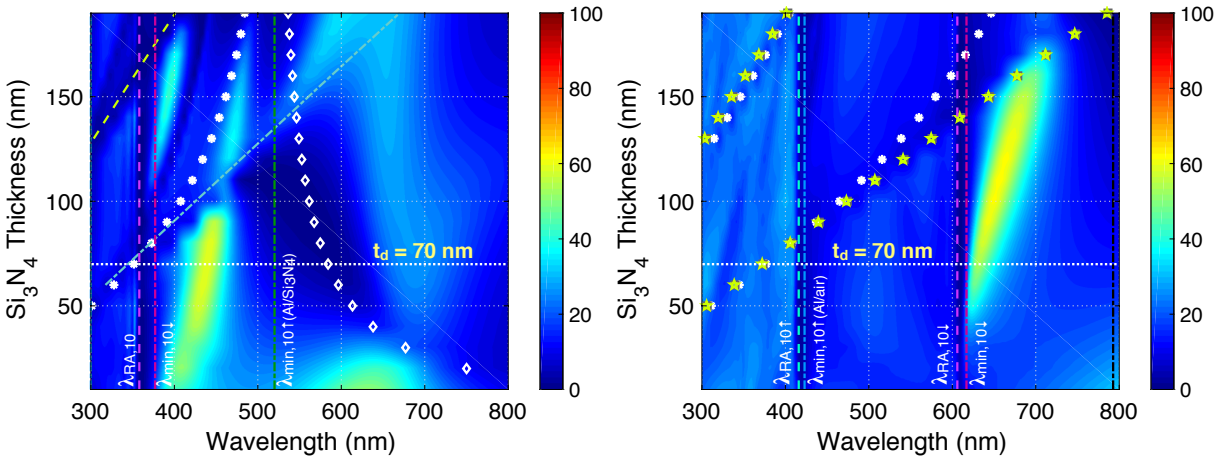
(a) Transmittance **(b)** T vs. λ vs. t_d

(c) R vs. λ vs. t_d **(d)** E vs. λ vs. t_d

Figure 7.8: Influence of the middle layer thickness on the optical response of the MIM structure. 2D plots and corresponding 2D images of the **(a)**, **(b)** transmission, **(c)** reflection, and **(d)** extinction efficiencies of a MIM array as a function of wavelength and middle layer thickness (and thus also total stack thickness). The thicker the MIM stack the larger the number of resonant modes within the structure. These modes are confined between $\lambda_{\text{min},10\downarrow}$ and $\lambda_{\text{min},10(Al/\text{Si}_3\text{N}_4)}$. Simulation parameters: $a_x = 380$ nm, $d = 250$ nm, $t_m = 40$ nm, middle layer is Si_3N_4, holes are filled with Si_3N_4, no cap layer.

gap thickness increases, this minimum does not 'cut-through' the $T_{\text{peak},2}$ in the EOT band, but instead it seems to be 'pushing' the peak towards longer wavelengths.

Note that even for a Si_3N_4 thickness of 600-700 nm the transmittance does not show any major decrease in efficiency as the gap thickness increases. However, at that point the thickness of the middle layer is already more than 6 times larger than the SPP penetration depth in the Si_3N_4. Therefore, the top and the bottom metal layers are not coupled anymore. The structure effectively works solely as a resonant cavity where the top and the bottom metal layers behaves like mirrors. However, it is interesting to notice that the



(a) T vs. λ vs. t_d ($a_x = 280$ nm) **(b)** T vs. λ vs. t_d ($a_x = 480$ nm)

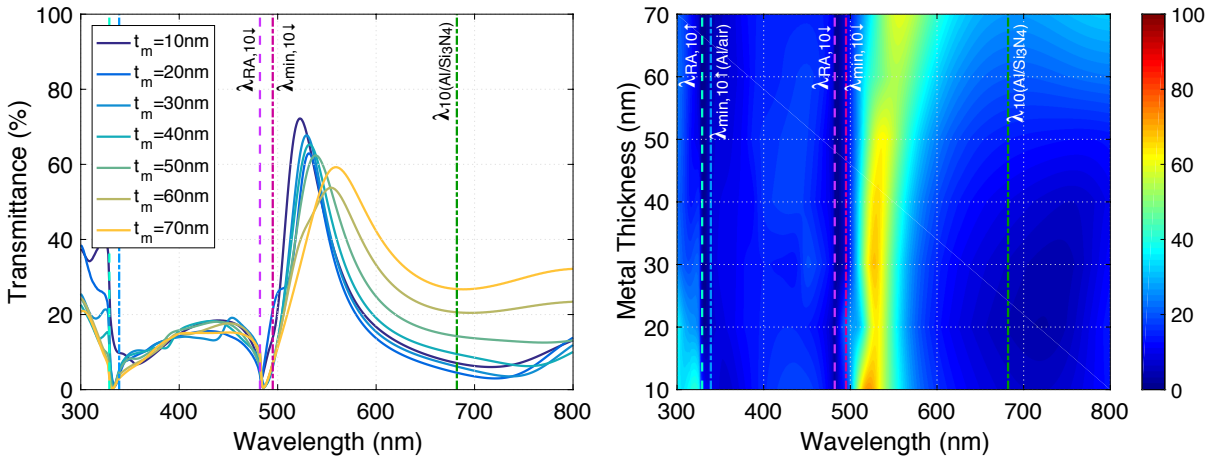
Figure 7.9: Comparison of the influence of the middle layer thickness on the optical response of the MIM structure in different optical regimes. 2D plots of the transmittance of the MIM filter as a function of wavelength and middle layer thickness. (a) $a_x = 280$ nm, (b) $a_x = 480$ nm. Simulation parameters: $d = 250$ nm, $t_m = 40$ nm, middle layer is Si_3N_4, holes are filled with Si_3N_4, no cap layer.

resonances in transmission remain confined between $\lambda_{\text{min},10\downarrow}$ and $\lambda_{\text{min},10(Al/Si_3N_4)}$.

Simulation results on the Asym-(thin)SML structure established that the 'optimal' stack thickness is not the same in every regime of the visible spectrum. However, to limit the lithography to a single step, a constant t_{stack} for all the filters is preferable. Therefore, we need to chose a stack thickness that is suitable for the entire visible range. The two plots in Figure 7.9 establish the influence of the gap thickness on the optical response of the MIM structure in the blue and red regimes of the visible spectrum, respectively. As expected, in the blue range $T_{\text{peak},2}$ makes it first appearance for lower values of gap thickness while in the red part of the spectrum for higher values. In line with the simulation results, we decided that a Si_3N_4 thickness of 70 nm is the best choice to optimise the performance of the MIM filter for the entire visible spectrum and avoid interference from higher order modes.

7.4.3 Metal Thickness

In order to gain better insights on the physical mechanism involved in the transmission process of the MIM structure, two cases will be considered: (i) varying the metal thickness while maintaining the same total stack thickness, (ii) varying the metal thickness while



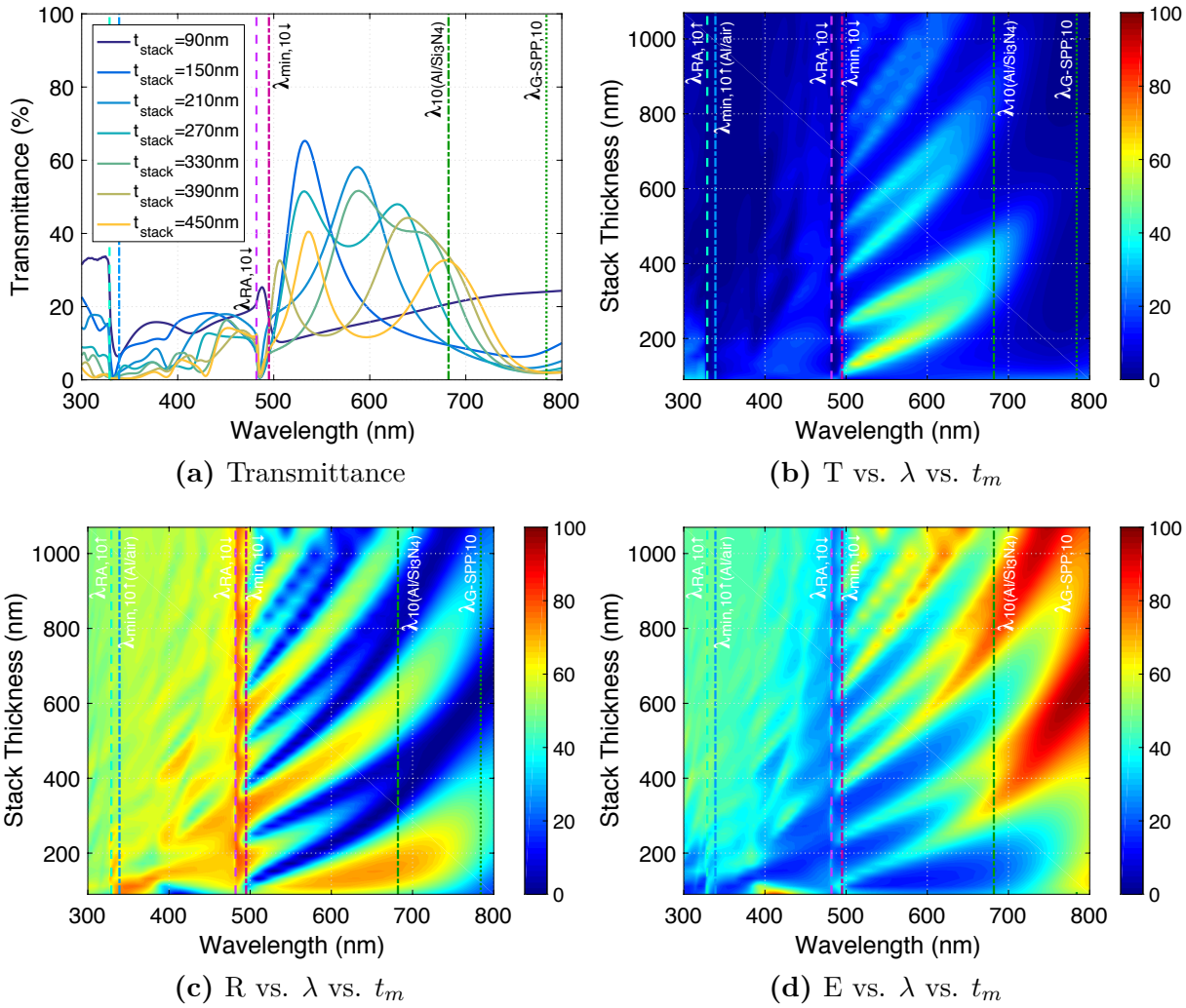
(a) Transmittance **(b)** T vs. λ vs. t_m

Figure 7.10: Influence of the total stack thickness on the optical response of the MIM structure by varying the thickness of the metallic layers, constant t_{stack}. (a) 2D plot and (b) 2D image of the transmittance of the MIM array as a function of wavelength and metal thickness while maintaining constant the total thickness of the MIM stack $t_{\text{stack}} = 150$ nm. Simulation parameters: $a_x = 380$ nm, $d = 250$ nm, middle layer is Si_3N_4, holes filled with Si_3N_4, no cap layer.

maintaining the same middle layer thickness. For simplicity both metal layers have the same metal thickness.

Figure 7.10 establishes the influence of the metal thickness on the optical response of the MIM structure when the total stack thickness of the filter is kept fixed at 150 nm. As the metal increases the transmission efficiency of $T_{\text{peak},2}$ slowly decreases. However, significant variations are recorded only when the metal thickness becomes larger than $40 - 45$ nm or, in other words, when the gap thickness becomes smaller than $30 - 25$ nm. In fact, for $10 < t_m < 40$ the position of the narrow peak $T_{\text{peak},2}$ is basically constant as well as the FWHM of the peak. When the thickness of the middle layer becomes of the order of few tens of nanometers, the transmission of the long-wavelength peak suddenly increases and the peak starts to blue-shift in wavelength until the lineshape matches the one of the Sym-SML structure with the holes filled with Si_3N_4. These observations confirm that the narrow resonance is a cavity resonance and thus doesn't vary in wavelength if the cavity length is maintained and the top and bottom surface are not too close to makes the structure behaves like a single metal layer.

On the other hand, Figure 7.11 establishes the influence of the metal thickness on the optical response of the MIM structure when the gap thickness of the middle layer



(a) Transmittance **(b)** T vs. λ vs. t_m

(c) R vs. λ vs. t_m **(d)** E vs. λ vs. t_m

Figure 7.11: Influence of the metal thickness on the optical response of the MIM structure, constant gap thickness t_d. (a) 2D plot and (b) 2D image of the transmittance of the MIM array as a function of wavelength and thickness of the metallic layers while maintaining constant the gap thickness $t_d = 70$ nm between them. 2D images of the (c) Reflectance and (d) Extinction efficiency. The metal layers have both the same thickness. Simulation parameters: $a_x = 380$ nm, $d = 250$ nm, $t_d = 70$ nm, middle layer is Si_3N_4, holes filled with Si_3N_4, no cap layer.

is kept fixed at 70 nm. Similarly to the Asym-(thin)SML case, the resonant modes in reflection and extinction now cross the upper limit set by the condition $k_{\mathrm{SPP(Al/Si_3N_4)}} = G_{10}$ and converge towards the position of $T_{\mathrm{peak},1}$. On the other hand, in the MIM case the resonances in transmission seem to be paired and as one pair disappears the next one appears and so on. Unsurprisingly, the transmission efficiency decreases as the metal thickness increases. This is because the higher the amount of metal in the structure the higher the absorption.

It is evident that increasing the metal thickness of the layers does not improve the

performance of the MIM structure.

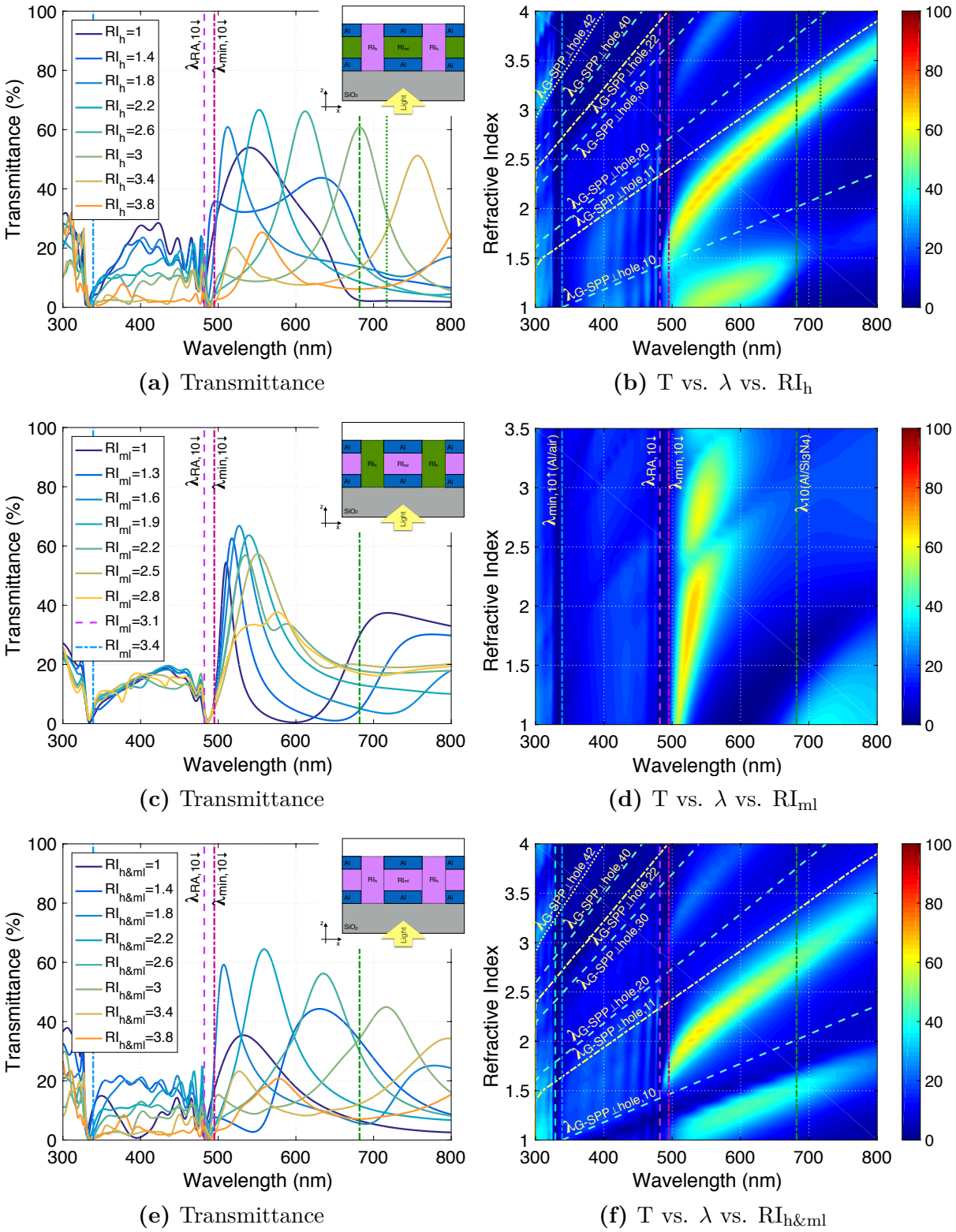
7.4.4 RI hole filling material and middle layer

The set of plots and images in Figure 7.12 establishes the influence of the RI of the hole filling material and of the middle layer on the optical response of the MIM structure for a constant t_{stack}. In the top pair of images, the transmission varies as a function of the RI of the hole filling material. In the middle pair, the transmission varies as a function of the RI of the middle layer material. In the bottom pair, the hole filling and the middle layer are composed of the same material and the transmission varies as a function of their RI.

As expected, both the modes red-shift as the RI of the hole filling material increases and the MD dipole resonance appears only when the cavity becomes optically thick enough to sustain the mode. Moreover, the lower the RI of the filling material the stronger the overlap of the modes, in particular when the RI is lower than the RI of the substrate.

It can be observed that: (i) the type of hole filling material has a major impact on the optical response of the filter than the material used as middle layer; (ii) using a middle layer with a lower RI narrows the bandwidth of $T_{\text{peak},1}$, but also significantly increases the transmission of $T_{\text{peak},2}$ and considerably blue-shifts its position in wavelength; (iii) a RI of approximately 2-2.2 is the best choice when both the hole filling and middle dielectric are composed by the same material and therefore Si_3N_4 remains the optimum choice for the hole filling material and middle layer.

Finally, consider the oblique lines in Figures 7.12b and 7.12f. These lines represent the intersections between the SPP dispersion relation $k_{\text{SPP,(Al/holeRI)}}$ and the reciprocal wavevectors G_{ij}. The majority of these lines matches maxima or minima in both the reflection and extinction spectra (see Figure 7.13). One possible explanation to these minima is that the sidewalls of the holes behave like a symmetric MIM system and that G-SPP modes arise between them. However, given the dimensions of the holes the G-SPP dispersion relation matches the dispersion relation of the single interface (for $t_d = \infty$), i.e. $k_{\text{SPP,(Al/holeRI)}}$. Note how $T_{\text{peak},2}$ is confined between $\lambda_{\text{min,10(hole)}}$ and $\lambda_{\text{min,11(hole)}}$, independently whether or not the middle layer and the hole filling material are the same.

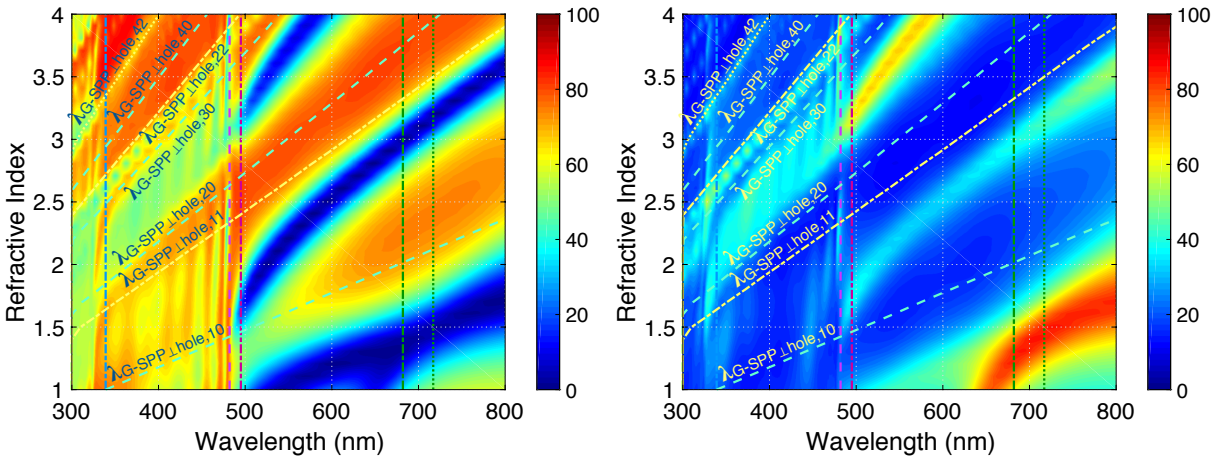


(a) Transmittance **(b)** T vs. λ vs. RI_h

(c) Transmittance **(d)** T vs. λ vs. RI_{ml}

(e) Transmittance **(f)** T vs. λ vs. $RI_{h\&ml}$

Figure 7.12: Influence of the RI of the hole filling material and middle layer on the optical response of the MIM structure. 2D plots and corresponding 2D images of the transmittance of the MIM structure as a function of wavelength and (a) RI of the hole filling material (Si_3N_4 middle layer) (b) RI of the middle layer material (holes are filled with Si_3N_4), (c) RI of the hole filling and middle layer which are both composed of the same material. The pink areas in the scheme highlight where the RI is varied. Simulation parameters: $a_x = 380$ nm, $d = 250$ nm, $t_m = 40$ nm, $t_d = 70$ nm, no cap layer.



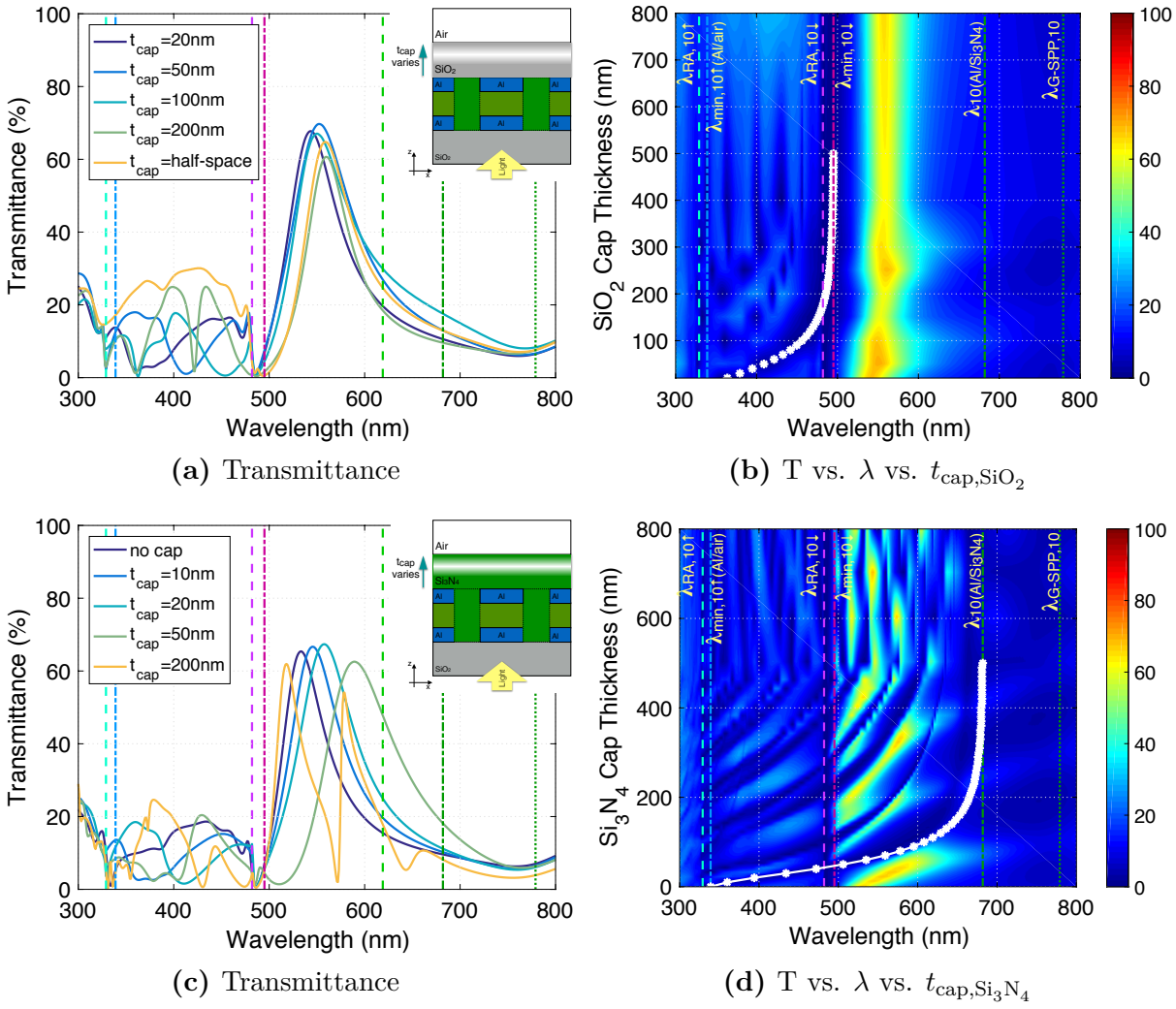
(a) R vs. λ vs. RI_h **(b)** E vs. λ vs. RI_h

Figure 7.13: Minima and maxima trends on the optical response of the MIM structure as a function of the hole RI . 2D images of the (a) reflectance and (b) extinction efficiency of the MIM structure as a function of wavelength and RI of the hole filling material. Simulation parameters: $a_x = 380$ nm, $d = 250$ nm, $t_m = 40$ nm, $t_d = 70$ nm, middle layer is Si_3N_4, no cap layer.

7.4.5 Cap Layer Thickness and RI

According to SPP theory, changing the dielectric of a metal/dielectric interface changes the SPPs propagation constant k_{SPP}. For the same frequency, the higher the permittivity of the dielectric at the interface, the larger the SPPs propagation constant. In this section it will be presented that, as for the case of a single metal layer structure, when the thickness of the dielectric at a metal/dielectric interface is of the same order of magnitude of the SPP penetration depth inside the material, the optical transmission properties of the structure might be affected. If the cap layer is the same as the substrate material, its influence is limited to small variations. Instead, if the cap layer has a refractive index higher than the one of the substrate, accordingly to its thickness, one or more resonant peaks can be generated that might interfere with the transmission properties of the filter in the EOT band.

Figure 7.14 shows how the presence of a SiO_2 or a Si_3N_4 cap layer affects the optical response of the MIM design. As stated before, the difference in RI between the hole filling material and the environment provides the degree of confinement along z. In fact, a SiO_2 cap layer does not significantly affect the filter behaviour. In contrast, when the cap layer matches the hole filling material, the effective length of the cavity increases.



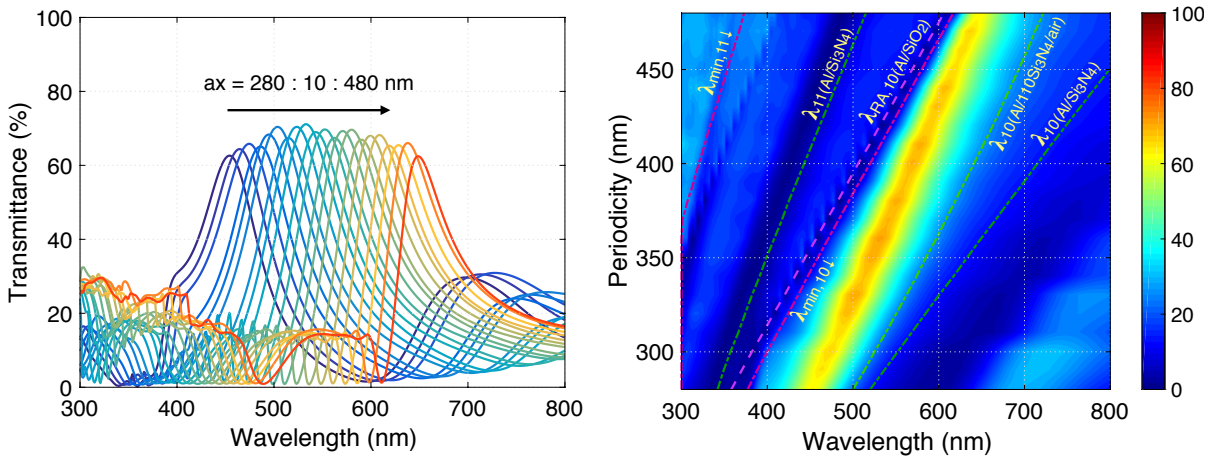
(a) Transmittance **(b)** T vs. λ vs. $t_{\text{cap,SiO}_2}$

(c) Transmittance **(d)** T vs. λ vs. $t_{\text{cap,Si}_3\text{N}_4}$

Figure 7.14: Influence of the RI and thickness of the cap layer on the optical response of the MIM structure. 2D plots and corresponding 2D images of the transmittance of the MIM structure as a function of wavelength and thickness of a (a) SiO_2 cap layer and (b) Si_3N_4 cap layer. Simulation parameters: $a_x = 380$ nm, $d = 250$ nm, $t_m = 40$ nm, $t_d = 70$ nm, middle layer is Si_3N_4, holes filled with Si_3N_4.

As a consequence, the MD resonance red-shifts in wavelength. In fact, for a given RI, the ratio $\lambda_{\text{res}}/h_{\text{eff}}$ is constant and thus a thicker optical cavity corresponds to a longer resonant wavelength, and vice versa.

However, as the Si_3N_4 cap becomes thicker and thicker new resonant modes appear. However, these modes are generated on the top surface of the Al layer and not inside the cavity, as in the case of the Asym-SML structure. Note in fact how the minima given by the intersection of the dispersion relation of the SPP at the top IIM interface with the reciprocal wavevector G_{10} cross the EOT band as a function of the cap thickness, affecting the transmission of the MIM structure. Above that line, the resonant modes belong to the top IIM waveguide.



(a) Transmission **(b)** T vs. λ vs. a_x

Figure 7.15: Influence of the periodicity on the optical response of the MIM structure. (a) 2D plot and corresponding (b) 2D image of the transmittance of the MIM structure as a function of the array periodicity. The transmission band shifts in wavelength with the periodicity. The smaller the periodicity the shorter the wavelength of the maximum peak in transmission. The main transmission band is confined between $\lambda_{\text{min},10\downarrow}$ and $\lambda_{10,(\text{Al}/\text{Si}_3\text{N}_4)}$. However, $\lambda_{10,(\text{Al}/110\text{Si}_3\text{N}_4/\text{air})}$ - where 110 nm indicate the distance between the top of the bottom Al layer and the top of the structure - seems to be an even better approximation to estimate the upper limit in wavelength of the transmission band. Simulation parameters: $d = 250$ nm, $t_m = 40$ nm, $t_d = 70$ nm, middle layer is Si_3N_4, holes filled with Si_3N_4, SiO_2 cap of 50 nm[7].

7.4.6 Periodicity

Figure 7.15 displays the transmission efficiencies of MIM arrays for a selected set of structural parameters as a function of the periodicity. This represents the chosen target for the nanofabrication. For a $t_{\text{stack}} = 150$ nm and a fixed periodicity to diameter ratio of 1.53, the MIM structure exhibits an almost constant transmission above 60% and FWHM of the order of 50-60 non along the entire optical visible range. Moreover, a 10 nm variation in periodicity corresponds to a 10 nm step in wavelength between adjacent peaks. Therefore, MIM filters can be easily designed to accurately target a desired working wavelength. Note that the bandwidth of $T_{\text{peak},2}$ can be more accurately defined by $\lambda_{\text{min1}\downarrow}$ for the lower limit and $\lambda_{10,(\text{Al}/\text{Si}_3\text{N}_4/\text{air})}$ for the upper limit, instead of $\lambda_{10,(\text{Al}/\text{Si}_3\text{N}_4)}$.

[7]which provides the highest transmission efficiency (see Figure 7.14a).

7.5 Summary

In this chapter, the optical characteristics of the MIM structure have been presented and described. Parametric dependences have been thoroughly examined and insights on the physical mechanisms of the transmission process provided.

Electromagnetic near-filed patterns established that the transmission spectrum of the MIM structure in the EOT band is dominated by the superposition of magnetic and electric resonant modes. The nanoholes behave like dielectric optical cavity resonators where the confinement of the field - instead of being the result of a large difference in permittivity between the resonator and the environment - is sustained by the presence of the metal at the top and bottom interfaces and the resonant wavelength depends strongly on the coupling of SPRs. As a consequence, the resonant modes arise from a collective response of the array and shift in wavelength with the periodicity, i.e. their resonance does not only depend on the structural parameters.

Since the nanoholes behave like cavity resonators, the total thickness of the MIM stack strongly affect the optical response of the filter. For small gap thicknesses t_d between the two thin metallic layers, the MIM structure displays two resonant peaks in the EOT band. A narrow, magnetic dipole (MD) mode at shorter wavelengths, $T_{\text{peak},2}$ and a broader, electric dipole (ED) mode at longer wavelengths, $T_{\text{peak},1}$. The MD is characterised by an electric displacement current loop, which induces an orthogonally-oriented magnetic dipole moment. The current loop can only exist when there is enough retardation of the $E_x(z)$ field between the cavity extremities. Therefore, the magnetic resonance depends on the effective optical length of the cavity, which can be approximated as $h_{\text{eff}} \approx \alpha\lambda_{\text{res}}/(2n)$, where α is an integer larger than zero, λ_{res} is the resonant wavelength and n is the RI of the cavity. It follows that if the thickness of the stack increases, or the RI of the hole filling material increases the MD mode red-shifts in wavelength. However, simulation results established that this mode, independently of the structural parameters, belongs to a specific waveband where the lower limit is given by $\lambda_{\text{min},10\downarrow}$ and the upper limit by $\lambda_{10,(\text{Al/hole RI})}$, when the RI of the material inside the holes is higher than the RI of the substrate.

Simulation data showed that the MD mode displays a very good stability to diameter variations. This is an excellent quality because implies that variations in the fabrication process that might affect the size of the holes will not affect the position of the resonant peak in wavelength. Finally, for the purpose of, eventually, integrate the MIM filter directly on top of a CMOS sensor, the presence of a dielectric cap layer on top of the MIM stack has been carefully considered. Simulation results established that in order to preserve intact the optical response of the MIM filter an additional cap layer must have a refractive index lower than or equal to the refractive index of the silicon dioxide substrate.

To conclude this chapter, we provide a list of the optimum set of structural parameters that has been chosen for the fabrication of the MIM filters. In the next Chapter, fabrication processes developed for the realisation of the MIM filters are described and the experimental data obtained presented.

- Thickness of the metallic layers: 40 nm.
- Thickness of the middle layer: 70 nm.
- Middle layer material: Si_3N_4.
- Hole filling material: Si_3N_4.
- Ratio periodicity to diameter: 1.53.
- Cap layer: SiO_2 or material with lower RI.

Chapter 8

Nanofabrication and Experimental Results

In the last chapter, MIM arrays of subwavelength nanoholes have been examined through a comprehensive parametric analysis. The simulation study provided an overview on the spectral characteristics of the filters and their parametric dependences, and allowed the determination of an 'optimal' set of structural parameters to use during the fabrication of the devices. Simulation data also established some of the physical mechanisms involved in the transmission process so that the structure might be optimised at need, accordingly to applications and filtering requirements.

In this chapter, the fabrication steps used to realise the MIM PCFs are described in detail and the experimental results presented. Issues and challenges in the fabrication process are addressed and viable solutions demonstrated. Nanofabrication of novel designs can be extremely challenging and often the results might not be what we expected, but I believe that it is important to record and make publicly available not only the successful data but also the negative outcomes. This provides knowledge and experience that might be at use one day to facilitate the development of a similar fabrication process that requires the patterning of nanoapertures in multilayer structures.

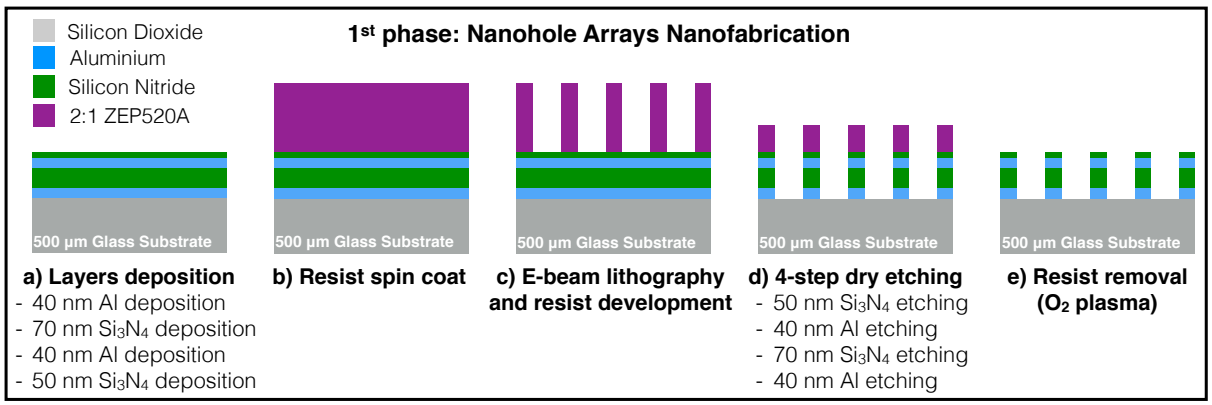


Figure 8.1: Patterning of the periodic hexagonal nanohole arrays in a MIM stack. Illustration of the fabrication steps used to pattern the periodic hexagonal nanohole arrays in the three-layer MIM stack. The process begins with the sequential deposition of the three layers that compose the MIM stack. An additional Si_3N_4 layer is deposited on top of the structure to improve adhesion of the resist. A positive resist is spun on the sample, baked and then exposed with e-beam lithography. After the development of the resist, a sequential 4-step plasma reactive ion etching (RIE) process reproduces the developed patterns in the underlying layers. A last Oxygen plasma removes eventual resist residual from the top surface.

8.1 Patterning of the hexagonal nanohole array

The nanofabrication process has been divided in two phases: (i) the patterning of periodic hexagonal nanohole arrays in the MIM stack and (ii) the filling of the nanoholes. Figure 8.1 depicts the steps for the first phase of the nanofabrication process. Devices have been fabricated on top of glass substrates, in order to allow the optical characterisation of the filters in transmission[1].

Phase I of the fabrication starts with the deposition of the three layers that compose the MIM structure: in sequence, Al, Si_3N_4, and Al. The chosen thicknesses of the metal and Si_3N_4 layers are 40 nm and 70 nm, respectively, as indicated in the image. Note that an additional Si_3N_4 film of 50 nm is deposited on top of the structure. This layer is used to improve the adhesion of the resist on top of the last metal layer and works as well as a hard mask, to protect the underlying structure during the etching process. The Al deposition was carried out by means of en electron beam evaporator, while Si_3N_4 deposition was performed using ICPECVD as described in Sections 4.2.1 and 4.2.2, respectively.

The sample is now ready for the lithographic step. A 2:1 dilution of positive resist

[1]Substrates were bought from *MicroChemicals*: 15 mm x 15 mm borosilicate pieces, 2-side polished and a thickness of 500 $\pm$ 25 μm.

ZEP520A[186] is spun on the substrate, baked at 180 °C and then exposed by mean of a EBL tool, as described in Section 4.2.3. After the development of the resist, the sample is ready for dry etch. Before the etching step, however, it is good practice to measure the thickness of the resist. The thickness of the resist gives information about the quality of the resist. For example, older resists tend to thickening which causes the generation of thicker films that thus require higher exposure doses. Moreover, the thicker the resist the higher the aspect ratio of the features in the developed pattern. This has to be considered during the etching process because it might require longer over-etching time. A resist heigh of approximately 230 nm is a typical value.

A sequential 4-step plasma reactive ion etching (RIE) process reproduces the e-beam patterns developed in the resist in the underlaying layers. To identify the correct etching time for each of the layers, an interferometer laser source is positioned inside a 1 mm x 1 mm square developed in the resist. The interferometer is used to measure the refractive index change that takes place when a layer is gradually etched way. This opening has been purposely made to allow an interferometer reading during each of the etching steps. Figure 8.2 depicts the sequence of dry etching steps used to milled the nanohole array through the MIM stack. On top of each step there is a plot of the interferometer reading recorded during that specific step. When a layer has been completely removed the output of the interferometer becomes stable. However, due to the high aspect ratio height to width of the nanoholes, it is necessary to account of an over-etch time (cyan regions). This is because the interferometer square is very large with respect the nanoscale of the features and thus it will be etched faster than the bottom of the holes. The over-etch is usually estimated as an additional 30% of the time at which the interferometer reading became stable.

For single-metal layer devices the patterning of the array is a quite straightforward process because involves only two etching steps, the hard mask and the aluminium layer. That is not the case for multilayer structures, in particular when the layers that compose the stack repeat in terms of materials. This is because the etching of one layer will affect all the layers composed by the same material and will likely increase the size of the features in the previously etched layers, especially if the etching process is not strictly anisotropic.

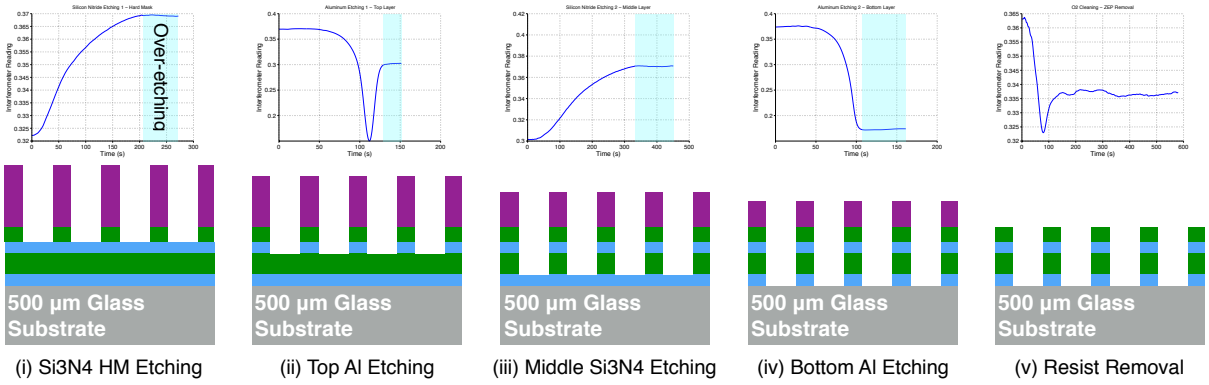


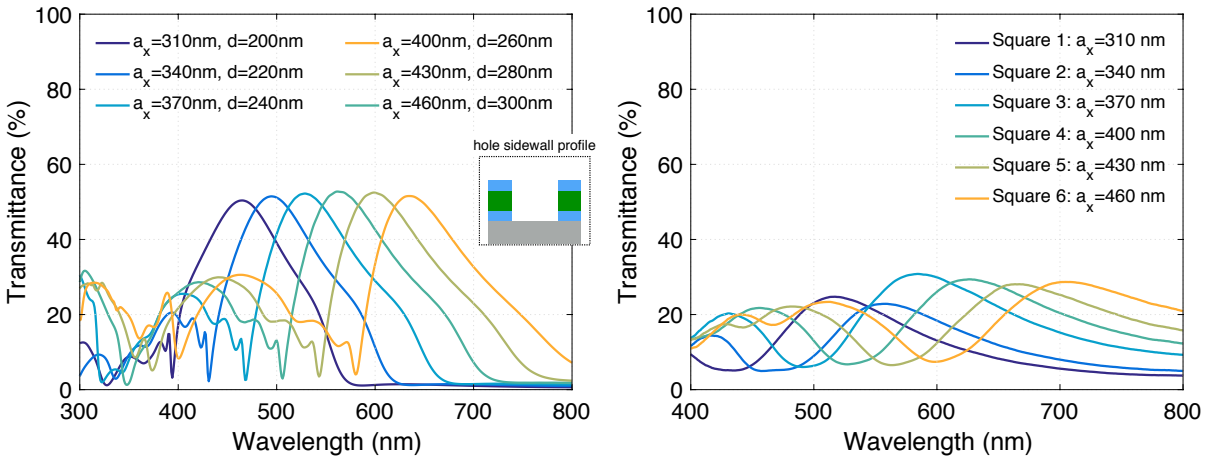
Figure 8.2: Dry etching process. Illustration of the 4-step plasma reactive ion etching process to reproduce the pattern in the resist in the underlying layers and oxygen plasma etching to remove eventual resist residual. The plots on top of each step display the interferometer readings recorded during the etching. The cyan regions indicate the over-etching time which is usually evaluate as an additional 30% of the time at which the interferometer stopped recording a variation in the refractive index.

At the end of the 4-step etching process, the remaining ZEP on top of the structure is removed through a five minutes oxygen plasma. This plasma does not affect either the Al or Si_3N_4 layers and thus it is not necessary to time-check its length. Finally, the hard mask should be removed. The removal of the hard mask is a critical step because if the the etching process utilised is not anisotropic, or it is simply performed for too long, that could affect also the Si_3N_4 middle layer and thus significantly modify the optical response of the filters. And this is, in fact, what happened.

8.1.1 Issue 1: Under-Etch of the Middle Layer

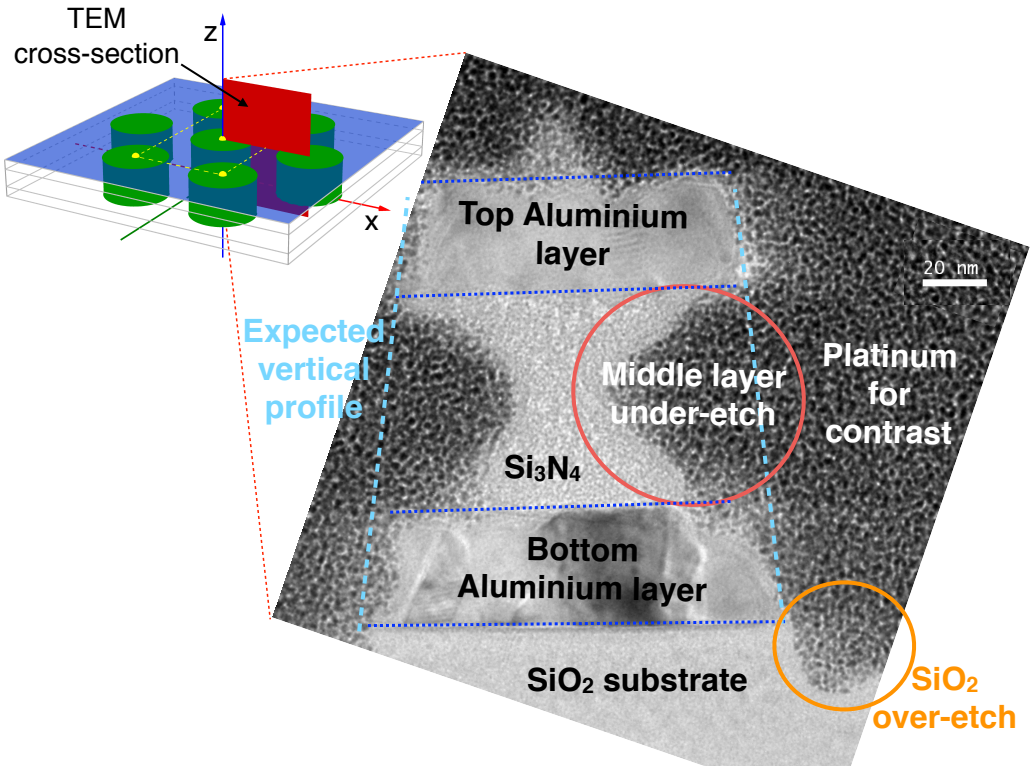
The under-etch of the Si_3N_4 middle layer caused severe interference to the transmittance of the filters. Figure 8.3a shows the simulated expected transmittance of six hexagonal nanohole arrays with different periodicities at the completion of the first phase of the fabrication process. In comparison, Figure 8.3b displays the experimental data obtained from six 1 mm x 1mm MIM hexagonal nanohole arrays from one of the samples affect by a conspicuous amount of under-etch of the middle Si_3N_4 layer. The spectral lineshapes of the filters are completely distorted.

The under-etch issue was identified by imaging a cross-section of one of the 'faulty' samples. Figure 8.3c is a TEM image of the MIM stack between two adjacent holes which shows how the additional Si_3N_4 etching step caused a considerable amount of under-etch



(a) Expected transmittance after Phase I

(b) Experimental data after Phase I



(c) TEM image of the cross-section of a 'faulty' sample

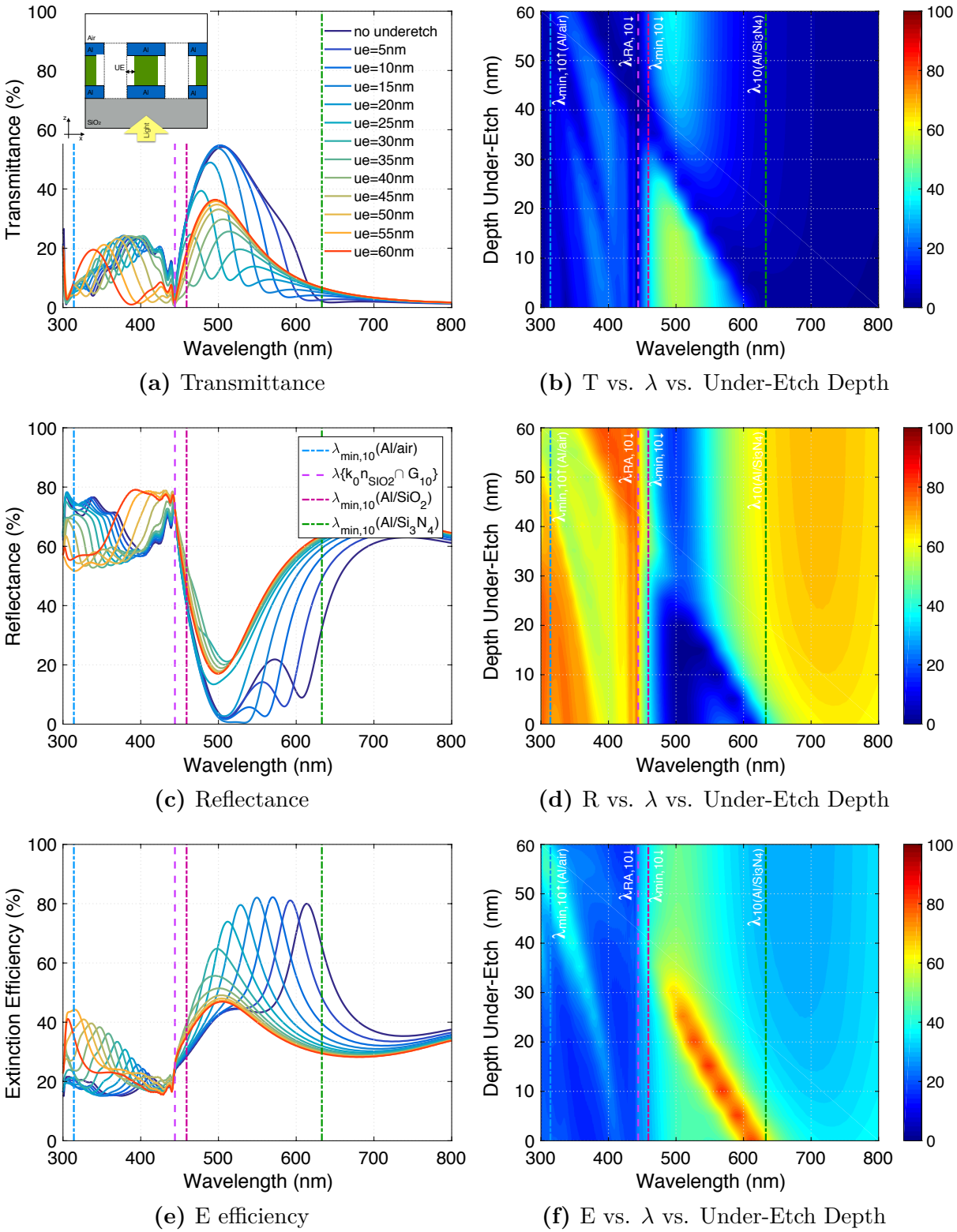
Figure 8.3: Under-etch of the middle layer. (a) Simulated optical transmission efficiency of six arrays and (b) corresponding experimental data of one of the samples (S21940) after Phase I of the fabrication process. Periodicities are indicated in the legends. Clearly, the experimental data do not resemble the expected results. (c) Sketch of the cross-section within the hexagonal array and respective TEM image (sample S21940) of the MIM stack in between two consecutive nanoholes along the x-direction. The removal of the hard mask results in a significant under-etch of the Si_3N_4 middle layer. Scale bar: 20 nm.

to the Si_3N_4 middle layer, of approximately 60-70 nm per side. It also caused a significant etch of the SiO_2 substrate at the bottom of the holes. In spite of that, some Si_3N_4 residuals are still visible on the top Al surface.

Figure 8.4 is a simulation study on the effect of the under etch on the optical response of the MIM filters. It seems as if the G-SPP mode could 'feel' the variation in the refractive index of the middle layer. Consider the middle layer as an effective medium, the larger the under-etch the lower the effective refractive index and thus the dispersion relation of the G-SPP would become smaller. As a consequence, the condition $k_{\text{G-SPP}} = G_{10}$ would be met at higher frequencies causing the minimum $\lambda_{\text{G-SPP},10}$ to blue-shift in wavelength. The larger the under-etch, the larger the blue-shift. Note, in fact, an imaginary blue line that crosses the EOT band from right to left as the depth of the under-etching increases. This interference 'pushes' the peak in the EOT band to lower wavelengths until it disappears and the lineshape of the peak becomes unrecognisable. To maintain almost intact the transmission efficiency of the filter and its lineshape, the under-etch should not exceed approximately 10 nm per side.

The first attempt to avoid the under-etch consisted in the replacement of the top Si_3N_4 layer with a primer. The primer does not 'have a thickness'. It is extremely thin and thus is function is merely as an adhesion layer and not as a hard mask. The samples displayed a significant improvement in transmission, a clear sign that the under-etch issue had been solved. However, SEM images showed a much larger difference in diameter between the top and the bottom layer. Likely, the absence of the hard-mask made the top Al layer more vulnerable to the multi-steps etching process. The ZEP resist is a quite 'soft' resist that get etched with a rate that is basically 1:1 to the etching rate of the material, so without the hard mask the top Al layer is more subjected to the effect of a double etching. Moreover, some SEM and AFM images also showed unexpected 'damages' in the proximity of the arrays that did not appear in the samples with the hard mask. We assigned those defects to adhesion issues between the resist and the top Al layer and thus decided to discard this approach.

Simulation results in Section 7.4.5 showed that a thin cap layer of Si_3N_4 - of few tens on nanometers - does not significantly affect the optical response of the filters in transmission. It was then decided to re-introduce the Si_3N_4 hard mask but contemporary to reduce its thickness down to 20 nm so that it could be left on top of the MIM stack without influencing its optical properties.



(a) Transmittance **(b)** T vs. λ vs. Under-Etch Depth

(c) Reflectance **(d)** R vs. λ vs. Under-Etch Depth

(e) E efficiency **(f)** E vs. λ vs. Under-Etch Depth

Figure 8.4: Influence of the under-etch of the Si_3N_4 middle layer on the spectral features of the of the 407040-MIM structure. 2D plots and corresponding 2D images of the **(a)**, **(b)** transmission, **(c)**, **(d)** reflection, and **(e)**, **(f)** extinction efficiencies of a MIM array as a function of wavelength and amount of under-etch of the middle Si_3N_4 layer. Simulation parameters: $a_x = 350$ nm, $d = 240$ nm, $t_m = 40$ nm, $t_d = 70$ nm, , middle layer is Si_3N_4, holes filled with air, no cap layer.

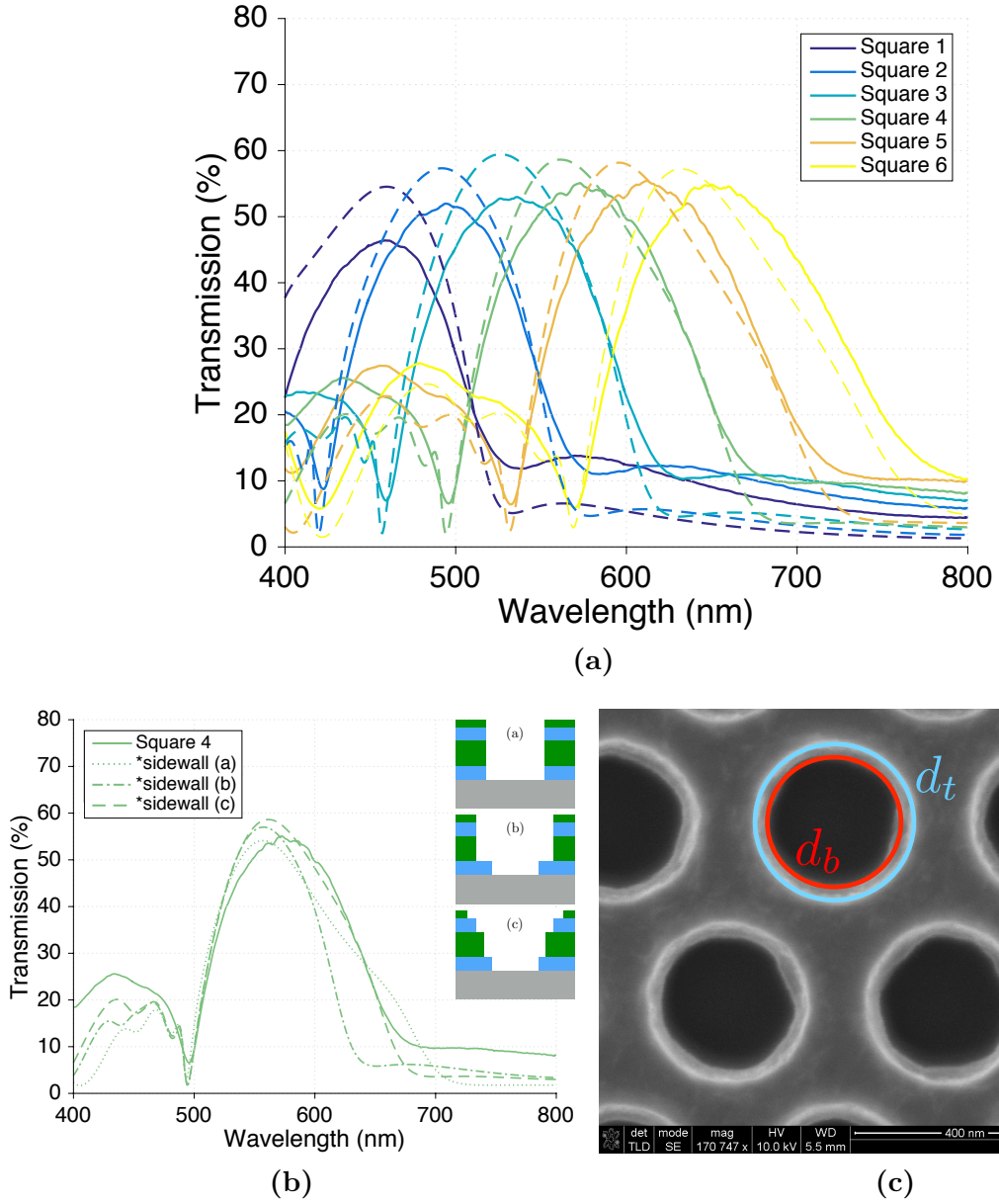


Figure 8.5: Experimental data after Phase I of the fabrication process. (a) Optical transmission efficiency of the six 300 μm x 300 μm arrays of sample S23800 (solid lines) after the last step of Phase I of the nanofabrication in comparison with the fitted simulation results (dashed lines). Structural parameters used in the simulations are listed in Appendix A.1, under the section dedicated to the sample S23800. Experimental measurements are in very good agreement with the simulated results. (b) Optical transmission of Square 4 (sample S23800). Sidewall (i) indicates the ideal case. In case (ii), it is assumed that the Si_3N_4 middle layer has been etched up to the top hole dimension, while in case (iii) a uniformly stepped sloped sidewall is considered. Excluding the ideal case (i) which is ruled out by Figure 8.5c, sidewall (iii) is the best parametric fitting. (c) SEM image of Square 4 (sample S23800) after the last step (v) of the first phase of the PCFs nanofabrication. Two circumferences, one at the bottom Al layer (d_b) and one at the top Al layer (d_t) can be identified. That means that the sidewalls of the nanoholes are not perfectly vertical. Scale bar: 400 nm.

Figure 8.5a shows the optical transmission efficiency of six 300 μm x 300 μm MIM hexagonal nanohole arrays (solid lines) after the last step of Phase I of the nanofabrication process - terminated before the removal of the hard mask - in comparison with the fitted simulation results (dashed lines). The good agreement of the simulated results with the experimental data is reflected by the high-quality matching of the critical features in the transmission spectra.

Each array was optically characterised by means of a SEM and a Microspectrophotometer. The SEM image in Figure 8.5c shows that each nanohole is composed by two concentric circles with a top, d_t, and a bottom, d_b, diameter. This means that the nanoholes in the bottom aluminium layer are slight smaller than the nanoholes in the top aluminium layer, by approximately 40 nm, and thus that the sidewalls of the apertures are not perfectly vertical. However, the top surface of the arrays appears free from resist residuals and the holes are nicely circular-shaped.

Figure 8.5b displays the measured transmission curve of one of the array in comparison with the simulated transmission efficiencies of three possible sidewall configurations, indicated in the inset. The ideal sidewall (i) can be ruled out by Figure 8.5c while the bandwidth of the simulation curve with a sidewall of the (ii)-type does not match the experimental data. Therefore, the (iii)-type sidewall profile is used to fit the remaining five squares with differing periodicities (Figure 8.5a). Finally, we have established a successful fabrication process for the patterning of the periodic HNAs in the MIM stack and so we can move on to the second phase of the fabrication.

8.2 Filling of the nanoholes

Phase II of the fabrication consists in the filling of the nanohole arrays, more specifically with silicon nitride, as depicted in Figure 8.6a. The planned fabrication method included (a) the deposition of a thick layer of silicon nitride by PECVD to fill the holes. A thick layer is supposed to reduce the steps at the nanoholes sidewalls given by the difference in height, (b) a slow chemical-mechanical polishing or RIE back-etching of the silicon nitride up to the top aluminium using an interferometer, and last (c) a silicon dioxide

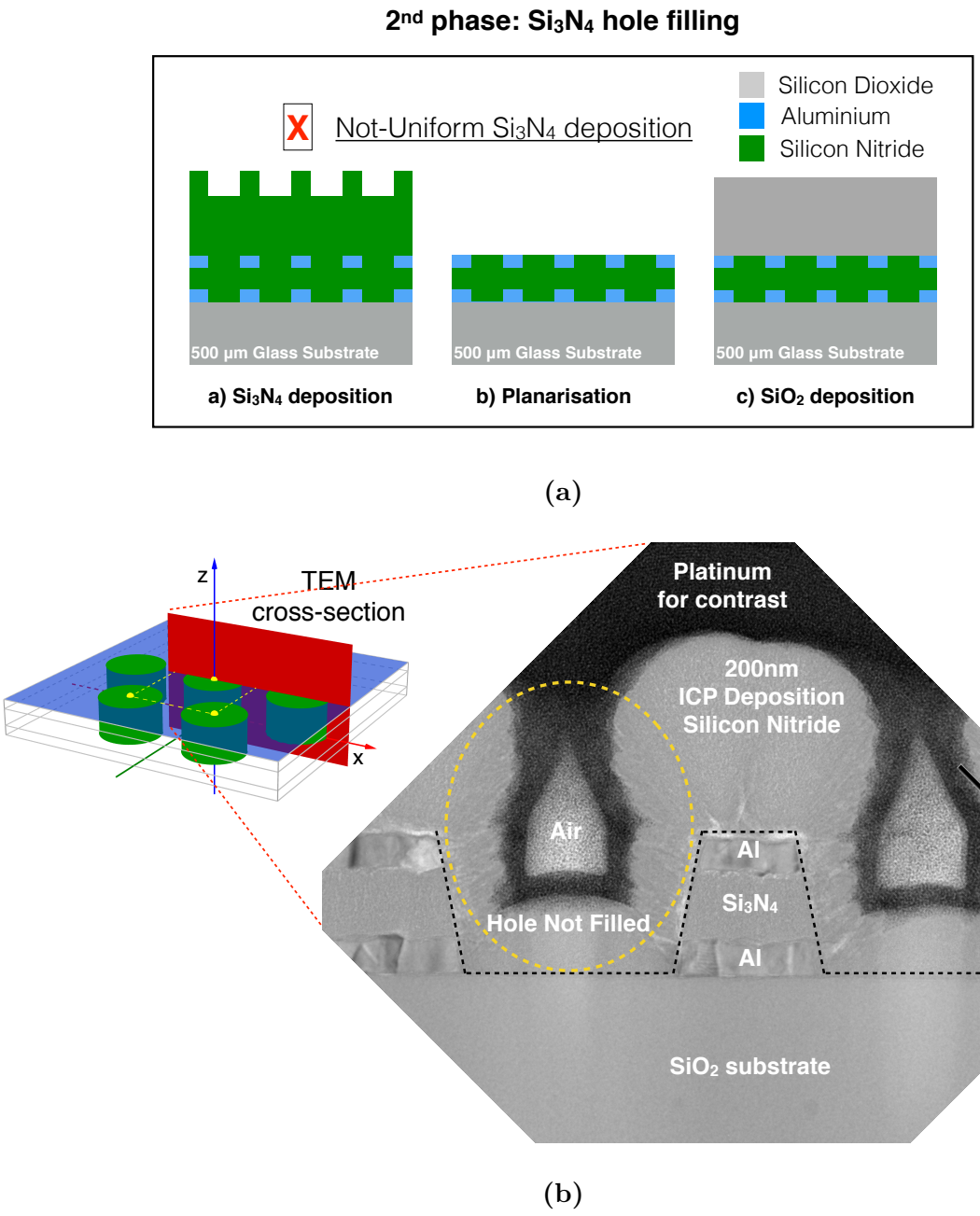


Figure 8.6: Phase II of the fabrication process. (a) Illustration of the fabrication steps to fill the holes with Si_3N_4. (b) Sketch of the cross-section within the hexagonal array and respective TEM image of one of the fabricated arrays (sample S23801 - see dedicated section in Appendix A.2). The deposition displays non-conformality, with a higher deposition rate on the top surface which creates mushroom-shaped accumulations at the side of the nanoholes that do not allow complete filling of the subwavelength apertures. Scale bar: 200 nm.

cap layer deposition. Unfortunately, the optical characterisation of the samples after the silicon nitride deposition did not show the expected results and a TEM image of the cross-section of one of the sample revealed that the problem lay in the silicon nitride deposition itself (see Figure 8.6b).

The image confirms that if the hard mask is left in situ, the under-cut of the middle layer is avoided. However, the Si_3N_4 deposition is highly non-conformal. A large void is visible inside each nanohole, a consequence of the mushroom-shaped accumulations between the holes - result of a higher deposition rate on the top surface with respect the bottom of the holes - that prevent complete filling. The presence of the voids interferes strongly with the filters' transmission by lowering the effective RI of the holes and thus decreasing the effective length of the cavity h_{eff}. As a result, the magnetic dipole disappears while the electric dipole mode blue-shifts significantly. The experimental data of the sample whose cross-section is displayed in the TEM image are reported in Appendix A.2.

The first approach to overcome the non-conformal deposition issue was to deposit a much thicker layer of Si_3N_4, planarise the top surface down to a few tens of nanometer above the top Al layer by mean of Chemical Mechanical Polishing (CMP) techniques, proceed with another Si_3N_4 deposition and so on until the holes were uniformly filled. However, optimisation of the CMP process demonstrated to be harder than expected and the Al had the tendency to easily peel off the substrate during the planarisation step, destroying the entire sample. On the other hand, using a RIE back-etching had simply removed the Si_3N_4 also from the holes. These unexpected difficulties in fabrication necessitated the identification of an alternative material to fill the holes.

8.2.1 Alternative Filling Material

Section 7.4.4 - on the influence of the RI of the hole filling material on the optical response of the MIM structure for a constant t_{stack} - established that both the resonant modes red-shifts as the RI increases and the MD resonance appears only when the cavity becomes optically thick enough to sustain the mode. Moreover, the lower the RI of the filling material the stronger the overlap of the modes, in particular when the RI is lower than the RI of the substrate. Based upon these results and the knowledge that a spinnable material could reduce the possibility of a non-uniform filling and of an irregular top surface, the S1805 Shipley[187] resist was chosen as the hole filling material.

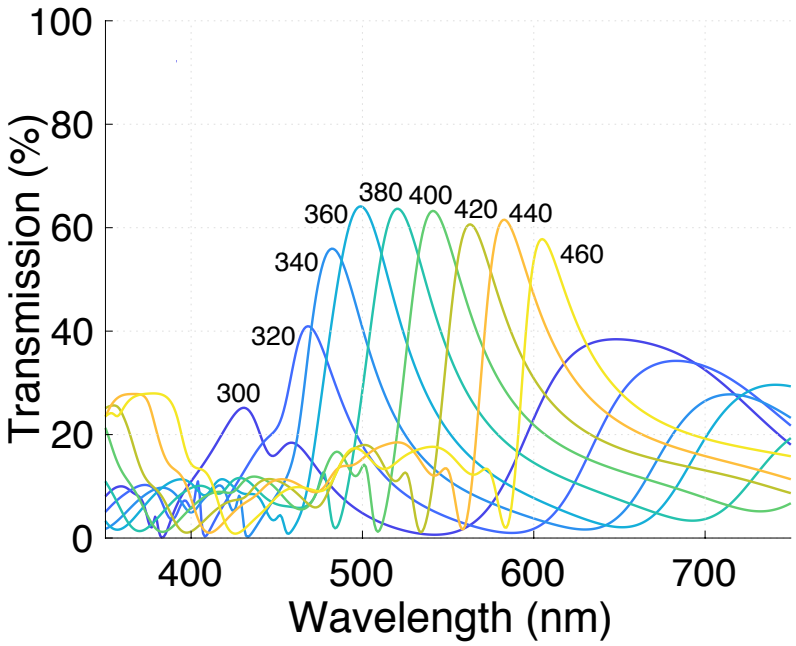


Figure 8.7: Simulation study of the new optimised structure with S1805 inside the holes. Expected optical transmission efficiency for 40-100-40 MIM arrays having different periodicities a_x (indicated on top of the peaks). The periodicity to diameter ratio is 1.53, t_m = 40 nm, t_d = 100 nm, no cap. A 10-nm Si3N4 hard mask is assumed. The chosen thickness t_d = 100 nm optimises the transmission efficiency in the middle range of the visible spectrum, but gives inferior passband characteristics in the blue and red parts of the spectrum, which would instead require a shorter and a longer stack thickness, respectively.

The RI of S1805 is in the range 1.6-1.7,[187] lower than the RI of Si_3N_4, and thus, to maintain the optical length, the total t_{stack} of the MIM filters was increased. Figure 8.7 displays the final expected transmission characteristics using S1805 hole filling instead of Si_3N_4, for several periodicities a_x and a taller t_{stack} = 180 nm. In this case, it appears that it is not possible to utilise the same thickness to uniformly filter the entire visible spectrum. The chosen thickness t_d = 100 nm optimises the transmission efficiency in the middle range of the visible spectrum, but gives inferior passband characteristics in the blue and red parts of the spectrum, which would require instead a shorter and a longer stack thickness, respectively. This is due to the fact that, for the first mode, $\delta h_{\text{eff}} \approx \delta\lambda/(2n)$, and thus, given the fixed wavelength range of visible light, a lower RI material requires a larger variation of the thickness δh_{eff}. Therefore, by filling the holes with a high-RI dielectric, narrowband filters can be realised across the entire visible spectrum with a single t_{stack} thickness.

The fabrication steps for the 40nm-100nm-40nm MIM hexagonal nanohole arrays filled with S1805, and the optical characterisation of an array from a 4010040-MIM sample

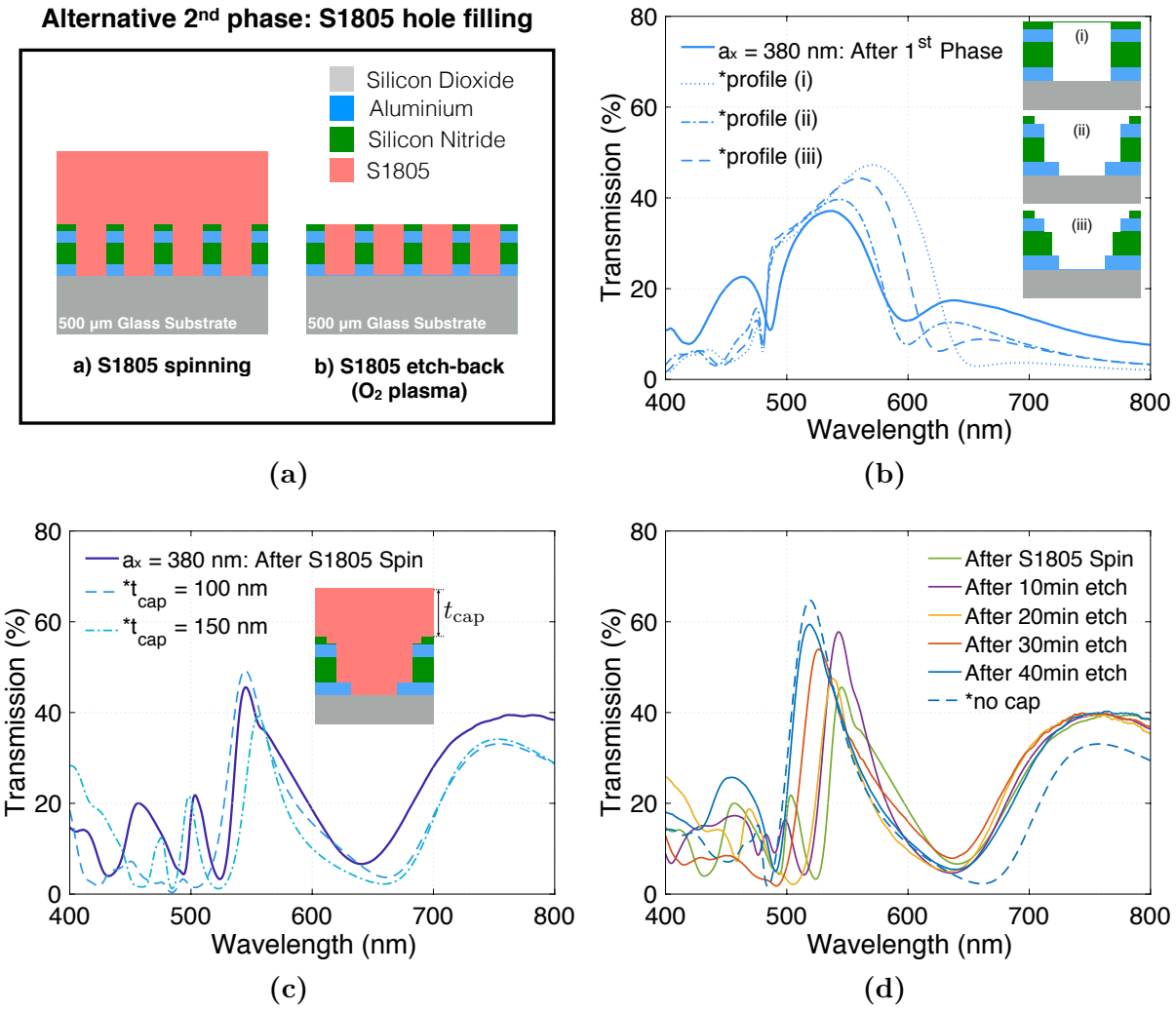


Figure 8.8: Fabrication steps and experimental results for the S1805 nanohole filling. (a) Illustration of the fabrication steps used to fill the holes with S1805. A10-nm Si_3N_4 hard mask was used. (b), (c), (d) Optical characterisation of Sample S24734: t_m = 40 nm, t_d = 100 nm, 10-nm hard mask. Each array occupies an area of 200 μm x 200 μm. See the dedicated section in Appendix A.3 for sample layout and measured hole dimensions. Measured transmission efficiencies of square 11, a_x = 380 nm, e-beam dose 408 $\mu C/cm^2$, (b) after Phase I of the fabrication process in comparison with parameterised simulation curves having different hole sidewalls, (c) after S1805 spin in comparison with simulated results having different cap thicknesses, and (d) as a function of the S1805 cap thickness after 10-minute steps of O_2 back-etching.

are reported in Figure 8.8. As previously, following the SEM characterisation of the top surface of the sample, the experimental measurements were compared to simulated results to determine the best fit for the hole sidewall profiles (see Figure 8.8b). Figure 8.8c shows that after the S1805 spin, the thickness of the resist on top of the MIM structure was of the order of around 100 nm. As in the case of the SiO_2 cap, etching back the resist decreases the optical length of the cavity. As expected, when the S1805 top layer is etched back the peaks blue-shifts in wavelength and only a smaller number of modes are allowed

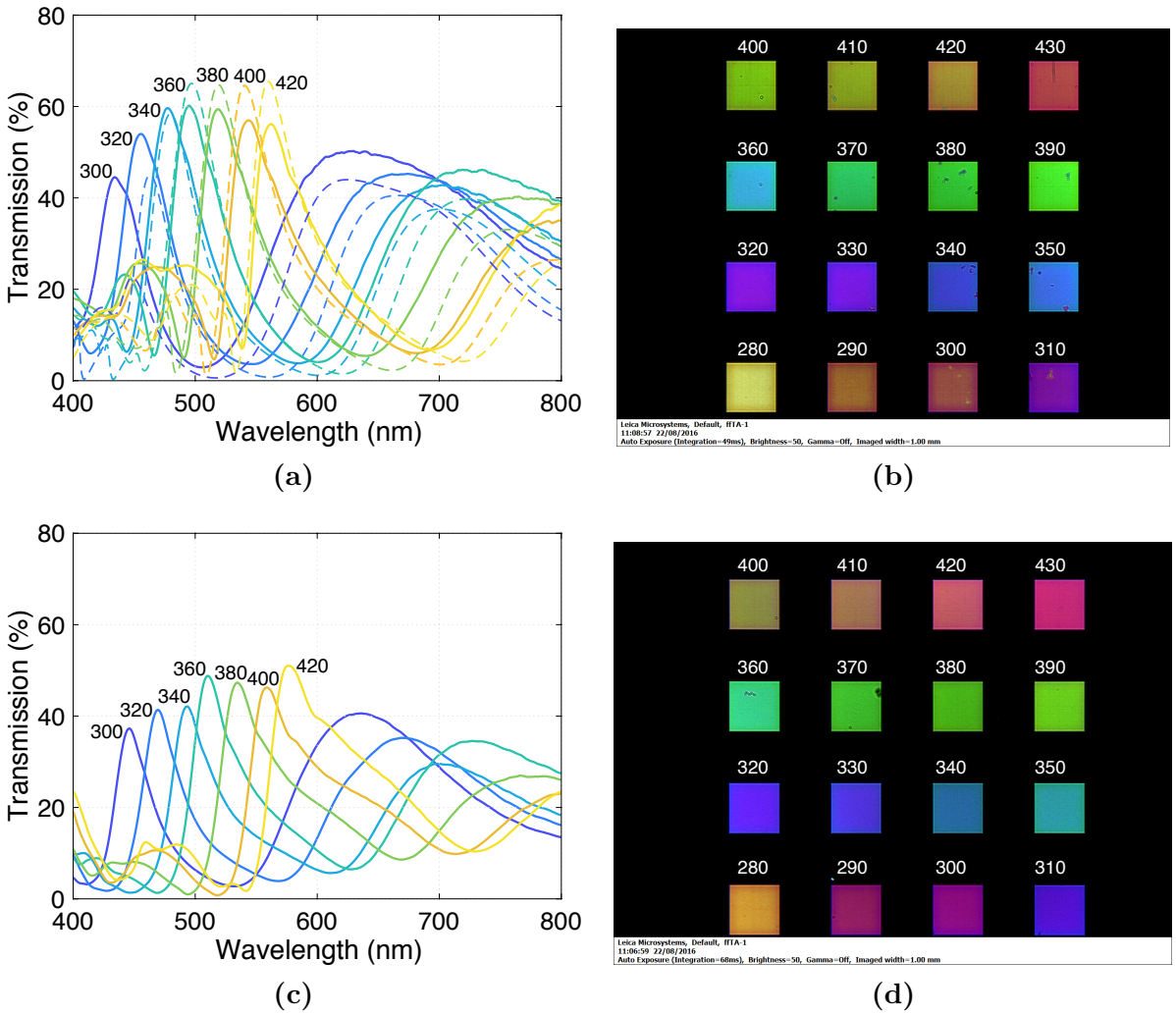


Figure 8.9: Final experimental results and microscope images of MIM arrays filled with S1805. (a) Comparison of measured transmission efficiencies (solid lines) of the arrays of sample S24734 exposed to a dose of 408 $\mu C/cm^2$ with the parameterised simulation results (dashed lines) obtained using a (ii)-type hole sidewall (refer to Figure 8.8d) and the diameters estimated from the SEM characterisation of each array. (b) Transmission microscope image of the 16 MIM colour filter whose measured transmittance curves are plotted in (a). (c) Measured transmission efficiencies of the arrays of sample S24734 exposed to a dose of 300 $\mu C/cm^2$ and respective transmission microscope image (d). Periodicities are indicated on top of the peaks/squares in each image. See the dedicated section in Appendix A.3 for details on the sample layout and measured hole dimensions.

inside the cavity, i.e. the second longer wavelength peak disappears (see Figure 8.8d).

The experimental results of two sets of the 40nm-100nm-40nm arrays after 40 minutes O_2 back etching, that were exposed to two different doses as indicated, are plotted in Figures 8.9a and 8.9c. For each set, Figure 8.9b and 8.9d are the respective transmission microscope image of the 16 MIM colour filter. For the lower dose (Figure 8.9b), which corresponds to smaller hole diameters, the colour cross-talk between filters is evidently lower when compared to the higher doses (refer to microscope images). On the other

hand, the transmission efficiency is significantly reduced by using the lower dose. In fact, for the higher dose, the sample displays transmission efficiencies up to 60%, and FWHM in the blue and green part of the spectrum between 45 and 55 nm. The experimental results are in very good agreement with the simulations, establishing the accuracy and validity of the simulation study with the Si_3N_4 hole filling.

8.3 Summary

In this chapter, the fabrication steps used to realise the MIM PCFs are described in detail and the experimental results presented. Issues and challenges in the fabrication process are addressed and viable solutions demonstrated. Through the high quality of the measured results obtained from the fabricated samples, we were able to demonstrate the impressive performance and versatility of our MIM plasmonic nanostructures. The MIM filters overcome the limitations of both existing PCFs and CMOS focal plane colour filters, and thanks to a reduced optical bandwidth down to as little as 45 nm in the visible range, and transmission efficiencies up to 60%, high accuracy image sensors will be made possible. Moreover, because these narrow band-pass filters for the entire visible range are fabricated using one single lithographic step, this CMOS-compatible plasmonic nanostructure is cost-efficient and extremely competitive with current multispectral filtering technologies.

Further improvements of the MIM filters will require a more reliable fabrication process, so that a higher refractive index material can be used to fill the holes and a lower colour cross-talk achieved between the blue and the red part of the spectrum. However, when we optimised the MIM structure to a different hole filling material in just few steps we clearly demonstrated that the concept presented in this manuscript is extremely versatile, and can be successfully extended to other materials or even to other wavelengths of the electromagnetic spectrum.

Chapter 9

Conclusions and Future Work

In the work presented in this Thesis I have developed a novel plasmonic colour filter architecture based on periodic hexagonal arrays of subwavelength holes milled through a Metal-Insulator-Metal stack of less than 200 nanometers. This structure overcomes the limitations of all previously reported PCFs, namely relatively low transmission efficiency and considerably broad bandwidth, and represents a potential candidate for integrated multispectral imaging sensors in the visible regime.

Thanks to comprehensive simulation studies and detailed analyses of the simulation data I was able to identify some of the physical mechanisms involved in the transmission process of the MIM structure and establish the influence that each of the structural and constitutive parameters has on the optical response of the device. This allows for a relatively easy and straightforward optimisation of the structure for different materials and applications.

The conclusions from the development of the MIM structures, in addition to some discussion on future work, are presented below.

9.1 From Broad- to Narrow-Band Plasmonic Colour Filters

In the last decades, transmissive plasmonic colour filters based on periodic arrays of nanoholes in an optically thick metal layer quickly became one of the most promising candidate to replace integrated colour filters for image sensor technologies[13,14,15,16]. Plasmonic colour filters are based upon the phenomenon of extraordinary optical transmission[17]. While transmission through a single isolated nanohole is extremely small, hole arrays can display surprisingly high transmission efficiency, sometime exceeding unity when normalised to the area of the holes[17,18]. This is because the surface plasmon polaritons launched at each hole interact and give rise to a collective resonant behaviour of all the holes together that boost the transmission efficiency.

Periodic hexagonal nanohole arrays milled in a 150-nm Al layer sandwiched between a bottom-half space and a top 200-nm silicon dioxide layers - in this Thesis referred to as the Sym-SML filters - were chosen to be the starting point for the development of more efficient plasmonic colour filters. At the time the project started, they were the most common and exploited architecture for CMOS image sensor applications and many studies were published on them. However, with transmission efficiencies below 50% and FWHM larger than 100 nm, the Sym-SML filters did not represent an actual competitive alternative to standard filter technologies.

In Chapter 5, the spectral characteristics of Sym-SML arrays have been re-examined in details through a comprehensive parametric simulation analysis in order to identify a novel way to improve their optical performance. The goal was to increase their transmission efficiency and narrow their optical bandwidth, in order to make them more suitable for integrated multispectral applications.

Simulation results established that the optical efficiency of the filters would benefit from a reduced amount of metal. Therefore, the metal has been thinned down to 40 nm. The thickness was chosen thin enough to reduce the absorption losses but contemporary thick enough to be approximately 3-4 times the SPPs penetration depth inside the Al

and thus avoid SPPs coupling between the top and bottom interfaces. The spectral lineshape of the Sym-SML structure was the result of the substantial overlap of two resonances. However, simulations results demonstrated that by filling the hole with a higher-RI material (than SiO_2) the two resonant modes could be separated in wavelength. The higher the RI the larger the split between the two resonances. A slight boost in the transmission efficiency of the narrower peak was observed for a range of RI between 1.8 and 2.2. Si_3N_4 was chosen as the hole filling material because it is a standard CMOS material and has the RI in the appropriate range of values. Simulation results also established that the number of resonant modes within the structure depends on its thickness. Therefore, to maintain unaltered the total thickness of the cavity, a cap layer made of the same high-RI material of the hole filling has been introduced on top of the 40-nm metal layer.

In the transmission spectrum of a Asym-(thin)SML structure two resonances can be identified: a narrower, antisymmetric resonant mode at shorter wavelengths, $T_{\mathrm{peak},2}$, and a broader, symmetric resonant mode at longer wavelengths, $T_{\mathrm{peak},1}$. $T_{\mathrm{peak},2}$ displayed a relatively high transmission, above 40%, and a considerably narrow FWHM, of approximately 30 nm, along the entire visible range. Moreover, this peak presented extremely interesting features: (i) it was stable to diameter variations; (ii) it was limited to a specific waveband, defined by the two minima resulting from the excitation of SPPs at the bottom and top interfaces, $\lambda_{\mathrm{min},10(\mathrm{Al/SiO_2})}$ and $\lambda_{\mathrm{min},10(\mathrm{Al/Si_3N_4})}$; (iii) its lineshape could be easily optimised by varying the thickness of the cap layer.

The main drawback of the Asym-(thin)SML configuration was the considerable optical interference of a long-wavelength peak, in particular for shorter periodicities, because it had a transmittance that was of the same order of magnitude of the transmittance of $T_{\mathrm{peak},2}$. Simulation results established that the main contribution to the transmittance of the long-wavelength peak could be attributed to the formation of magnetic dipoles along the y-direction on the top Al surface, in between adjacent holes. Therefore, to 'screen' the radiation pattern from these magnetic dipoles and thus reduce the optical efficiency of $T_{\mathrm{peak},2}$, a second Al layer - exact copy of the bottom one - has been added on top of the Si_3N_4 cap layer of the Asym-(thin)SML structure. However, knowing that the resonance of the narrow peak was sensitive to the total thickness of the structure, the thickness of

the Si_3N_4 has been reduced to maintain the latter unvaried. The addition of a second metallic layer not only reduced the interference from the long-wavelength peak observed in the Asym-(thin)SML structure, but also increased the efficiency of the short-wavelength cavity mode by increasing the confinement of the resonant mode inside the nanoholes.

In Chapter 7, the optical characteristics of the MIM structure have been presented and described. Parametric dependences have been thoroughly examined and insights on the physical mechanisms of the transmission process provided. Electromagnetic near-filed patterns established that the transmission spectrum of the MIM structure in the EOT band was dominated by the superposition of magnetic and electric resonant modes. For small gap thicknesses t_d between the two thin metallic layers, the MIM structure displayed two resonant peaks in the EOT band. A narrow, magnetic dipole (MD) mode at shorter wavelengths, $T_{\text{peak},2}$ and a broader, electric dipole (ED) mode at longer wavelengths, $T_{\text{peak},1}$. The MD resonance displayed a strong dependence to the thickness of the MIM stack and to changes in RI of the hole filling material that could be explained in terms of cavity resonator and effective optical length of the cavity.

The thicker the effective length of the cavity, the higher the red-shift of the peak. Moreover, the thicker the stack the higher the number of resonant modes within the structure. Similarly, the higher the RI of the hole filling material, the higher the red-shift of the peak and vice versa. In addition, it has been established that the thicker the gap thickness between the two metal layers the higher the number of oscillatory modes that arise in the MIM waveguide. These modes should be avoided because they can interfere with the transmission features of the EOT band.

These insights on the physical mechanisms involved in the transmission of the MIM structure and a comprehensive analysis of the effect that the structural parameters have on the optical response of the MIM structure enabled the determination of an 'optimal' set of structural parameters to use during the fabrication of the filters with the required characteristics. The optimal set of structural parameters read as follow: ratio periodicity to diameter equals 1.53, metal thickness of the array $t_m = 40$ nm, distance between the metal layers $t_d = 70$ nm, Si_3N_4 has been chosen as both filling of the hole and middle layer material.

The nanofabrication of the MIM filters has been divided in two phase: the patterning of the hole array in the MIM stack and the filling of the holes. The fabrication process presented a few challenges in either of the phases. In Phase I, a conspicuous under-etch of the middle layer made it necessary to remove an etching step and re-evaluate the thickness of the top Si_3N_4 layer, used as adhesion layer between the top metal layer and the resist and as hard mask layer during the etching. In Phase II, the non-conformal Si_3N_4 deposition made it necessary to substitute the hole filing material. Since the hole filling material had a different RI the structural parameters of the MIM structure had to be re-evaluated accordingly. Thankfully the MIM structure is an extremely versatile structure and the understanding acquired on its physical mechanisms meant that the re-optimisation was relatively quick and straightforward.

Once the fabrication process had been developed, measured transmission efficiencies up to 60% and FWHM between 45 and 55 nm along the entire visible range were achieved - an impressive and unique combination of features that has never been reported before in a plasmonic colour filter. Experimental results were in very good agreement with the simulations, establishing the accuracy and validity also of the simulations study with the Si_3N_4 hole filling.

9.2 Future Works

The objective of the work presented in this Thesis has been the development of a photonic nanostructure that could overcome the limitations of previously reported plasmonic colour filter technologies, namely relatively low transmission efficiency and considerably broad bandwidth, and eventually replace current filter technologies for integrated multispectral CMOS image sensors.

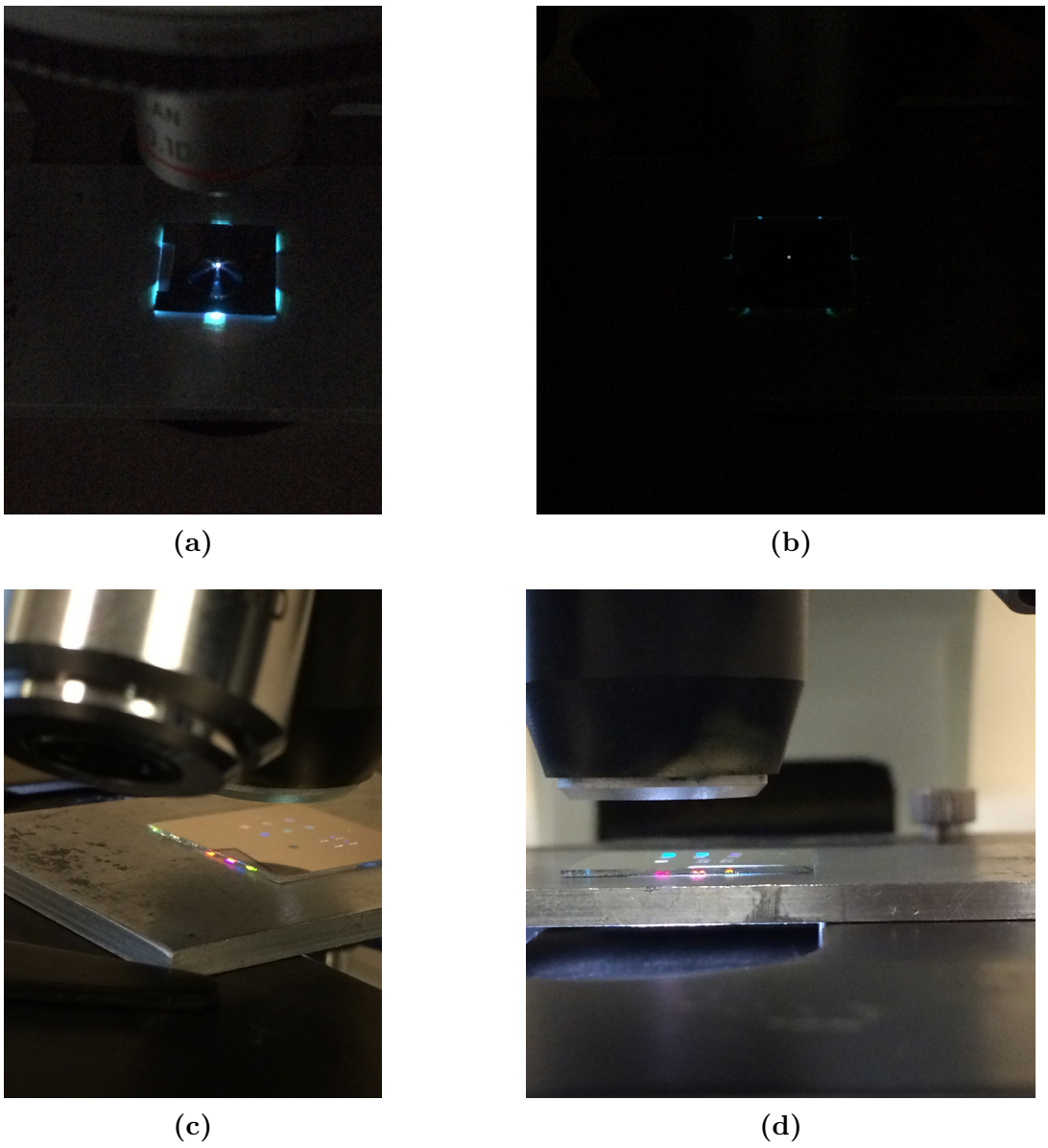
Experimental results were in good agreement with the simulations and demonstrated the versatility of the MIM structure. However, it was necessary to replace the initial CMOS-compatible choice of the hole filling material with an organic substitute. In addition, the alternative filling material had a much lower refractive index that prevented to achieve uniform spectral filtering characteristics along the entire visible spectrum. There-

fore, in the immediate term, the next step would be to develop a process to fill the holes with silicon nitride and demonstrate the resulting performance improvement.

Once the MIM filters have been successfully fabricated with Si_3N_4 as the hole filling material, in the medium to long term, the next step would then be the integration of the devices directly on top of a photodetectors or within the first layers of the CMOS layer stack. At that stage, it would also be necessary to develop imaging processing algorithms to extract the individual colours, perform interpolation and reconstruct the full colour image. Initially, the colour filter array could be composed of the standard red, green and blue channels. Without the restriction of multiple colour bands, the size of the holes could be increased in order to increase the efficiency of the filters. For example, with a ratio periodicity to diameter of 1.26, transmission efficiencies up to 80% could be achieved. The FWHM of the filters would be of about 75 nm, i.e. still 25% smaller than the Sym-SML case. After the acquisition of the first colour image using a trichromatic colour filter array, colour reproduction could be improved by using a larger number of colour filters so to have a multispectral image sensor. The ratio periodicity to diameter could be varied at need according to the requirements on the number of wavebands and transmission efficiency.

Plasmonic nanostructures are renowned for their sensitivity to refractive index variations. In this thesis, we have established with several simulation studies that the optical response of the arrays varies as a function of the RI of the material inside the holes or as a function of the top cladding material. Therefore, the MIM structure could also be exploited for sensing applications.

In addition, I believe that one interesting feature worth to explore further is the local resonance that appeared at the condition $k_{\mathrm{SPP},(\mathrm{Al/SiO_2})} = G_{10}$ in the reflectance of the Asym-(thin)SML structure during the analysis of the size of the holes. That resonance reaches a zero-reflection minimum for large diameters and is very narrow, with a FWHM of less than 10 nm. Therefore, it might display a quite interesting figure of merit if exploited in sensing applications.



(a) **(b)**

(c) **(d)**

Figure 9.1: Light diffraction patterns from MIM nanohole arrays.

Finally, during the optical characterisation of the devices I noticed a diffraction behaviour which intrigued me. Figure 9.1 shows some images of samples under the light of the microspectrophotometer. The arrays seem to diffract the light (almost) horizontally, along the two-dimensional plane of the array, and in six specific directions which resemble the hexagonal pattern. The light seems to be diffracted in each direction with the 'shape' of the square and varies colour according to the periodicity, the smaller the periodicity the shorter the wavelength of the diffracted light. So maybe the MIM arrays could be used for example as optical router for nanophotonic applications.

Bibliography

[1] R. P. Feynman, "There's plenty of room at the bottom," *California Institute of Technology, Engineering and Science*, vol. 23, no. 5, pp. 22–36, 1960.

[2] P. D. Burns and R. S. Berns, "Analysis multispectral image capture," in *Color and Imaging Conference*, vol. 4, 1996, pp. 19–22.

[3] M. Yamaguchi, T. Teraji, K. Ohsawa, T. Uchiyama, H. Motomura, Y. Murakami, and N. Ohyama, "Color image reproduction based on multispectral and multiprimary imaging: Experimental evaluation," in *Color Imaging: Device-Independent Color, Color Hardcopy, and Applications VII*, vol. 4663. International Society for Optics and Photonics, 2001, pp. 15–26.

[4] G. A. Shaw and H. K. Burke, "Spectral imaging for remote sensing," *Lincoln Laboratory Journal*, vol. 14, no. 1, pp. 3–28, 2003.

[5] D. Wu and D.-W. Sun, "Advanced applications of hyperspectral imaging technology for food quality and safety analysis and assessment: A review – part II: Applications," *Innovative Food Science & Emerging Technologies*, vol. 19, pp. 15–28, 2013.

[6] Y. Fawzy and H. Zeng, "Spectral imaging technology – A review on skin and endoscopy applications," *Recent Patents on Medical Imaging*, vol. 4, no. 2, pp. 101–109, 2014.

[7] J. M. Eichenholz and J. Dougherty, "Ultracompact fully integrated megapixel multispectral imager," in *Integrated Optics: Devices, Materials, and Technologies XIII*, vol. 7218. International Society for Optics and Photonics, 2009, p. 721814.

[8] J. M. Eichenholz, N. Barnett, Y. Juang, D. Fish, S. Spano, E. Lindsley, and D. L. Farkas, "Real-time megapixel multispectral bioimaging," in *Imaging, Manipulation, and Analysis of Biomolecules, Cells, and Tissues VIII*, vol. 7568. International Society for Optics and Photonics, 2010, p. 75681L.

[9] N. Tack, A. Lambrechts, P. Soussan, and L. Haspeslagh, "A compact, high-speed, and low-cost hyperspectral imager," in *Silicon Photonics VII*, vol. 8266. International Society for Optics and Photonics, 2012, p. 82660Q.

[10] B. Geelen, N. Tack, and A. Lambrechts, "A compact snapshot multispectral imager with a monolithically integrated per-pixel filter mosaic," in *Advanced Fabrication Technologies for Micro/Nano Optics and Photonics VII*, vol. 8974. International Society for Optics and Photonics, 2014, p. 89740L.

[11] A. Kristensen, J. K. Yang, S. I. Bozhevolnyi, S. Link, P. Nordlander, N. J. Halas, and N. A. Mortensen, "Plasmonic colour generation," *Nature Reviews Materials*, vol. 2, no. 1, pp. 1–14, 2016.

[12] V. Flauraud, M. Reyes, R. Paniagua-Dominguez, A. I. Kuznetsov, and J. Brugger, "Silicon nanostructures for bright field full color prints," *ACS Photonics*, vol. 4, no. 8, pp. 1913–1919, 2017.

[13] C. Genet and T. Ebbesen, "Light in tiny holes," *Nature*, vol. 445, no. 7123, pp. 39–46, 2007.

[14] P. B. Catrysse and B. A. Wandell, "Integrated color pixels in 0.18-μm complementary metal oxide semiconductor technology," *JOSA A*, vol. 20, no. 12, pp. 2293–2306, 2003.

[15] Q. Chen, D. Chitnis, K. Walls, T. D. Drysdale, S. Collins, and D. R. Cumming, "CMOS photodetectors integrated with plasmonic color filters," *IEEE Photonics Technology Letters*, vol. 24, no. 3, pp. 197–199, 2011.

[16] S. P. Burgos, S. Yokogawa, and H. A. Atwater, "Color imaging via nearest neighbor hole coupling in plasmonic color filters integrated onto a complementary metal-oxide semiconductor image sensor," *ACS Nano*, vol. 7, no. 11, pp. 10 038–10 047, 2013.

[17] T. W. Ebbesen, H. J. Lezec, H. Ghaemi, T. Thio, and P. A. Wolff, "Extraordinary optical transmission through sub-wavelength hole arrays," *Nature*, vol. 391, no. 6668, pp. 667–669, 1998.

[18] T. Søndergaard, S. I. Bozhevolnyi, S. M. Novikov, J. Beermann, E. Devaux, and T. W. Ebbesen, "Extraordinary optical transmission enhanced by nanofocusing," *Nano letters*, vol. 10, no. 8, pp. 3123–3128, 2010.

[19] S. A. Maier, *Plasmonics: Fundamentals and Applications*. Springer, New York, 2007.

[20] M. L. Brongersma and P. G. Kik, *Surface Plasmon Nanophotonics*. Springer, Dordrecht, 2007.

[21] F. J. Garcia-Vidal, L. Martin-Moreno, T. Ebbesen, and L. Kuipers, "Light passing through subwavelength apertures," *Reviews of Modern Physics*, vol. 82, no. 1, pp. 729–787, 2010.

[22] F. G. De Abajo, "Colloquium: Light scattering by particle and hole arrays," *Reviews of Modern Physics*, vol. 79, no. 4, pp. 1267–1290, 2007.

[23] N. Pinton, J. Grant, S. Collins, and D. R. Cumming, "Exploitation of magnetic dipole resonances in metal–insulator–metal plasmonic nanostructures to selectively filter visible light," *ACS Photonics*, vol. 5, no. 4, pp. 1250–1261, 2018.

[24] M. Chalfie, "GFP: Lighting up life," *Proceedings of the National Academy of Sciences*, vol. 106, no. 25, pp. 10 073–10 080, 2009.

[25] G. Lu and B. Fei, "Medical hyperspectral imaging: A review," *Journal of biomedical optics*, vol. 19, no. 1, p. 010901, 2014.

[26] A. El Gamal and H. Eltoukhy, "CMOS image sensors," *IEEE Circuits and Devices Magazine*, vol. 21, no. 3, pp. 6–20, 2005.

[27] A. F. Goetz, "Three decades of hyperspectral remote sensing of the Earth: A personal view," *Remote Sensing of Environment*, vol. 113, pp. S5–S16, 2009.

[28] Q. Li, X. He, Y. Wang, H. Liu, D. Xu, and F. Guo, "Review of spectral imaging technology in biomedical engineering: Achievements and challenges," *Journal of biomedical optics*, vol. 18, no. 10, p. 100901, 2013.

[29] A. N. Belbachir and P. M. Göbel, "Smart cameras: a historical evolution," in *Smart Cameras*. Springer, Boston, MA, 2009, pp. 3–17.

[30] P. Cambou and J. Jaffard, "Status of the CMOS image sensor industry 2018 report," Yole Développement, 2018.

[31] A. K. Jain, *Fundamentals of Digital Image Processing*. Englewood Cliffs, NJ: Prentice Hall, 1989.

[32] www.digitalcameraworld.com, "Turning light into a digital file." [Online]. Available: http://www.jthonline.com/WordPress/wp-content/uploads/Post-LM-subject-thru-to-card.jpg

[33] "CMOS image sensor." [Online]. Available: http://www.jthonline.com/WordPress/wp-content/uploads/Post-LM-bayer-filter.jpg

[34] A. Hoffman, M. Loose, and V. Suntharalingam, "CMOS detector technology," *Experimental Astronomy*, vol. 19, no. 1-3, pp. 111–134, 2005.

[35] T. Graham, "Seeing the light," Science News, 2015. [Online]. Available: https://www.sciencenews.org/article/how-rewire-eye

[36] C. J. Kazilek and K. Cooper, "Rods and cones," Arizona State University School of Life Sciences, Ask A Biologist, 2010. [Online]. Available: https://askabiologist.asu.edu/rods-and-cones

[37] J. Adams, K. Parulski, and K. Spaulding, "Color processing in digital cameras," *IEEE Micro*, vol. 18, no. 6, pp. 20–30, 1998.

[38] J. Nakamura, *Image Sensors and Signal Processing for Digital Still Cameras*. CRC press, 2017.

[39] B. E. Bayer, "Color imaging array," Google Patents, 1976, - US Patent 3,971,065.

[40] H. Honda, Y. Iida, and Y. Egawa, "High sensitivity color CMOS image sensor with WRGB color filter array and color separation process using edge detection," in *Proc. Int. Image Sens. Workshop*, 2007, pp. 263–266.

[41] H. S. Malvar, L.-w. He, and R. Cutler, "High-quality linear interpolation for demosaicing of bayer-patterned color images," in *2004 IEEE International Conference on Acoustics, Speech, and Signal Processing*, vol. 3. IEEE, 2004, pp. iii–485.

[42] C. Fernandez-Maloigne, *Advanced Color Image Processing and Analysis*. Springer, New York, 2012.

[43] E. A. Newman and P. H. Hartline, "The infrared "vision" of snakes," *Scientific American*, vol. 246, no. 3, pp. 116–127, 1982.

[44] J. Fang, "Snake infrared detection unravelled," *Nature*, 2010.

[45] P. Skorupski and L. Chittka, "Photoreceptor spectral sensitivity in the bumblebee, Bombus impatiens (Hymenoptera: Apidae)," *PLoS One*, vol. 5, no. 8, p. e12049, 2010.

[46] D. Moshou, C. Bravo, R. Oberti, J. West, L. Bodria, A. McCartney, and H. Ramon, "Plant disease detection based on data fusion of hyper-spectral and multi-spectral fluorescence imaging using Kohonen maps," *Real-Time Imaging*, vol. 11, no. 2, pp. 75–83, 2005.

[47] Y. Garini and E. Tauber, "Spectral imaging: methods, design, and applications," in *Biomedical Optical Imaging Technologies*. Springer, Berlin, Heidelberg, 2013, pp. 111–161.

[48] K. J. Zuzak, M. D. Schaeberle, E. N. Lewis, and I. W. Levin, "Visible reflectance hyperspectral imaging: characterization of a noninvasive, in vivo system for determining tissue perfusion," *Analytical Chemistry*, vol. 74, no. 9, pp. 2021–2028, 2002.

[49] G. Stamatas, B. Zmudzka, N. Kollias, and J. Beer, "In vivo measurement of skin erythema and pigmentation: new means of implementation of diffuse reflectance spectroscopy with a commercial instrument," *British Journal of Dermatology*, vol. 159, no. 3, pp. 683–690, 2008.

[50] "Multispectral vs. hyperspectral imagery explained," GIS Geography, 2020. [Online]. Available: https://gisgeography.com/multispectral-vs-hyperspectral-imagery-explained/

[51] "Hyperspectral imaging," Wikipedia, 2020. [Online]. Available: https://en.wikipedia.org/wiki/Hyperspectral_imaging

[52] N. Gat, "Imaging spectroscopy using tunable filters: a review," in *Wavelet Applications VII*, vol. 4056. International Society for Optics and Photonics, 2000, pp. 50–64.

[53] K.-B. Cho, C. Lee, S. Eikedal, A. Baum, J. Jiang, C. Xu, X. Fan, and R. Kauffman, "A 1/2.5 inch 8.1 Mpixel CMOS image sensor for digital cameras," in *2007 IEEE International Solid-State Circuits Conference. Digest of Technical Papers*. IEEE, 2007, pp. 508–618.

[54] C.-R. Moon, J.-C. Shin, J. Kim, Y. K. Lee, Y.-J. Cho, Y.-Y. Yu, S.-H. Hwang, D.-C. Park, B. J. Park, H.-Y. Kim *et al.*, "Dedicated process architecture and the characteristics of 1.4 μm pixel CMOS image sensor with 8M density," in *2007 IEEE Symposium on VLSI Technology*. IEEE, 2007, pp. 62–63.

[55] W. L. Barnes, A. Dereux, and T. W. Ebbesen, "Surface plasmon subwavelength optics," *Nature*, vol. 424, no. 6950, pp. 824–830, 2003.

[56] B. Zeng, Y. Gao, and F. J. Bartoli, "Ultrathin nanostructured metals for highly transmissive plasmonic subtractive color filters," *Scientific Reports*, vol. 3, p. 2840, 2013.

[57] V. R. Shrestha, S.-S. Lee, E.-S. Kim, and D.-Y. Choi, "Aluminum plasmonics based highly transmissive polarization-independent subtractive color filters exploiting a nanopatch array," *Nano Letters*, vol. 14, no. 11, pp. 6672–6678, 2014.

[58] G. Si, Y. Zhao, J. Lv, M. Lu, F. Wang, H. Liu, N. Xiang, T. J. Huang, A. J. Danner, J. Teng *et al.*, "Reflective plasmonic color filters based on lithographically patterned silver nanorod arrays," *Nanoscale*, vol. 5, no. 14, pp. 6243–6248, 2013.

[59] A. S. Roberts, A. Pors, O. Albrektsen, and S. I. Bozhevolnyi, "Subwavelength plasmonic color printing protected for ambient use," *Nano Letters*, vol. 14, no. 2, pp. 783–787, 2014.

[60] J. S. Clausen, E. Højlund-Nielsen, A. B. Christiansen, S. Yazdi, M. Grajower, H. Taha, U. Levy, A. Kristensen, and N. A. Mortensen, "Plasmonic metasurfaces for coloration of plastic consumer products," *Nano Letters*, vol. 14, no. 8, pp. 4499–4504, 2014.

[61] F. Cheng, J. Gao, T. S. Luk, and X. Yang, "Structural color printing based on plasmonic metasurfaces of perfect light absorption," *Scientific Reports*, vol. 5, p. 11045, 2015.

[62] S. Yokogawa, S. P. Burgos, and H. A. Atwater, "Plasmonic color filters for CMOS image sensor applications," *Nano Letters*, vol. 12, no. 8, pp. 4349–4354, 2012.

[63] R. Zia, M. D. Selker, P. B. Catrysse, and M. L. Brongersma, "Geometries and materials for subwavelength surface plasmon modes," *JOSA A*, vol. 21, no. 12, pp. 2442–2446, 2004.

[64] J. Dionne, H. Lezec, and H. A. Atwater, "Highly confined photon transport in subwavelength metallic slot waveguides," *Nano Letters*, vol. 6, no. 9, pp. 1928–1932, 2006.

[65] R. K. Sinha, T. Srivastava, R. Bhattacharyya *et al.*, "Propagation characteristics of coupled surface plasmon polaritons in pvdf slab waveguides at terahertz frequencies," *Journal of Optics*, vol. 15, no. 3, p. 035001, 2013.

[66] S. A. Maier, S. R. Andrews, L. Martin-Moreno, and F. Garcia-Vidal, "Terahertz surface plasmon-polariton propagation and focusing on periodically corrugated metal wires," *Physical Review Letters*, vol. 97, no. 17, p. 176805, 2006.

[67] K. Diest, J. A. Dionne, M. Spain, and H. A. Atwater, "Tunable color filters based on metal- insulator- metal resonators," *Nano Letters*, vol. 9, no. 7, pp. 2579–2583, 2009.

[68] E. Laux, C. Genet, T. Skauli, and T. W. Ebbesen, "Plasmonic photon sorters for spectral and polarimetric imaging," *Nature Photonics*, vol. 2, no. 3, pp. 161–164, 2008.

[69] T. Xu, Y.-K. Wu, X. Luo, and L. J. Guo, "Plasmonic nanoresonators for high-resolution colour filtering and spectral imaging," *Nature Communications*, vol. 1, no. 1, pp. 1–5, 2010.

[70] D. Fleischman, L. A. Sweatlock, H. Murakami, and H. Atwater, "Hyper-selective plasmonic color filters," *Optics Express*, vol. 25, no. 22, pp. 27 386–27 395, 2017.

[71] Y. D. Shah, J. Grant, D. Hao, M. Kenney, V. Pusino, and D. R. Cumming, "Ultra-narrow line width polarization-insensitive filter using a symmetry-breaking selective plasmonic metasurface," *ACS Photonics*, vol. 5, no. 2, pp. 663–669, 2018.

[72] S. A. Maier, P. G. Kik, H. A. Atwater, S. Meltzer, E. Harel, B. E. Koel, and A. A. Requicha, "Local detection of electromagnetic energy transport below the diffraction limit in metal nanoparticle plasmon waveguides," *Nature Materials*, vol. 2, no. 4, pp. 229–232, 2003.

[73] L. Yin, V. K. Vlasko-Vlasov, J. Pearson, J. M. Hiller, J. Hua, U. Welp, D. E. Brown, and C. W. Kimball, "Subwavelength focusing and guiding of surface plasmons," *Nano Letters*, vol. 5, no. 7, pp. 1399–1402, 2005.

[74] C. R. Williams, S. R. Andrews, S. Maier, A. Fernández-Domínguez, L. Martín-Moreno, and F. García-Vidal, "Highly confined guiding of terahertz surface plasmon polaritons on structured metal surfaces," *Nature Photonics*, vol. 2, no. 3, pp. 175–179, 2008.

[75] A. G. Brolo, E. Arctander, R. Gordon, B. Leathem, and K. L. Kavanagh, "Nanohole-enhanced Raman scattering," *Nano Letters*, vol. 4, no. 10, pp. 2015–2018, 2004.

[76] B. Liedberg, C. Nylander, and I. Lunström, "Surface plasmon resonance for gas detection and biosensing," *Sensors and Actuators*, vol. 4, pp. 299–304, 1983.

[77] A. J. Haes and R. P. Van Duyne, "A nanoscale optical biosensor: sensitivity and selectivity of an approach based on the localized surface plasmon resonance spectroscopy of triangular silver nanoparticles," *Journal of the American Chemical Society*, vol. 124, no. 35, pp. 10 596–10 604, 2002.

[78] L. J. Sherry, S.-H. Chang, G. C. Schatz, R. P. Van Duyne, B. J. Wiley, and Y. Xia, "Localized surface plasmon resonance spectroscopy of single silver nanocubes," *Nano Letters*, vol. 5, no. 10, pp. 2034–2038, 2005.

[79] E. M. Larsson, J. Alegret, M. Käll, and D. S. Sutherland, "Sensing characteristics of NIR localized surface plasmon resonances in gold nanorings for application as ultrasensitive biosensors," *Nano Letters*, vol. 7, no. 5, pp. 1256–1263, 2007.

[80] M. Agrawal and P. Peumans, "Broadband optical absorption enhancement through coherent light trapping in thin-film photovoltaic cells," *Optics Express*, vol. 16, no. 8, pp. 5385–5396, 2008.

[81] R. R. Lunt, T. P. Osedach, P. R. Brown, J. A. Rowehl, and V. Bulović, "Practical roadmap and limits to nanostructured photovoltaics," *Advanced Materials*, vol. 23, no. 48, pp. 5712–5727, 2011.

[82] P. V. Kamat, "Boosting the efficiency of quantum dot sensitized solar cells through modulation of interfacial charge transfer," *Accounts of Chemical Research*, vol. 45, no. 11, pp. 1906–1915, 2012.

[83] I. J. Kramer and E. H. Sargent, "Colloidal quantum dot photovoltaics: a path forward," *ACS Nano*, vol. 5, no. 11, pp. 8506–8514, 2011.

[84] A. Krishnan, T. Thio, T. Kim, H. Lezec, T. Ebbesen, P. Wolff, J. Pendry, L. Martin-Moreno, and F. Garcia-Vidal, "Evanescently coupled resonance in surface plasmon enhanced transmission," *Optics Communications*, vol. 200, no. 1-6, pp. 1–7, 2001.

[85] W. L. Barnes, W. A. Murray, J. Dintinger, E. Devaux, and T. Ebbesen, "Surface plasmon polaritons and their role in the enhanced transmission of light through periodic arrays of subwavelength holes in a metal film," *Physical Review Letters*, vol. 92, no. 10, p. 107401, 2004.

[86] S. Enoch and N. Bonod, *Plasmonics: From Basics to Advanced Topics*. Springer, Berlin, Heidelberg, 2012, vol. 167.

[87] J. Zhang, L. Zhang, and W. Xu, "Surface plasmon polaritons: physics and applications," *Journal of Physics D: Applied Physics*, vol. 45, no. 11, p. 113001, 2012.

[88] C. A. Balanis, *Advanced Engineering Electromagnetics*. John Wiley & Sons, 2012.

[89] S. J. Orfanidis, *Electromagnetic Waves and Antennas*. Rutgers University New Brunswick, NJ, 2002.

[90] L. Solymar and E. Shamonina, *Waves in Metamaterials*. Oxford University Press, Oxford, 2009.

[91] A. Otto, "Excitation of nonradiative surface plasma waves in silver by the method of frustrated total reflection," *Zeitschrift für Physik A Hadrons and nuclei*, vol. 216, no. 4, pp. 398–410, 1968.

[92] E. Kretschmann and H. Raether, "Radiative decay of non radiative surface plasmons excited by light," *Zeitschrift für Naturforschung A*, vol. 23, no. 12, pp. 2135–2136, 1968.

[93] Lumerical Inc. [Online]. Available: https://www.lumerical.com/products/

[94] E. Verhagen, "Subwavelength light confinement with surface plasmon polaritons," Ph.D. dissertation, Utrecht University, 2009.

[95] S. I. Bozhevolnyi and T. Søndergaard, "General properties of slow-plasmon resonant nanostructures: nano-antennas and resonators," *Optics Express*, vol. 15, no. 17, pp. 10 869–10 877, 2007.

[96] E. Economou, "Surface plasmons in thin films," *Physical Review*, vol. 182, no. 2, pp. 539–554, 1969.

[97] J. Burke, G. Stegeman, and T. Tamir, "Surface-polariton-like waves guided by thin, lossy metal films," *Physical Review B*, vol. 33, no. 8, pp. 5186–5201, 1986.

[98] J. A. Dionne, E. Verhagen, A. Polman, and H. A. Atwater, "Are negative index materials achievable with surface plasmon waveguides? A case study of three plasmonic geometries," *Optics Express*, vol. 16, no. 23, pp. 19 001–19 017, 2008.

[99] C. Della Giovampaola and N. Engheta, "Digital metamaterials," *Nature Materials*, vol. 13, no. 12, pp. 1115–1121, 2014.

[100] H. A. Bethe, "Theory of diffraction by small holes," *Physical Review*, vol. 66, no. 7-8, pp. 163–182, 1944.

[101] H. Ghaemi, T. Thio, D. e. a. Grupp, T. W. Ebbesen, and H. Lezec, "Surface plasmons enhance optical transmission through subwavelength holes," *Physical Review B*, vol. 58, no. 11, pp. 6779–6782, 1998.

[102] B. A. Munk, *Frequency Selective Surfaces: Theory and Design*. John Wiley & Sons, 2005.

[103] C.-C. Chen, "Transmission through a conducting screen perforated periodically with apertures," *IEEE Transactions on Microwave Theory and Techniques*, vol. 18, no. 9, pp. 627–632, 1970.

[104] C. J. Bouwkamp, "Diffraction theory," *Reports on Progress in Physics*, vol. 17, no. 1, pp. 35–100, 1954.

[105] C. Bouwkamp, "On Bethe's theory of diffraction by small holes," *Philips Research Reports*, vol. 5, pp. 321–332, 1950.

[106] A. Adam, J. Brok, M. Seo, K. Ahn, D. Kim, J. Kang, Q. H. Park, M. Nagel, and P. Planken, "Advanced terahertz electric near-field measurements at sub-wavelength diameter metallic apertures," *Optics Express*, vol. 16, no. 10, pp. 7407–7417, 2008.

[107] J. Porto, F. Garcia-Vidal, and J. Pendry, "Transmission resonances on metallic gratings with very narrow slits," *Physical Review Letters*, vol. 83, no. 14, pp. 2845–2848, 1999.

[108] F. G. De Abajo, "Light transmission through a single cylindrical hole in a metallic film," *Optics Express*, vol. 10, no. 25, pp. 1475–1484, 2002.

[109] L. Rayleigh, "XVIII. on the passage of electric waves through tubes, or the vibrations of dielectric cylinders," *The London, Edinburgh, and Dublin Philosophical Magazine and Journal of Science*, vol. 43, no. 261, pp. 125–132, 1897.

[110] D. Grupp, H. Lezec, T. Ebbesen, K. Pellerin, and T. Thio, "Crucial role of metal surface in enhanced transmission through subwavelength apertures," *Applied Physics Letters*, vol. 77, no. 11, pp. 1569–1571, 2000.

[111] H. Shin, P. B. Catrysse, and S. Fan, "Effect of the plasmonic dispersion relation on the transmission properties of subwavelength cylindrical holes," *Physical Review B*, vol. 72, no. 8, p. 085436, 2005.

[112] P. B. Catrysse, H. Shin, and S. Fan, "Propagating modes in subwavelength cylindrical holes," *Journal of Vacuum Science & Technology B: Microelectronics and Nanometer Structures Processing, Measurement, and Phenomena*, vol. 23, no. 6, pp. 2675–2678, 2005.

[113] K. Webb and J. Li, "Analysis of transmission through small apertures in conducting films," *Physical Review B - Condensed Matter and Materials Physics*, vol. 73, no. 3, pp. 73–76, 2006.

[114] A. Degiron and T. Ebbesen, "The role of localized surface plasmon modes in the enhanced transmission of periodic subwavelength apertures," *Journal of Optics A: Pure and Applied Optics*, vol. 7, no. 2, pp. S90–S96, 2005.

[115] R. Gordon and A. G. Brolo, "Increased cut-off wavelength for a subwavelength hole in a real metal," *Optics Express*, vol. 13, no. 6, pp. 1933–1938, 2005.

[116] H. J. Lezec, A. Degiron, E. Devaux, R. Linke, L. Martin-Moreno, F. Garcia-Vidal, and T. Ebbesen, "Beaming light from a subwavelength aperture," *Science*, vol. 297, no. 5582, pp. 820–822, 2002.

[117] C. Sönnichsen, A. Duch, G. Steininger, M. Koch, G. Von Plessen, and J. Feldmann, "Launching surface plasmons into nanoholes in metal films," *Applied Physics Letters*, vol. 76, no. 2, pp. 140–142, 2000.

[118] L. Yin, V. Vlasko-Vlasov, A. Rydh, J. Pearson, U. Welp, S.-H. Chang, S. Gray, G. C. Schatz, D. Brown, and C. W. Kimball, "Surface plasmons at single nanoholes in Au films," *Applied Physics Letters*, vol. 85, no. 3, pp. 467–469, 2004.

[119] S.-H. Chang, S. K. Gray, and G. C. Schatz, "Surface plasmon generation and light transmission by isolated nanoholes and arrays of nanoholes in thin metal films," *Optics Express*, vol. 13, no. 8, pp. 3150–3165, 2005.

[120] A.-L. Baudrion, F. de Leon-Perez, O. Mahboub, A. Hohenau, H. Ditlbacher, F. J. Garcia-Vidal, J. Dintinger, T. W. Ebbesen, L. Martin-Moreno, and J. R. Krenn, "Coupling efficiency of light to surface plasmon polariton for single subwavelength holes in a gold film," *Optics Express*, vol. 16, no. 5, pp. 3420–3429, 2008.

[121] D. E. Grupp, H. J. Lezec, T. Thio, and T. W. Ebbesen, "Beyond the bethe limit: Tunable enhanced light transmission through a single sub-wavelength aperture," *Advanced Materials*, vol. 11, no. 10, pp. 860–862, 1999.

[122] R. W. Wood, "On a remarkable case of uneven distribution of light in a diffraction grating spectrum," *Proceedings of the Physical Society of London*, vol. 18, no. 1, pp. 269–275, 1902.

[123] L. Rayleigh, "On the dynamical theory of gratings," *Proceedings of the Royal Society of London. Series A, Containing Papers of a Mathematical and Physical Character*, vol. 79, no. 532, pp. 399–416, 1907.

[124] U. Fano, "The theory of anomalous diffraction gratings and of quasi-stationary waves on metallic surfaces (Sommerfeld's waves)," *JOSA*, vol. 31, no. 3, pp. 213–222, 1941.

[125] A. A. Darweesh, S. J. Bauman, D. T. Debu, and J. B. Herzog, "The role of Rayleigh-Wood anomalies and surface plasmons in optical enhancement for nano-gratings," *Nanomaterials*, vol. 8, no. 10, p. 809, 2018.

[126] D. Maystre, "Theory of Wood's anomalies," in *Plasmonics*. Springer, Berlin, Heidelberg, 2012, pp. 39–83.

[127] A. Maradudin, I. Simonsen, J. Polanco, and R. Fitzgerald, "Rayleigh and Wood anomalies in the diffraction of light from a perfectly conducting reflection grating," *Journal of Optics*, vol. 18, no. 2, p. 024004, 2016.

[128] A. E. Miroshnichenko, S. Flach, and Y. S. Kivshar, "Fano resonances in nanoscale structures," *Reviews of Modern Physics*, vol. 82, no. 3, pp. 2257–2298, 2010.

[129] B. Luk'yanchuk, N. I. Zheludev, S. A. Maier, N. J. Halas, P. Nordlander, H. Giessen, and C. T. Chong, "The Fano resonance in plasmonic nanostructures and metamaterials," *Nature Materials*, vol. 9, no. 9, pp. 707–715, 2010.

[130] U. Fano, "Sullo spettro di assorbimento dei gas nobili presso il limite dello spettro d'arco," *Il Nuovo Cimento (1924-1942)*, vol. 12, no. 3, pp. 154–161, 1935.

[131] C. Genet, M. P. van Exter, and J. Woerdman, "Fano-type interpretation of red shifts and red tails in hole array transmission spectra," *Optics Communications*, vol. 225, no. 4-6, pp. 331–336, 2003.

[132] D. Pacifici, H. J. Lezec, L. A. Sweatlock, R. J. Walters, and H. A. Atwater, "Universal optical transmission features in periodic and quasiperiodic hole arrays," *Optics Express*, vol. 16, no. 12, pp. 9222–9238, 2008.

[133] F. Przybilla, A. Degiron, J. Laluet, C. Genet, and T. Ebbesen, "Optical transmission in perforated noble and transition metal films," *Journal of Optics A: Pure and Applied Optics*, vol. 8, no. 5, pp. 458–463, 2006.

[134] M. Tanaka, F. Miyamaru, M. Hangyo, T. Tanaka, M. Akazawa, and E. Sano, "Effect of a thin dielectric layer on terahertz transmission characteristics for metal hole arrays," *Optics Letters*, vol. 30, no. 10, pp. 1210–1212, 2005.

[135] K. Van der Molen, K. K. Koerkamp, S. Enoch, F. B. Segerink, N. Van Hulst, and L. Kuipers, "Role of shape and localized resonances in extraordinary transmission through periodic arrays of subwavelength holes: experiment and theory," *Physical Review B*, vol. 72, no. 4, p. 045421, 2005.

[136] J. B. Pendry, A. Holden, W. Stewart, and I. Youngs, "Extremely low frequency plasmons in metallic mesostructures," *Physical Review Letters*, vol. 76, no. 25, pp. 4773–4776, 1996.

[137] K. K. Koerkamp, S. Enoch, F. B. Segerink, N. Van Hulst, and L. Kuipers, "Strong influence of hole shape on extraordinary transmission through periodic arrays of subwavelength holes," *Physical Review Letters*, vol. 92, no. 18, p. 183901, 2004.

[138] F. Garcia-Vidal, E. Moreno, J. Porto, and L. Martin-Moreno, "Transmission of light through a single rectangular hole," *Physical Review Letters*, vol. 95, no. 10, p. 103901, 2005.

[139] S. G. Rodrigo, O. Mahboub, A. Degiron, C. Genet, F. García-Vidal, L. Martín-Moreno, and T. W. Ebbesen, "Holes with very acute angles: a new paradigm of extraordinary optical transmission through strongly localized modes," *Optics Express*, vol. 18, no. 23, pp. 23 691–23 697, 2010.

[140] F. Przybilla, A. Degiron, C. Genet, T. Ebbesen, F. de Léon-Pérez, J. Bravo-Abad, F. García-Vidal, and L. Martín-Moreno, "Efficiency and finite size effects in enhanced transmission through subwavelength apertures," *Optics Express*, vol. 16, no. 13, pp. 9571–9579, 2008.

[141] H. Petroski, *The Essential Engineer: Why Science Alone Will Not Solve Our Global Problems*. Vintage, 2011.

[142] K. Yee, "Numerical solution of initial boundary value problems involving Maxwell's equations in isotropic media," *IEEE Transactions on antennas and propagation*, vol. 14, no. 3, pp. 302–307, 1966.

[143] J. B. Schneider, "Understanding the finite-difference time-domain method," *School of electrical engineering and computer science Washington State University*, p. 181, 2010.

[144] A. Z. Elsherbeni and V. Demir, *The Finite-Difference Time-Domain Method for Electromagnetics with MATLAB Simulations*. SciTech Publishing, Inc Raleigh, NC, 2016.

[145] K. E. Spear and R. R. Dirkx, "Role of high-temperature chemistry in CVD processing," *High Temperature Science*, vol. 27, p. 107, 1989.

[146] M. Quirk and J. Serda, *Semiconductor Manufacturing Technology*. Prentice Hall Upper Saddle River, NJ, 2001, vol. 1, ch. 11 - Deposition. [Online]. Available: https://jupiter.math.nctu.edu.tw/~weng/courses/IC_2007/PROJECT_MATH_CLASS3/%E5%8D%8A%E5%B0%8E%E9%AB%94%E8%A3%BD%E7%A8%8B%E7%B0%A1%E4%BB%8B2.pdf

[147] I. J. H. McCrindle, "Structured photonic materials for multi-spectral imaging applications," Ph.D. dissertation, University of Glasgow, 2015.

[148] P. Rai-Choudhury, *Handbook of Microlithography, Micromachining, and Microfabrication. Volume 1: Microlithography*. SPIE Optical Engineering Press, Bellingham, Washington USA, & The Institution of Electric Engineers, London UK, 1997.

[149] M. A. McCord, "Introduction to electron-beam lithography (short course notes)," SPIE's International Symposium on Microlithography, 1999.

[150] D. Kyser and N. Viswanathan, "Monte carlo simulation of spatially distributed beams in electron-beam lithography," *Journal of Vacuum Science and Technology*, vol. 12, no. 6, pp. 1305–1308, 1975.

[151] N. Posseme, *Plasma Etching Processes for CMOS Devices Realization*. Elsevier, 2017.

[152] "What is reactive ion etching?" Plasma Etch, Inc. [Online]. Available: https://www.plasmaetch.com/reactive-ion-etching-systems-rie.php

[153] S. Franssila and L. Sainiemi, "Reactive ion etching (RIE)," *Encyclopedia of Microfluidics and Nanofluidics*, 2013.

[154] R. Erni, M. D. Rossell, C. Kisielowski, and U. Dahmen, "Atomic-resolution imaging with a sub-50-pm electron probe," *Physical Review Letters*, vol. 102, no. 9, p. 096101, 2009.

[155] A. Nanakoudis, "Sem: Types of electrons and the information they provide," Thermo Fisher Scientific. [Online]. Available: https://www.thermofisher.com/blog/microscopy/sem-types-electrons-and-the-information-they-provide/

[156] ——, "SEM and TEM: what's the difference?" Thermo Fisher Scientific Inc., 2019. [Online]. Available: https://blog.phenom-world.com/sem-tem-difference

[157] A. Tankeshwar, "Difference between scanning electron microscopy (SEM) and transmission electron microscopy (TEM)," Microbe Online, 2018. [Online]. Available: https://microbeonline.com/difference-electron-microscopy-between-sem-tem/

[158] "Electron microscope," New World Encyclopedia, 2017. [Online]. Available: http://www.newworldencyclopedia.org/entry/Electron_microscope

[159] H. Fuchs, H. Hölscher, and A. Schirmeisen, "Scanning probe microscopy," *Encyclopedia of Materials: Science and Technology*, 2005.

[160] "Scanning Probe Microscopy," The Center for Probing the Nanoscale (CPN) at Stanford University. [Online]. Available: https://teachers.stanford.edu/activities/SPMReference/SPMReference.pdf

[161] "Scanning Probe Microscopes," Bruker. [Online]. Available: https://www.bruker.com/products/surface-and-dimensional-analysis/atomic-force-microscopes/campaigns/spm-microscopes-intro-to-scanning-probe-microscopy.html

[162] "STM – scanning Tunneling Microscope," The University of Warwick, Department of Physics. [Online]. Available: https://warwick.ac.uk/fac/sci/physics/current/postgraduate/regs/mpagswarwick/ex5/techniques/electronic/microscopy/

[163] "Scanning Tunneling Microscopes (STM) - Functionality and applications," AZoNano. [Online]. Available: https://www.azonano.com/article.aspx?ArticleID=1725

[164] "Scanning Tunneling Microscope," Wikipedia. [Online]. Available: https://en.wikipedia.org/wiki/Scanning_tunneling_microscope

[165] B. Smith, "The differences between atomic force microscopy and scanning electron microscopy," AZoMaterials, 2015. [Online]. Available: https://www.azom.com/article.aspx?ArticleID=11879

[166] "Atomic Force Microscopy," Nanoscience Instruments. [Online]. Available: https://www.nanoscience.com/techniques/atomic-force-microscopy/

[167] "How AFM works," Park Systems. [Online]. Available: https://www.parksystems.com/index.php/medias/nano-academy/how-afm-works

[168] A. Hayley, "Atomic Force Microscope (AFM)," MicroscopeMaster.com. [Online]. Available: https://www.microscopemaster.com/atomic-force-microscope.html

[169] M. Chassé, G. Lelong, P. Van Nijnatten, I. Schoofs, J. De Wolf, L. Galoisy, and G. Calas, "Optical absorption microspectroscopy (μ-oas) based on schwarzschild-type cassegrain optics," *Applied Spectroscopy*, vol. 69, no. 4, pp. 457–463, 2015.

[170] H. Zhao, "Spectral sensitivity database," The University of Tokyo. [Online]. Available: https://nae-lab.org/~rei/research/cs/zhao/database.html

[171] "UV/VIS bandpass and laser line filters - part no: FB450-40, FB550-40, FB650-40," Thorlabs Inc. [Online]. Available: http://www.thorlabs.de/newgrouppage9.cfm?objectgroup_id=1001

[172] J. M. McMahon, J. Henzie, T. W. Odom, G. C. Schatz, and S. K. Gray, "Tailoring the sensing capabilities of nanohole arrays in gold films with Rayleigh anomaly-surface plasmon polaritons," *Optics Express*, vol. 15, no. 26, pp. 18 119–18 129, 2007.

[173] H. Gao, J. McMahon, M. Lee, J. Henzie, S. Gray, G. C. Schatz, and T. W. Odom, "Rayleigh anomaly-surface plasmon polariton resonances in palladium and gold subwavelength hole arrays," *Optics Express*, vol. 17, no. 4, pp. 2334–2340, 2009.

[174] E. J. Zeman and G. C. Schatz, "An accurate electromagnetic theory study of surface enhancement factors for silver, gold, copper, lithium, sodium, aluminum, gallium, indium, zinc, and cadmium," *Journal of Physical Chemistry*, vol. 91, no. 3, pp. 634–643, 1987.

[175] I. R. Hooper and J. R. Sambles, "Surface plasmon polaritons on thin-slab metal gratings," *Physical Review B*, vol. 67, no. 23, p. 235404, 2003.

[176] M. Sarrazin, J.-P. Vigneron, and J.-M. Vigoureux, "Role of Wood anomalies in optical properties of thin metallic films with a bidimensional array of subwavelength holes," *Physical Review B*, vol. 67, no. 8, p. 085415, 2003.

[177] H. Stein, V. Wells, and R. Hampy, "Properties of plasma-deposited silicon nitride," *Journal of the Electrochemical Society*, vol. 126, no. 10, pp. 1750–1754, 1979.

[178] T. Müller, M. Brandl, O. Brand, and H. Baltes, "An industrial CMOS process family adapted for the fabrication of smart silicon sensors," *Sensors and Actuators A: Physical*, vol. 84, no. 1-2, pp. 126–133, 2000.

[179] N. Pinton, J. Grant, B. Choubey, D. Cumming, and S. Collins, "Recent progress in plasmonic colour filters for image sensor and multispectral applications," in *Nanophotonics VI*, vol. 9884. International Society for Optics and Photonics, 2016, p. 988438.

[180] A. B. Evlyukhin, S. M. Novikov, U. Zywietz, R. L. Eriksen, C. Reinhardt, S. I. Bozhevolnyi, and B. N. Chichkov, "Demonstration of magnetic dipole resonances of dielectric nanospheres in the visible region," *Nano Letters*, vol. 12, no. 7, pp. 3749–3755, 2012.

[181] J. Van de Groep and A. Polman, "Designing dielectric resonators on substrates: Combining magnetic and electric resonances," *Optics Express*, vol. 21, no. 22, pp. 26 285–26 302, 2013.

[182] I. Staude, A. E. Miroshnichenko, M. Decker, N. T. Fofang, S. Liu, E. Gonzales, J. Dominguez, T. S. Luk, D. N. Neshev, I. Brener *et al.*, "Tailoring directional scattering through magnetic and electric resonances in subwavelength silicon nanodisks," *ACS Nano*, vol. 7, no. 9, pp. 7824–7832, 2013.

[183] M. A. van de Haar, J. van de Groep, B. J. Brenny, and A. Polman, "Controlling magnetic and electric dipole modes in hollow silicon nanocylinders," *Optics Express*, vol. 24, no. 3, pp. 2047–2064, 2016.

[184] D. Kajfez and A. A. Kishk, "Dielectric resonator antenna-possible candidate for adaptive antenna arrays," in *Proceedings VITEL 2002, International Symposium on Telecommunications, Next Generation Networks and Beyond*, 2002, pp. 13–14.

[185] Y. Kobayashi and S. Tanaka, "Resonant modes of a dielectric rod resonator short-circuited at both ends by parallel conducting plates," *IEEE Transactions on Microwave Theory and Techniques*, vol. 28, no. 10, pp. 1077–1085, 1980.

[186] "High performance positive EB resist - ZEP520A series," Zeon Corporation. [Online]. Available: http://www.zeon.co.jp/business_e/enterprise/imagelec/zep520A.html

[187] "Shipley Microposit S1800 series photo resists," Shipley Corporation. [Online]. Available: https://amolf.nl/wp-content/uploads/2016/09/datasheets_S1800.pdf

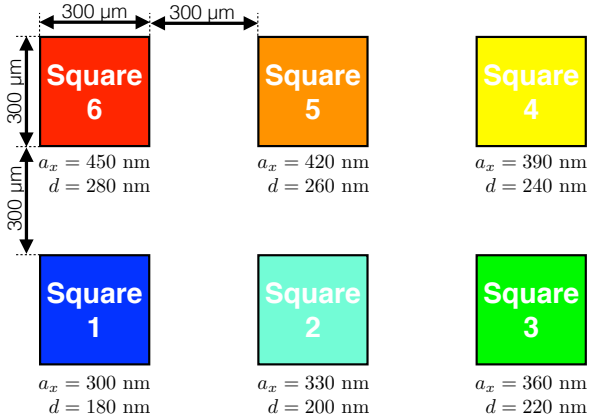
Appendices

Appendix A

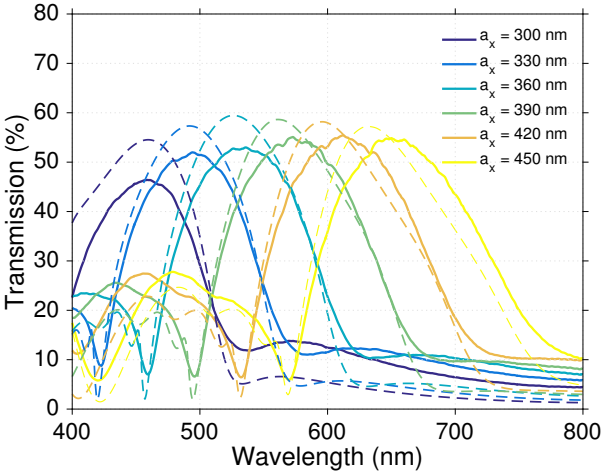
Samples

This Appendix provides the e-beam layouts, the optical measurements and the SEM characterisations of the MIM plasmonic filter arrays presented in this Thesis.

A.1 Sample S23800: 40/70/40 MIM



(a) E-beam layout - Dose 470 $\mu C/cm^2$



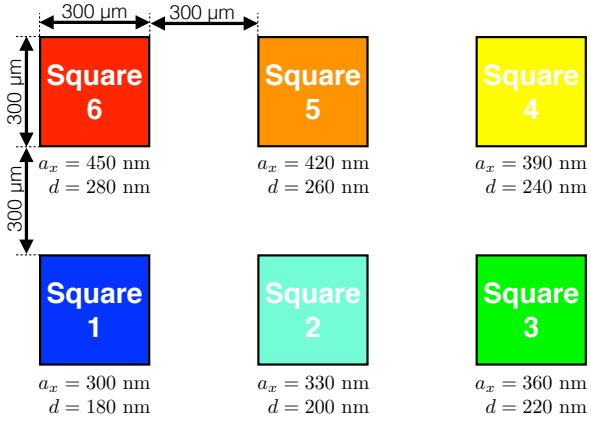
(b) Optical characterization

Array	SEM Images	Measured diameters
Square 1 $a_x = 300$ nm $d = 180$ nm		$d_b = 190$ nm $d_t = 220$ nm
Square 2 $a_x = 330$ nm $d = 200$ nm		$d_b = 205$ nm $d_t = 245$ nm
Square 3 $a_x = 360$ nm $d = 220$ nm		$d_b = 225$ nm $d_t = 265$ nm
Square 4 $a_x = 390$ nm $d = 240$ nm		$d_b = 240$ nm $d_t = 280$ nm
Square 4 $a_x = 420$ nm $d = 260$ nm		$d_b = 260$ nm $d_t = 300$ nm
Square 4 $a_x = 450$ nm $d = 280$ nm		$d_b = 280$ nm $d_t = 320$ nm

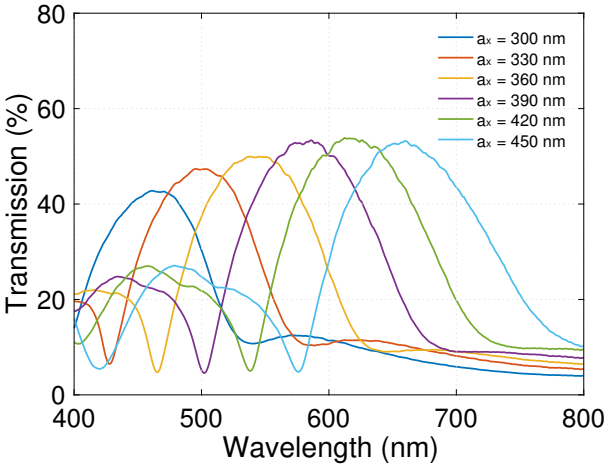
(c) SEM characterization

Figure A.1: Sample S23800: (a) E-beam layout, (b) Optical characterisation and (c) SEM characterisation.

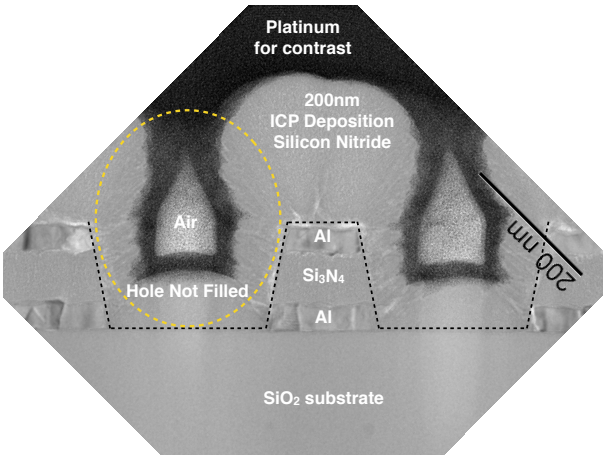
A.2 Sample S23801: 40/70/40 MIM



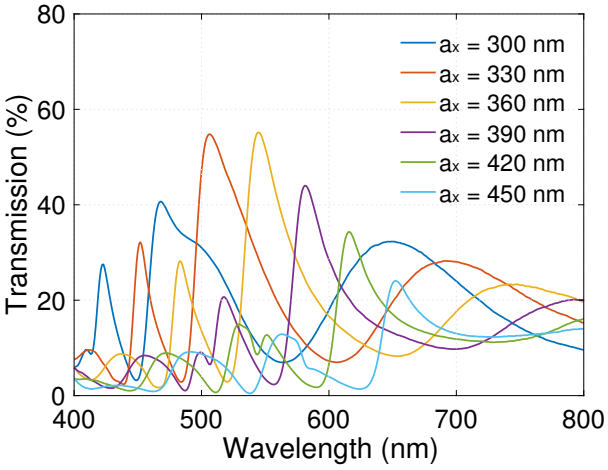
(a) E-beam layout - Dose 470 $\mu C/cm^2$



(c) Optical characterisation after nanohole patterning



(b) TEM of Square 3 ($a_x = 360$ nm)



(d) Optical characterisation after 200 nm Si_3N_4 ICP dep.

Figure A.2: Sample S23801: (a) E-beam layout, (b) TEM characterisation of Square 3, (c) Optical characterisation after nanohole patterning (empty holes) and (d) Optical characterisation after 200 nm Si_3N_4 ICP deposition as imaged in (b).

A.3 Sample S24734: 40/100/40 MIM

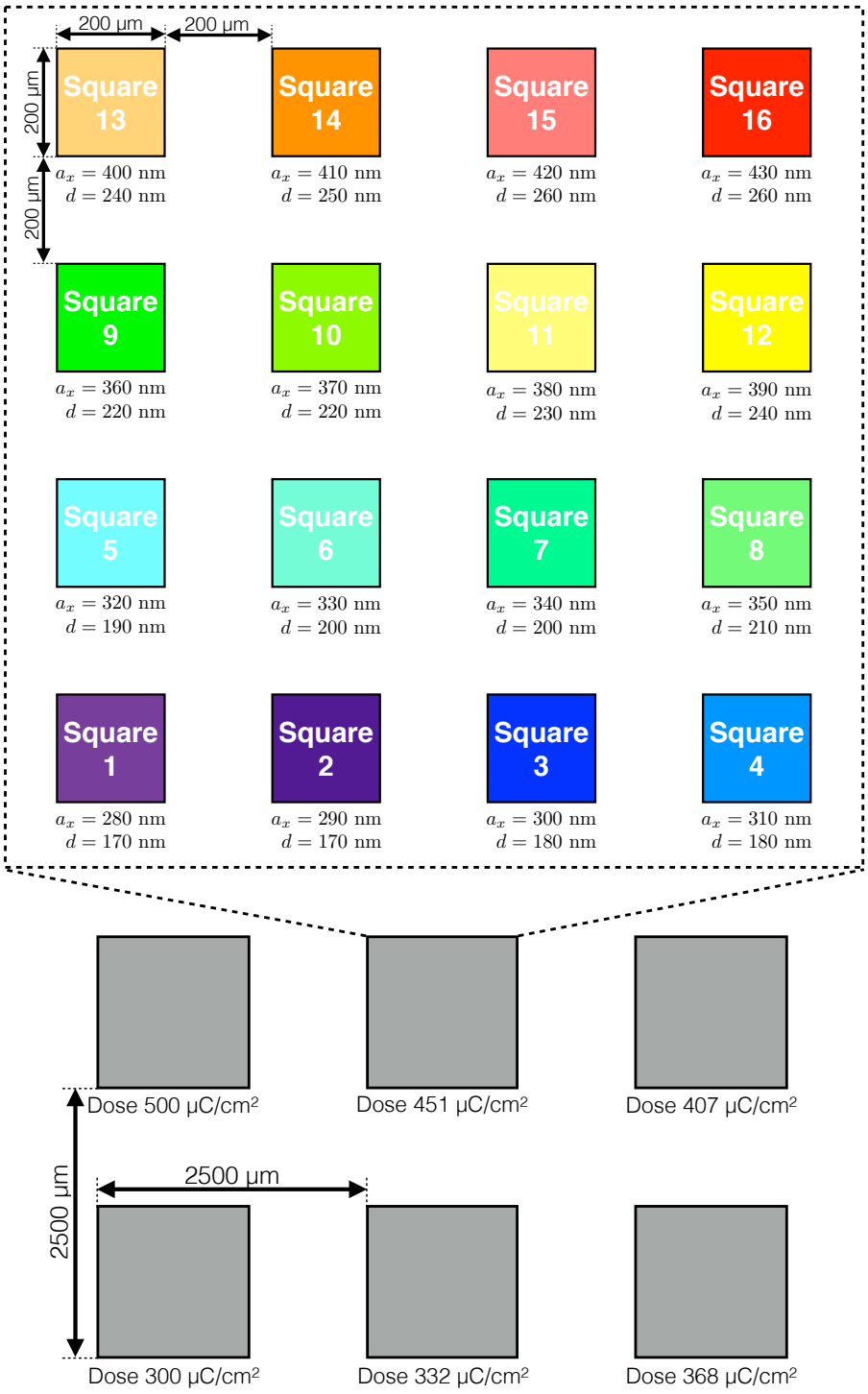
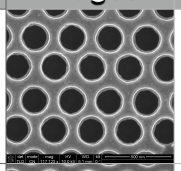
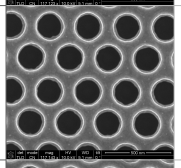
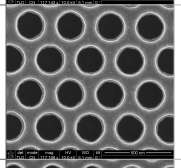
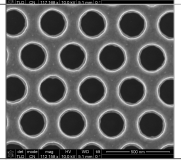
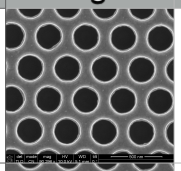
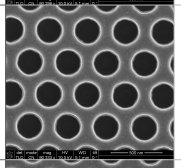
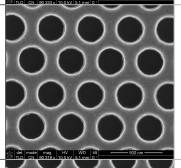
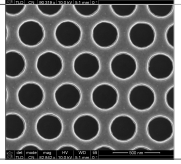
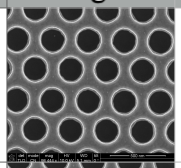
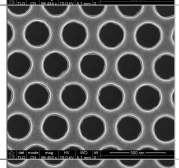
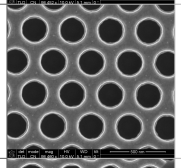
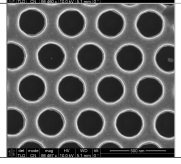


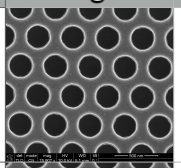
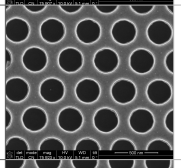
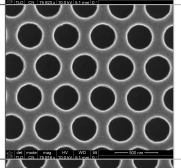
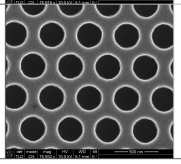
Figure A.3: S24374 E-beam layout

Table A.1: SEM characterization Dose 408 $\mu C/cm^2$

Array	SEM Images	Measured diameters
Square 1 $a_x = 280$ nm $d = 170$ nm		$d_b = 185$ nm $d_t = 210$ nm
Square 2 $a_x = 290$ nm $d = 170$ nm		$d_b = 185$ nm $d_t = 210$ nm
Square 3 $a_x = 300$ nm $d = 180$ nm		$d_b = 195$ nm $d_t = 220$ nm
Square 4 $a_x = 310$ nm $d = 180$ nm		$d_b = 195$ nm $d_t = 220$ nm

Array	SEM Images	Measured diameters
Square 9 $a_x = 360$ nm $d = 220$ nm		$d_b = 240$ nm $d_t = 260$ nm
Square 10 $a_x = 370$ nm $d = 220$ nm		$d_b = 220$ nm $d_t = 245$ nm
Square 11 $a_x = 380$ nm $d = 230$ nm		$d_b = 250$ nm $d_t = 270$ nm
Square 12 $a_x = 390$ nm $d = 240$ nm		$d_b = 260$ nm $d_t = 280$ nm

Array	SEM Images	Measured diameters
Square 5 $a_x = 320$ nm $d = 190$ nm		$d_b = 205$ nm $d_t = 230$ nm
Square 6 $a_x = 330$ nm $d = 200$ nm		$d_b = 220$ nm $d_t = 240$ nm
Square 7 $a_x = 340$ nm $d = 200$ nm		$d_b = 220$ nm $d_t = 240$ nm
Square 8 $a_x = 350$ nm $d = 210$ nm		$d_b = 230$ nm $d_t = 250$ nm

Array	SEM Images	Measured diameters
Square 13 $a_x = 400$ nm $d = 240$ nm		$d_b = 260$ nm $d_t = 280$ nm
Square 14 $a_x = 410$ nm $d = 250$ nm		$d_b = 270$ nm $d_t = 290$ nm
Square 15 $a_x = 420$ nm $d = 260$ nm		$d_b = 280$ nm $d_t = 300$ nm
Square 16 $a_x = 430$ nm $d = 260$ nm		$d_b = 285$ nm $d_t = 300$ nm